

**UNCLASSIFIED**

---

**AD 266 109**

*Reproduced  
by the*

**ARMED SERVICES TECHNICAL INFORMATION AGENCY  
ARLINGTON HALL STATION  
ARLINGTON 12, VIRGINIA**



---

**UNCLASSIFIED**

NOTICE: When government or other drawings, specifications or other data are used for any purpose other than in connection with a definitely related government procurement operation, the U. S. Government thereby incurs no responsibility, nor any obligation whatsoever; and the fact that the Government may have formulated, furnished, or in any way supplied the said drawings, specifications, or other data is not to be regarded by implication or otherwise as in any manner licensing the holder or any other person or corporation, or conveying any rights or permission to manufacture, use or sell any patented invention that may in any way be related thereto.

266109 AFCRL-555(1)



# RADIO CORPORATION OF AMERICA RCA LABORATORIES

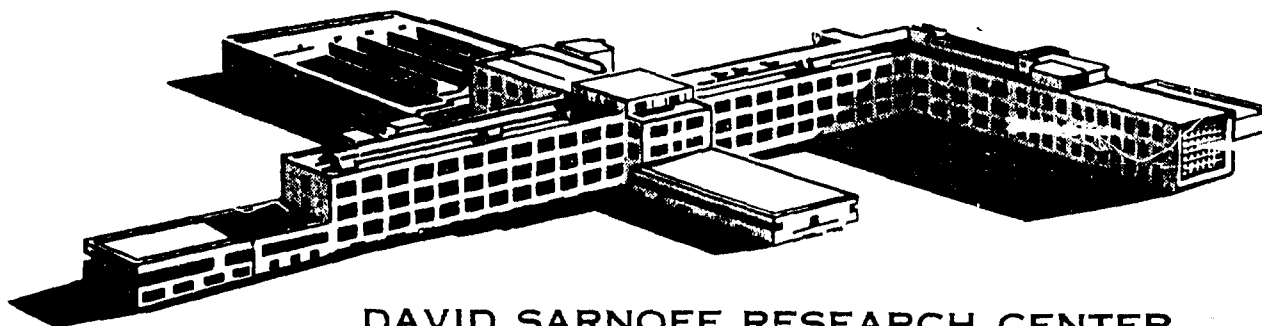
FINAL REPORT

## ELECTRONIC SPECTRA OF TRANSITION METAL IONS IN CRYSTALS

CONTRACT NO. AF19(604)-5541

ELECTRONICS RESEARCH DIRECTORATE  
AIR FORCE CAMBRIDGE RESEARCH LABORATORIES  
OFFICE OF AEROSPACE RESEARCH  
UNITED STATES AIR FORCE  
BEDFORD, MASSACHUSETTS

REPORT DATE: JUNE 1, 1961



DAVID SARNOFF RESEARCH CENTER  
PRINCETON, NEW JERSEY

AFCRL-555(I)

ELECTRONIC SPECTRA OF TRANSITION METAL IONS IN CRYSTALS

Donald S. McClure, Santiago R. Polo, and Herbert A. Weakliem

RCA Laboratories  
Radio Corporation of America  
Princeton, N. J.

Final Report  
Contract No. AF 19(604)-5541

June 1, 1961

Prepared for  
Electronics Research Directorate  
Air Force Cambridge Research Laboratories  
Office of Aerospace Research  
United States Air Force  
Bedford, Massachusetts

Requests for additional copies by Agencies of the Department of Defense their contractors, and other Government agencies should be directed to:

ARMED SERVICES TECHNICAL INFORMATION AGENCY  
ARLINGTON HALL STATION  
ARLINGTON 12, VIRGINIA

Department of Defense contractors must be established for ASTIA services or have their "need-to-know" certified by the cognizant military agency of their project or contract."

All other persons and organizations should apply to the:

U.S. DEPARTMENT OF COMMERCE  
OFFICE OF TECHNICAL SERVICES  
Washington 25, D.C.

## Table of Contents

### Preface

- I. "Optical Spectra of Transition Metal Ions in Corundum", Donald S. McClure
- II. "Optical Spectra of  $\text{Ni}^{++}$ ,  $\text{Co}^{++}$ , and  $\text{Cu}^{++}$  in Tetrahedral Sites in Crystals", Herbert A. Weakliem
- III. "The Optical Absorption Spectrum of  $\text{NiSiF}_6 \cdot 6\text{H}_2\text{O}$ ", Donald S. McClure
- IV. "Exchange Coupled  $\text{Mn}^{++}$  Ions in  $\text{ZnS}$  Single Crystals", Donald S. McClure

The reports in this volume represent two years of work under a contract with the Air Force Cambridge Research Center. These reports are presented as separate investigations, and will be submitted as such to scientific journals.

They form a coherent group of studies, however, much more so than would appear from reading them separately. This is due partly to the overlap of subject matter but more importantly to the fact that they illustrate or depend upon the same general principles. Our main interest is to bring out matters of general importance although these may appear to the reader to have become lost in a mass of details. Consequently the new results will be summarized in this preface.

The research has been (1) a systematic study of the optical spectra of transition metal ions in corundum (2) a systematic study of transition metal ions in wurtzite type lattices (3) an interpretation of the absorption spectrum of nickel fluosilicate (4) a study of the exchange coupled ion pairs in  $\text{ZnS:MnS}$  and (5) completely organizing all of crystal field theory in a form sufficiently general for application to any transition metal or rare earth ion in any crystal field.

The main new result of this work is that we now have a clear understanding of the principles which must be applied in order to interpret optical spectra of ions in crystals. At the beginning of our work it appeared that crystal field theory could be used to calculate the spectra with the only complication being the occurrence of lattice vibration structure superimposed upon the electronic structure. We tacitly assumed that when a foreign cation is introduced into a crystal lattice it occupies

a substitutional cation site and that the surrounding anions have the same symmetry as in the pure crystal. This assumption has now been abandoned, and evidence for three types of exceptions to it has been found:

1. In a non-cubic crystal having a cation site which lacks an inversion center, a foreign cation may move away from the substitutional site without altering the symmetry. The example we have investigated is corundum in which the foreign cation probably moves about  $0.1 \text{ \AA}$  away from the substitutional site along the threefold axis.

2. At a site of high symmetry, such as the tetrahedral sites in ZnS, the foreign ion may destroy the local symmetry if its electronic structure causes large quartic terms to appear in the potential function. This can be interpreted as a second order Jahn-Teller effect. We have a little spectroscopic evidence for this type of distortion in the spectrum of  $\text{Ni}^{++}$  in ZnO, ZnS, etc. and it fits in with magnetic evidence.

3. For ions whose excited states are degenerate in a symmetrical configuration there exists the possibility of the Jahn-Teller effect and the consequent displacement of the equilibrium configuration toward a less symmetrical form. We have found numerous examples in which the electronically excited ion and its immediate surroundings do not have the symmetrical configuration of the ground state. It has become a general rule that the optical spectra do not reflect the symmetry one expects from the ground state except in a few cases. The most probable type of distortion appears to be tetragonal.



These results do not mean that crystal field theory is inapplicable; in fact without the comprehensive theoretical work which has been carried out in crystal field theory it would be impossible to interpret the spectra. The theoretical calculations must be carried out for the stable equilibrium configuration of each electronic state, and this may mean several different calculations for the same ion-host crystal combination. Since we usually do not know this configuration in advance the calculations must be programmed with great flexibility to permit making a number of trials until the spectrum can be fitted. We have only carried out a few rather crude approximations to this procedure, but have reached the point where it is now possible and profitable to do the more complete calculations.

Further, we find that crystal field theory applied to ions in tetrahedral sites accurately describes the observed spectra. This means that configuration mixing between  $(3d)^n$  and  $(4p)(3d)^{n-1}$ , which arises from the lack of a center of symmetry, gives a negligible contribution to the relative energies. The cubic crystal field parameters  $Dq$  which are found are about half as large as those found for the same transition metal ion and ligands in octahedral coordination, which is a result predicted by the simple point charge model for the potential. We have found it necessary to go to a high order of perturbation theory in order to get an accurate fit of theory with experiment since the spin-orbit, crystal field, and electrostatic repulsion energies are all roughly comparable. The parameter  $B$ , which is related to the difference in the interelectronic repulsion energy between the angular momenta states  $P$  and  $F$ , is found to be depressed from the free-ion value. We have obtained an empirical correlation between

the parameter  $B$  for the ion in the crystal and the polarizability of the ligands. We have also related the relative depression of the  $B$  values to a rough measure of the covalent character of the bonding and find that the covalency is in the order  $S^{2-} > Br^{-} > Cl^{-} > O^{2-}$  and is the same for both cobalt and nickel bonded to the same ligands.

The foundation of all the interpretations of spectra are the theoretical calculations. These have been carried out systematically so that any crystal field problem involving  $d$  or  $f$  electrons (except for a few states of some  $f^n$  configurations) can be set up on a computing machine and solved completely. It is no longer necessary to work in either of the extremes of coupling. This work is presented here in the form of tables of transformation coefficients and reduced matrix elements. The Wigner coefficients which have been calculated are not given here because they form a very bulky table, and they have already been published by another group.

The persons principally involved were Dr. Santiago Polo, who carried out the bulk of the theoretical work, Dr. Herbert Weakliem who did spectroscopic, preparative and theoretical work, Dr. Donald McClure who carried out experimental and theoretical work and was responsible for the direction of the project, and Mr. Clyde Neil who capably assisted in all of the experimental work. Important assistance was rendered by Mr. Sherwood Skillman who programmed several lattice sums for the IBM 650, and Mr. Phillip Baltzer who made available his program for the energy levels of the  $d^2$  system in tetragonal crystal fields.

# Optical Spectra of Transition Metal Ions in Corundum

Donald S. McClure

RCA Laboratories, Princeton, N. J.

## ABSTRACT

The polarized optical spectra of the ions  $Ti^{+++}$ ,  $V^{+++}$ ,  $Cr^{+++}$ ,  $Mn^{+++}$ ,  $Co^{+++}$  and  $Ni^{+++}$  in corundum single crystals have been studied at temperatures from 4.2°K to 1200°K. A theory of the intensity based on the point charge model and p-d mixing has been developed and applied to the data with results in fair agreement with experiment. The effects of temperature show that the vibrational-electronic contribution to intensity is quite small at low temperature but may be appreciable at high temperatures. The crystal field parameters have been calculated as convergent lattice sums. The observed trigonal field parameter has the opposite sign from that calculated by the point charge model if the impurity ion is assumed to occupy an  $Al^{+++}$  ion position in the lattice, but has the same sign as calculated for an ion 0.1 Å displaced along the  $c_3$  axis toward the empty octahedral site. Details of the spectra have been interpreted as showing that the surroundings of an ion are distorted in some electronic states.

## Optical Spectra of Transition-Metal Ions in Corundum

Donald S. McClure

RCA Laboratories, Princeton, N. J.

### I. Introduction

A foreign cation at a substitutional site in a crystal will be subject to a crystal field which is approximately that of the undisturbed crystal. In a cubic crystal the foreign ion either resides exactly on the cation site or the symmetry of the crystal is reduced in its vicinity. Electronic transitions at a cubic site are forbidden in transition-metal ions and their spectra are complicated by the presence of vibrational-electronic interaction. The crystal field must, however, have cubic symmetry except in cases where the radius ratios are quite different for host and guest cations, or when the Jahn-Teller effect occurs. In a crystal of the corundum type, there is no center of symmetry at the cation site and electronic transitions occurring in transition-metal ions are permitted without the intercession of vibrations. The spectra may be considerably simplified as a result. On the other hand, the impurity cation need not change the symmetry of the lattice if it moves away from the cation site. The normal adjustments of the positions of the ions in the locale of the impurity following the change in ionic radii will cause a shift of the impurity along the three-fold axis. The crystal field is therefore not as well defined as in cubic crystals.

In this study of the spectra of the first transition-group ions in corundum, we have attempted first of all to understand the spectra in detail: this includes relative intensities and polarizations, band

energies and details of band features. The interpretation has been made by using the point charge model in various ways, but never to rely on its predictions of absolute magnitudes. By studying the entire series of ions, regularities are found and the level of confidence in specific results is made clearer. Some deductions relevant to the position of the ion in the lattice are then made.

## II. Experimental

The crystals used were grown by the flame fusion method. The impurity content added to the starting material was on the order of 0.2 mole percent. The crystals were oriented by x-rays and were then cut to the required dimensions and polished with a diamond abrasive. The cut most often used was one in which the c-axis lay in the plane perpendicular to the direction of propagation of the light. In this way, one could observe spectra in both polarizations of light with the same crystal.

The spectra were taken with a Cary Model 14 spectrophotometer, and a Jarrell-Ash 3-meter grating (15000 lines/in) in the Ebert mounting. In each case, the spectra were polarized: by means of a Foucault prism mounted between the final slit and the chopper compartment in the Cary 14; and by means of a Wollaston double image prism mounted far enough in front of the slit of the grating spectrograph to produce separated images of the crystal on the plate.

All spectra were observed at temperatures of 77 and 298°K. In some cases noted later, it was necessary to use helium temperatures, and sometimes to go to high temperatures, on the order of 1300°K. The high temperature spectra were done with a nichrome wound furnace which fits

into the Cary 14 cell compartment. A chromel-alumel thermocouple mounted in contact with the sample was used to measure temperatures. The temperature was not controlled, but never fluctuated more than 10 degrees, which was not serious for the experiments being done. The infra-red optics of the Cary 14 were used so as to remove most of the black body radiation of the sample by the monochrometer. Since most of the measurements were in the visible or ultraviolet, the sample radiation was not a serious factor as high as  $1000^{\circ}\text{C}$  with this arrangement.

Wavelengths were converted to wavenumbers by using Kayser's tables<sup>(1)</sup>.

### III. Theoretical Framework

The crystal structure of corundum<sup>(2),(3)</sup> is illustrated in figs. 1a and 1b, showing respectively a view parallel to  $c$  and perpendicular to  $c$ . Pairs of  $\text{Al}$ -atoms are stacked along the  $c$ -direction. These are surrounded by trigonally distorted octahedra of oxygen. The two  $\text{Al}$ -atoms of the pair share the equilateral triangle of  $\text{O}$ -atoms lying between them. The  $\text{Al}-\text{O}$  distance in this case is  $1.969 \text{ \AA}$ . The other triangle of each octahedron is larger and lies closer to the  $\text{Al}$ -atom than does the first. This  $\text{Al}-\text{O}$  distance is  $1.856 \text{ \AA}$ . Thus the site symmetry of the  $\text{Al}$  atom would be  $\text{C}_{3v}$  if no other distortions occurred. However, the upper and lower triangles are rotated away from the  $\sigma_v$  planes by  $2^{\circ}8.5'$  in opposite directions, thus destroying the  $\sigma_v$  planes. This loss of symmetry is so slight however, that the site group  $\text{C}_{3v}$  may be retained for many purposes. The relations between the relevant symmetry groups are given in Table I.

The potential function of crystal field theory for an impurity ion in the crystal lattice<sup>(4)</sup> may be calculated assuming that the ion occupies the  $Al^{+++}$  position. The symmetry of the surroundings of the ion are not altered if it moves along the c-axis away from the  $Al^{+++}$  position. Potential constants were therefore calculated for two displaced positions:  $+0.1 \text{ \AA}$ , toward empty octahedral site on c-axis and  $-0.1 \text{ \AA}$ , the opposite direction. These calculations were made assuming no other atoms moved.

The computations were made by summing directly over the lattice. This procedure is adequate for the second and higher powers, but not for the first, where the Ewald method should be used. The zeroth term is simply the Madelung energy per  $Al^{+++}$  ion. Since the calculations were made on a small machine (IBM 650) the summations over the lattice were not carried out to convergence of the second power term, but for this case we could compare the results to Bersohn's<sup>(5)</sup>.

The lattice parameters and atomic positions used are given in Table II. The impurity atom was placed at  $00w$  plus  $000$ ,  $00z$ , or  $00-z$ , where  $z$  corresponds to the  $0.1 \text{ \AA}$  displacement.

The potential function for an electron on the impurity ion may be written:

$$\begin{aligned}
 V = & B_0^0 + B_1^0 r \cos \theta + B_2^0 r^2 (3 \cos^2 \theta - 1) + B_3^0 r^3 (5 \cos^3 \theta - 3 \cos \theta) \\
 & + B_3^3 r^3 \sin^3 \theta \cos 3\phi + C_3^3 r^3 \sin^3 \theta \sin 3\phi \\
 & + B_4^0 r^4 (35 \cos^4 \theta - 30 \cos^2 \theta + 3) + B_4^3 r^4 \sin^3 \theta \cos \theta \cos 3\phi \\
 & + C_4^3 r^4 \sin^3 \theta \cos \theta \sin 3\phi + \text{higher power terms.}
 \end{aligned} \tag{1}$$

Here,  $r$ ,  $\theta$  and  $\phi$  are coordinates of an electron. The B constants are the ones which appear when the site symmetry is assumed to be  $C_{3v}$ , while

the C constants are brought in when the true symmetry,  $C_3$ , is used. Terms higher than the fourth power are not needed when we are only dealing with problems involving d-electrons.

The potential constants are the following lattice sums over functions of the atomic coordinates when the point charge model is assumed:

$$\begin{aligned}
 B_0^0 &= \frac{ne}{R} \\
 B_1^0 &= \frac{ne}{R^2} \cos \theta \\
 B_2^0 &= \frac{ne}{4R^3} (3 \cos^2 \theta - 1) \\
 B_3^0 &= \frac{ne}{4R^4} (5 \cos^3 \theta - 3 \cos \theta) \\
 B_3^3 &= \frac{5ne}{8R^4} \sin^3 \theta \cos 3\phi \\
 C_3^3 &= \frac{5ne}{8R^4} \sin^3 \theta \sin 3\phi \\
 B_4^0 &= \frac{ne}{64R^5} (35 \cos^4 \theta - 30 \cos^2 \theta + 3) \\
 B_4^3 &= \frac{70ne}{16R^5} \sin^3 \theta \cos \theta \cos 3\phi \\
 C_4^3 &= \frac{70ne}{16R^5} \sin^3 \theta \cos \theta \sin 3\phi
 \end{aligned} \tag{2}$$

Here,  $R$ ,  $\theta$ ,  $\phi$  are coordinates of a lattice site;  $n$  is either 1 or 3 depending on whether or not the representative atom lies on the threefold axis passing through the impurity atom. Thus each term of  $B$  or  $C$  refers to a set of equivalent atoms. The orientation of the coordinate axes is important. Take the  $c$ -axis to be positive in the vertical direction. The impurity is located in the Al site lying immediately below the empty octahedral site. The angle  $\theta$  is measured from the positive  $c$ -axis and the angle  $\phi$  is measured counterclockwise around  $c$  from one of the upper



TABLE I

Character tables for symmetry groups and correlations among groups for Al site in corundum.

O	E	$\bar{E}$	$8C_3$	$8\bar{C}_3$	$3C_2, 3\bar{C}_2$	$6C'_2, 6\bar{C}'_2$	$6C_4$	$6\bar{C}_4$	$C_{3v}$
$A_1$	1		1		1	1	1		$A_1$
$A_2$	1		1		1	-1	-1		$A_2$
E	2		-1		2	0	0		E
$T_1$	3		0		-1	-1	1		$A_2 + E$
$T_2$	3		0		-1	1	-1		$A_1 + E$
$E_{1/2}$	2	-2	1	-1	0	0	$\sqrt{2}$	$-\sqrt{2}$	$E_{1/2}$
$E_{3/2}$	2	-2	1	-1	0	0	$-\sqrt{2}$	$\sqrt{2}$	$E_{3/2}^+ + E_{3/2}^-$
G	4	-4	-1	1	0	0	0	0	$E_{1/2} + E_{3/2}^+ + E_{3/2}^-$

$C_{3v}$	E	$\bar{E}$	$C_3, \bar{C}_3^2$	$\bar{C}_3, C_3^2$	$3\sigma_v$	$3\bar{\sigma}_v$	$C_3$
$A_1$	1		1		1		$A$
$A_2$	1		1		-1		$A$
E	2		-1		0		E
$E_{1/2}$	2	-2	1	-1	0	0	$E_{1/2}^+ + E_{1/2}^-$
$E_{3/2}^+$	1	-1	-1	1	i	-i	$A_{3/2}$
$E_{3/2}^-$	1	-1	-1	1	-i	i	$A_{3/2}$

$C_3$	E	$\bar{E}$	$C_3$	$\bar{C}_3$	$C_3^2$	$\bar{C}_3^2$	
$A$	1		1		1		
$E^+$	1		$\omega$		$\omega^2$		
$E^-$	1		$\omega^2$		$\omega$		
$E_{1/2}^+$	1	-1	$-\omega^2$	$\omega^2$	$\omega$	$-\omega$	$\omega = e^{2\pi i/3}$
$E_{1/2}^-$	1	-1	$-\omega$	$\omega$	$\omega^2$	$-\omega^2$	
$A_{3/2}$	1	-1	-1	1	1	-1	

TABLE II

Atomic positions and lattice parameters for corundum. Hexagonal coordinates. Space group  $D_{3d}^6$ . (parameters and lattice constants from R. Newnham, ref. 3).

$$\text{Aluminum:} \quad \begin{array}{ccc} a & b & c \\ 0 & 0 & w \\ 0 & 0 & -w \\ 0 & 0 & 1/2+w \\ 0 & 0 & 1/2-w \end{array} \left. \vphantom{\begin{array}{ccc} a & b & c \\ 0 & 0 & w \\ 0 & 0 & -w \\ 0 & 0 & 1/2+w \\ 0 & 0 & 1/2-w \end{array}} \right\} + \left\{ \begin{array}{ccc} 0 & 0 & 0 \\ 1/2 & 2/3 & 2/3 \\ 2/3 & 1/3 & 1/3 \end{array} \right\} + h k l$$

$$\text{Oxygen:} \quad \begin{array}{ccc} v & 0 & 0 \\ \bar{v} & \bar{v} & 0 \\ 0 & \bar{v} & 0 \\ \bar{v} & 0 & 1/2 \\ v & v & 1/2 \\ 0 & \bar{v} & 1/2 \end{array} \left. \vphantom{\begin{array}{ccc} v & 0 & 0 \\ \bar{v} & \bar{v} & 0 \\ 0 & \bar{v} & 0 \\ \bar{v} & 0 & 1/2 \\ v & v & 1/2 \\ 0 & \bar{v} & 1/2 \end{array}} \right\} + \left\{ \begin{array}{ccc} 0 & 0 & 0 \\ 1/3 & 2/3 & 2/3 \\ 2/3 & 1/3 & 1/3 \end{array} \right\} + h k l$$

$$w = 0.102 \quad v = 0.306$$

$$A_o = 4.7588 \text{ \AA} \quad C_o = 12.987 \text{ \AA}$$

oxygens in the nearest neighbor shell. The quantity  $e$  was given the value 14.3923 eV,  $R$  is expressed in  $\text{\AA}$ . In the summations over the lattice, the oxygen contributions were multiplied by +1 and the aluminum contributions by -3/2, and these were then added. The summations were carried out to several values of  $R_{\text{max}}$ : 3.86, 5.81, 7.59 and 9.52  $\text{\AA}$ . The convergence behavior of the sums could be judged from these results. The third and fourth power terms changed very little after 5.81  $\text{\AA}$ . The term  $B_2^0$  kept the same sign as for nearest neighbors but changed considerably between 7.59 and 9.52  $\text{\AA}$ . Bersohn carried out the sum to about 20  $\text{\AA}$  and showed that the sum had ceased to fluctuate appreciably. He obtained  $10.4209 \text{ ea}_0^{-3}$  while we obtained  $13.335 \text{ ea}_0^{-3}$ . Bersohn's result has some experimental verification since it gives an antishielding factor for the Al nucleus having the correct sign and approximately the correct magnitude. His value will be used in this paper. The values of the second power term in displaced positions were obtained from our results at 9.52  $\text{\AA}$  multiplied by 10.4209/13.3350. The potential constants are given in Table III.

The basis functions which have been used in this paper are the transforms of cubic field basis functions shown in Table IV. Also shown in Table IV are their functional forms in a cartesian coordinate system whose  $z$  axis is the 111 axis of a cubic coordinate system. The  $x$ -axis lies in the approximate reflection plane when the surroundings of the ion are supposed to have the symmetry  $C_{3v}$ . Therefore one partner  $E^+$  of an  $E$  function is invariant under  $\sigma_v$  and the other partner,  $E^-$ , changes sign. The same transformation matrix converts both the basis functions and the

TABLE III

Potential constants for impurity ion in corundum. Ion in  $\text{Al}$  position, 0.0, or displaced  $\pm 0.1 \text{ \AA}$  along  $c$  (see text). Metal to nearest oxygen distances: 0.0  $\text{\AA}$  position; 1.969, 1.856  $\text{\AA}$ ; 0.1  $\text{\AA}$  position; 2.037, 1.813  $\text{\AA}$ ; -0.1  $\text{\AA}$  position; 1.903  $\text{\AA}$ , 1.903  $\text{\AA}$ . The numbers in the table are in electron volts per unit charge on the  $\text{O}^{2-}$  ion per ( $\text{\AA}$ )<sup>3</sup>, and have the correct sign for a negative test charge.

Ion Position	Summation Distance, $\text{\AA}$	$B_0^0$	$B_1^0$	$B_2^0$	$B_3^0$	$E_3^3$	$C_3^3$	$B_4^0$	$B_4^3$	$C_4^3$
+ 0.1 $\text{\AA}$	nn					1.2389			4.307	
	7.59					1.1715			4.112	
	9.52			- .2981	- .5018	1.1770		- .0829	4.115	
	$\infty$			(- .2335)						
0.0 $\text{\AA}$	nn	45.16	- 1.826	- .1441	- .4575	.8519	.327	- .1290	4.435	1.008
	7.59			- .0907	- .2968	.7590	.049	- .1435	4.240	
	9.52			- .1775	- .3001	.7593	.038	- .1434	4.239	
	$\infty$			- .1378						
- 0.1 $\text{\AA}$	nn					.4010			4.589	
	7.59					.3303			4.393	
	9.52			- .1243	- .0501	.3202		- .1736	4.391	
	$\infty$			(- .0973)						

The number of atoms in the summations are as follows:

Al	nn	7.59	9.52
	0	88	146
O	6	129	243

coordinate system when the correlations of Table IV are followed. Four of the basis functions fall into two E representations of  $C_{3v}$  and one falls into  $A_1$  of  $C_{3v}$ .

The matrix elements of the potential between d-electron states only involve the second and fourth power potential terms. The energy of a d-electron is affected mainly by the cubic field, a fourth power term, and very little by the trigonal field which arises from a second and a fourth power term. The actual field is conveniently expressed as the sum of a cubic and axial field. In a strictly cubic field we would have the relation  $(B_4^3)_c = -20\sqrt{2}(B_4^0)_c$ . The trigonal component of the fourth power term can thus be expressed as the deviation from this equality, and we may write:

$$V_4 = [B_4^0 - (B_4^0)_c] (35 \cos^4 \theta - 30 \cos^2 \theta + 3)r^4 + B_4^3 [\sin^3 \theta \cos \theta \cos 3\phi - \frac{1}{20\sqrt{2}} (35 \cos^4 \theta - 30 \cos^2 \theta + 3)] r^4 \quad (3)$$

where the first part is the trigonal (axial) field, the second the cubic field. For  $B_4^0 - (B_4^0)_c$  we can substitute  $B_4^0 + \frac{B_4^3}{20\sqrt{2}}$ .

The energy matrix of this potential has in it different diagonal elements of the trigonal field in each of the states  $A_1$ , E and E. The t states are split apart by the trigonal field but the e state is only displaced. The separation of the e state from the center of gravity of the t states will be called  $10 Dq$  even though a small part of this splitting is due to the trigonal field. This traditional constant must therefore be defined in the following way:

TABLE IV

Transformation from cubic to trigonal one-electron functions, and from cubic to trigonal coordinates. The  $t_2$  functions and coordinates are transferred by the same matrix, T. The cubic functions transform like:  $t_{xy} = xy$ ,  $t_{xz} = xz$ ,  $t_{yz} = yz$ ,  $e_b = \frac{1}{2\sqrt{3}}(2z^2 - x^2 - y^2)$ ,  $e_a = \frac{1}{2}(x^2 - y^2)$ .

$$T = \begin{vmatrix} 2/\sqrt{6} & -1/\sqrt{6} & -1/\sqrt{6} \\ 0 & -1/\sqrt{2} & 1/\sqrt{2} \\ 1/\sqrt{3} & 1/\sqrt{3} & 1/\sqrt{3} \end{vmatrix}; \quad T = \begin{array}{c|c|c} \text{cubic} & & \text{trigonal} \\ \hline z & & x \\ y & = & y \\ x & & z \end{array}$$

$$T = \begin{array}{c|c|c|c} \text{cubic} & & \text{trigonal} & \text{Rep'n in } C_{3v} \\ \hline t_{xy} & & t_x & E^+ \\ t_{xz} & = & t_y & E^- \\ t_{yz} & & t_z & A_1 \end{array} \begin{array}{c} \frac{1}{\sqrt{6}}(x^2 - y^2 - \sqrt{2} xz) \\ -\frac{\sqrt{15}}{4\pi} - \frac{1}{\sqrt{3}}(\sqrt{2} xy + yz) \\ \frac{1}{\sqrt{3}}(z^2 - \frac{1}{2}x^2 - \frac{1}{2}y^2) \end{array}$$

$$\begin{array}{c|c|c|c} \text{cubic} & & \text{trigonal} & \\ \hline 1 & 0 & e_b & = e_x \\ 0 & 1 & e_a & = e_y \end{array} = \begin{array}{c} \frac{1}{2\sqrt{3}}(x^2 - y^2 + 2\sqrt{2} xz) \\ -\frac{1}{\sqrt{3}}(xy - \sqrt{2} yz) \end{array} \begin{array}{c} E^+ \\ E^- \end{array}$$

$$Dq = \left[ \frac{3\sqrt{2}}{4} B_4^3 - \frac{4}{27} (B_4^0 + \frac{B_4^3}{20\sqrt{2}}) \right] \frac{2}{105} \overline{r^4} \quad (4)$$

The splitting between the  $t(A_1)$  and  $t(E)$  levels will be given by

$$v = \frac{6}{7} B_2^0 \overline{r^2} + \frac{160}{63} (B_4^0 + \frac{B_4^3}{20\sqrt{2}}) \overline{r^4} \quad (5)$$

and the small coupling term between the  $t(E)$  and  $e(E)$  states by

$$v' = -\frac{2\sqrt{2}}{7} B_2^0 \overline{r^2} + \frac{40\sqrt{2}}{63} (B_4^0 + \frac{B_4^3}{20\sqrt{2}}) \overline{r^4} \quad (6)$$

The energy matrix then has the following form:

$$\begin{array}{l} A_1(t) \\ E(t) \\ E(e) \end{array} \left| \begin{array}{cc} \frac{2}{3} v - 4 Dq & \\ -\frac{1}{3} v - 4 Dq & v' \\ v' & 6 Dq \end{array} \right| \quad (7)$$

The three parameters in these equations are in principal directly measurable spectroscopically. Their formulas in terms of the point charge model are given in Table V.

In this work we have avoided using the values of  $\overline{r^n}$  by taking ratios or by considering them as adjustable parameters. The values were actually computed from Watson's S.C.F. functions<sup>(6)</sup>, but were used only as rough guides as to magnitudes of the potential constants. Their variation with atomic number is much too strong to result in realistic comparisons with experiment. For example,  $\overline{r^4}$  changes from 7.07 a.u. in  $Ti^{+++}$  to 2.38 a.u. in  $Co^{+++}$ , while the values of  $Dq (\sim \overline{r^4})$  change from 1980 to 1830  $cm^{-1}$ . Clearly some other very important factor is not taken into account by the point charge model. We may be able to believe the types of predictions

TABLE V

Values of  $Dq$ ,  $v$  and  $v'$  in point charge model.Numbers are eV per unit charge on  $O^{2-}$   $\bar{r}^n$  in  $(\text{\AA})^n$ 

Ion Position	$Dq$	$v$	$v'$
+ 0.1 $\text{\AA}$	$0.07558 \bar{r}^4$	$- 0.200 \bar{r}^2 + 0.167 \bar{r}^4$	$0.00945 \bar{r}^2 + 0.0591 \bar{r}^4$
0.0 $\text{\AA}$	$0.08665 \bar{r}^4$	$- 0.119 \bar{r}^2 + 0.0261 \bar{r}^4$	$0.00562 \bar{r}^2 + 0.00922 \bar{r}^4$
- 0.1 $\text{\AA}$	$0.09350 \bar{r}^4$	$- 0.0833 \bar{r}^2 - 0.0261 \bar{r}^4$	$0.00394 \bar{r}^2 - 0.00922 \bar{r}^4$



of this model which do not depend on  $\overline{r^n}$ , or we may be able to determine empirically such ratios as  $\overline{r^4}/\overline{r^2}$ , and use them for valid predictions.

In fact the results obtained by these procedures do seem to be believable.

The absence of a center of symmetry in the corundum lattice makes it possible for electric dipole  $d \longrightarrow d$  transitions to occur. This can come about because odd power terms may mix the even d-functions with odd functions. The latter may be either atomic p-functions or odd molecular orbitals on the ligands. We will be concerned mainly with one-electron transitions of the type  $t \longrightarrow e$ . Then whatever the type of perturbation, there will be certain symmetry relations between the various possible transitions. These are expressed by the following relations for the symmetry  $C_{3v}$ :

$$\begin{aligned} (t_x | x | e_x) &= - (t_x | y | e_y) = - (t_y | y | e_x) = - (t_y | x | e_y) \equiv A \\ (t_z | x | e_x) &= (t_z | y | e_y) \equiv B \\ (t_x | z | e_x) &= (t_y | z | e_y) \equiv C \end{aligned} \quad (8)$$

The direction of the transition moment is given by x, y, or z, where these are in the trigonal coordinate system. x and y are perpendicular to the c-axis while z is parallel to it. The constants A, B and C represent the magnitude of the three types of transition moment. Their values in terms of the point charge model, and assuming that p-states are mixed with the d-orbitals, are given in Table VI.

It was found that the selection rules for  $C_{3v}$  are not accurately followed and it is necessary to use the true site symmetry,  $C_3$ . Then eight additional one-electron transitions are possible. Note that there

would be 18 when no symmetry is present, and 16 are possible in  $C_3$ . Three additional constants appear on reduction of symmetry from  $C_{3v}$  to  $C_3$ . However, since the departure from  $C_{3v}$  is slight, only one additional constant will be introduced, the other two being related to the first by means of the point charge model. Any error introduced by this procedure will only be an error in a rather small correction term. The constant introduced is the magnitude  $D$  of the one-electron transition  $(e_y | x | t_z)$ . This is representative of transition moment integrals which change sign under reflection in the pseudo symmetry plane. The one-electron transitions are summarized in Table VI.

The four constants which determine the intensity may, in principle, be obtained empirically from the spectra. They are expressed in terms of only two constants,  $\bar{r}$  and  $\bar{r}^3$ , when the point charge model is used.

The optical spectra are expected to be determined mainly by selection rules for  $C_{3v}$ , shown in Table VII, but strictly by  $C_3$ , also shown in this Table. The states are mainly determined by the cubic field but split into trigonal components as shown in Table I.

The intensity formulas for several-electron atoms are derived from the results of Table V with the help of wave functions for the many electron case. The wave functions chosen are shown in Table VIII, and the intensity formulas are given in Table IX for one, two and three electrons. The high-spin states of  $d^4$  have the same intensity formulae as  $d^1$  and the singlets of  $t^5e$  in  $d^6$  have the same formulae as  $d^3$  when the proper correlations are made, namely:  ${}^1A_1(t^6) \longrightarrow {}^4A_2(t^3)$ ;  ${}^1T_1(t^5e) \longrightarrow {}^4T_2(t^2e)$ ;  ${}^1T_2(t^5e) \longrightarrow {}^4T_1(t^2e)$ .

TABLE VI  
One-electron transition moments in corundum structure.

	$M_x$	$M_y$	$M_z$
$e_x t_x$	A	$-2\sqrt{2}D$	C
$e_y t_y$	-A	$2\sqrt{2}D$	C
$e_x t_y$	$-2\sqrt{2}D$	-A	-3D
$e_y t_x$	$-2\sqrt{2}D$	-A	3D
$e_x t_z$	B	-D	0
$e_y t_z$	D	B	0

Values of constants for p-d mixing in point charge model:

$$A = \frac{1}{3} B_1^0 \bar{r} - \frac{2}{7} B_3^0 \bar{r}^3$$

$$B = \frac{\sqrt{2}}{3} B_1^0 \bar{r} + \frac{8\sqrt{2}}{7} B_3^0 \bar{r}^3 + \frac{2}{7} B_3^3 \bar{r}^3$$

$$C = \frac{-2\sqrt{2}}{3} B_1^0 \bar{r} + \frac{4\sqrt{2}}{7} B_3^0 \bar{r}^3 + \frac{6}{7} B_3^3 \bar{r}^3$$

$$D = \frac{2}{7} C_3^3 \bar{r}^3$$

TABLE VII

Selection and polarization rules for electric dipole transitions in ions in corundum.

$C_3$		A	A	E	$E_{1/2}$	$A_{3/2}$
	$C_{3v}$	$A_1$	$A_2$	E	$E_{1/2}$	$E_{3/2}$
A	$A_1$		O	$\perp$		
A	$A_2$	O		$\perp$		
E	E	$\perp$	$\perp$	$\perp +   $		
$E_{1/2}$	$E_{1/2}$				$\perp +   $	$\perp$
$A_{3/2}$	$E_{3/2}$				$\perp$	

The notation for electronic states which will be used in this paper is illustrated in Table VIII. The cubic field parent such as  ${}^3T_1$  is given first, showing the multiplicity and the cubic field representation. Following this is the strong field configuration such as  $t^2$ , and following this is the trigonal field representation, such as  $A_2$ , giving a complete three part symbol  ${}^3T_1 t^2 A_2$ .

#### IV. Results: Intensities and Energies

The questions to which we have obtained some answers are these:

- 1) How well does the point charge model give the energies and intensities of the spectra?
- 2) What is the explanation of the band shapes?
- 3) Do cations which substitute in the corundum lattice occupy the  $Al^{+++}$  positions fairly closely, or do they move away appreciably in order to accomodate the different ionic radius?

The data which has been collected are: integrated band intensities as a function of temperature, band positions as a function of temperature, trigonal splitting measured from spectra or from high temperature experiments, and details of band structure. Figures 2 through 7 give a general comparison of the spectra from  $Ti^{+++}$  to  $Ni^{+++}$ ,  $d^1$  to  $d^7$ . Table X gives the centroid positions and integrated intensities of the observed bands at  $77^\circ K$ , and the ground states. The bands are labeled according to the cubic field state from which they arise and their polarization. Chemical analyses were carried out on some of the samples so that absolute intensities have been given. Although the relative band intensity values are correct for a given ion, there are uncertainties in the absolute values which will be discussed at the end of this section. In section V the spectral details

TABLE VIII

Wave functions for two and three electrons for high-spin strong-field states of ions in corundum. A term such as  $e_x t_z t_x$  means  $e_x(1)t_z(2)t_x(3)$ . The antisymmetrizing operator must be applied to the functions given.

 $d^2$  State

$${}^3T_1 t^2 A_2 \quad t_x t_y$$

$${}^3T_1 t^2 E \quad t_z t_x, t_y t_z$$

$${}^3T_2 et A_1 \quad \frac{1}{\sqrt{2}} (e_x t_x + e_y t_y)$$

$${}^3T_2 et E \quad \frac{1}{2} (e_x t_x - e_y t_y) + \frac{1}{\sqrt{2}} e_x t_z, \frac{1}{2} (e_x t_y + e_y t_x) - \frac{1}{\sqrt{2}} e_y t_z$$

$${}^3T_1 et A_2 \quad \frac{1}{\sqrt{2}} (e_x t_y - e_y t_x)$$

$${}^3T_1 et E \quad \frac{1}{2} (e_x t_x - e_y t_y) - \frac{1}{\sqrt{2}} e_x t_z, \frac{1}{2} (e_x t_y + e_y t_x) + \frac{1}{\sqrt{2}} e_y t_z$$

 $d^3$  State

$${}^4A_2 t^3 A_2 \quad t_x t_y t_z$$

$${}^4T_2 t^2 e A_1 \quad \frac{1}{\sqrt{2}} (e_x t_x t_x - e_y t_y t_z)$$

$${}^4T_2 t^2 e E \quad \frac{1}{2} (e_x t_y t_z - e_y t_z t_x) - \frac{1}{\sqrt{2}} e_x t_x t_y, \frac{1}{2} (e_x t_x t_x + e_y t_y t_z) + \frac{1}{\sqrt{2}} e_y t_x t_y$$

$${}^4T_1 t^2 e A_2 \quad \frac{1}{\sqrt{2}} (e_x t_y t_z + e_y t_x t_x)$$

$${}^4T_1 t^2 e E \quad \frac{1}{2} (e_x t_y t_z - e_y t_x t_x) + \frac{1}{\sqrt{2}} e_x t_x t_y, \frac{1}{2} (e_x t_x t_x + e_y t_y t_z) - \frac{1}{\sqrt{2}} e_y t_x t_y$$

TABLE IX

Intensity formulas for one, two and three d-electron ions in corundum.

No. of d-electrons	Ground State	Excited State	Intensity	
			$\perp C$	$\parallel C$
1	${}^2T_2 \text{ t E}$	${}^2E \text{ e E}$	$2A^2 + 16D^2$	$2C^2 + 18D^2$
	${}^2T_2 \text{ t A}$	${}^2E \text{ e E}$	$B^2 + D^2$	0
2	${}^3T_1 \text{ t}^2 A^2$	${}^3T_2 \text{ et A}$	0	$18D^2$
		${}^3T_2 \text{ et E}$	$A^2 + 8D^2$	0
		${}^3T_1 \text{ et A}$	0	$2C^2$
		${}^3T_1 \text{ et E}$	$A^2 + 8D^2$	0
	${}^3T_1 \text{ t}^2 E$	${}^3T_2 \text{ et A}$	$B^2 + D^2$	0
		${}^3T_2 \text{ et E}$	$(A - B/\sqrt{2})^2 + 9/2 D^2$	$C^2 + 9/2 D^2$
		${}^3T_1 \text{ et A}$	$B^2 + D^2$	0
		${}^3T_1 \text{ et E}$	$(A + B/\sqrt{2})^2 + 25/2 D^2$	$C^2 + 9/2 D^2$
3	${}^4A_2 \text{ t}^3 A$	${}^4T_2 \text{ et}^2 A$	0	$18D^2$
		${}^4T_2 \text{ et}^2 E$	$(A - B/\sqrt{2})^2 + 9/2 D^2$	0
		${}^4T_1 \text{ et}^2 A$	0	$2C^2$
		${}^4T_1 \text{ et}^2 E$	$(A + B/\sqrt{2})^2 + 25/2 D^2$	0

observed at low temperatures are interpreted; in section VI the high temperature results are given and in section VIII the nature of the trigonal field is considered. Further discussion must be carried out for individual ions.

Ti<sup>+++</sup>

The polarized spectrum at 77° is shown in Fig. 2. The diffuse double humped band due to  ${}^2T_2 \longrightarrow {}^2E$  is stronger when observed with light polarized parallel to the  $C_3$  axis than with light polarized perpendicular to it. The polarization ratio was determined by integrating the absorption over frequency for each component. The ratio found at 77°K is  $\frac{I_{||}}{I_{\perp}} = 3.2$ . Both the total intensity and the polarization ratio change by less than ten percent when the temperature is raised to 300°K.

The observed polarization is compatible only with the assumption  $v > 0$ . In this case the E component of the  ${}^2T_2$  state lies below the  $A_1$  component and the transition may occur in x, y or z directions. If  $A_1$  were to lie lowest, the z-polarized absorption would be forbidden, in either  $C_{3v}$  or  $C_3$ , according to Table VII, whereas it is observed to appear strongly. The theoretical polarization ratio in  $C_{3v}$  symmetry as obtained from Table IX is:

$$\frac{I_{||}}{I_{\perp}} = \frac{C^2}{A^2} \quad (9)$$

Using a point charge model of the surrounding anions, the intensity ratio is calculated to be 8 when only the dipolar part of the anion field is used, and 17 when only the octupolar part is used. The calculation is thus qualitatively correct. When the symmetry is reduced to  $C_3$ , the intensity



TABLE X

Ground States, centroids of strong bands ( $\nu$  in  $\text{cm}^{-1}$ ) and integrated band intensities ( $f \times 10^4$ ) for trivalent ions in corundum at 77°K. For a one-dimensional oscillator  $f = 0.143 \times 10^{-8} \int \epsilon d\nu$ .

State	Ti	V	Cr	Mn	Fe	Co	Ni
ground	${}^2T_2 t E$	${}^3T_1 t^2 A_2$	${}^4A_2 t^3 A_2$	${}^5E t^3 e E$	${}^6A_1 t^3 e^2 A_1$	${}^1A_1 t^6 A_1$	${}^2E t^6 e E$
1 <sup>st</sup> . exc.	${}^2E$	${}^3T_2 et$	${}^4T_2 et^2$	${}^5T_2 t^2 e^2$	${}^4T_1 t^4 e$	${}^1T_1 t^5 e$	?
$\nu$	20300	17510	18450	20700		15740	16800
$\nu$	18450						
f	0.144	0.093	0.43	0.59		0.09	1.1
$\perp \nu$	20300	17420	18000	18700		15380	16300
$\nu$	18450						
f	0.044	0.12	1.6	0.89		0.29	1.5
2 <sup>nd</sup> . exc.	—	${}^3T_1 et$	${}^4T_1 et^2$	—	${}^4T_2$	${}^1T_2 t^3 e$	
$\nu$		24930	25200		17200	23170	
f		1.87	3.72			0.35	
$\perp \nu$		25310	24400		17800	22800	
f		0.53	1.96			0.20	
3 <sup>rd</sup> . exc.	—	${}^3A_2 e^2$	${}^4T_1 e^2 t$		${}^4A_1, {}^4E t^3 e^2$		
$\nu$		31240	39400		25770		
f			0.43				
$\perp \nu$			39000		25830		
f			0.40				
Dq $\text{cm}^{-1}$	2030	1750	1815	1990	1650	1830	

ratio becomes 4.4 and therefore is in nearly quantitative agreement. The addition of the dipole term as an adjustable parameter never results in a value lower than 4.4.

The actual magnitude of  $v$  can be found by measuring the absorption spectrum at a series of temperatures high enough to populate the  $A_1$  component of  ${}^2T_2$ . The polarization ratio would change as the absorption from  $A_1$  became significant, and presumably could be calculated in terms of the intensity parameters. No such effect was observed up to  $800^\circ\text{K}$ , however; the value of  $v$  must therefore be greater than  $500\text{ cm}^{-1}$ .

The excited state  ${}^2E$  does not split in a trigonal field, yet a double peak is observed. This can be taken as evidence for a distorted state<sup>(7)</sup>. The Jahn-Teller theorem<sup>(4)</sup> shows that an E state is unstable when the three-fold axis is present. The potential is double valued, and the two peaks represent transitions ending on the two sheets of the potential surface. The separation of the peaks is  $1850\text{ cm}^{-1}$  at  $77^\circ\text{K}$ . This is larger than the trigonal splitting parameter measured for  $V^{+++}$ ,  $\text{Cr}^{+++}$  or  $\text{Co}^{+++}$ . In spite of the presence of a strong distortion of the upper state, the polarization seems to be unaffected.

The centroid of the absorption band lies at  $19380\text{ cm}^{-1}$ , giving  $Dq = 1938\text{ cm}^{-1}$ .

$V^{+++}$

The polarized spectrum of  $V^{+++}$  in corundum at  $77^\circ\text{K}$  is shown in Fig. 3. The spectrum has been discussed by Low<sup>(8)</sup> and in great detail by Pryce and Runciman<sup>(9)</sup>. The ground state in an octahedral field is  ${}^3T_1(t^2)$ , and in corundum, the trigonal field forces the  ${}^3A_2$  component below  ${}^3E$  by an

amount  $v$ . Second order spin-orbit coupling, mainly between the two trigonal components, causes the  ${}^3A_2$  state to split by  $8\text{ cm}^{-1}$ , leaving the  $S_z = 0$  state lowest. At low resolution both components are observed at once and the selection rules are based on the orbital part of the  ${}^3A_2$  state.

There are two excited triplets which arise from the  $et$  configuration,  ${}^3T_2$  and  ${}^3T_1$ . In the  $C_{3v}$  field they split into  ${}^3A_1 + {}^3E$  and  ${}^3A_2 + {}^3E$  respectively. The  ${}^3A_2 \longrightarrow {}^3A_1$  transition is forbidden, but in  $C_3$  the transition becomes the permitted  ${}^3A \longrightarrow {}^3A$ . These two states of  $et$  should give rise to absorption bands polarized  $\parallel C$  and  $\perp C$  whose maxima are displaced from each other by  $v/2$  by the trigonal field. The  $A$  component of each should be the lower one when  $v > 0$  as in  $Ti^{+++}$ .

The remaining triplet state is  ${}^3A_2$ , arising from the  $e^2$  configuration. The intensity of this transition must arise from configuration interaction as a  $t^2 \longrightarrow e^2$  transition is a two-electron change. Ballhausen<sup>(10)</sup> has suggested that the main source of this interaction is the coupling between  ${}^3T_1(A_2)$  and  ${}^3A_2(A_2)$  in the trigonal field. The cubic field is not sufficient.

Weak sharp lines from the doublets of the  $t^2$  configuration are also observed.

The experimental situation is as follows. The  ${}^3T_1$  state behaves as expected. The splitting between the absorption maxima in the two polarizations is  $380\text{ cm}^{-1}$  apparently giving  $v = 760\text{ cm}^{-1}$  (but see later). The sign of  $v$  is therefore the same as found for  $Ti^{+++}$ . The magnitude is less than assumed by Pryce and Runciman,  $1200\text{ cm}^{-1}$ . The intensity ratio of

the oppositely polarized components of  ${}^3T_1$  is 6, the largest anisotropy found in any of these spectra. The theoretical formula for this intensity ratio is

$$\frac{I_z}{I_x} = \frac{2C^2}{A^2 + 8D^2} \quad (10)$$

The ratio using the point charge model and only the dipole term (so that  $\bar{r}$  cancels out) is 16; and using only the octupole term it is 8. If we could ignore the interference between these terms it would be possible to fit the observed result. For the moment, we shall consider ourselves fortunate that the simple model gives qualitatively correct results, as was true for the case of  $Ti^{+++}$ . We observe however that if the symmetry  $C_{3v}$  is used, eliminating  $D$  in (10), the polarization ratio is calculated to be much too high.

The  ${}^3T_2$  band has some unexpected characteristics; namely, it is just about as strong in the parallel spectrum as in the perpendicular; and there is no appreciable trigonal splitting. Furthermore there is very pronounced vibrational structure, and a band which appears clearly to be an electronic origin.

The parallel spectrum can be explained by again using the correct site symmetry  $C_3$  rather than  $C_{3v}$ , which would require zero intensity. The theoretical formula for the intensity ratio is:

$$\frac{I_z}{I_x} = \frac{18D^2}{A^2 + 8D^2} \quad (11)$$

The experimental value is 0.8 at 77°K. This value is given approximately by using the point charge model: it is 1.7 using octupole terms only and would be reduced by inclusion of the dipole term.

The absence of trigonal splitting calls for a new feature in the interpretation; considering the possibility that the upper state may be distorted into a configuration of low symmetry. This will be discussed in section V. It is related to the appearance of the vibrational structure. The polarization does not appear to be affected by the distortion, as we will see in section V.

The absorption in the region of the  ${}^3A_2$  state also has unexpected features. It should be a weak transition appearing only in the parallel spectrum. What is observed are unresolved shoulders on a strongly rising background at  $31,000\text{ cm}^{-1} \perp C$ ,  $33,000\text{ cm}^{-1} \parallel C$ . Another shoulder occurs at  $39,500\text{ cm}^{-1}$  and is more distinct  $\perp C$  than  $\parallel C$ . These bands must not arise from pure  $d \rightarrow d$  transitions.

An important prediction of the intensity formulae is that in  $C_{3v}$  or  $C_3$  the E components of  $T_1$  and  $T_2$  should have the same intensity of absorption. Assuming that  $I(T_2E)$  is the intensity of perpendicular absorption in the region of the  ${}^3T_2$  state, and that  $I(T_1E)$  is that in the region of  ${}^3T_1$ , their apparent ratio is 
$$\frac{I(T_2E)}{I(T_1E)} = \frac{1}{4.5}$$

This discrepancy can only be explained by a special perturbation. The predicted equality of  $T_1(E)$  and  $T_2(E)$  band intensities does not even depend on the use of the point charge model, since it is independent of the constants. It is a symmetry condition which depends for its validity upon the purity of the configurations. Configuration mixing cannot explain the large difference of intensity here.

The perturbation which seems most likely to operate here is the vibrational transfer of intensity. The  $T_1(A)$  band is predicted to be 8 or 9 times stronger than  $T_1(E)$ , so that a small fraction (about 15 percent) of the intensity of the A component appearing in the perpendicular spectrum would add an appreciable intensity increment. This can come about because the absolute value of the intensity induced by the asymmetry of the environment is not very much higher than that capable of being induced by vibrations. Vibrations belonging to the E representation of  $C_3$  would be responsible for transferring intensity from the parallel spectrum of  $T_1A$  to the perpendicular spectrum.

These observations on the spectrum of  $V^{+++}$  in corundum suggest that the most efficient way to compare the theoretical and observed intensities is first to use ratios which are independent of polarization then to compare the calculations to the polarization ratios which are least sensitive to vibrational perturbations.

The two bands of the  $et$  configuration provide a comparison with the intensity formulae which is independent of polarization. The total absorption strength to either band is measured by  $A_{||} + 2 A_{\perp}$ , where  $A$  is the area under the absorption band component. The ratio of this quantity for the two bands is 8.8 and the theoretical formula is

$$\frac{A_{||} + 2 A_{\perp}(T_1)}{A_{||} + 2 A_{\perp}(T_2)} = \frac{C^2 + A^2 + 8D^2}{9D^2 + A^2 + 8D^2} \quad (12)$$

In this instance the octupole terms alone give a value of about 2.7, but the dipole term added in makes agreement with experiment possible.

A systematic comparison of all the intensity data with theory is given by the following list. The results using octupole terms alone and dipole terms alone, are given in the second and third columns. The dipole terms always spoil the agreement when the value of  $B_1^0$  from Table III, and the S.C.F. value of  $\bar{r}/r^3$  are added to the octupole terms. Therefore the quantity  $x = B_1^0 \bar{r}/r^3$  is considered as a parameter and its most favorable value is sought. This value and the resulting relative intensities are given in the third column. The unadjusted value of  $x$  is  $-3.04 \text{ ev/A}^3$ .

	Exp.	Oct. Only	Dipole Only	$x = -\frac{1}{2}$
$T_2A$	0.77	1.7	0	0.81
$T_2E$	1	1	1	1
$T_1A$	15.5	8.1	16	21
$T_1E$	4.4	1	1	1
$T_1/T_2$	8.8	2.7	9	8

The agreement of the values for  $x = -\frac{1}{2}$  with experiment is nearly perfect if intensity transfer from  $T_1A$  to  $T_1E$  is permitted. Subtracting 5.5 from 21 to give the observed 15.5 for  $T_1A$ , we must add  $5.5/2$  to the  $T_1E$  intensity giving 3.2, in good agreement with observation. The value of  $x$  is only small relative to the octupole term, and its difference from the unadjusted value is due to our uncertainty about the value of  $B_1^0$  and to the failings of the point charge model. This model probably is much less reliable when comparisons of terms differing in the power of  $r$  are made than for terms with the same power.

We can state some important conclusions at this point. The absorption we see in a given polarization is not entirely that due to a single electronic

state. This means that the separation of absorption maxima in two polarizations may not be an accurate measure of the trigonal field. The effect of the  ${}^3T_1$  A state on the perpendicular absorption in the region of  ${}^3T_1$  E is to shift the maximum toward lower energies by an amount equal to  $v/2 - hv_e$ , where  $v_e$  is the frequency of the depolarizing vibration. The apparent trigonal splitting could be less than the real splitting unless  $v/2 = hv_e$ . The conclusion of this problem is discussed in section VI.

A second conclusion is that we must use the correct site symmetry,  $C_3$ , in order to explain the intensity of the transitions forbidden in  $C_{3v}$ . The transition  ${}^3A_2 \longrightarrow {}^3T_2 A_1$  forbidden in  $C_{3v}$ , is too strong relative to  ${}^3A_2 \longrightarrow {}^3T_2 E$  to be explained by depolarizing vibrations, and only the use of the  $C_3$  intensity formulas gives an adequate explanation.

$Cr^{+3}$

The polarized spectrum at 77°K is shown in Fig. 4. The two bands of the transition from  ${}^4A_2 (t^3)$  to the quartets of the  $t^2e$  configuration dominate the spectrum. The transition to the next higher configuration,  $te^2$ , is forbidden in the approximation neglecting configuration interaction, as it is a two electron change. It probably appears, however, as the weak band at  $39,000\text{ cm}^{-1}$ , partially hidden by stronger bands to the violet.

The splitting of the  $t^2e$  bands is easily measured, as the individual peaks can be located to within  $50\text{ cm}^{-1}$ , and are not overlapped by other absorption bands. The  $T_1$  bands are separated by  $800\text{ cm}^{-1}$ ; the  $T_2$  by  $450\text{ cm}^{-1}$ . The splitting of the  $te^2$  band is not accurately measurable, but appears to be around  $500\text{ cm}^{-1}$ . These splittings are somewhat higher than in the case of  $V^{+++}$ , and do not match the theoretical expectations for first order splittings. These would be  $v/2$ ,  $v/2$  and  $v$ , respectively.



Tanabe and Sugano showed that the bands of the  $t^3 \longrightarrow t^2e$  transitions have approximately the correct polarizations when the dipole term  $B_1^0$ , of the crystal field potential is used<sup>(11)</sup>. The relative intensity of the two bands was not explainable in this way however.

The two bands of the  $et^2$  configuration of  $Cr^{+++}$  are analogous to those of the  $et$  configuration of  $V^{+++}$ , but the intensity formulas are somewhat different. The systematic comparison of relative intensities as carried out for  $V^{+++}$  yields for  $Cr^{+++}$  the following table:

	Exp.	Oct. Only	Dipole Only	$C_3^3 \frac{1}{2} (C_3^3)^0$ , $x = -.1$
$T_2A$	0.27	0.55	0	0.30
$T_2E$	1	1	0	1
$T_1A$	2.3	2.6	4	4.5
$T_1E$	1.2	.52	1	0.57
$T_1/T_2$	2.1	1.4		2.9

The additional adjustment in the last column is to reduce the value of  $C_3^3$  to one half of its value from Table III. Its only effect is to reduce the value of  $T_2A$ , while adjusting  $x$  only affects  $T_1A$  and  $T_1E$ . The conclusion again seems to be that the dipolar perturbation is unimportant relative to the octupole, and that it is much smaller than the computed value of Table III.

The temperature effects discussed in section VI show that  $T_2A$  probably gains much of its intensity from vibrations. Thus  $C_3^3$  may be even smaller than supposed. However, the other octupole terms are essential to explain the intensity ratios.

Mn<sup>+++</sup>

The spectrum of this ion shown in Fig. 5 consists of one strong band centered at  $19,650 \text{ cm}^{-1}$ . This is the spectrum expected for the ion in a  $^5E(t^3e)$  ground state, since there is only one excited quintet,  $^5T_2(t^2e^2)$ . The polarized spectrum should correspond to transitions from the degenerate  $^5E$  state to components of  $^5T_2$ . The  $^5E$  state does not split in a trigonal field, nor is it split in first order by spin orbit interaction. The  $^5T_2$  components should be determined mainly by the trigonal field, giving  $^5A_1$  below  $^5E$ , separated by the amount  $v$  which is expected to be about  $1000 \text{ cm}^{-1}$ . The polarized spectrum under these conditions should consist of a perpendicular band ( $^5E \longrightarrow ^5A_1$ ) at about  $19,000 \text{ cm}^{-1}$ , and a band of mixed polarization at about  $20,000 \text{ cm}^{-1}$  ( $^5E \longrightarrow ^5E$ ).

The spectrum actually observed is in fair agreement with these expectations. Two peaks are observed in opposite polarizations, but they are separated by  $1900 \text{ cm}^{-1}$ , about twice the value expected. The lower energy peak at  $18700 \text{ cm}^{-1}$  is predominantly in the perpendicular polarization, while the higher peak at  $20,600 \text{ cm}^{-1}$  has mixed polarization.

The intensity ratios which can be measured are the ratios of the two peaks summing over both polarizations, and the polarization ratios. If the first absorption region is identified as the  $A_1$  component and the second as the  $E$  component, the theoretical intensity ratio which does not depend on polarization is

$$\frac{I(A)}{I(E)} = \frac{B^2 + D^2}{2A^2 + C^2 + 25D^2} \quad (13)$$

where the absorption is calculated for both partners of the ground state and both of the upper E state. A reliable experimental value of this quantity is difficult to obtain. Probably the best procedure is to choose an energy which appears to separate the absorption to the E component from that due to the A component. The value  $19100 \text{ cm}^{-1}$  appears to be correct, and the quantity:

$$\frac{A(<,11) + 2A(<,\perp)}{A(>,11) + 2A(>,\perp)} = 0.5, \quad (14)$$

where  $A(<,11)$  means the area under the parallel absorption band less than  $19,100 \text{ cm}^{-1}$ .

The calculated value of the ratio (14) is 0.42 using octupole terms alone, and is 0.2 using dipole terms alone. The octupole term gives nearly correct results and these are not improved upon by using the dipole term as an adjustable parameter.

The polarization ratio for the transition to the E component of  ${}^5T_2$  is

$$\frac{A(>,11)}{A(>,\perp)} = 1.25 \quad (15)$$

This ratio is given by the intensity theory as

$$\frac{I(11)}{I(\perp)} = \frac{C^2 + 9D^2}{A^2 + 8D^2} \quad (16)$$

Its experimental measurement is quite inaccurate because of the uncertainty associated with the cutoff position of  $19100 \text{ cm}^{-1}$ . This is the same ratio which was evaluated to explain the polarization of the  $\text{Ti}^{+++}$  spectrum, and it was successful there. In this case the observed polarization ratio is

much less than the 4.4 given by the octupole terms. This result must be regarded as an even more drastic failure of the unmodified intensity theory to give correct polarization ratios than in the cases of vibrational transfer in  $V^{+++}$  and  $Cr^{+++}$ .

The polarization ratio of the A component of  ${}^5T_2$  is quite high and therefore in agreement with the selection rule forbidding parallel absorption to this component.

Since the  $Mn^{+++}$  ion has a  ${}^5E$  ground state arising from the configuration  $t^3e$ , it may well be unstable in the nearly cubic configuration of the  $Al^{+++}$  site in corundum. The distortion expected to result would be the tetragonal elongation of the octahedron observed in  $Mn^{+++}$  salts. If the ground state is so distorted, the upper state may be split under the resulting potential plus that due to the natural trigonal field. The resulting symmetry would be  $C_s$  if  $C_{3v}$  were the original site symmetry, and  $C_1$  if the true site symmetry  $C_3$  is considered. The energy matrix for a single d-electron in  $C_s$  symmetry is shown in Table XI. The matrix elements for  $d^4$  quintets are one-electron matrix elements with signs changed. For a tetragonal elongation of the octahedron in  $d^4$ ,  $Dt < 0$ ,  $Ds < 0$ , so that for this distortion  $e_a$  falls below  $e_b$  and  $t^+ < t^- < t_{xy}$  if  $Dt \approx Ds > v/3$ . The transitions must therefore begin on  $e_a$  and end on  $t^+$ ,  $t^-$ ,  $t_{xy}$ , with the intensity ratios:

$$\frac{I_{II}}{I_I} = \frac{9D^2}{6D^2 + \frac{1}{3}(A + \sqrt{2}B)^2}, \quad \frac{C^2}{A^2 + 8D^2}, \quad \frac{9D^2}{\frac{25}{3}D^2 + \frac{2}{3}(A - \sqrt{2}B)^2} \quad (17)$$

respectively. The agreement with experiment is only moderately good here.

The formulas predict a lower degree of polarization for the first band than the unmodified ones, and predict almost the same high polarization of the rest of the spectrum, which we previously found did not agree with observations. The agreement with a purely trigonal field seems therefore to be much better than the assumption that the Jahn-Teller distortion of the ground state persists in the upper state. The only way to obtain agreement with the intensity formulas is to have  $t_2$  the lowest component of the upper state, in which case the zeros of Table VI give the perpendicular polarization which is observed. Only a trigonal field can do this. The conclusion here is that the upper state of  $Mn^{+++}$  is subject to the unmodified trigonal field of corundum. The parentage of the upper state is  $t_2^2 ({}^3T_1)e^2 ({}^3A_2)$ , and the absence of distortion may be connected with the fact that the e-electrons are coupled into a shell having nearly full cubic symmetry. In Sec. V we will present evidence that the ground state actually is distorted, however. The low polarization ratio of the E component might be explainable if we abandon the first order calculation and use perturbed wave functions appropriate to the distorted ground state. This has not been done however.

$Fe^{+++}$

The spectrum of this ion is due to transitions from the  ${}^6A_1(t^3e^2)$  ground state to excited quartets, and is therefore very weak. The optical spectrum observed in crystals containing about 0.1 percent of Fe was of poor quality. The broad band expected to appear at  $8000\text{ cm}^{-1}$  ( ${}^4T_1$ ) (as in aqueous solutions) could not be seen, but the bands at 25,600 ( ${}^4A_1 + {}^4E$ ) and  $18200\text{ cm}^{-1}$  ( ${}^4T_2$ ) were observed. The upper states of these

TABLE XI

One-electron matrices for  $C_{2h}$  symmetry; trigonal plus tetragonal field.  
 (Same for  $C_s$  within the d-configuration)

$A'$	$t_{xy}$	$-4Dq + 2Ds - Dt$	$\sqrt{2v/3}$	$2v'/\sqrt{6}$
	$t^+$	$\sqrt{2v/3}$	$-4Dq + \frac{v}{3} - Ds + 4Dt$	$-v'/\sqrt{3}$
	$e_b$	$2v'/\sqrt{6}$	$-v'/\sqrt{3}$	$6Dq - 2Ds - 6Dt$
$A''$	$t^-$	$-4Dq - v/3 - Ds + 4Dt$	$-v'$	
	$e_a$	$-v'$	$6Dq + 2Ds - Dt$	

cubic field basis functions:  $t_{xy}, e_a, e_b, t^+ = \frac{t_b + t_c}{\sqrt{2}}, t^- = \frac{t_b - t_c}{\sqrt{2}}$

bands arise principally from the  $^4G$  state. The value of  $Dq$  obtained from these measurements is about  $1650\text{ cm}^{-1}$ , but the bands are so broad that this value is quite uncertain.

### $\text{Co}^{+++}$

The spectrum of this ion Fig. 6 shows that its ground state is the non-magnetic  $^1A_1(t^6)$  state. The other possible ground state is  $^5T_2(t^4e^2)$ , and the corresponding spectrum would then consist of one transition to  $^5E$ , probably a double band similar to that observed in  $\text{Ti}^{+++}$ . The observed spectrum, however, consists of two well separated bands plus a number of very weak ones. The strong bands are the singlets of the configuration  $t^5e$ ,  $^1T_1$  ( $15,560\text{ cm}^{-1}$ ) and  $^1T_2$  ( $22,980\text{ cm}^{-1}$ ). They are split by the trigonal field by  $360$  and  $370\text{ cm}^{-1}$  ( $A > E$ ) respectively, at  $77^\circ\text{K}$ . The first order splitting of each band is  $v/2$ , so that  $v = 720\text{ cm}^{-1}$ , and is therefore of the same sign and of about the same magnitude as for  $\text{V}^{+++}$ .

There is a suggestion of another strong band at  $30,000\text{ cm}^{-1}$  near the sharply rising absorption (probably charge transfer absorption). This is in the right position to be the transition to  $^1T_2(t^4e^2)$ .

Two weak bands, undoubtedly due to transitions to triplet states are seen at  $18,880\text{ cm}^{-1}$  and  $19,800\text{ cm}^{-1}$ . These are probably the lowest  $^3T_2$  of  $t^4e^2$  and the accidentally degenerate pair  $^3T_1 + ^3T_2$  of  $t^4e^2$ .

The  $^1T_2(t^5e)$  band is doubled. It is believed that the low energy component in the parallel spectrum is a triplet state intensified by coupling to the singlet.

There is an exact correspondence between the states of the  $et^2$  configuration of  $\text{Cr}^{+++}$  and of the  $et^5$  configuration of  $\text{Co}^{+++}$ . The intensity

formulas for  $\text{Co}^{+++}$  are identical to those for  $\text{Cr}^{+++}$  when the correspondence  ${}^4T_1 (\text{Cr}^{3+}) \rightarrow {}^1T_2 (\text{Co}^{3+})$   ${}^4T_2 (\text{Cr}^{3+}) \rightarrow {}^1T_1 (\text{Co}^{3+})$  is established.

The lower band of  $\text{Co}^{+++}$  is forbidden in the parallel polarization, as in  $\text{V}^{+++}$  and  $\text{Cr}^{+++}$ , and is actually found to be very weak. The same type of intensity comparison as was made for  $\text{Cr}^{+++}$  can be made for  $\text{Co}^{+++}$ :

	Exp.	Oct. Only	Dipole Only	X= 0.1	X= 0.05
$T_1A$	0.31	0.55	0	0.55	0.55
$T_1E$	1	1	0	1	1
$T_2A$	1.2	2.6	4	1.1	1.9
$T_2E$	0.69	0.52	1	0.36	0.44
$T_2/T_1$	1.12	1.5	$\infty$	0.74	1.11

The results in this case also seem to be improved by adding in a small dipole contribution  $x = 0.05$ , but it is of the opposite sign from  $\text{V}^{+++}$  and  $\text{Cr}^{+++}$ . Intensity transfer from  $T_2A$  to  $T_2E$  amounting to 35 percent is needed to explain these relative intensities. As for  $\text{Cr}^{+++}$ , the value of  $C_3^3$  seems too large.

#### $\text{Ni}^{+++}$

The spectrum of this ion, Fig. 7, consists of a weak sharp band at  $12300 \text{ cm}^{-1}$ , two broad bands in the visible and some bands in the near ultraviolet which are too strong to be crystal field bands. The absolute intensity of the visible bands is about right for crystal field bands, and the infrared band could be an intercombination. It is difficult to assign the ground state of this ion from its spectrum. The choices are  $t^4 e^3 {}^4T_1$  as in  $\text{Co}^{+++}$  salts, or  $t^6 e^2 {}^2E$  a spin paired state which would be similar to the ground state of  $\text{Mn}^{+++}$ ,  ${}^5E$ .



In the spin-unpaired state the lowest multiplet component of  ${}^4T_1$  would be  $E_{1/2}$  (cubic field) and the next multiplet component would be a G state about  $500\text{ cm}^{-1}$  higher. At all temperatures below room temperature, only the transitions from  $E_{1/2}$  would appear. The trigonal field is not expected to change the symmetry of the ground state.

In the spin paired state  ${}^2E$ , the spin-orbit representation in a cubic field is G, which splits in a trigonal field into  $E_{1/2} + E_{3/2}$ . The splitting between these components could only be on the order of  $10\text{ cm}^{-1}$  as it arises from the product of trigonal and spin-orbit perturbations. There is the additional possibility, as was the case for the  $Mn^{+++} {}^5E$  ground state, that the Jahn-Teller effect removes the degeneracy.

The relevant selection rules for transitions in  $C_3$  are given in the lower right hand corner of Table VII. In the spin-unpaired case, transitions have to be either perpendicular, or unpolarized; in the paired case, they will follow either  $E_{1/2}$  or  $E_{3/2}$  rules, or be a combination of the two, depending on the magnitude of the Jahn-Teller splitting.

The observed polarizations are as follows:

Band Position, $\text{cm}^{-1}$	Description	Polarization
12,300	line	$\perp$
16,300	broad band max	$\perp$
16,350	origin of group of lines	$\parallel$
16,700	broad band max	$\parallel$
17,750	line	$\perp$
17,850	line	$\parallel$
19,600	broad band	$\perp + \parallel$

The occurrence of features polarized exclusively along  $c$  is compatible only with a ground state  $E_{3/2}$ . Such a level can arise only from the spin-paired ground state, but in order for the polarization to remain strongly marked, the ground state must be split, with  $E_{3/2}$  lowest and  $E_{1/2}$  not contributing to the absorption. If there is a distortion, however, the symmetry  $C_3$  is no longer correct and the selection rules have to be re-examined. Since the new symmetry is probably  $C_1$ , only intensity calculations can be used, but it is probable that these would give results closely resembling the symmetry rules of  $C_3$  (as was found for the similar case of  $Mn^{+++}$ ). The assignments of these absorption bands is not at all clear, however.

The trigonal splitting parameter  $v$  might be measurable from the first band, which has its maximum at  $16300 \perp C$ ,  $16800 \parallel C$ . This splitting is probably  $v/2$ . Thus  $v = +1000 \text{ cm}^{-1}$ , and has the same sign and about the same magnitude as in the other ions.

In this section we have been concerned with spectral assignments, energy parameters and intensities. The results of the comparison of the intensities to the theory we have been using are perhaps rather unclear at this point, so we will summarize them. We have made little use of the absolute intensities because their *a priori* calculation involves too many numbers which are difficult to evaluate.

The variations in total intensity from one ion to the next are also not well understood. A possible source of error in these numbers is the chance that the ion may be present in more than one valence state. The divalent ions are very weakly absorbing relative to the trivalent, and they

would not be detected in spectral absorbance measurements. A block of corundum 3 x 3 x 10 mm containing  $\text{Ni}^{+++}$  was heated in a vacuum at  $1600^{\circ}\text{C}$  for 15 min. The yellow color of  $\text{Ni}^{+++}$  was entirely removed by this treatment, and the expected green or blue of  $\text{Ni}^{++}$  did not appear. The spectrum of this colorless crystal showed some weak ultraviolet absorption, but none which could be ascribed to  $\text{Ni}^{++}$ . Upon reheating this sample in an oxygen rich oxyhydrogen flame at  $1600^{\circ}\text{C}$  for 30 min, the yellow color of  $\text{Ni}^{+++}$  was restored. In order to determine the spectrum of  $\text{Ni}^{++}$  in corundum, a corundum slab was embedded in  $\text{NiO}$  and heated in a corundum crucible at  $1700^{\circ}\text{C}$  in a vacuum for 1 hour. The slab turned sky blue, and showed the optical spectrum of  $\text{Ni}^{++}$ , with  $Dq = 930 \text{ cm}^{-1}$ . The colored region of the crystal was, however, very close to the surface of the corundum slab, and the exact phase in which  $\text{Ni}^{++}$  was present is in some doubt. In the case of  $\text{Ti}^{+++}$ , the samples all contained what appeared to be a cloudy precipitate. This may be  $\text{TiO}_2$ , and of course the chemical analysis would not distinguish this from  $\text{Ti}^{+++}$ . This may account for the low apparent intensity. These few experiments show that considerable additional work will have to be done if reliable absolute intensities are to be obtained.

The relative intensity values of bands of the same ion are experimentally in very little doubt. The interpretation by the point charge theory is qualitatively correct in every case so far observed. The degree of polarization is always less than the theory gives, and it appears that vibrational transfer of intensity can explain this. The ratio of intensity of two bands where measured by the quantity  $A_{||} + 2 A_{\perp}$  is independent of polarization, and a reasonable fit, using only octupole terms is found for

$V^{+++}$ ,  $Cr^{+++}$  and  $Co^{+++}$ . By adjusting one parameter,  $x = B_1^0 \bar{r}/r^3$ , good agreement of all intensity ratios with experiment is possible for these three ions. The value of this parameter changes from -0.5 for  $V^{+++}$  to -0.1 for  $Cr^{+++}$  to +0.05 for  $Co^{+++}$ , but the significance of this change, if any is not known. It might be interpreted as a change in ion position, in which case the ion moves from a region of negative to positive electric field as it is changed from  $V^{+++}$  to  $Co^{+++}$ . The intensity data all seem to require that the octupole perturbation of the ion by the lattice is greater than the dipole perturbation.

#### V. Analysis of Spectral Details

Up to this point we have discussed only the gross features of the spectra. At 77°K and below, fine structure is observed in all spectra except that of  $Ti^{+++}$ . This is generally identifiable as vibrational structure, the vibrational intervals being characteristic of the corundum lattice. The best available assignment of these vibrations, due to Krishnan<sup>(12)</sup>, is shown in Table XII.

The introduction of an impurity atom reduces the symmetry from  $D_{3d}$  to  $C_3$ , therefore vibrations in the non-degenerate classes of  $D_{3d}$  may all interact with each other, and vibrations within the two degenerate classes may interact with each other. There is therefore a possibility that the vibration frequencies around the impurity may be different from those of pure corundum. The extent of the change will depend on changes in force constants, which probably will not be great, and on the difference in mass between  $Al$  and the impurity atom. The atomic weight of  $Al$  is 27 and of  $Ti$  through  $Cu$  47.9 to 63.6. The frequencies involving motion

of the metal atom can change at most by the square root of the mass ratio, assuming the same force constants, or by a factor of from 1.3 to 1.53. If the motion involves the oxygens for the most part, the frequency change will be much less.

Co<sup>+++</sup>

+++

The spectrum of Co<sup>+++</sup> shows a great deal of vibrational structure on the  ${}^1T_1$  to  ${}^5E$  peak, and many corundum vibrations may be identified. Most of these frequencies appear to be nearly the same as corundum frequencies. The correlation is shown in Fig. 8. Spectra were taken at 4.2°K under high resolution, but no features other than those visible with the Cary 14 were found.

Among the most definite features are the strong bands at 666 and 742  $\text{cm}^{-1}$  from the origin. They correlate well with 642  $e_g$  and 751  $a_g$ , although the latter could be an overtone of 393. The 393 peak appears strongly and in association with two other peaks. It could be related to 375  $e_g$  of pure corundum. A peak at 235  $\text{cm}^{-1}$  could be the 244  $a_{2u}$  corundum vibration. The equally strong 259 is not obviously related to any corundum frequency, although it might be one of the normally inactive ones.

Although the bands are broad there are enough near coincidences so it seems safe to conclude that the local vibration frequencies around the impurity are not very different from those of the pure crystal.

According to the identifications made in Fig. 8, not only non-degenerate vibrations, which become totally symmetric under  $C_3$ , but also degenerate vibrations, are excited. The degenerate modes are non-totally

TABLE XII  
 Vibrations of Corundum Lattice. Symmetry Classification  $D_{3d}$ .  
 (R. S. Krishnan, Proc. Ind. Acad. Sci. **26A**, 450 (1947))

Rep'n	Number of Modes	Activity		Observed Frequencies				
		Raman	I.R.					
$A_{1g}$	2	+		578	751			
$A_{1u}$	3							
$A_{2u}$	2		+	244	847			
$A_{2g}$	2							
$E_u$	4		+	194	328-55	434	909	.
$E_g$	5	+		375	417	432	450	642

symmetric in  $C_3$ , and their appearance in the spectrum can be ascribed either to vibrational-electronic interaction or to a distorted equilibrium configuration in the upper state. There is no progression of eg modes as in the case of  $Cr^{+++}$  and  $V^{+++}$ , so there is no obvious way to distinguish these two possibilities. The effect of temperature is the same as for  $Cr^{+++}$ ; the  $T_2$  E band increases by a factor of 1.36 from room temperature to  $1300^\circ K$  (see Sec. VI). It appears therefore that vibrational-electronic coupling is no more important here than for  $Cr^{+++}$ . If the excited state is distorted, the distortion must be smaller than in  $Cr^{+++}$  because only single quanta of the eg modes appear; and it must be different from  $Cr^{+++}$  because many eg modes appear rather than one. In particular, the 194 eg mode does not appear in the  $Co^{+++}$  spectrum, so the distortion must be orthogonal to this particular displacement. The fact that the 0-0 band of  $Co^{+++}$  is much stronger relative to the rest of the band than in the case of  $Cr^{+++}$  is another indication that its excited state is geometrically more similar to the ground state than for  $Cr^{+++}$ .

Figure 8 shows that there is a weak band in the parallel spectrum  $53\text{ cm}^{-1}$  to the red of the strong 0-0 band. This could be a "hot band", but the helium temperature spectrum has not been sufficiently investigated to determine whether or not this is true. There is also a band  $+80\text{ cm}^{-1}$  from the 0-0 band. What these intervals are is not known as they are less than any of the reported vibration frequencies of corundum. It may be that  $-53$  represents the origin of the parallel transition and that  $+80$  is a  $133\text{ cm}^{-1}$  interval. An interval of about this magnitude ( $110\text{ cm}^{-1}$ ) is observed in  $Ni^{+++}$ . It is possible that it represents one of the inactive modes, the twisting motion of the octahedron about the  $C_3$  axis. This

mode might be easily excited because the transition is made allowed by the parameter  $C_3^3$  which measures the twist of the octahedron from the ideal  $C_{3v}$  geometry. It is a totally symmetric mode in  $C_3$ , and is permitted to appear by the selection modes.

$V^{+++}$  and  $Cr^{+++}$

These two ions have similar  $T_2$  bands as shown in Figs. 9 and 10. The most significant difference is that the sharp line structure a progression of  $200\text{ cm}^{-1}$  intervals, in the  $Cr^{+++}$  band is highly polarized  $\perp C$ , while in  $V^{+++}$  the structure appears with about the same intensity in both polarizations.

The origin band in  $Cr^{+++}$  would appear in the perpendicular spectrum according to selection rules for  $C_3$ , because the lower component of  ${}^4T_2$  is  ${}^4E$ , and the  ${}^4A_2 \rightarrow {}^4E$  transition is polarized x,y. But in the  $V^{+++}$  case the  ${}^3A$  component of  ${}^3T_2$  is lower in the trigonal field, and the polarization for  ${}^3A \rightarrow {}^3A$  is z. The x,y absorption is just as strong as the z, however, This cannot be explained on the basis of  $C_3$  selection rules, and no vibrational perturbation is possible if this is the origin band. It was therefore important to establish whether or not these first bands (in the low temperature spectra) of  $V^{+++}$  and  $Cr^{+++}$  are really 0-0 bands.

A series of spectra at various temperatures was obtained in order to locate the first "hot bands". If the apparent origins are actually 0-1 bands of an enabling vibration, this vibration would appear as a 1-0 band at temperatures high enough to populate its first quantum level in



the ground state. On heating the crystal from 77°K, the first feature to appear is a broad weak band  $200\text{ cm}^{-1}$  from the apparent origin. It is most distinct at 120°K and can still be distinguished at 175°K. The spectrum becomes quite broad at high temperatures but there seems to be no evidence for the hot band which should appear at an interval roughly twice the 0-1 energy from the apparent origin. The apparent origin is probably a real origin, therefore, and the one hot band at  $-200\text{ cm}^{-1}$  is one quantum of the progression-forming frequency in the ground state.

The same experiment performed with  $\text{Cr}^{+++}$  again showed the  $200\text{ cm}^{-1}$  hot band but it was less distinct. There was no evidence of any other band. Although this evidence is not conclusive it seems most likely that the apparent origins are really 0-0 bands in both cases.

According to Table XII the totally symmetric frequencies of corundum are 578 and  $751\text{ cm}^{-1}$ . In the locale of an impurity the inactive vibrations and the two  $A_{2u}$  vibrations, 244 and 847, become totally symmetric. The progression frequency is not as close to any of these as it is to the  $194\text{ cm}^{-1}$  Eu mode, and this is its probable assignment. If this is the correct assignment the appearance of such a progression is evidence that the excited state is distorted so as to destroy  $C_3$ .

The appearance of the unpolarized origin in  $\text{V}^{+++}$  is also evidence that the upper state has lost  $C_3$ . Since the same progression appears in both  $\text{Cr}^{+++}$  and  $\text{V}^{+++}$  they must both have the same distortion. If we knew the normal coordinate corresponding to the progression mode we could calculate the equilibrium configuration of the excited state from the intensity distribution on the progression. The distortion must be quite

large as the maximum intensity occurs in the eighth or ninth member in  $V^{+++}$  and in the seventh in  $Cr^{+++}$ . A crude application of the Franck-Condon principle gives the order of magnitude of the oxygen displacements as  $0.3 - 0.4 \text{ \AA}$ . This is based on a harmonic oscillator model, however, and we must be cautious about applying such calculations to a system in which there are undoubtedly important linear, cubic and quartic contributions in the potential function from Jahn-Teller effects and Renner effects. These could make a vibrational progression stretch out without there being large displacements in the upper state.

The origin of the distortion of the  $T_2$  state is undoubtedly electronic in nature and could be considered as a static Jahn-Teller effect. In the case of ions in corundum there is already a large trigonal potential which splits  $T_2$ . The commonest type of Jahn-Teller splitting results in a tetragonal distortion of the octahedron. The axis of this distortion lies at  $54.7^\circ$  to the trigonal axis of the octahedron and may be directed along any of the three equivalent cubic axes. In corundum the octahedron is distorted, but there will still be three equivalent pseudo-cubic axes. In order to see if the observed spectra are consistent with an upper state having a tetragonal distortion, a calculation of the spectral energy and intensity under these conditions was made.

The basis functions were chosen as cubic functions combined so as to transform properly under the symmetry plane containing the axis  $C_3$  and the distortion axis,  $C_4$ . This is only a pseudo-symmetry plane in the true site group of the impurity, but it should have considerable validity in energy calculations. These basis functions are those of Table XI and

the cubic functions are designated as in Table IV. Two- and three-electron functions were constructed and the matrices of trigonal plus tetragonal plus spin-orbit were then constructed. Some of these results are shown in Table XIII. The one-electron matrices shown in Table XI define the perturbations used. The eigenvectors of the matrix in Table XIII are essentially the basis functions when  $Dt > v$ , as is likely to be the case. These were used to calculate intensities. The intensity formulas and energy diagram are shown in Fig. 11 for  $Dt > v$ .

The sum of the parallel intensities is the same as is given in Table IX for the  $A \rightarrow A$  transition, and similarly for the perpendicular intensity. The tetragonal field merely redistributes the intensity. The discussion of Sec. IV is therefore not affected by these new considerations.

The intensities would agree with experiment if  $A^2 = 6D^2$ , a reasonable requirement. The spin-orbit splitting of the lowest component must be small since we see only very closely spaced lines in the origin band. Fig. 9 shows that the origin band consists of at least two lines, differently polarized. The calculated spin-orbit splitting of the lowest level,  $\phi_3$ , is a second order effect given approximately by:

$$E_3(\pm 1) - E_3(0) = \frac{\zeta^2}{140Dt} \quad (18)$$

TABLE XIII

Wave functions for  $et$  configuration in  $C_{2h}$  (or  $C_s$ ) symmetry, and matrix for tetragonal + trigonal + spin orbit energy of  $^3T_2(et)$  (cross terms between trig. and tetrag. potentials are negligible). The roots of the analogous matrix for  $^4T_2(et^2)$  are very similar to the roots of this matrix. The cubic basis functions of Table IV are used here except that  $t^+ = 1/\sqrt{2} (t_{xz} + t_{yz})$ ,  $t^- = 1/\sqrt{2} (t_{xz} - t_{yz})$ .

$$\begin{array}{llll}
 ^3T_2(et) & \phi_1 = 1/2(\sqrt{3} e_a t^+ + e_b t^-) & A'' & ^3T_1(et) \quad \phi_4 = 1/2(\sqrt{3} e_b t^+ - e_a t^-) \quad A' \\
 & \phi_2 = 1/2(\sqrt{3} e_a t^- + e_b t^+) & A' & \phi_5 = 1/2(\sqrt{3} e_b t^- - e_a t^+) \quad A'' \\
 & \phi_3 = e_b t_{xy} & A' & \phi_6 = e_a t_{xy} \quad A''
 \end{array}$$

(The reflection plane is  $x = y$ ,  $A'$  symmetric,  $A''$  anti-symmetric under reflection)

	31	$3\bar{1}$	20	10	30	21	$2\bar{1}$	11	$1\bar{1}$
31	$-7Dt$		$a^*$	$a$		$v/3\sqrt{2}$			
$3\bar{1}$		$-7Dt$	$a$	$a^*$			$v/3\sqrt{2}$		
20	$a$	$a^*$	$\frac{7}{4}Dt - \frac{v}{6}$		$v/3\sqrt{2}$				
10	$a^*$	$a$		$\frac{7}{4}Dt + \frac{v}{6}$					
30			$v/3\sqrt{2}$		$-7Dt$	$a$	$a^*$	$a^*$	$a$
21	$v/3\sqrt{2}$				$a^*$	$\frac{7}{4}Dt - \frac{v}{6}$		$b$	
$2\bar{1}$		$v/3\sqrt{2}$			$a$		$\frac{7}{4}Dt - \frac{v}{6}$		$b^*$
11					$a$	$b^*$		$\frac{7}{4}Dt + \frac{v}{6}$	
$1\bar{1}$					$a^*$		$b$		$\frac{7}{4}Dt + \frac{v}{6}$

$$a = (1+i)\zeta/8$$

$v$  = trigonal parameter

$$b = i\zeta/4$$

$Dt$  = 4th power tetragonal parameter

$$3\bar{1} = \phi_3 (S = -1), \text{ etc.}$$

Using  $35Dt/4 = 1500 \text{ cm}^{-1}$ ,  $\zeta = 140 \text{ cm}^{-1}$  a splitting  $0.8 \text{ cm}^{-1}$  results. This pattern would not be resolved by the Cary 14, nor was it clearly resolved by Pryce and Runciman<sup>(9)</sup> in their higher resolution work, although they state that there appear to be several components at the origin.

The assumption that the  ${}^3T_2$  level of  $V^{+++}$  is tetragonally distorted is therefore consistent with experiment: the spin-orbit splitting is quenched and the intensity distribution is reasonable. The calculation for  $Cr^{+++}$  is the same as for  $V^{+++}$  except that the trigonal, tetragonal and spin-orbit matrix elements must be given the opposite signs. The state  $\phi_1$  is the lowest one in this case. The intensity formulas are not the same (see Fig. 11), but the essential feature of  $\phi_1$  is unchanged from the case of  $d^2$ : it has zero moment  $\parallel C$ . This is a necessary requirement for agreement with experiment. Thus the similarities and differences of the two spectra are all explained by the same theory, and we conclude that the  $T_2$  states of  $Cr^{+++}$  and  $V^{+++}$  are tetragonally distorted.

There is one point which must be examined. The state  $\phi_1$  in  $d^3$  has appreciable spin-orbit splitting. The bands in the progression in  $Cr^{+++}$  are broader than those in  $V^{+++}$ , and this may be the reason why spin orbit structure is not resolved, or the spin orbit structure may be the reason for the broadening.

$Mn^{+++}$

Vibrational structure appears exclusively in the perpendicular spectrum of  $Mn^{+++}$  near the beginning of the absorption band. (Fig. 5)

The first line,  $16760\text{ cm}^{-1}$  probably marks the electronic origin, although a more concentrated sample is needed in order to be sure of this. The intervals do not form a nearly regular progression as in  $\text{V}^{+++}$  and  $\text{Cr}^{+++}$ . Each interval measured from the origin is close to one found in  $\text{Co}^{+++}$ ; but there are some remarkable omissions such as 666 and 742.

One feature of the  $\text{Mn}^{+++}$  spectrum is not observed in any of the previous spectra of the series. A pair of narrow bands at  $19130\text{ cm}^{-1}$  and  $19340\text{ cm}^{-1}$  appear, just barely resolved in the middle of the broad absorption band. These must mark the origin of the second component of the  ${}^5\text{T}_2$  state,  ${}^5\text{E}$ . The origins of the A and E components are thus separated by about  $2500\text{ cm}^{-1}$ . The separation between the two lines,  $210\text{ cm}^{-1}$ , could be spin-orbit splitting, but the polarization and energy calculation should be carried out to check on the reasonableness of this suggestion.

The large separation of the origins of the two components would be understandable if the upper and lower states have quite different configurations. The long buildup of vibrational progressions in the first band is evidence that the configurations are different. The origin band  $16760\text{ cm}^{-1}$  is relatively weaker in  $\text{Mn}^{+++}$  than it is in  $\text{V}^{+++}$ ,  $\text{Cr}^{+++}$  or  $\text{Co}^{+++}$ . The failure to observe an effective tetragonal splitting in the upper state of  $\text{Mn}^{+++}$  (sec. IV), due to the suspected Jahn-Teller effect in the ground state is now understandable. The upper state, belonging to the configuration  $t^2e^2$  does not have a great tendency toward distortion as the e-shell is half filled (the parentage of this state is  $t^2({}^3\text{T}_1)e^2({}^3\text{A}_2)$ ). In addition, the trigonal field forces the non-degenerate component lowest, reducing even more the tendency toward distortion. This lower component, which appears in the perpendicular spectrum must be a nearly pure " $t_z$  hole" with the trigonal field around it quite undisturbed.

The long vibrational progression can only be accounted for if the ground state equilibrium position is appreciably displaced away from the trigonal geometry. Again, if we could identify all of the vibrations in the spectrum and knew their normal coordinates, we could determine what the ground state is like. It is possible to correlate most of the intervals with an  $e_g$  or  $e_u$  vibration of the corundum lattice: this of course would establish the distortion as one which destroys the three-fold axis. This correlation is as follows:

Observed interval:	224	380	492	694	885	1021
Corundum vibration:	224( $a_u$ )	375 $e_u$	450 $e_u$	642 $e_u$	909 $e_g$	?

Within the rather large limits which must be allowed, this correlation could be carried out in other ways. It is at least suggestive that the distortion is present and of the form required for a Jahn-Teller static distortion of the ground state.

#### VI. Absorption Strength as a Function of Temperature

By studying the strength of the optical absorption as a function of temperature, one can determine the contribution of vibrations to the absorption process, and can determine the excitation energy of low lying components of the ground multiplet if there are any.

$\text{Cr}^{+++}$

The spectrum of ruby at various temperatures is shown in Fig. 12. The total absorption strength to the  $t^2e$  configuration is measured by  $A_{\parallel} + 2A_{\perp}$ , where  $A_{\parallel}$  and  $A_{\perp}$  are the areas under the absorption bands observed parallel and perpendicular to the  $C_3$  axis. These areas are taken as the sum of those of the  ${}^4T_2$  and  ${}^4T_1$  bands. Absorption strengths of

individual bands are measured similarly. The total absorption strength does not increase by more than two percent (the error of measurement) between 77 and 300°K. Above 400°K, the increase can be represented by the formula

$$\frac{A(T)}{A(0)} = 1 + e^{-\Theta_D/T} \quad (19)$$

where  $\Theta_D = 1050 \pm 30^\circ\text{K}$ . This is nearly equal to the Debye temperature of the corundum lattice, 980°K. At 1000°K, the absorption strength has increased to about 1.35 times its value at 77°K.

Individual bands have temperature dependences differing somewhat from each other. The strongest bands increase least with rising temperature. The region of the forbidden transition,  ${}^4A_2 \longrightarrow {}^4T_2(A_1)$ , increases far more rapidly than the others. These effects are illustrated in Fig. 13, where the function 19 is also plotted.

Two effects of temperature are to permit transitions from vibrations of the ground state, and to change the lattice constants. The excitation of certain vibrations will permit allowed transitions to appear in the opposite polarization from that given by the electronic selection rules and will cause violation of electronic selection rules of forbidden transitions.

In the case of  $\text{Cr}^{+++}$ , we must distinguish between two possibilities: does the increase of absorption in the region of the partially forbidden transition to  ${}^4T_2 A_1$  indicate, (1) vibrational intensification of this transition, or (2) depolarization of the "allowed" transition to  ${}^4T_2 E$ ? If the process is vibrational-electronic coupling to "enabling" vibrations, the forbidden transition will gain intensity from excited vibrations of the



ground state and will ultimately shift to the red with rising temperature by an amount roughly equal to the frequency of the enabling vibration. If it is the depolarization of the transition to the E state the parallel and perpendicular absorption should eventually have their maxima at the same wavelength, and the trigonal splitting should disappear. Superimposed on these shifts would be the one due to expansion of the lattice.

Figure 12 shows that the  ${}^4T_2$  band maxima remain about the same distance apart from 300°K to 1200°K. At the latter temperature all of the corundum vibrations are fully excited to at least the first quantum level, and more transitions will be taking place from vibrational levels than from the vibrationless level. It is clear therefore that the depolarizing process is less important here than vibration-induced transitions to the  ${}^4T_2 A_1$  state. The forbidden transition almost triples its strength between 300 and 1200°K and its strength becomes nearly as great as that of the allowed transitions. Thus the vibrational-electronic contribution to the intensity in the corundum lattice can become comparable to the contribution of the static field.

The shift of the band maxima of the allowed transitions should reflect the changes of the crystal field with temperature. Theoretically, the band positions depend on Dq. In the cubic approximation, Dq varies with  $R^{-5}$  where R is the metal-oxygen bond length and changes in R, in turn, are related to the thermal expansion coefficient. In the equation

$$Dq = \frac{a}{R^n} \quad (20)$$

where  $a$  is a constant determined by the metal ion and the ligands, and  $R$  is the ion-ligand distance, the exponent  $n$  can be found from the temperature dependence of the band maxima. The energy of an electronic state is given by

$$E = b Dq + C \quad (21)$$

where  $b$  and  $C$  depend on the state. We can take the logarithmic derivative of this equation and obtain

$$\frac{1}{\frac{E - C}{R}} \frac{\partial (E - C)}{\partial R} = -n \quad (22)$$

The temperature dependence of the band maxima give  $\frac{1}{(E-C)} \frac{\partial (E - C)}{\partial T}$  and the thermal expansion coefficient gives  $\frac{1}{R} \frac{\partial R}{\partial T}$ , and their ratio is  $-n$  according to Eqn. 22. The data of Fig. 13 for the  ${}^4T_2$  band of  $\text{Cr}^{+++}$  give  $\frac{\partial E}{\partial T} = -1.1 \text{ cm}^{-1}/^\circ\text{C}$  and since  $C = 0$  this can be used directly. The linear thermal expansion coefficient of corundum is approximately  $\frac{\Delta \ell}{\ell \Delta T} = 8 \times 10^{-6} \text{ }^\circ\text{C}^{-1}$ . Assuming that the bond distance  $R$  is proportional to macroscopic dimensions,  $\ell$ , we find from Eq. 25,  $n = 7$ . This is in good agreement with expectations based on a point charge model ( $n = 5$ ) or a point dipole model ( $n = 6$ ). We cannot take the exact value seriously until more examples become available.

$\text{V}^{+++}$

The intensity of the two principal absorption bands of  $\text{V}^{+++}$  in corundum as a function of temperature are shown in Fig. 14. The points give the integrated band areas at each temperature divided by the area at  $77^\circ\text{K}$ . Some of the data on which the figure is based is given in Table XIV.

The integral of the  ${}^3T_1$  band is somewhat uncertain at high temperatures because of overlapping by strong ultraviolet bands. It is relatively certain, however, that the quantity  $A_{||} + 2A_{\perp}$  for this absorption does not change significantly with temperature. This is in spite of the fact that the parallel absorption decreases rapidly in maximum extinction coefficient as the temperature rises. The increase of band width and transfer of intensity to the perpendicular component makes up for the loss of maximum absorption strength. The area ascribed to the  ${}^3T_2$  band is actually the area measured from the peak to longer wavelengths. This area is free of overlapping by the  ${}^3T_1$  band. If the asymmetry of the  ${}^3T_2$  band remains constant with temperature, the portion we have integrated will remain proportional to the entire band area. This assumption appears to be justified, as the band shape does not change below temperatures at which overlapping begins to become important, i.e. below  $500^{\circ}\text{C}$ .

The total absorption to the first excited state of  $V^{+++}$  increases by a factor of 2.15 from  $300^{\circ}$  to  $1000^{\circ}\text{K}$ , while in  $\text{Cr}^{+++}$  this band increased by 1.36. Furthermore, the so-called forbidden component,  ${}^3T_2 (A_1)$  in the z-polarized spectrum, which is 75 percent as strong as the E component at  $77^{\circ}\text{K}$ , becomes stronger rapidly and at about  $700^{\circ}\text{K}$  surpasses the intensity of the allowed component. At  $1300^{\circ}\text{K}$  it is about 18 percent more intense. This would not be expected if the mechanism of intensification were vibrational-electronic coupling or the depolarization process described previously. The two components could at most become equal in this way.

The additional fact which must be considered in order to explain these observations is that the  ${}^3E$  component of the ground  ${}^3T_1$  state lies

Table XIV

The integrated areas,  $A_{||} + 2A_{\perp}$ , for the  ${}^3T_2$  and  ${}^3T_1$  bands of  $V^{+++}$  in corundum (expressed as optical density  $\times$  wave number).  $I(T)/I(77^\circ K)$  is the ratio of  $A_{||} + 2A_{\perp}$  for  $T^\circ K$  and  $77^\circ K$ .  $\nu_{||}$  and  $\nu_{\perp}$  are band maxima in  $\text{cm}^{-1}$ . The sample used for study of the  ${}^3T_2$  band had the same concentration as the one for  ${}^3T_1$ , but 7.5 times the path length.

${}^3T_2$	$T^\circ K$	$\frac{1}{2}A_{  }$	$\frac{1}{2}A_{\perp}$	$I(T)/I(77)$	$\nu_{  }$	
	77	333	429	1.000	17450	
	300	435	508	1.218	17450	
	375	556	590	1.455	17360	
	425	566	570	1.430	17280	
	475	586	615	1.520	17300	
	530	642	651	1.630	17270	
	575	684	723	1.785	17220	
	675	722	726	1.825	17100	
	780	867	774	2.020	16990	
	875	877	875	2.200	16890	
	975	972	867	2.270	16750	
	1080	1010	908	2.370	16690	
	1175	1099	940	2.500	16660	
	1275	1169	991	2.640	16610	
${}^3T_1$	$T^\circ K$	$A_{  }$	$A_{\perp}$	$I(T)/I(77)$	$\nu_{  }$	$\nu_{\perp}$
	77	2547	725	1.000	24960	25340
	300	2550	754	1.01	24880	
	525	2117	1100	1.08	24560	
	775	2110	1081	1.07	24440	

only a little way above the  ${}^3A_2$  ground component and becomes populated at moderate temperatures. Determination of this splitting provides a measure of the parameter  $v$ . The intensity of the transition from  ${}^3T_1(E) t^2$  to the  ${}^3T_2$  state is theoretically quite high in the  $\pi$ -polarization, and moderately high in the other. The intensity formulas for transitions from the components of the ground state to those of the  ${}^3T_2$  upper state are shown in Table IX. The ratio of the absorption strength to  ${}^3T_2$  from the E state compared to that from the  $A_2$  state is

$$a = \frac{I(E)}{I(A)} = \frac{3B^2 + 2A^2 - 2\sqrt{2}AB + C^2 + 31/2 D^2}{2A^2 + 34D^2} \quad (23)$$

Using the dipolar potential of the lattice this ratio becomes 6 and the octupole part gives 20. Thus the observed increase of intensity with temperature is qualitatively explained.

A value of the splitting between the E and A components of  ${}^3T(t^2)$  may be obtained from a detailed analysis of the data. The populations of the two states at a temperature  $T$  are:

$$\begin{aligned} N_A(T) &= N/(1 + 2e^{-\theta/T}) \\ N_E(T) &= 2N e^{-\theta/T}/(1 + 2e^{-\theta/T}) \end{aligned} \quad (24)$$

where the factor 2 is the ratio of statistical weight of the E to the A state,  $\theta$  is the energy of E above A and  $N = N_E + N_A$ . Combining this information with the intensity formulas above, the intensity as a function of temperature may be derived:

$$\frac{I(T)}{I(0)} = \frac{1 + 2a e^{-\theta/T}}{1 + 2e^{-\theta/T}} = P \quad (25)$$

where  $a$  is the limiting ratio of absorption strengths given in (23).

This formula must, however, be corrected for the vibrational intensification which was shown to operate for  $\text{Cr}^{+++}$ . We will not be much in error if we assume that the same functional dependence on temperature applies to both  $\text{Cr}^{+++}$  and  $\text{V}^{+++}$ . Therefore the theoretical absorption strength of transitions beginning with  ${}^3\text{T}_1 \text{ t}^2 \text{ A}_2$  of  $\text{V}^{+++}$  should contain the factor  $1 + e^{-\theta_0/T}$ , and that for transitions beginning with  ${}^3\text{T}_1 \text{ t}^2 \text{ E}$  should contain  $1 + e^{-(\theta + \theta_D)/T}$ . The ratio of these two factors will be denoted g:

$$g = \frac{1 + e^{-(\theta + \theta_D)/T}}{1 + e^{-\theta_0/T}} \quad (26)$$

and in place of  $\underline{a}$  in eq. 25, we will have  $ag$ . The value of  $\theta$  will be close to  $\theta_D$ , so we simply substituted  $\theta = \theta_D$  in g. Then the value of  $\theta$  can be obtained from the equation

$$\theta = 2.31 T \log \frac{2(ag-P)}{P-1} \quad (27)$$

The values of  $\theta$  for  $a = 8$  and  $a = 6$  are shown for a series of temperatures in Fig. 15. The values are moderately constant for  $a = 6$  and give  $\theta = 1380 \pm 100^\circ\text{K}$  or  $960 \text{ cm}^{-1}$ . This is also the value of  $\nu$ .

The value of  $\nu$  obtained this way is somewhat larger than that obtained from the splitting of the  ${}^3\text{T}_1$  band. The 960 value is probably more reliable, as the other value may be affected by the vibrational transfer discussed in Sec. IV. The value obtained by Pryce and Runciman from an analysis of the spin-orbit splitting of the  ${}^3\text{T}_1 \text{ t}^2 \text{ A}_2$  state is  $1200 \text{ cm}^{-1}$ . This value is affected by uncertainty in the value of the spin-orbit coupling factor and the spin-spin coupling correction. At this

stage, however, the differences between the values of  $v$  obtained in different ways seem minor, and it is gratifying that they all have the same sign and approximately the same magnitude.

The value of  $\underline{a}$  obtained from the temperature effect is equal to that calculated from the dipole terms of the crystal field perturbation. This is in slight disagreement with the low temperature results, where a mixture of dipole and octupole terms was necessary. A value of  $a = 12$  is calculated for the case  $x = \frac{1}{2}$  used in the low temperature case.

The quantity corresponding to  $\underline{a}$  calculated for the  ${}^3T_1$  band does not differ much from unity for any value of  $x$ . This is in agreement with the results shown in Fig. 14, where the total absorption to this state is shown to be virtually independent of temperature. For this reason, it would not be possible to obtain a value of  $v$  from the temperature dependence of the  ${}^3T_1$  band, and because of the intensity transfer phenomenon, one cannot use the temperature dependence of the polarization ratio.

$\text{Co}^{+++}$

The high temperature spectra of this ion are shown in Fig. 16. There was a possibility that the  ${}^5T_2$  ( $e^2t^4$ ) state could become populated sufficiently at  $1000^\circ\text{K}$  to give an absorption band due to the  ${}^5T_2 \longrightarrow {}^5E$  transition. Although there is a strong absorption at about  $25,000\text{ cm}^{-1}$  this is probably a charge transfer band, as the  ${}^5T_2 \longrightarrow {}^5E$  transition should appear at  $18,000 - 19,000\text{ cm}^{-1}$ . The temperature dependence of the  ${}^1T_1$  band ( $6500\text{ Å}$ ) is the same as for the corresponding band of  $\text{Cr}^{+++}$ .

## VII. The Trigonal Field

The study of six ions in the corundum lattice has made possible a comparison of the effects of the trigonal field on each. The separation

of band maxima of the components of a  $T_1$  or  $T_2$  cubic field parent have been taken as the measure of the trigonal field. In Sec. IV it was shown that intensity transfer from a strong oppositely polarized component may shift the band maximum. In  $V^{+++}$  the absorption where  ${}^3T_1$  at E is supposed to appear probably is largely the  $A_2$  component which could absorb in the perpendicular direction in its e vibronic states. Since the e-vibration energies are not too different from the trigonal field energy and the  $A_2$  component lies below the E, the depolarization may not have much effect on the position of the band maximum. The value of  $\nu$  obtained from the temperature dependance certainly agrees well with the directly measured band splitting.

In the first broad band of  $V^{+++}$  the parallel and perpendicular absorption are mixed by the Jahn-Teller effect, as shown in Sec. V. The splitting of  $-90 \text{ cm}^{-1}$  has nothing to do with the trigonal field. In the analogous band of  $Cr^{+++}$ , however, it can be seen by reference to Fig. 11 that the observed splitting may well be the trigonal splitting. The first component is polarized purely in the perpendicular direction and has the greatest intensity in this direction of any of the component states. The second component has the greatest parallel intensity, and is separated by  $\nu/3$  from the lower one. The splitting of  $450 \text{ cm}^{-1}$  is therefore  $\nu/3$ , unless the depolarizing processes are appreciable. The value of  $\nu = 1350 \text{ cm}^{-1}$  is in fairly good agreement with the value obtained from the  $800 \text{ cm}^{-1}$  splitting of the  ${}^4T_1$  band,  $1600 \text{ cm}^{-1}$ .

The analysis of the  $Mn^{+++}$  spectrum given in Sec. V requires  $\nu = 1950 \text{ cm}^{-1}$  for this ion.  $Co^{+++}$  and  $Ni^{+++}$  seem to have smaller values 720 and  $1000 \text{ cm}^{-1}$ .



The excited states of these two ions probably do not undergo as large Jahn-Teller distortions as  $V^{+++}$  and  $Cr^{+++}$ , so that the band splitting measurements give the correct values of  $v$ .

The second order corrections to the splitting do not amount to more than ten percent, so they have been neglected. The best values of  $v$  for the different ions are given in Table XV. The values are not all the same, but they all have the same sign.

TABLE XV

Trigonal field parameters for ions in corundum. In  $\text{cm}^{-1}$ .

	Ti	V	Cr	Mn	Co	Ni
$v$	$> 0$	960	1425	1950	720	1000

The optical determination of the values of  $v$  has some uncertainties connected with it, as noted earlier. It does not seem possible that there is any error in the sign of  $v$  for all the ions, and it seems highly probable that the values of  $v$  are not the same for all the ions.

The sign of  $v$  is given incorrectly by the point charge model if the S.C.F. values of  $\overline{r^n}$  are used. Another method of calculation is to find  $\overline{r^4}$  from the value of  $Dq$ . For the constants given in Table V and the formulas for the constants in the normal and displaced positions, the results are as follows:

Position	$\overline{r^4}_e$	$v$ (ev.)
+0.1	2.95	$-0.200 \overline{r^2}_e + 0.494$
0.0	2.58	$-0.119 \overline{r^2}_e + 0.067$
-0.1	2.39	$-0.083 \overline{r^2}_e - 0.062$

The value of  $Dq$  is taken to be 0.223 eV or  $1800 \text{ cm}^{-1}$ , which is almost the normal value for all the ions in corundum.  $e$  is the charge assigned to the O atom. Since  $v = 0.1$  eV or greater, the correct sign and magnitude cannot be achieved in the normal position for any value of  $r^2 e$ , but they can be achieved in the 0.1 position. The validity of this conclusion depends upon the assumption that the point charge model gives correct ratios of terms of the same power. The actual value of the displacement would depend on the value taken for  $r^2 e$ , but there are too many uncertainties connected with this choice to make further calculations profitable.

The variations of  $v$  are seen to be quite possible theoretically if the ion position in the lattice changes a little from one ion to another. The fourth power term in  $v$  is particularly sensitive to displacement. Thus the positive sign of  $v$  may be caused by a displacement of the ion along the threefold axis, and the variations of its magnitude could be caused by differing amounts of this displacement.

The reason why a displacement of the impurity ion occurs has been suggested in the introduction. The increase of the ionic radius of the impurity over that of  $\text{Al}^{+++}$ , 0.57 Å is about 0.08 Å. The increase in the force of repulsion due to this increase in radius can not be the same from the upper triangle as from the lower (Fig. 1), because these two arrays of  $\text{O}^{2-}$  ions are at different distances and they form triangles of differing size. In order to calculate in a simple way the magnitude and direction of the force acting on the impurity we will first assume that  $\text{O}^{2-}$  ions are not displaced and that they interact with the impurity ion by way of a repulsion potential of the form

$$V = Ae^{-\frac{(R_B - r_n)}{\rho}} \quad (28)$$

where  $R_B$  is the bond length,  $r_n$  is the radius of the impurity and  $\rho$  is a scale factor like the Born-Mayer constant. The increment of the potential upon changing an  $Al^{+++}$  ion into an impurity ion can be written down easily. When we do this for the corundum geometry we have:

$$V = A \left[ \exp \left( -\frac{1}{\rho} (R_u - r_n - z \cos \theta_u) \right) + \exp \left( -\frac{1}{\rho} (R_l - r_n + z \cos \theta_l) \right) \right. \\ \left. - \exp \left( -\frac{1}{\rho} (R_u - r_A - z \cos \theta_u) \right) - \exp \left( -\frac{1}{\rho} (R_l - r_A + z \cos \theta_l) \right) \right] \quad (29)$$

where  $z \cos \theta_u$  is the shortening of the bond length to an upper oxygen, and  $z$  is the displacement along  $C_3$ , measured positive toward the empty octahedral site;  $r_A$  is the radius of  $Al^{+++}$ . The force due to this potential term may be calculated directly: the resulting displacement would have to be calculated from the complete potential, and for this, other terms would have to be added, perhaps a harmonic restoring force, for example. In the undisplaced  $Al^{+++}$  position the force is:

$$F_z = - \frac{\partial V}{\partial z} = \frac{A}{\rho} \left[ \exp \left( -\frac{r_n}{\rho} \right) - \exp \left( -\frac{r_A}{\rho} \right) \right] \left[ -\cos \theta_u \exp \left( -\frac{R_u}{\rho} \right) + \cos \theta_l \exp \left( -\frac{R_l}{\rho} \right) \right] \quad (30)$$

The force is positive (toward empty octahedral site) when  $r_n > r_A$  and when  $\rho > 0.238$ . The larger  $\rho$  the "softer" the force, and it is not unreasonable to have  $O^{=}$  ions with a fairly large value of  $\rho$ .

This calculation makes it reasonable to expect ion displacement, but can it account for the observed differences between the ions studied? The ionic radii of the trivalent ions are all very similar and it does not seem

possible to explain the large differences in the values of  $v$  in these terms. More likely we must consider differences between the polarizabilities of the metal ions as well as that of the  $O^{=}$  ions. It is clear that the simple models do not explain these fine details and a more sophisticated approach will be necessary.

#### Acknowledgements

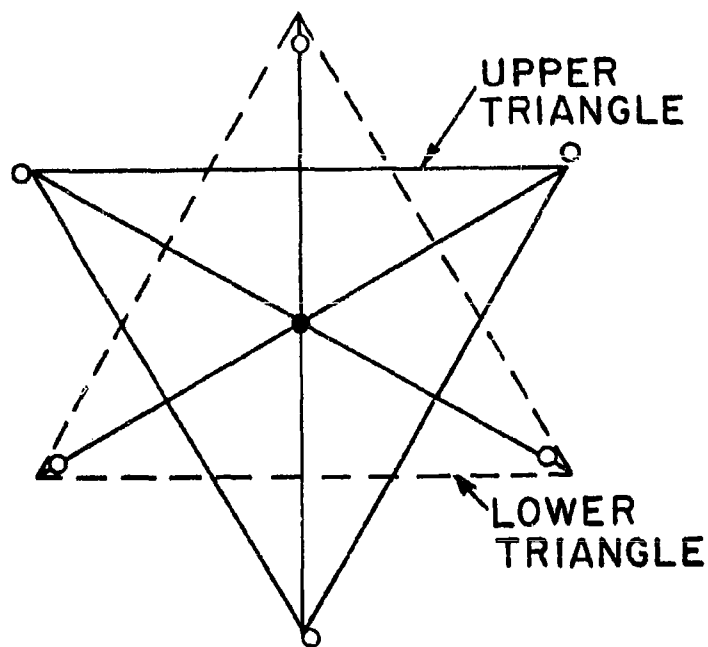
The writer wishes to thank his colleagues S.R. Polo and H.A. Weakliem for many valuable discussions of this work and Mr. Clyde Neil for his capable assistance with the experimental work.

## REFERENCES

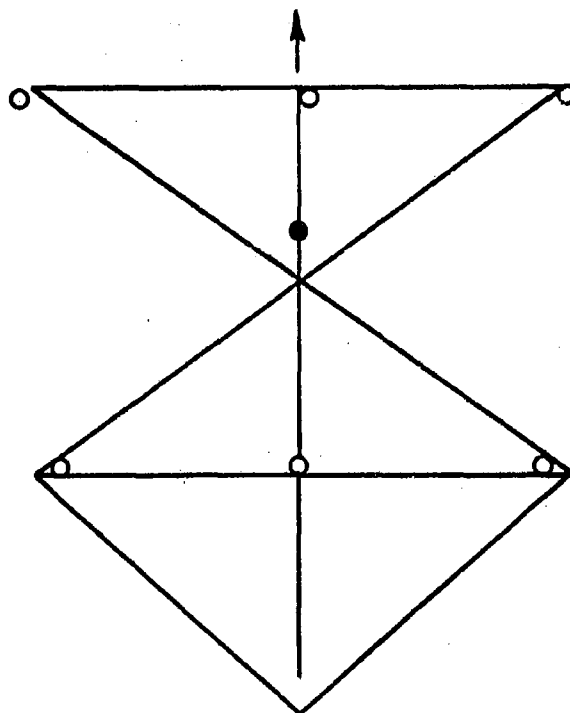
1. Tabelle der Schwingungszahlen, H. Kayser revised by W.F. Meggers, 1944, J. W. Edwards Co.
2. L. Pauling and S.B. Hendricks, J. Am. Chem. Soc. 47, 78 (1925).
3. R. Newnham, private communication. The writer wishes to thank Dr. Newnham for supplying him with improved values of the lattice constants and the parameters. These values have been used throughout this work.
4. J. S. Griffith, The Theory of Transition Metal Ions, Cambridge University Press 1960.
5. R. Bersohn, J. Chem. Phys. 29, 326 (1958).
6. R.E. Watson, Technical Report No. 12, June 1959 Solid State and Molecular Theory Group, M.I.T. Cambridge Mass. The reduction of Watson's functions to  $r^n$  was carried out by Dr. H.A. Weakliem.
7. H.C. Longuet-Higgins, U. Opik, M.H.L. Pryce and R.A. Sack, Proc. Roy. Soc. (London) A244:1 (1958).
8. W. Low, Z. Physik. Chem. 13, 107 (1957).
9. M. H. L. Pryce and W. A. Runciman, Disc. Faraday Soc. No. 26, 34 (1958).
10. C.H. Ballhausen, Z. Physik. Chem. (Frankfurt) 17, 246 (1958).
11. Tanabe and Sugano, J. Phys. Soc. (Japan) 13, 880 (1958).
12. R. S. Krishnan, Proc. Ind. Acad. Sci. 26A 450 (1947).

## FIGURE CAPTIONS

1. Position of neighbors of Al-ion in corundum crystal. The lines shown outline an ideal octahedral site to illustrate the departures in the real crystal.
2. Absorption spectrum of  $Ti^{+++}$  in corundum at  $77^{\circ}K$ .
3. Absorption spectrum of  $V^{+++}$  in corundum at  $77^{\circ}K$ .
4. Absorption spectrum of  $Cr^{+++}$  in corundum at  $77^{\circ}K$ .
5. Absorption spectrum of  $Mn^{+++}$  in corundum at  $77^{\circ}K$ .
6. Absorption spectrum of  $Co^{+++}$  in corundum at  $77^{\circ}K$ .
7. Absorption spectrum of  $Ni^{+++}$  in corundum at  $35^{\circ}K$ .  
The high energy band of this spectrum may be a charge transfer band.
8. Vibrational structure of the first strong band of  $Co^{+++}$  in corundum at  $77^{\circ}K$ . The vibrations of pure corundum and their assignments (ref. 12, see text) are boxed in.
9. Vibrational structure of the first strong absorption band of  $V^{+++}$  at about  $5^{\circ}K$ .
10. Vibrational structure of the first strong absorption band of  $Cr^{+++}$  at about  $5^{\circ}K$ . The trace of structure in the  $\parallel$ -spectrum is thought to be due to crystal imperfections or polarizer imperfections.
11. Energy diagram and intensity formulae for  ${}^3T_2(et)$  of  $V^{+++}$  and  ${}^4T_2(et^2)$  of  $Cr^{+++}$  in trigonal plus tetragonal field. The  $A'$  and  $A''$  designate the representation in  $C_s$ . The spin splitting of  $3A'$  is given in the text. The diagrams given here apply to the case  $Dt \gg v \gg J$ .
12. Absorption spectra of  $Cr^{+++}$  in corundum at various temperatures ( $^{\circ}K$ )  
Upper set  $\perp C$ , lower set  $\parallel C$ .
13. The increase in the area of absorption bands of  $Cr^{+++}$  with temperature; given as the ratio at temperature  $T^{\circ}K$  to  $298^{\circ}K$ .
14. Change of area of absorption bands of  $V^{+++}$  with temperature.
15. Plot of  $\theta/2.31$  vs  $T$  for  $a = 8$  and  $a = 6$  (see text).
16. Absorption spectrum of  $Co^{+++}$  in corundum at various temperatures. The  $1300^{\circ}K$  spectrum is from a separate run.



DIRECTION TOWARD  
EMPTY OCTAHEDRAL SITE



○ OXYGEN  
● ALUMINUM

POSITION OF NEIGHBORS OF Al-ION IN  
CORUNDUM CRYSTAL

Figure 1 - I

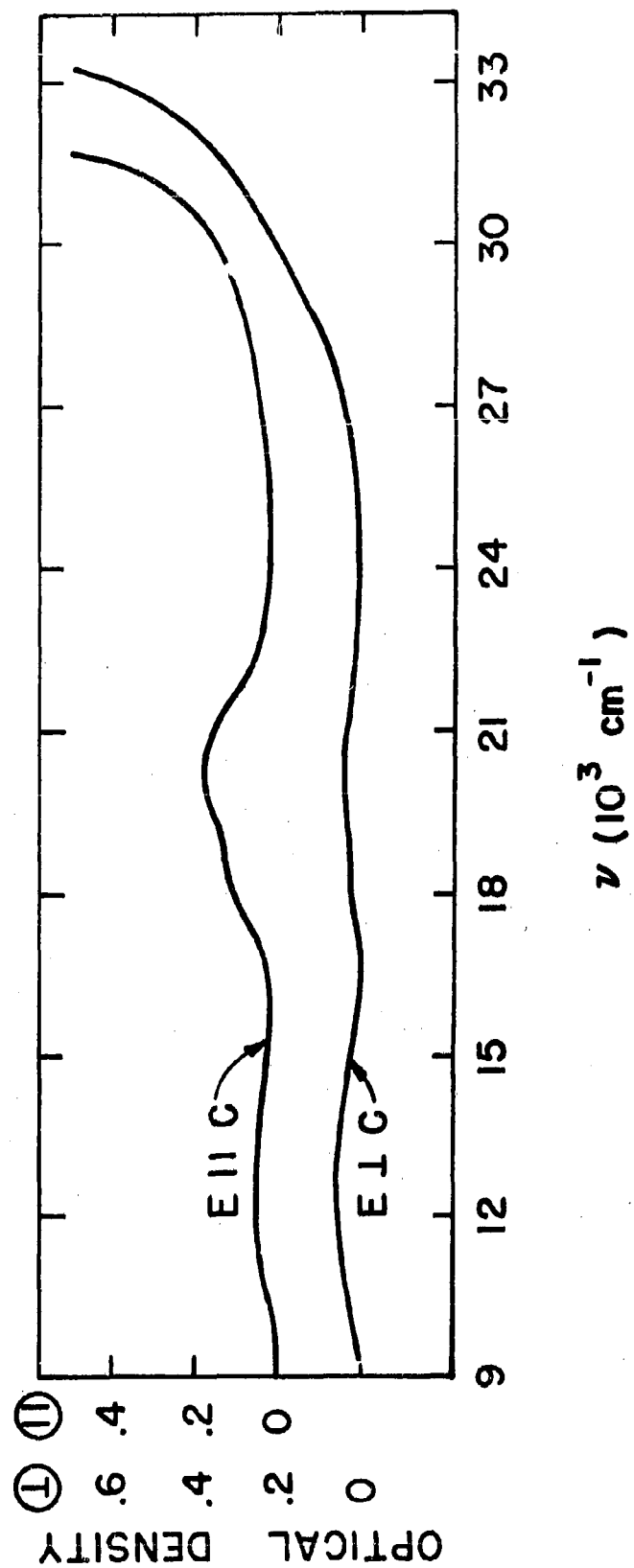


Figure 2 - I



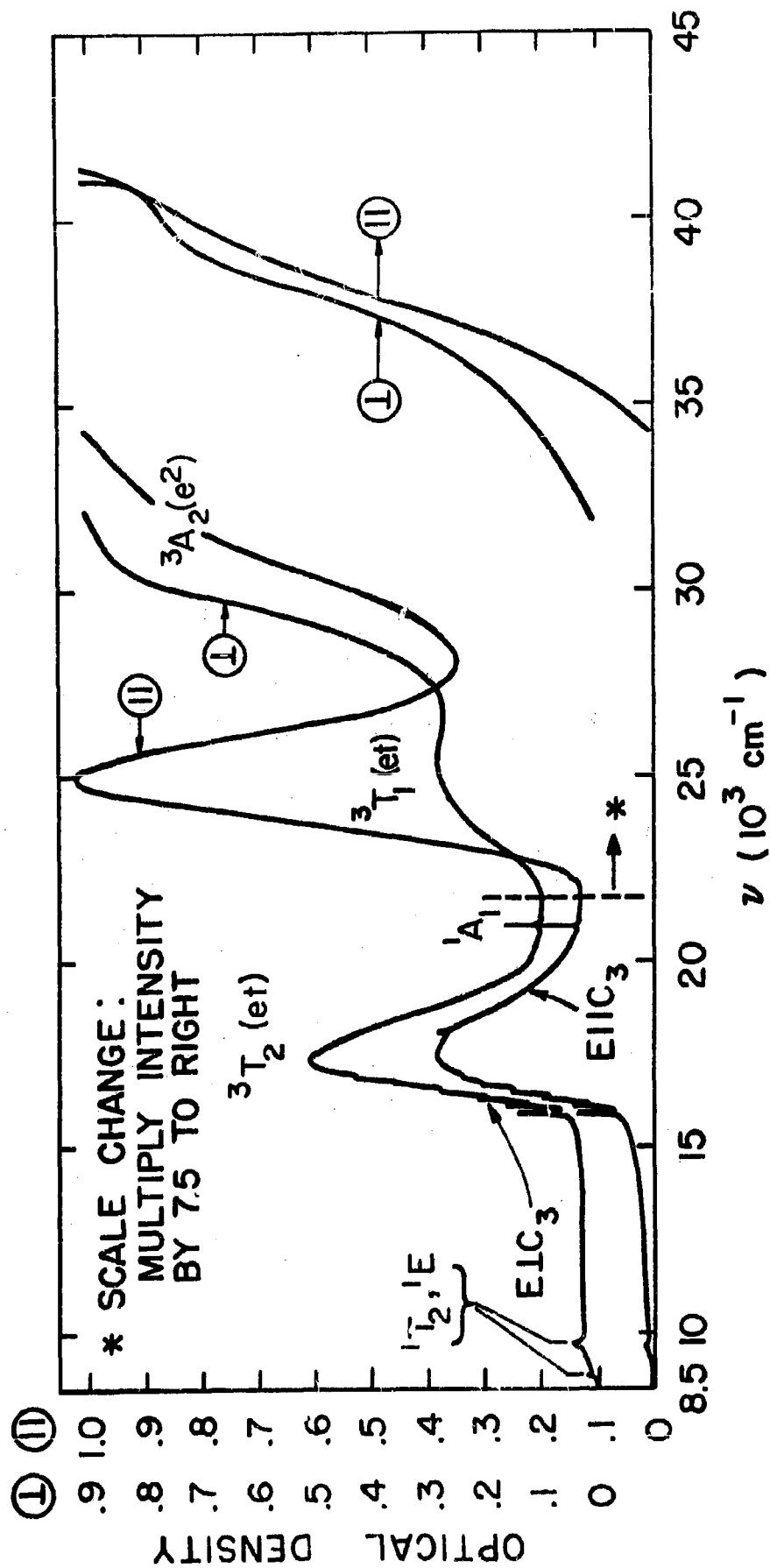


Figure 3 - I



**Figure 4 - I**

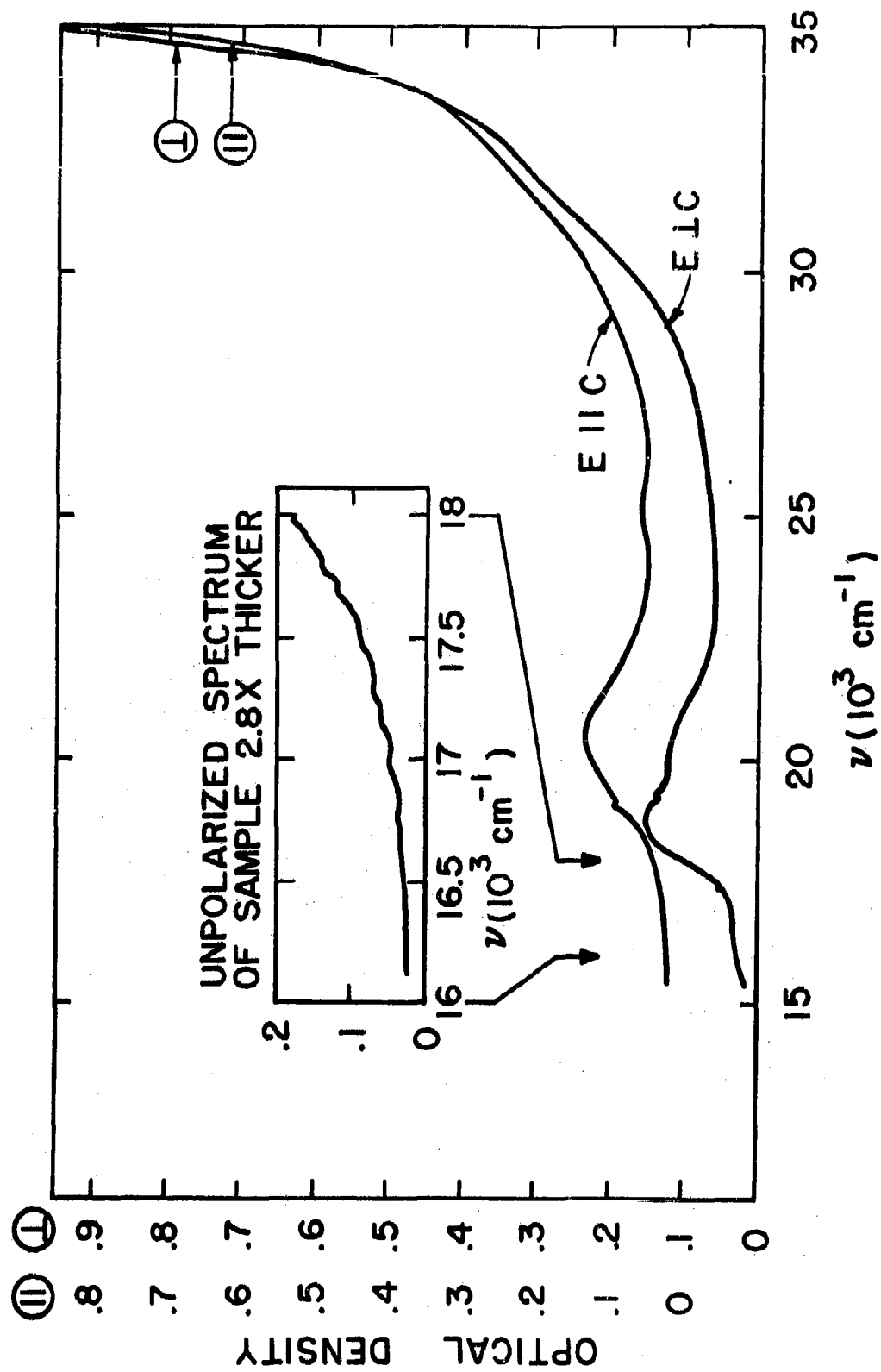


Figure 5 - I

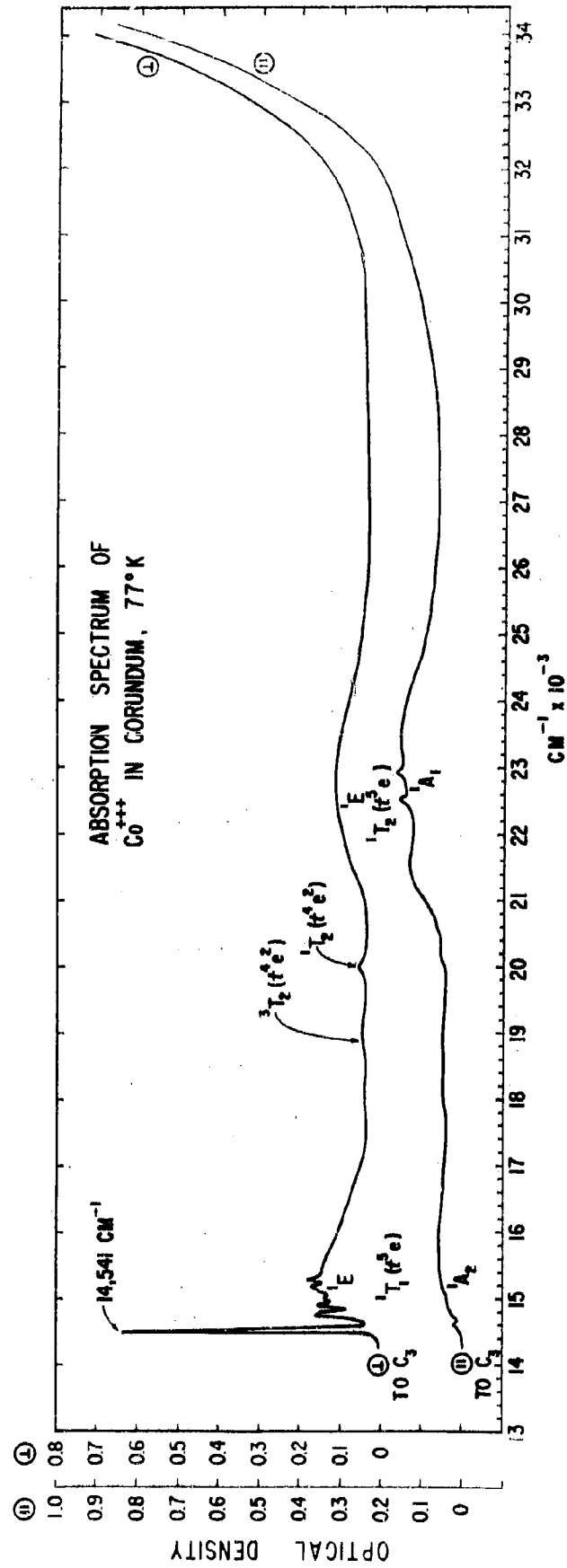


Figure 6 - I

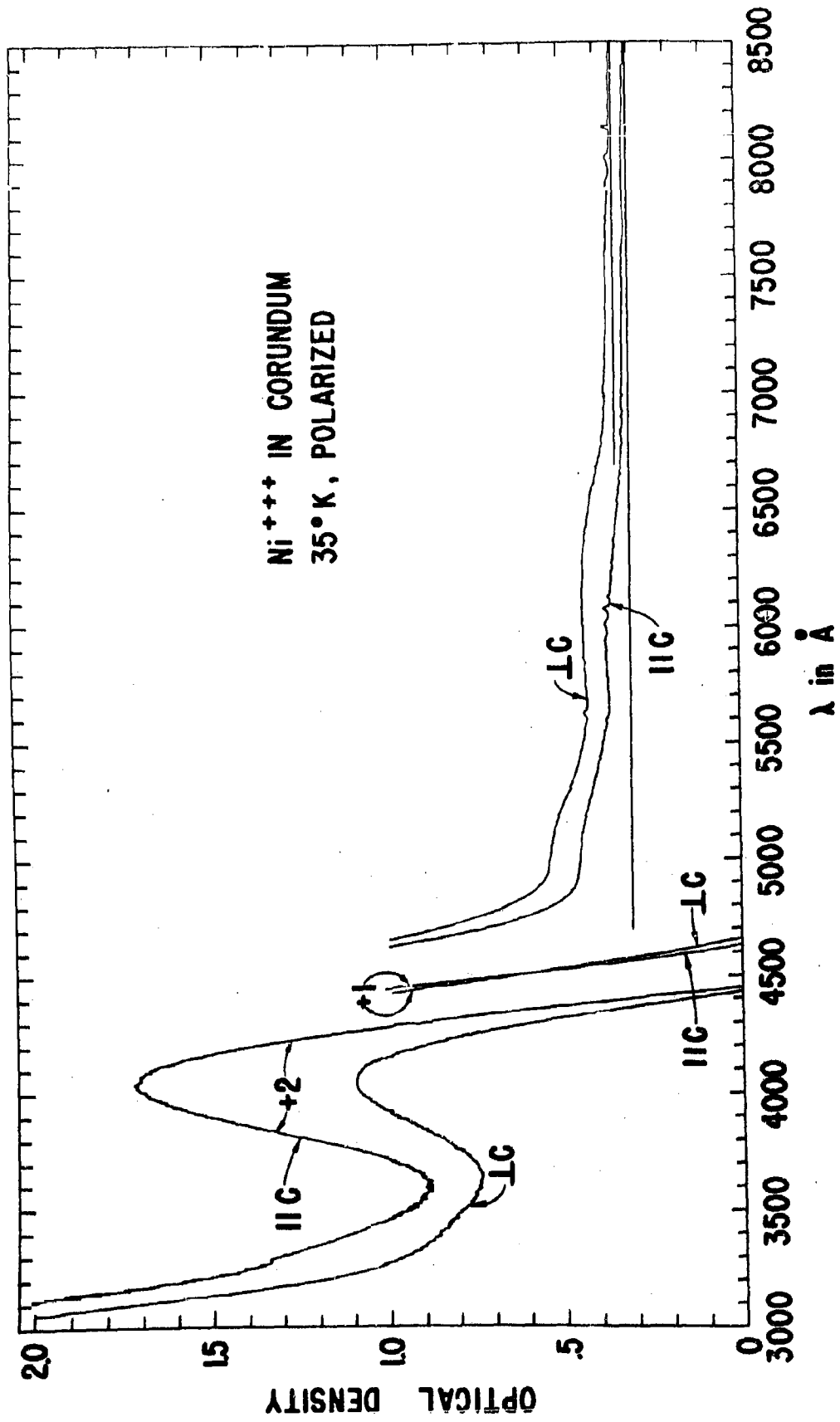


Figure 7 - I

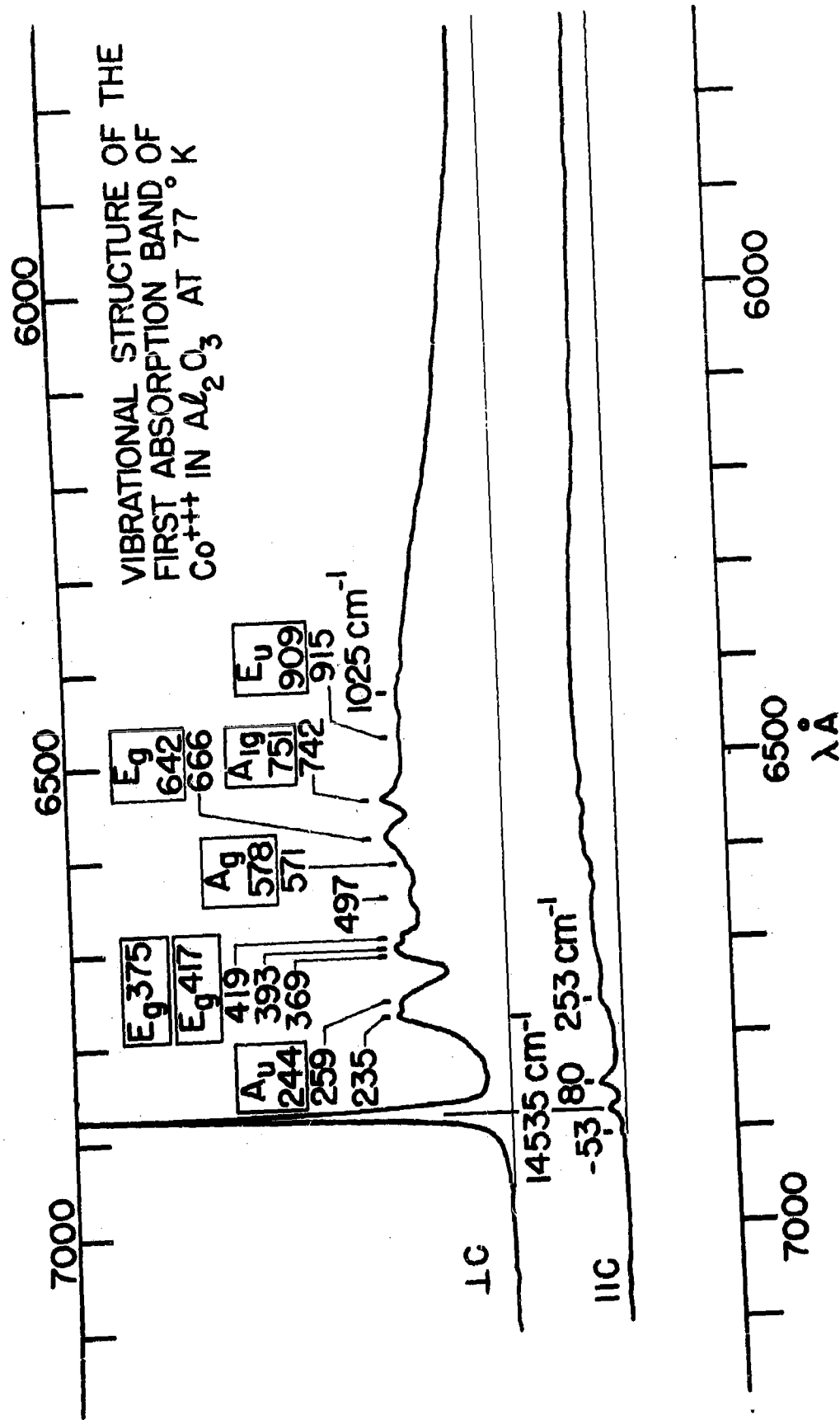


Figure 8 - I

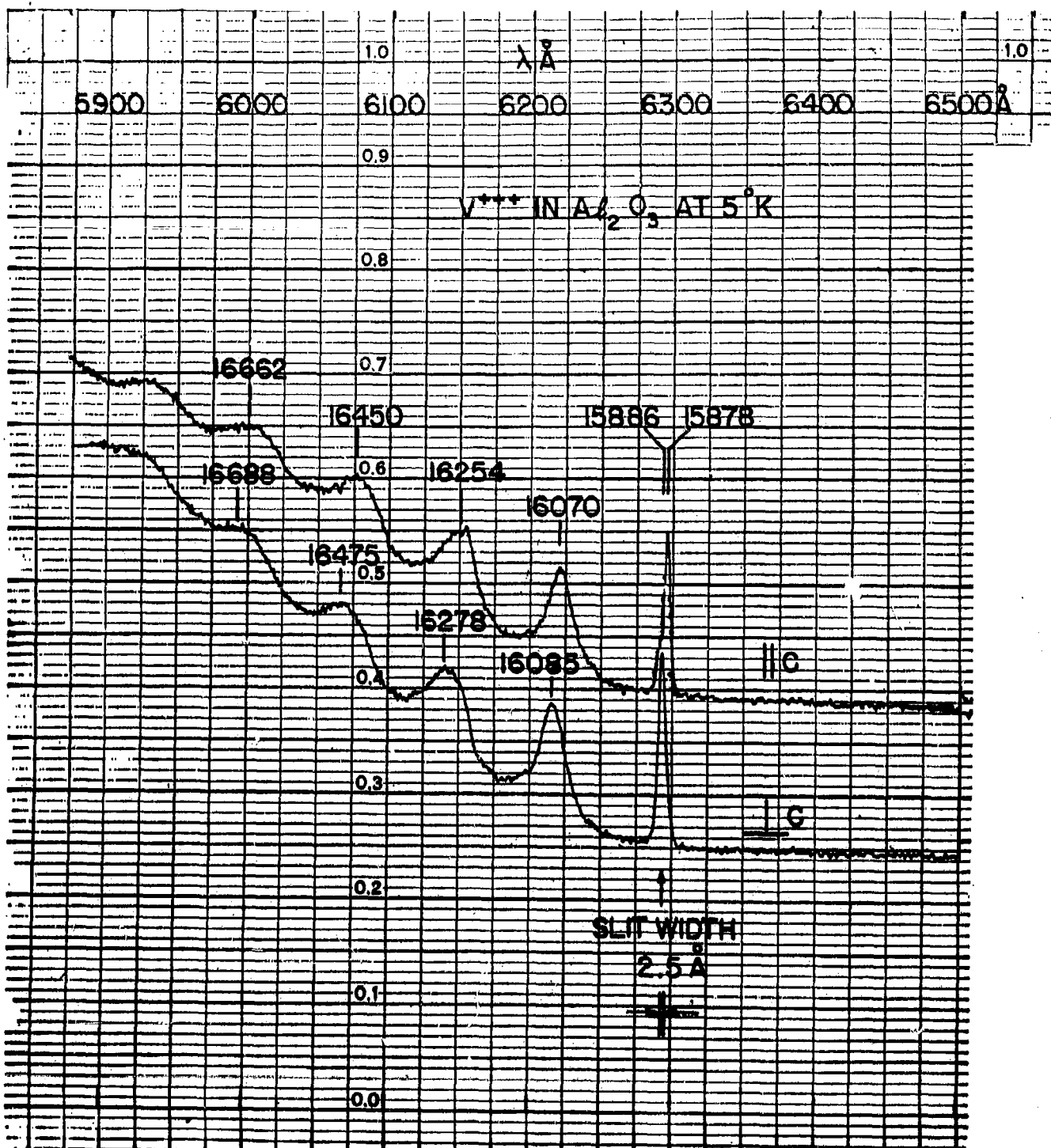
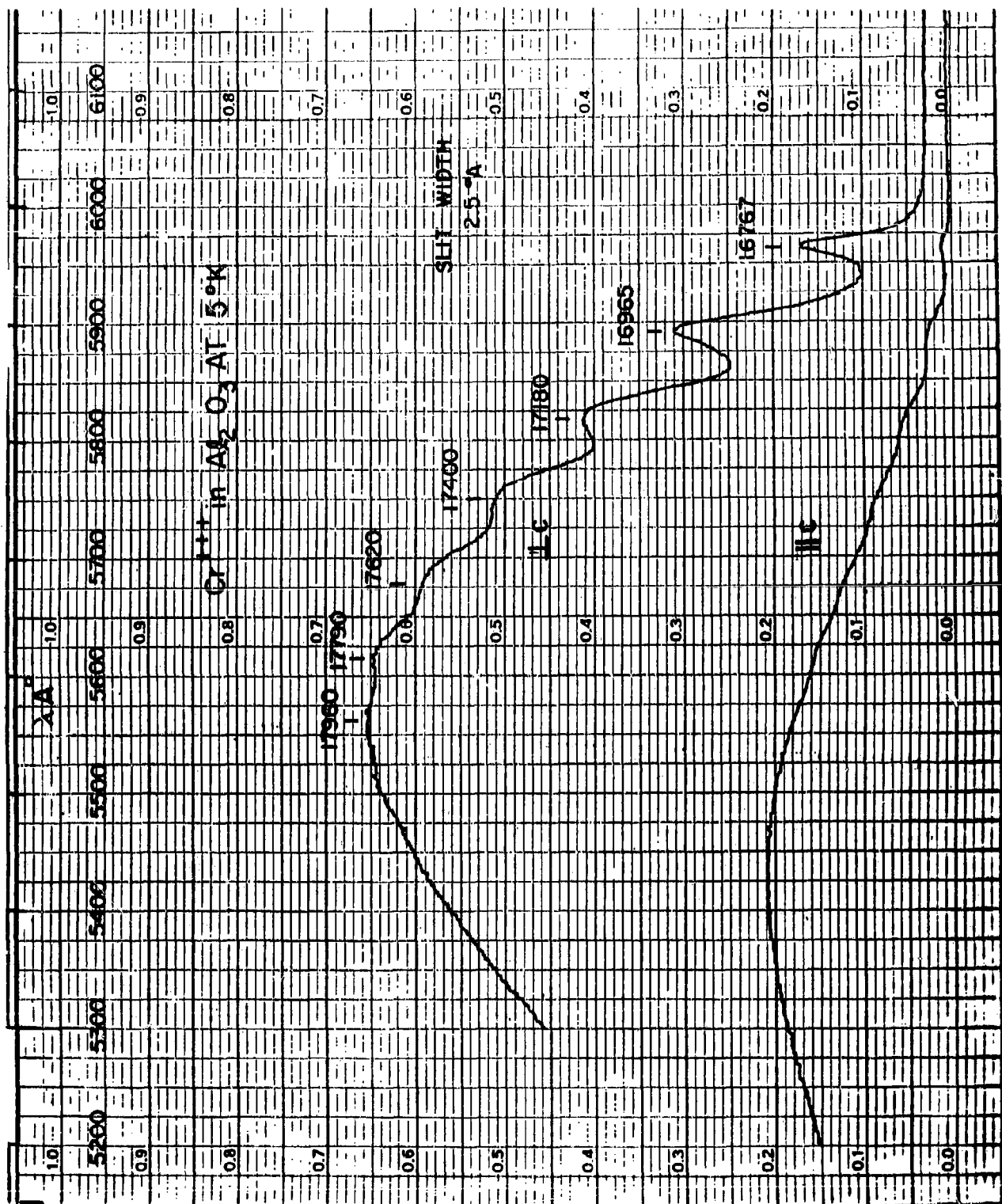


Figure 9 - I





$$\phi_1 A'' \frac{\frac{7}{4}Dt + \frac{v}{6}}{\pm 1} = \frac{0}{A^2 + 8D^2}$$

$$\phi_2 A' \frac{\frac{7}{4}Dt - \frac{v}{6}}{0} = \frac{12D^2}{\frac{1}{3}A^2 + \frac{8}{3}D^2}$$

$$\phi_3 A' \frac{-7Dt}{0} = \frac{6D^2}{\frac{2}{3}A^2 + \frac{16}{3}D^2}$$

EFFECT OF TRIGONAL PLUS  
TETRAGONAL FIELD ON  
 $v + + + 3T_2(et)$  STATE.

$$\phi_3 A' \frac{7Dt}{\pm \frac{1}{2}} = \frac{\pm \frac{1}{2} \frac{I_{II}}{I_I}}{\pm \frac{3}{2}} = \frac{6D^2}{\frac{2}{3}(A-B/\sqrt{2})^2 + 3D^2}$$

$$\phi_2 A' \frac{-\frac{7}{4}Dt + \frac{v}{3}}{\pm \frac{3}{2}} = \frac{\pm \frac{3}{2} \frac{I_{II}}{I_I}}{\pm \frac{1}{2}} = \frac{12D^2}{\frac{1}{2}(A-B/\sqrt{2})^2 + \frac{3}{2}D^2}$$

$$\phi_1 A'' \frac{-\frac{7}{4}Dt - \frac{v}{3}}{\pm \frac{1}{2}} = \frac{\pm \frac{1}{2} \frac{I_{II}}{I_I}}{\pm \frac{3}{2}} = \frac{0}{(A-B/\sqrt{2})^2 + \frac{9}{2}D^2}$$

EFFECT OF TRIGONAL PLUS  
TETRAGONAL FIELD ON  
 $cr + + + 4T_2(et^2)$  STATE.

Figure 11 - I

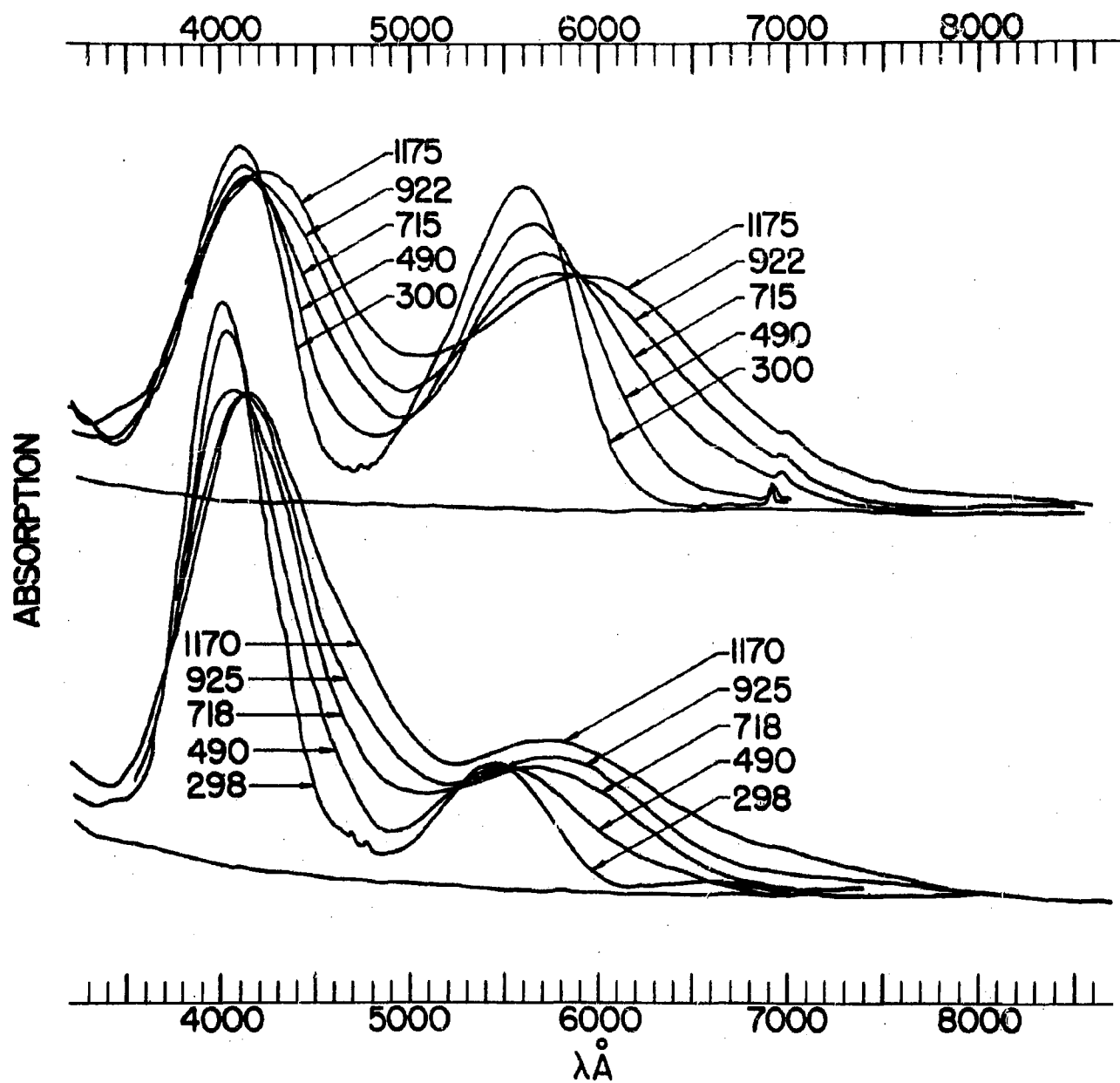
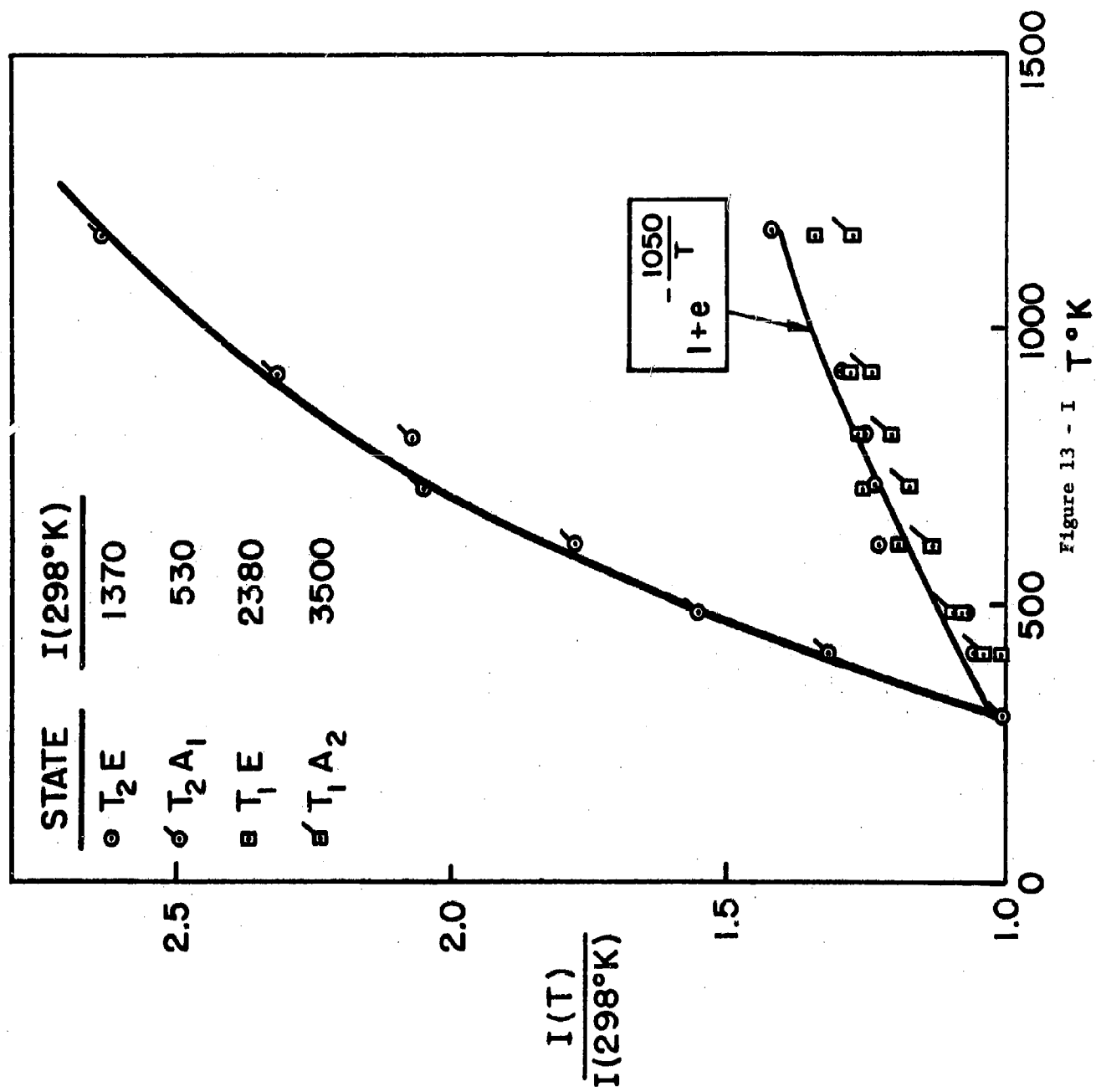


Figure 12 - I



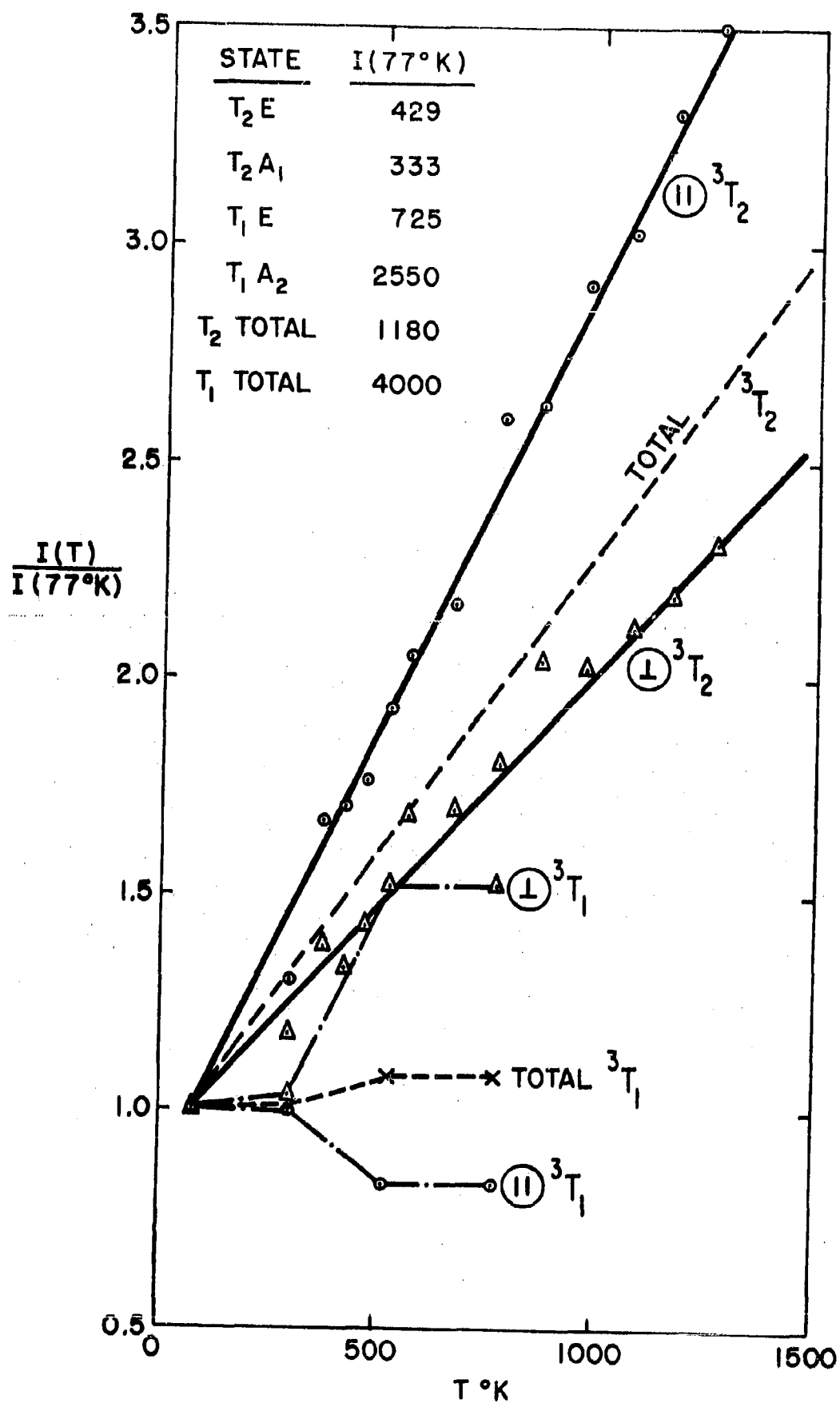


Figure 14 - I

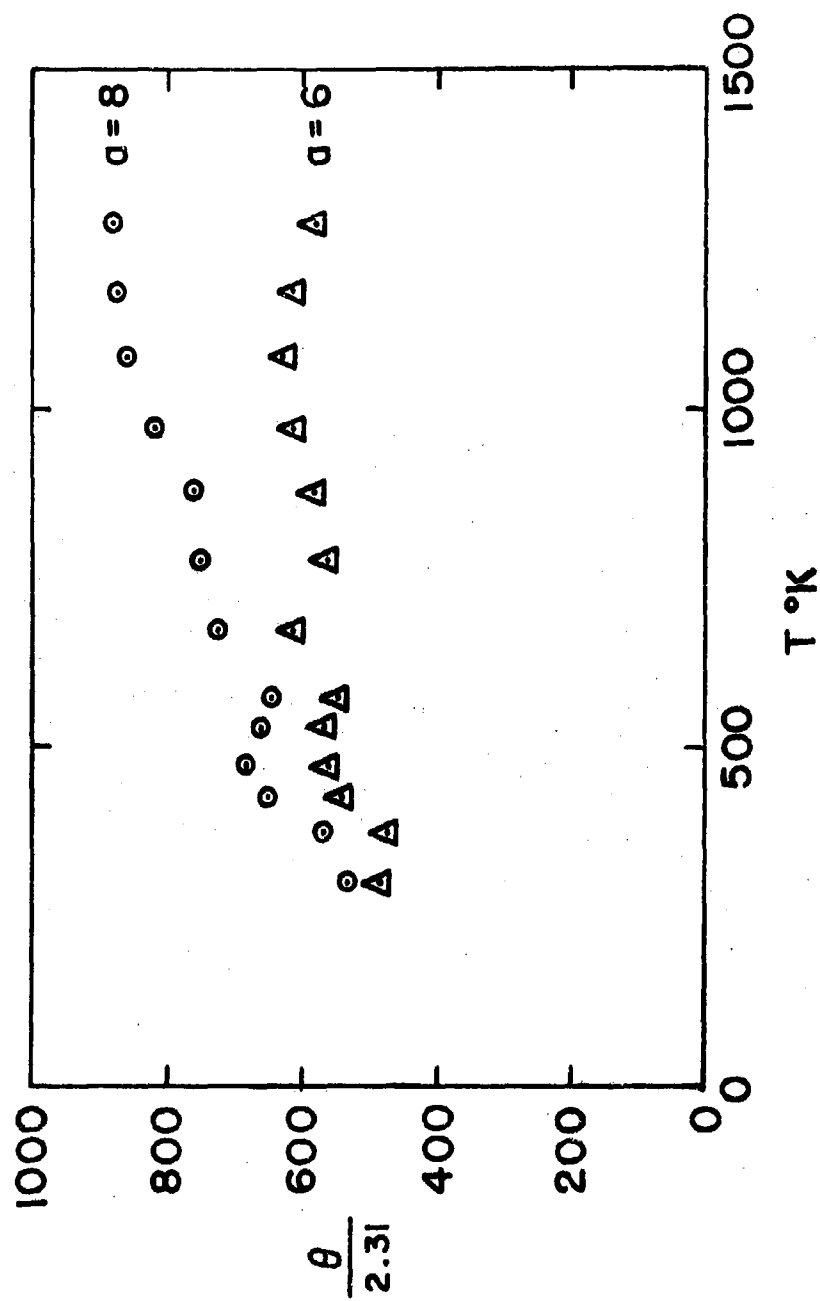


Figure 15 - I

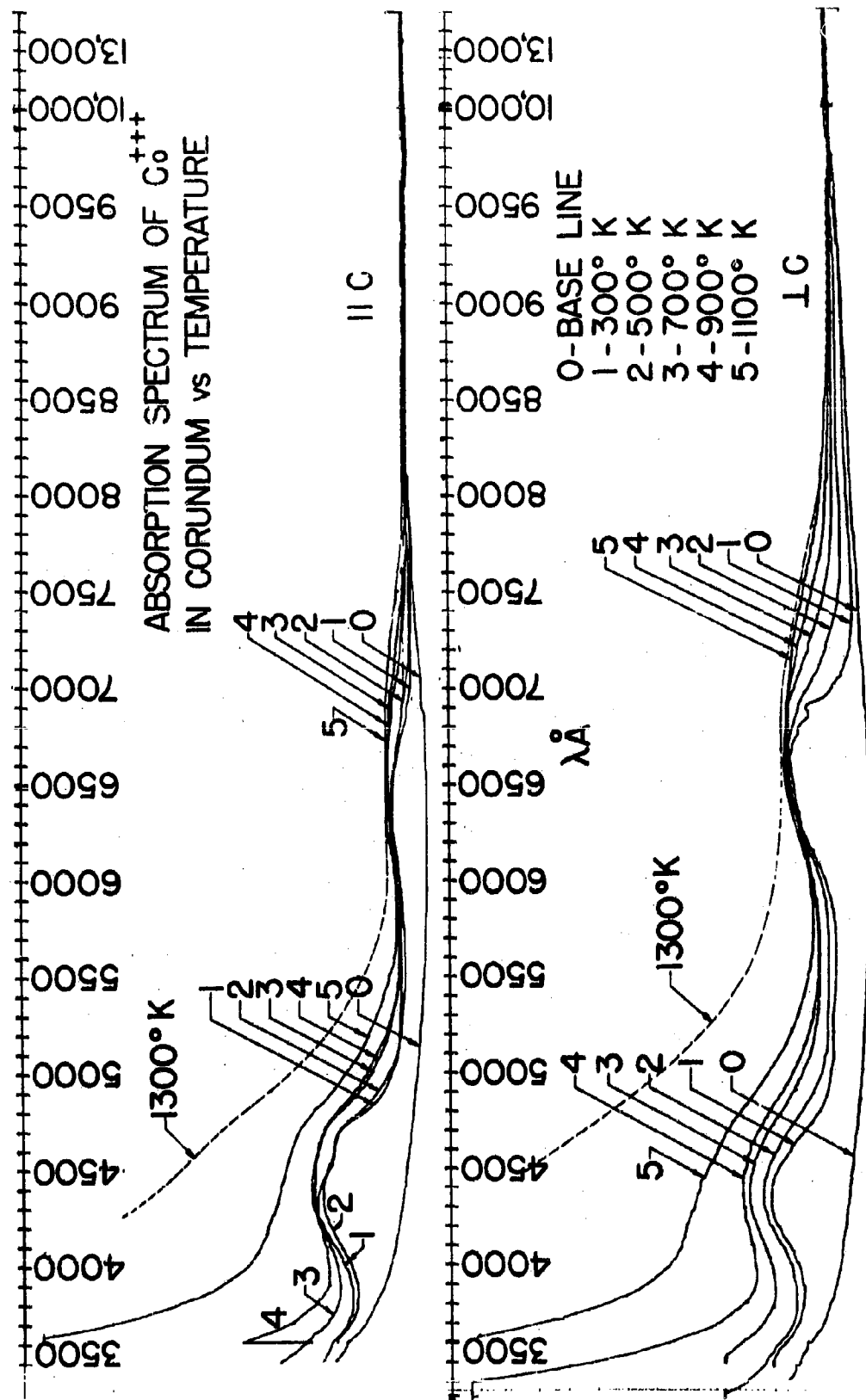


Figure 16 - 1

# Optical Spectra of $\text{Ni}^{++}$ , $\text{Co}^{++}$ , and $\text{Cu}^{++}$ in Tetrahedral Sites in Crystals\*

Herbert A. Weakliem  
RCA Laboratories, Princeton, New Jersey

## ABSTRACT

The polarized absorption spectra of  $\text{Ni}^{++}$  and  $\text{Co}^{++}$  in crystals of  $\text{ZnO}$ ,  $\text{ZnS}$ , and  $\text{CdS}$ ;  $\text{Ni}^{++}$  in crystals of  $\text{Cs}_2\text{ZnCl}_4$  and  $\text{Cs}_2\text{ZnBr}_4$ ; and  $\text{Cu}^{++}$  in  $\text{ZnO}$  have been measured at  $4^\circ\text{K}$ ,  $77^\circ\text{K}$ , and room temperature. The spectra have been interpreted by the use of crystal field theory for the states of the  $(3d)^n$  configuration acted on by a potential of predominately  $T_d$  symmetry. Certain details of the spectra are accounted for by smaller contributions from fields of lower symmetry, notably a  $C_{3v}$  potential contribution for the transition metal ions in  $\text{ZnO}$ . Crystal field, electrostatic repulsion, and spin-orbit parameters have been obtained for all these cases. An empirical correlation between the electrostatic repulsion parameter,  $B$ , for the ions in the crystals and the ligand polarizability has been obtained. Although the configuration mixing between the states of the configurations  $(3d)^n$  and  $(3d)^{n-1}(4p)$  has been found to give a negligible contribution to the calculated relative energies of the levels, it does partially explain the large values of the observed intensities of the transitions. The relative intensities of transitions between the spin-orbit components have been calculated by using models for both  $p-d$  mixing and  $\sigma$ -bonding with the ligands. Neither model gives a quantitatively good account of the observed relative intensities and there is evidence, at least for the  $\text{Ni}^{++}$  spectra, that the observed low energy, intense charge transfer absorptions play a predominant role in the intensity mechanisms of the  $d-d$  transitions.

---

\*The research reported in this paper has been sponsored by the Electronics Research Directorate of the Air Force Cambridge Research Laboratories, Office of Aerospace Research under Contract AF19 (604)-5541.

## INTRODUCTION

A study of the absorption spectra of tetrahedrally coordinated transition metal ions in crystals has been undertaken. The spectra of  $\text{Ni}^{++}$  in  $\text{ZnO}$ ,  $\text{ZnS}$ ,  $\text{CdS}$ ,  $\text{Cs}_2\text{ZnCl}_4$ , and  $\text{Cs}_2\text{ZnBr}_4$ ;  $\text{Co}^{++}$  in the former three crystals; and  $\text{Cu}^{++}$  in  $\text{ZnO}$  are discussed in this paper. The room temperature spectra of powdered solid solutions of  $\text{NiO}$  and  $\text{CoO}$  in  $\text{ZnO}$ <sup>1</sup>; the visible region of the spectrum of  $\text{Cs}_2(\text{Zn}_{.75}\text{Ni}_{.25})\text{Cl}_4$ <sup>2</sup>; and the 77°K axial spectrum of a crystal of  $\text{ZnO}:\text{Cu}^3$  have been measured previously. In each of these cases, the spectrum has been interpreted as being due to the transition metal ion in tetrahedral coordination. Our results on the crystal spectra are in agreement with this conclusion. Crystal field theory<sup>4,5</sup> has been used successfully for detailed interpretations of the results. Many of the formal aspects of the theory for ions in octahedral coordination, for which an extensive literature exists\*, are directly applicable to the case of tetrahedral coordination since the point groups  $O$  and  $T_d$  are isomorphous. One non-trivial difference in the theory applied to these two cases is that the potential of a tetrahedral array of charges has an odd power term proportional to  $xyz$ . This term causes no further splitting of the degenerate  $d^n$  levels, but may be effective in removing the parity classification of the eigenfunctions, for example by causing the ground state  $(3d)^n$  even parity configuration to be mixed with the higher energy  $(3d)^{n-1}(4p)$  odd parity configuration. The effect of such mixing on the relative energies of the  $(3d)^n$  levels and on the intensities of transitions between the energy levels has been examined. Corrections to the relative energies are shown to be negligibly small, which agrees with recent corrected estimates by Low and Weger<sup>6</sup>.

The odd parity contributions to the wave functions due to  $p-d$  mixing qualitatively account for the observed intensities of the bands, but fails to give a good account of the relative strengths of individual spin-orbit

---

\*The review articles cited in References 4 and 5 are devoted to crystal field theory and contain most of the pertinent literature references.



components. Other contributions to the intensity of the transitions, including a molecular orbital (MO) model and mixing with charge transfer states, are discussed, but a detailed model which gives agreement with experiment has not been developed.

Spin-orbit, electron repulsion, and crystal field parameters have been obtained and are correlated with certain physical properties of the host lattice. It has been found that the electron repulsion parameter  $B$  depends linearly on the ligand polarizability. The values of  $\lambda$  obtained for  $\text{Co}^{++}$  are larger than those found from spin resonance<sup>7,8</sup> and magnetic susceptibility<sup>9,10</sup> studies on similar materials.

Each section of the paper is usually subdivided into several parts. The first part, which treats the general case, is followed by three sections specifically concerned with  $\text{Cu}^{++}$ , with  $\text{Ni}^{++}$ , and with  $\text{Co}^{++}$  and the last part deals with general conclusions.

#### EXPERIMENTAL

The ZnO crystals were grown from a lead fluoride melt by slow cooling<sup>11</sup>. The transition metal ions were incorporated in the crystals by adding about 1% of the oxide or carbonate to the initial mixture of zinc oxide and lead fluoride. The crystals usually grow in the form of thin hexagonal plates with the hexagonal  $c$  axis normal to the plate face. Other crystal habits were sometimes obtained, but the crystals were of too poor a quality for optical studies. Spectra obtained with the plate face of the crystals oriented normal to the beam are polarized with  $\vec{E}$  and  $\vec{H}$  perpendicular to  $\vec{c}$ . The other polarization was obtained by mounting a section of one of the more dilute crystals so that  $\vec{c}$  was perpendicular to the direction of propagation of the light. In this orientation, the crystals

were at most 0.2 mm in one direction, but by carefully masking with a slotted copper disc and placing the crystal at the exact focus of the spectrophotometer, satisfactory spectra were obtained.

ZnS crystals grown from the vapor phase\* which were predominately hexagonal, but which had numerous stacking faults, were doped with the transition metal ions by vapor phase diffusion of the metal sulfide in the presence of a sulfur atmosphere. The same method was used to obtain crystals of CdS:Ni and CdS:Co. Pure CdS crystals obtained from the Eagle-Picher Co. and crystals grown from the vapor phase\*\* in these laboratories were both used. Nickel diffused quite rapidly into these crystals at 800°C, as much as 0.1 percent being incorporated in a few hours. The incorporation of cobalt proceeded more slowly at this temperature and heating for several days was required in order to obtain concentrations as high as 0.1%.

$\text{Cs}_2\text{ZnX}_4$  (where  $\text{X}^- = \text{Cl}^-$  or  $\text{Br}^-$ ) were prepared<sup>2</sup> by crystallization from an aqueous solution containing stoichiometric amounts of CsX and  $\text{ZnX}_2$  acidified by the addition of HX. To the molten salt under an atmosphere of HX was added the desired amount of either  $\text{NiX}_2$  or  $\text{CoX}_2$ . The melt contained in a sealed, evacuated Vycor tube was then crystallized by use of the Bridgeman technique. The resulting large single crystal fragments were readily cleaved to give suitable samples for the measurement of spectra.

The crystal spectra in the range 0.2  $\mu$  to 2.5  $\mu$  were obtained with a Cary model 14M spectrophotometer. Low temperature spectra were measured with the crystals attached with silver paste to the cold finger of a brass,

---

\* Grown by C. W. Struck, RCA Princeton.

\*\* Grown by L. A. Barton, RCA Princeton.

two chamber cryostat equipped with quartz windows. A Foucault prism which was placed in the optical path between the beam divider and the entrance slit was used to obtain the polarized spectra. The degree of polarization was better than 95% in the visible region of the spectrum. The resolution generally obtained was  $10 - 20 \text{ cm}^{-1}$ . Infrared spectra were measured for some of the crystals at room temperature with the Perkin-Elmer models 21 and 221 spectrophotometers.

#### CRYSTAL STRUCTURES

The crystal structure of the host lattice, and in particular the site symmetry at the transition metal ion position, are of central importance to the understanding of the spectra. The crystals of ZnO, ZnS, and CdS used all have the wurtzite structure<sup>12</sup>, space group  $P 6_3 \text{ } \bar{m} \text{ } c_2 = C_{6v}^4$ , with the atoms occupying two sets of special positions (b) whose coordinates are (00v) and which have the point symmetry  $3 \text{ } \bar{m} = C_{3v}$ . It is convenient to think of the wurtzite structure as consisting of a hexagonal close-packed lattice of anions with cations occupying one half of the tetrahedral holes (and also forming a hexagonal close-packed lattice). Each atom is tetrahedrally surrounded by four atoms of the opposite type. There are also octahedral holes in the anion lattice which are normally unoccupied in the pure compound and which lie on lines parallel to the hexagonal  $c$  axis. These normally empty sites form a rather open channel along the  $c$  axis. The ideal structure has  $c/a = (\frac{8}{3})^{\frac{1}{2}}$ ,  $v = 0$  for M, and  $v = \frac{3}{8}$  for X which makes the M-X bond length equal to  $(\frac{3}{8})^{\frac{1}{2}} a$ . An atom at the center of an octahedral hole in the anion lattice has a slightly larger bond distance, equal to  $\frac{a}{\sqrt{2}}$ . This position is also surrounded by an octahedron of M atoms, three of which are at a distance  $(\frac{3}{8})^{\frac{1}{2}} a$  and the other three are at a distance  $(\frac{17}{24})^{\frac{1}{2}} a$ . The actual value of  $c/a$  is slightly less than the ideal value for the three compounds being discussed. The  $M - X_4$  tetrahedra

are therefore not regular; the M - X distance which is parallel to  $c_m$  is slightly shorter than the other three equivalent distances. Taking  $\delta$  to be the difference between the two bond lengths (negative if the unique distance is the smaller one) and calling the three equal bond lengths  $d$ , one finds

-  $\delta/d = 0.0154, 0$ , and  $0.008$  for ZnO, ZnS, and CdS, respectively.

Both  $\text{Cs}_2\text{ZnCl}_4$ <sup>13</sup> and  $\text{Cs}_2\text{ZnBr}_4$ <sup>14</sup> are isostructural with  $\text{K}_2\text{SO}_4$  which is orthorhombic, space group  $Pnma = D_{2h}^{16}$ , with four molecules per unit cell. The structure contains discrete tetrahedral  $\text{ZnX}_4$  ions, lying in mirror planes, and surrounded by eight  $\text{Cs}^+$  ions. The tetrahedra can be described by taking a regular tetrahedron and tilting one bond in the mirror plane by about  $5^\circ$  away from the other bond which lies in the mirror plane. There is also a difference of about  $0.2 \text{ \AA}$  between the pairs of bond lengths lying in the mirror plane and the pair perpendicular to the mirror plane for the bromide, whereas the lengths are all nearly equal for the chloride. The true symmetry of the anion is  $m = C_s$ .

#### RESULTS

The unpolarized absorption spectra of  $\text{Ni}^{++}$  in ZnO, ZnS, and CdS at  $77^\circ\text{K}$  and  $298^\circ\text{K}$  are shown in Fig. 1. The unpolarized absorption spectra of  $\text{Co}^{++}$  in the same compounds and at the same temperatures are shown in Fig. 2. In each of these cases, the same crystal was used for the two different temperatures and the curves were drawn to the same scale, the base lines being arbitrarily shifted in order to minimize overlap of the two curves. It is apparent upon comparison of the spectra for these two temperatures that the integrated intensity of each of the bands is not very temperature dependent. Some of the spectra have been measured at temperatures up to  $1000^\circ\text{K}$  and it was found that the integrated intensity of the bands decreases slightly with increasing temperature. This clearly indicates that the transitions are not vibrationally induced<sup>15</sup>. The  $f$  numbers (oscillator strengths) of the principal room temperature bands for four cases are given in Table I, together with the wave numbers of the band

maxima and the assignment of the upper level of the transitions. The  $f$  numbers were calculated from the formula

$$f = \left[ 0.431 \times 10^{-8} \right] \left[ \frac{1}{cd} \right] \int_0^{\infty} \rho(\nu) d\nu$$

where  $\rho(\nu)$  is the optical density as a function of frequency  $\nu$  measured in  $\text{cm}^{-1}$ ,  $c$  is the concentration of absorbing species in moles/liter and  $d$  is the thickness in cm. The integral was estimated by a graphical integration of the area under the curve for each band. The  $f$  numbers are factors of 10 to 100 higher than typical values found for the same ions situated in a centrosymmetric ligand environment. This is one piece of evidence that the ions substitute for a host lattice cation at its regular lattice site and are therefore tetrahedrally coordinated. This is also supported by the assignment of the transitions which is discussed later.

#### Spectra of $\text{Ni}^{++}$

The room temperature spectra of  $\text{Ni}^{++}$  all show three rather broad bands of increasing intensity in the direction of higher energy of absorption. The near infrared-visible band is the most intense of the three and is split into two components in each case. With the exception of  $\text{CdS:Ni}$ , a steep absorption edge several thousand wave numbers less than the band gap energy of the pure host crystal is observed. The spectra of very dilute crystals have a very intense absorption band to the violet end of the spectrum. This is shown in the lowest curve of Fig. 1b for  $\text{ZnS:Ni}$  which is the  $77^\circ\text{K}$  spectrum of a  $35 \mu$  thick crystal containing about 0.005%  $\text{Ni}^{++}$ . The absorption band has its intensity maximum at  $25,000 \text{ cm}^{-1}$  and at higher absorption energies only the very steep absorption edge associated with the valence band to conduction band transition of  $\text{ZnS}$  is observed. The  $f$  number of this band is estimated to be nearly unity. This is clearly not a transition of the  $d-d$  type and is associated

with an electronic process involving both the nickel ion and its ligand environment which will be referred to as a charge transfer process. There is some evidence, discussed in the Intensity section, that this transition plays a role in providing the observed intensity of the weaker, lower energy, predominately  $d-d$  transitions.

A similar charge transfer process in dilute CdS:Ni was not observed, as Fig. 1c shows. However the lower band gap energy of pure CdS may be too small to permit one to observe the transition. The lower curve of Fig. 1d shows the charge transfer transition, which has a peak maximum at  $22,500\text{ cm}^{-1}$ , for ZnO:Ni. The band gap energy for ZnO is about  $4100\text{ cm}^{-1}$  less than that for ZnS whereas the charge transfer transition for these crystals containing  $\text{Ni}^{++}$  is only  $2500\text{ cm}^{-1}$  less. Similar high intensity, high energy transitions have been observed for  $\text{Ni}^{++}$  in crystals of  $\text{Cs}_2\text{ZnCl}_4$  and  $\text{Cs}_2\text{ZnBr}_4$  but are not shown here and will be the subject of a later paper. We only remark here that, unlike the case of  $\text{Ni}^{++}$  in the wurtzite lattices, there is a whole series of intense, anisotropic absorption bands in the near uv for nickel in the cesium tetrahalozincates. Figure 3 shows the  $d-d$  transitions at room temperature for  $\text{Ni}^{++}$  in the latter compounds.

Polarized spectra of the near infrared-visible bands of  $\text{Ni}^{++}$  in the wurtzite lattices measured at liquid helium temperatures are shown in Fig. 4. These curves were traced directly from the spectrophotometer recordings and are therefore plotted on a wavelength scale, unlike the previous figures referred to which are plotted on an energy scale. Each curve is labeled to show the orientation of the electric vector of the light beam with respect to the crystallographic  $c$  axis of the host crystal. The numbers on the figures are the wave numbers of the indicated peak maxima and more prominent shoulders and were obtained from the wave lengths by the use of Kayser's tables<sup>16</sup>. The two polarizations are nearly

identical for ZnS:Ni and CdS:Ni. Since the splitting of the degenerate  $d^n$  levels of the free-ion is caused primarily by the electric field of the nearest neighbor ligands in the crystal, it is concluded that either the environment of the nickel ion is cubic or local anisotropies are randomly oriented throughout the crystal. The observed anisotropy for ZnO:Ni, shown in Fig. 4a, has been interpreted as being due to a small trigonal field superimposed on a predominately tetrahedral field. The spectrum with  $E \perp c$  is identical with that obtained by directing the light beam along the  $c$  axis. In the latter case, it has been pointed out that both  $E$  and  $H$  are  $\perp c$ , but since this spectrum has been found to be identical with the  $E \perp c$  spectrum, we conclude that the transitions are electric dipole ones.

#### Spectra of $Co^{++}$

The spectra of  $Co^{++}$  in the wurtzite lattices, shown in Fig. 2, are somewhat similar to those of  $Ni^{++}$ . There are three broad bands (the weakest one in the region of  $3500\text{ cm}^{-1}$  is not shown for ZnO:Co), the higher energy one being more intense, and the visible band is split into two main components at room temperature. The band at about  $3500\text{ cm}^{-1}$  is quite difficult to detect for the concentrations used and has only been observed at room temperature. The  $77^\circ\text{K}$  spectra show that the infrared band centered near  $6000\text{ cm}^{-1}$  is split into four main components whereas the visible band is split into a larger number of bands, some of which are rather narrow.

A careful search using dilute crystals failed to reveal the presence of a charge transfer transition at energies less than the band gap energy. If the charge transfer process roughly corresponds to exciting an electron from the valence band into the ground state of the transition metal ion, the larger value for the second ionization potential of nickel compared to that of cobalt indicates that the charge transfer process for cobalt would be at a higher energy than for nickel. This can be described as a greater trap depth for nickel compared to cobalt, and has been discussed by Klasens<sup>17</sup> in a paper dealing with impurity centers in ZnS.

The 4°K polarized spectra of  $\text{Co}^{++}$  are shown in Fig. 5. The spectra are presented on a wavelength scale with the wave numbers of the individual components shown, just as for the corresponding  $\text{Ni}^{++}$  spectra. Many of the individual components are quite narrow, especially for  $\text{ZnO:Co}$ , which is not usually the case for spin allowed  $d-d$  transitions. The sharper components appear on the low energy side of the band whereas the higher energy components are usually broad. The spectra of the sulfides are found to be isotropic but the spectrum of  $\text{ZnO:Co}$  is highly anisotropic. The  $E \perp c$  spectrum is identical with the axial spectrum for the latter case. The conclusions discussed in the last paragraph of the section on  $\text{Ni}^{++}$  spectra apply here to  $\text{Co}^{++}$  as well.

The uppermost curve in Fig. 2b, covering only part of the spectrum, was taken with a very concentrated sample and clearly shows some of the weak doublet states which are not discernible in the dilute samples. Concentrated, thick samples of  $\text{ZnO:Co}$  failed to reveal any weak transitions to the low energy side of main visible band, however a few extra details on the high energy side were seen.

#### The Spectrum of $\text{ZnO:Cu}$

The spectrum taken with the light beam directed along the  $c$  axis is shown in Fig. 6a and the polarized spectrum measured at liquid helium temperature in the  $6000 \text{ cm}^{-1}$  region is shown in Fig. 6b. The energy level diagram for  $d^9$  in a tetrahedral field including spin-orbit splitting is also shown in Fig. 6a. Mulliken's notation extended to the double group<sup>5</sup> is used for the representations;  $E_{5/2}$  is doubly degenerate and  $G$  has fourfold degeneracy. The broad weak absorption observed at room temperature, which corresponds to the  $t_2 - e$  transition in the cubic field approximation, breaks up into a pattern of narrow absorption bands when the temperature is reduced to that of liquid helium. When spin-orbit splitting is included, two transitions are expected in  $T_d$  symmetry. The spin-orbit



parameter,  $\zeta$ , for the  $\text{Cu}^{++}$  free-ion is  $829 \text{ cm}^{-1}$ , therefore the lowest energy transition  $E_{5/2} (^2T_2) \rightarrow G (^2T_2)$  is expected to be found in the region  $1000 - 1200 \text{ cm}^{-1}$ . There is a very strong absorption due to a combination band of the transverse and longitudinal optical mode lattice vibrations of pure ZnO in this energy range. Therefore, the crystal field transition cannot easily be observed and has not been observed.

The G levels are split by fields of lower symmetry into two Kramers doublets. The G ( $^2E$ ) level has only a second order splitting due to the combined effect of spin-orbit coupling and a low symmetry field. The pair of sharp lines to the low energy side of the spectrum have been interpreted as the two trigonal field components of G ( $^2E$ ). The lowest energy component is almost entirely absent in the parallel spectrum. The pattern of lines between  $5780 \text{ cm}^{-1}$  and  $6100 \text{ cm}^{-1}$  is repeated at intervals of  $430 \text{ cm}^{-1}$ . The pattern broadens and becomes quite weak rapidly, appearing only as a weak structureless band after the first interval. The interval of  $430 \text{ cm}^{-1}$  is close to the reported value for the transverse optical mode frequency of  $414 \text{ cm}^{-1}$  for  $\text{ZnO}^{18}$ .

#### DISCUSSION

The Hamiltonian appropriate to the problem being considered is given by

$$H = \sum_{i=1}^n \left\{ -\frac{\hbar^2}{2m} \nabla_i^2 - \frac{Ze^2}{r_i} + \zeta(r_i) \frac{L_i \cdot S_i}{\hbar^2} + e \langle V_c \rangle_i \right\} + \sum_{i>j} \frac{e^2}{r_{ij}} \quad (1)$$

where the sum runs over all the  $n$  electrons of the central atom and  $V_c$  is the crystal field potential acting on the ion. The first two terms uniformly shift all levels of the degenerate  $d^n$  configuration, the next three terms, which partially remove the degeneracy, are arranged in increasing order of magnitude of their effect on the level scheme under consideration. The terms are all of such relative magnitudes that it has been necessary to diagonalize the matrix of  $H$  for the  $d^n$  configuration in order to obtain a good fit between the calculated

energies and the observed spectra. This approach has been discussed by Liehr and Ballhausen<sup>19</sup> who give the matrices of  $\hat{V}_c$  for both weak field and strong field basis functions for the  $d^2$  configuration. The potential given by the point charge model for a regular tetrahedron oriented so that the two-fold axes of the tetrahedron lie along the  $x$   $y$   $z$  axes is

$$V_c = \frac{4ze}{d} + \frac{e}{d} \left(\frac{r}{d}\right)^3 \left(\frac{40}{9}\right)^{\frac{1}{2}} \left(\frac{4\pi}{7}\right)^{\frac{1}{2}} \left[ Y_3^{-2} - Y_3^2 \right] \\ + \frac{4}{9} \frac{e}{d} \left(\frac{r}{d}\right)^4 \frac{7}{2} \left(\frac{4\pi}{9}\right)^{\frac{1}{2}} \left[ Y_4^0 + \left(\frac{5}{14}\right)^{\frac{1}{2}} (Y_4^4 + Y_4^{-4}) \right] , \quad (2)$$

where  $d$  is the distance from the central atom to the point charge  $e$  and the  $Y_l^m$  are the spherical harmonics with relative phase specified by Condon and Shortley<sup>20</sup>.

In order to examine the effect of a field of trigonal symmetry, it is convenient to choose the  $C_3$  axis as the  $z'$  axis. In this case the cubic potential term for the tetrahedron, which is oriented so that one apex lies on the positive  $z'$  axis and a second lies in the  $x'z'$  plane with direction cosines  $(-\frac{2}{3}\sqrt{2}, 0, -\frac{1}{3})$ , is given by

$$V'_c = \frac{4ze}{d} + \frac{e}{d} \left(\frac{r}{d}\right)^3 \frac{20}{9} \left(\frac{4\pi}{7}\right)^{\frac{1}{2}} \left[ Y_3^0 - \left(\frac{2}{5}\right)^{\frac{1}{2}} (Y_3^3 - Y_3^{-3}) \right] \\ + \frac{e}{d} \left(\frac{r}{d}\right)^4 \frac{28}{27} \left(\frac{4\pi}{9}\right)^{\frac{1}{2}} \left[ Y_4^0 - \left(\frac{10}{7}\right)^{\frac{1}{2}} (Y_4^3 - Y_4^{-3}) \right] \quad (3)$$

If the crystal field potential is neglected, the states of a  $d^n$  configuration may be classified by the angular momenta functions  $|SLJM\rangle$ , terms with different  $S$ ,  $L$ , and  $J$  values having in general different energies. The functions may be expressed as linear combinations of Slater determinant product functions of the individual  $d$ -electrons by standard techniques for the coupling of angular momenta<sup>20</sup>. The effect of  $V_c$  is to partially remove the  $(2J+1)$  degeneracy of the  $SL$  terms and the resulting functions may be classified according to the irreducible

representations of the symmetry group of  $V_c$ . The new functions  $|SLJ\Gamma\rangle$ , where  $\Gamma$  denotes the irreducible representation of the group and  $\gamma$  labels one of the set of basis functions, are degenerate with respect to  $\Gamma$  and can be expressed as linear combinations of functions with different  $M$  for each  $SLJ$ . Using these functions as a basis, the matrix of the Hamiltonian (1) may be factored into a number smaller of matrices, one for each  $\Gamma$ . The first contribution to the splitting of free-ion  $d^n$  levels from (2) or (3) comes from the fourth power potential term  $V_4$ . The effect of the odd power term  $V_3$  is to mix in states of higher energy, odd parity configurations with the states of the  $d^n$  configuration. Low and Weger<sup>6</sup> have used second order perturbation theory in order to estimate the relative shift of the  $E$  and  $T_2$  tetrahedral crystal field levels of  $(3d)^6$  because of mixing with  $(3d)^5(4p)$  and  $(3d)^5(4f)$  via  $V_3$ . They find, in a corrected estimate for divalent iron, a relative depression of the levels amounting to less than 10% of the energy separation given by the  $(3d)^6$  configuration alone. Calculations we have performed for  $(3d)^6$  and  $(3d)^7$  indicate less than a 1% admixture of the odd parity functions with  $(3d)^n$  functions. This gives a negligible correction to the energies, but is capable of giving a large contribution to the observed intensity of transitions between the energy levels. Discussion of the latter point is reserved for the section concerning intensities.

The  $V_4$  term of Eq. (2) is just  $-4/9$  times the corresponding term for an octahedron with the same bond distance  $d$ . Taking the splitting of a single  $d$ -electron in a tetrahedral field to be  $10 Dq$ , one expects to find  $Dq$  values for an ion in tetrahedral coordination to be about one half the value for the ion in octahedral coordination with the same ligands. Since the sign of the splitting parameter is opposite for the two cases, the level schemes will be inverted for  $T_d$  symmetry compared to  $O_h$ , and thus in  $T_d$  the  $e$  orbitals of the

d-electron have lower energy than the  $t_2$  orbitals. We will be concerned entirely with  $d^n$  configurations of more than a half filled shell, which may be correlated with the simpler  $d^{10-n}$  configuration if the particles are taken to be holes and therefore have a positive charge.  $Dq$  will then be positive for  $d^7$ ,  $d^8$ , and  $d^9$  which are the configurations for  $Co^{++}$ ,  $Ni^{++}$ , and  $Cu^{++}$ .

The matrix elements of  $\mathcal{H}$  for states of  $d^7$ , which have half-integral  $J$  values, were calculated and are given in Appendix I. The basis functions  $|d^7 SLJ\rangle$  needed to calculate the matrix elements of  $V_4$  were obtained by applying the projection operators for the  $T_d$  double group to  $|JM\rangle$  functions. This procedure gives the correct linear combination of functions with different  $M$  values for every set of  $SLJ$  values. The matrix of  $\sum \frac{e^2}{r_{ij}}$  is diagonal with respect to  $S$  and  $L$  and is independent of  $M_S$  and  $M_L$  and the matrix of  $\sum L_i \cdot S_i$  is diagonal with respect to  $J$  and independent of  $M = M_S + M_L$ . The matrices of these quantities calculated for the free-ion functions were added to the matrix of  $V_4$  to give the matrix of  $\mathcal{H}$ , which is factorable into two  $9 \times 9$  and one  $21 \times 21$  matrices. For the  $d^8$  configuration, the matrices given by Liehr and Ballhausen were used<sup>19</sup>.

Using trial parameters obtained from the spectra by the application of perturbation theory, successive approximations were made by diagonalizing the matrices using an IBM 650 (which also gave the corresponding eigenfunctions) until a good fit was obtained between the observed spectra and the calculated energy levels. The final set of parameters obtained are given in Table II and the predicted energy levels are drawn on each of the spectra of  $Co^{++}$  and  $Ni^{++}$ , shown in Figs. 1, 2, and 3, together with the identification of the component states. The notation used for the irreducible representations is Mulliken's extended to include the double group. The energy levels are designated by  $\Gamma_i - 2S + 1 \Gamma_j(L)$ , where  $L$  is the orbital symbol for the level in zero crystal

field,  $2S+1$  is the spin multiplicity of the level,  $\Gamma_j$  denotes the irreducible representation for the orbital part, and  $\Gamma_i$  stands for the irreducible representation of a spin-orbit component of the  $^{2S+1}\Gamma_j$  level. For example,  $T_2 - {}^3T_1(F)$  stands for the spin-orbit component transforming like  $T_2$  which arises from coupling the spin triplet, orbital  $T_1$  symmetry states of the (free-ion) ${}^3F$  level. Of course, states of the same representation are in general mixed, and such a designation for an eigenstate is meant to imply that the true eigenfunction is composed mostly of the designated function. The character table for  $T_d$  which is given in Table III shows how certain elementary functions transform, and lists only the "unbarred" operations of the single group. The characters of the three extra classes  $\bar{E}$ ,  $8\bar{C}_3$ , and  $6\bar{S}_4$  of "barred" operations needed when the double group is considered are simply the negatives of the characters for the "unbarred" classes. The degeneracy associated with an irreducible representation is given by the character for the identity operation  $E$ . The last column in Table III gives the representations in  $C_{3v}$  which are correlated with the  $T_d$  representations in the first column when the symmetry is reduced from  $T_d$  to  $C_{3v}$ .

The appropriate first order descriptions of the energy levels for the  $d^8$  and  $d^7$  configurations are shown in Figs. 7 and 8 respectively. The diagrams are drawn in the spirit of successive perturbations of decreasing magnitude on the free-ion levels which are given on the extreme left of the figures. The energies of the free-ion levels relative to the lowest one (set equal to zero) are given in terms of the Racah<sup>21</sup> parameters  $B$  and  $C$ , where  $B = F_2 - 5 F_4$  and  $C = 35 F_4$  and the  $F_k$  are the Slater-Condon-Shortley integrals<sup>20</sup>. Application of the crystal field perturbation splits the free-ion levels into levels characterized by irreducible representations of the group whose energies in units of  $Dq$  relative to the unperturbed level are shown in parentheses. Spin-orbit interaction gives further splittings into components whose representations are shown and whose energies relative to the crystal field levels are given in terms

of the free-ion spin-orbit parameter,  $\lambda$ . Certain aspects of the two diagrams are common. There are only two states of the highest spin multiplicity, P and F, separated by  $15B$  with F being lowest. The P state is not split in the crystal field and the splitting of the F state for  $d^7$  is inverted from that of  $d^8$ . The spectra of  $Ni^{++}$  and  $Co^{++}$  are thus expected to bear some resemblance to each other which is, in fact, the case.

The observed splitting and relative intensities of some of the bands in the two polarizations of the ions in ZnO are explained by a small trigonal field in the presence of the predominant cubic field. It was pointed out in the section on Crystal Structures that the departure from  $T_d$  symmetry is due to the fact that the bond distance lying along the hexagonal  $c$  axis is slightly shorter than the other three equivalent distances. This gives rise to an axial field and the extra potential term which must be added to the cubic potential term is

$$V_t = \sqrt{4\pi} \frac{e}{d} \left( \frac{B}{d} \right) \left\{ 1 - \sqrt{\frac{2}{3}} \left( \frac{r}{d} \right) Y_1^0 - \sqrt{\frac{3}{5}} \left( \frac{r}{d} \right)^2 Y_2^0 - \sqrt{\frac{4}{7}} \left( \frac{r}{d} \right)^3 Y_3^0 - \frac{5}{3} \left( \frac{r}{d} \right)^4 Y_4^0 \right\}$$

where  $\frac{B}{d}$  is the measure of departure from  $T_d$  symmetry defined earlier. The second and fourth power terms in Eq. (4) may cause additional splitting of the degenerate cubic field levels.

In the discussion of the spectra of the individual ions which follows, it will be necessary to know the selection and polarization rules for electric dipole transitions. These are given in Table IV for the groups  $T_d$  and  $C_{3v}$ . There are no polarization rules for  $T_d$  and a cross simply means that the transition is allowed. The electric dipole moment for  $T_d$  transforms like  $T_2$ , whereas in  $C_{3v}$  the moment in the  $z$  direction transforms like  $A_1$  and the moment in the  $x$   $y$  plane transforms like E.

## The Spectrum of ZnO:Cu

We will discuss the simplest electronic system first; that of  $\text{Cu}^{++}$  which has the  $(3d)^9$  configuration. Since this configuration may be treated as one hole in a filled  $3d$  shell, the problem is formally equivalent to that of one electron and one need only change the sign of  $Dq$  and of the spin-orbit matrix in order to obtain the correct cubic field matrices. The last column in Table III shows that the cubic  $G(^2E)$  level splits into a pair of doubly degenerate levels having the representations  $E_{1/2}$  and  $E_{3/2}$  and the ground state becomes  $E_{1/2}$  in  $C_{3v}$ . According to the selection rules given in Table IV, the transition  $E_{1/2} \rightarrow E_{3/2}$  is forbidden in the parallel spectrum, whereas  $E_{1/2} \rightarrow E_{1/2}$  is allowed in both polarizations. We therefore identify the line at  $5784 \text{ cm}^{-1}$  as  $E_{3/2}$  and the line at  $5821 \text{ cm}^{-1}$  as  $E_{1/2}$ . Therefore, the trigonal field splitting of the upper state is  $37 \text{ cm}^{-1}$ . In a cubic field, the energy of the transition is  $10 Dq + \zeta$ , and taking  $\zeta = 800 \text{ cm}^{-1}$  one finds  $Dq \approx 500 \text{ cm}^{-1}$ .

The energy matrices for a trigonal field given by Liehr<sup>22</sup> were used in order to obtain the second order splitting,  $\Delta = E[E_{1/2}(^2E)] - E[E_{3/2}(^2E)]$ . The result, expressed in terms of the potential given by Eq. (4), is

$$\Delta = \frac{e^2}{d} \left\{ \frac{12}{7} \left\langle \frac{r^2}{d^2} \right\rangle - \frac{100}{63} \left\langle \frac{r^4}{d^4} \right\rangle \right\} \left( \frac{\delta}{d} \right) + \frac{\zeta}{10Dq},$$

where  $\left\langle \frac{r^n}{d^n} \right\rangle$  is the radial average value of the quantity  $r^n/d^n$ . We can estimate the magnitude of the second term by using the point charge definition of

$Dq = \frac{2}{27} \frac{e^2}{d} \left\langle \frac{r^4}{d^4} \right\rangle$ , which is appropriate for this case, in order to eliminate  $\left\langle \frac{r^4}{d^4} \right\rangle$ . Taking  $\zeta = 800 \text{ cm}^{-1}$ , and  $\left( \frac{\delta}{d} \right) = -0.015$ , the value for pure ZnO, we find the contribution to  $\Delta$  from the second term  $-2.14 \left( \frac{\delta}{d} \right) \zeta \approx 26 \text{ cm}^{-1}$ .

It is more difficult to estimate the first term since we do not know the relative values of  $\left\langle \frac{r^2}{d^2} \right\rangle$  and  $\left\langle \frac{r^4}{d^4} \right\rangle$  for the ion in the crystal. We have, however, estimated this term on the basis of three different assumptions, where in each case we have used the values  $\left( \frac{\delta}{d} \right) = -0.015$ ,  $\zeta = 800 \text{ cm}^{-1}$ ,  $d = 3.7 \text{ a.u.}$ , and

$Dq = 500 \text{ cm}^{-1}$ . a) The Hartree-Fock wave functions for  $\text{Cu}^{++}$  recently tabulated by Watson<sup>23</sup> were used to calculate the moments  $\langle r^n \rangle$ . We find  $\langle r^2 \rangle = 1.028$  and therefore obtain  $\Delta = 8 \text{ cm}^{-1}$ . b) We have obtained  $\langle r^2 \rangle$  from the spectrum of  $\text{ZnO:Ni}$  (vide infra) and have scaled it to the case of  $\text{Cu}^{++}$  by use of the factor obtained from Watson's H-F functions and find  $\langle r^2 \rangle = 0.685$ . The splitting in this case is calculated to be  $\Delta = 14 \text{ cm}^{-1}$ . c) The H-F value for  $\langle r^4 \rangle = 2.498$  and for  $d = 3.7 \text{ a.u.}$ ,  $\langle \frac{r^2}{d^2} \rangle = 5.60 \langle \frac{r^4}{d^4} \rangle$ . Substituting this value for  $\langle \frac{r^2}{d^2} \rangle$  and eliminating  $\langle \frac{r^4}{d^4} \rangle$  as before, we obtain  $\Delta = -130 \text{ cm}^{-1}$ . With the exception of the last case, the sign of  $\Delta$  is given correctly, albeit the values are low. The magnitude of  $\Delta$  is also rather high for the last estimate. In this connection, it is interesting to note that the H-F value of  $\langle r^2 \rangle$  gives a good account of the strain-induced splitting of the  ${}^2E$  state of  $\text{MgO:Cr}^{+3}$ , whereas the ratio  $\langle \frac{r^2}{d^2} \rangle / \langle \frac{r^4}{d^4} \rangle$  together with the observed  $Dq$  leads to too large a splitting<sup>24</sup>. This is similar to the result we find here, and in addition the H-F ratio gives the sign incorrectly. Although one should not place too much reliance on such calculations of potential constants because of the inadequacy of the point charge model, a fact which has been thoroughly discussed in some recent papers<sup>25</sup>, we think they do lend support to the assignment and indicate that the trigonal field is reasonably well accounted for by the local distortion of the tetrahedron in  $\text{ZnO}$ .

The relative values of the intensities of the three observed transitions were calculated by assuming the mechanism to be configuration mixing of  $(4p)$  with  $(3d)$  via the third power potential term in Eq. (3). Since the  $3p$  functions transform like  $T_2$  in  $T_d$ , only the  $t_2$  ( $3d$ ) orbitals are mixed. The orbital functions in trigonal orientation given by Liehr<sup>22</sup> were used to calculate the  $t_2 \rightarrow e$  moments. Liehr's notation has been used for the orbital functions, and



the results are

$$\begin{aligned}
 \langle t_{2a} | r_m | e_b \rangle &= - \langle t_{2c} | r_m | e_a \rangle = - \left( \frac{1}{15} \right)^{1/2} \omega' (i_m - i_j) \\
 \langle t_{2a} | r_m | e_a \rangle &= \langle t_{2b} | r_m | e_b \rangle = - \left( \frac{1}{15} \right)^{1/2} \omega' (i_m + i_j) \\
 \langle t_{2b} | r_m | e_a \rangle &= - \langle t_{2c} | r_m | e_b \rangle = \left( \frac{2}{15} \right)^{1/2} \omega' k_m
 \end{aligned}$$

where  $\omega' = \langle p_1 | V_3 | t_{2i} \rangle / (E_{3d}^0 - E_{4p}^0)$ . We now use the zero order functions appropriate to  $E_{5/2} (^2T_2)$  and  $G (^2E)$  in order to obtain the relative intensities. It is unnecessary to use the first order functions or the odd power moment contributions from the terms in Eq. (4), since this would only give additional terms reduced by a factor of  $(\frac{\delta}{d})$ . We have furthermore assumed that the Kramers degeneracy is effectively lifted for the partner wave functions, and have taken the intensity to be proportional to the sum of the squares of the four individual moments for a given transition. The intensities are then found to be

$$\begin{aligned}
 E_{1/2} (^2T_2) - E_{1/2} (^2E) &= K \frac{4}{45} (\omega')^2 \quad || \\
 E_{1/2} (^2E) &= K \frac{8}{45} (\omega')^2 \quad \perp \\
 E_{3/2} (^2E) &= K \frac{4}{15} (\omega')^2 \quad \perp
 \end{aligned}$$

where the constant of proportionality between the intensity and the square of the moment is very nearly equal for the three transitions and has been called K. The observed intensity ratios are  $E_{1/2} (^2E) || : E_{1/2} (^2E) \perp : E_{3/2} (^2E) \perp = 1:2.5:5.3$  compared with the calculated ratios of 1:2:3. The agreement is satisfactory and further supports the assignment.

The spectrum therefore consists of the two trigonal field components of  $G(^2E)$  followed by a vibrational progression characteristic of the host lattice whose frequency is perhaps slightly modified by the  $Cu^{++}$  impurity. It may be seen

in Fig. 6b that the pair of sharp 0-0 bands appear with approximately the same splitting in 0-1 and although the lower energy band at  $6223\text{ cm}^{-1}$  is not completely polarized, it is stronger in the perpendicular spectrum whereas the  $6257\text{ cm}^{-1}$  band is stronger in the parallel spectrum. This leaves unexplained the nature of the weak bands lying in the energy range  $5900 - 6100\text{ cm}^{-1}$  (and the repeated pattern at  $430\text{ cm}^{-1}$  higher energy). They may be due to local vibrational modes coupled with the electronic state; however we have no quantitative information concerning this point.

#### Spectra of $\text{Ni}^{++}$

The three main bands observed at room temperature for each of the  $\text{Ni}^{++}$  spectra are transitions from the ground state  $^3T_1(F)$  to the excited states  $^3T_2(F)$ ,  $^3A_2(F)$ , and  $^3T_1(P)$ . The symmetry selection rules for electric dipole transitions given in Table IV are that  $T_1 \rightarrow A_2$ ,  $E$ ,  $T_1$ , and  $T_2$  are allowed. At low temperatures when all the electrons are in the lowest spin-orbit state, the allowed transitions to excited spin-orbit components are given by the selection rule  $A_1 \rightarrow T_2$  only. Fig. 7 shows that each of the excited states mentioned above has a  $T_2$  level lowest in spin-orbit coupling. Both the  $^3T_2(F)$  and  $^3T_1(P)$  bands are observed to split at low temperatures with the lowest energy component of each band being the most intense and usually being the sharpest one. This is particularly evident for  $\text{ZnO:Ni}$ . It has not been possible to pick out the four components of  $^3T_2(F)$ ; however, diagonalization of the matrix of  $\mathcal{H}$  shows that three components are grouped rather closely in energy with a total energy separation of approximately  $\lambda/2$  with the fourth component,  $A_2$ , lying about  $3\lambda/4$  above the mean of the other three. The diagonalization also shows that the total splitting of the  $^3T_1(P)$  band is very nearly  $2\lambda$ , rather than the first-order result of  $3\lambda$ . More than four components are found in the spectral region of  $^3T_1(P)$  and the total energy separation is  $1000 - 1500\text{ cm}^{-1}$ . The appearance of components with representations other than  $T_2$  violates the selection rule  $A_1 \rightarrow T_2$  only, which may be accomplished

by fields of lower symmetry and/or coupling with vibrational modes which cause the forbidden states to be mixed with allowed ones in higher order. Under these circumstances, it is difficult to obtain an accurate value of  $\lambda$ , and the value  $\lambda = -250 \text{ cm}^{-1}$  applies reasonably well to all the spectra. Table V gives the comparison between the calculated (using the parameters of Table II) and observed spectra of  $\text{Ni}^{++}$  in the three wurtzite-type crystals at  $4^\circ\text{K}$ . The four observed bands which are correlated with the four calculated components of  ${}^3\text{T}_1(\text{P})$  may be identified by reference to Fig. 4.

In all three spectra, there are reasonably intense broad bands to the high energy side of the  ${}^3\text{T}_1(\text{P})$  components which are not identified. Some of the extra bands which appear are probably due to transitions to different vibrational levels of the upper state. Detailed examination of the effect of coupling of degenerate electronic and vibrational (localized or impurity modified lattice mode) motions have not been undertaken for these cases. However, some calculations have been made of the effect on the energy levels in  $\text{T}_d$  symmetry of adding potential fields having tetragonal and trigonal symmetry\*. It should be possible to use these results in treating the dynamical case by the addition of a restoring potential to the problem. The low symmetry field can be considered to arise in part from certain of the normal vibrational modes of the complex whose instantaneous spatial configuration contributes to the low symmetry potential field. The result for both types of distortion is that the ground state remains a non-degenerate  $\text{A}_1$  state. The  $\text{A}_1$  component of  ${}^3\text{T}_1(\text{P})$  has an energy shift in the opposite sense to the other components of  ${}^3\text{T}_1(\text{P})$  and the  $\text{A}_1$  ground state for both types of distortion. Similarly, both components of  ${}^1\text{D}$  have quite different energy slopes than the ground state. The implication is that at the value of the

---

\* Performed in collaboration with P. K. Baltzer and D. S. McClure, RCA Princeton.

distortion coordinate where the ground level has a minimum, these excited levels will not have a minimum and the excited state potential surfaces may in fact have a steep energy slope. Therefore a transition from the lowest vibrational level to these excited states will cover a rather large number of excited state vibrational levels, giving rise either to a broad band or to a series of excited vibrational bands. This argument is identical to that given by Orgel<sup>26</sup> who considered only the difference between the slopes of potential surfaces which are functions of a totally symmetric mode in order to account for the relative breadths of absorption bands. These considerations qualitatively account for the fact that the higher energy bands in the  $^3T_1(F)$  spectral region and the bands identified as the E and  $T_2$  components of  $^1D$  are observed to be broad. A consideration of only a totally symmetric mode predicts in fact that the transitions to states of  $^1D$  should be sharp, since the configuration of the ground state and  $^1D$  are nearly the same and consequently the energy of these two levels plotted vs Dq have nearly the same slope.

The rather high intensity of the spin-forbidden transitions  $A_1 - ^3T_1(F) \rightarrow E, T_2 - (^1D)$  is the result of appreciable mixing of the latter states through spin-orbit interaction with triplet states. In the case of ZnS, which shows the most mixing, the (primarily)  $^1D$  levels lie below  $T_2 - ^3A_2(F)$ . The energies of all three levels are close to one another and the energies and eigenfunctions given by the matrix diagonalization procedure are:

$$E = 9150 \text{ cm}^{-1}, \psi(\Gamma = T_2) = .36(^1G) - .75(^1D) - .16 ^3T_1(P) + .53 ^3A_2(F) - .06 ^3T_2(F) - .09 ^3T_1(F)$$

$$E = 9604 \text{ cm}^{-1}, \psi(\Gamma = E) = -.57(^1G) + .77(^1D) + .24 ^3T_1(P) + .14 ^3T_2(F) - .02 ^3T_1(F)$$

$$E = 9805 \text{ cm}^{-1}, \psi(\Gamma = T_2) = -.28(^1G) + .38(^1D) + .12 ^3T_1(P) + .80 ^3A_2(F) + .24 ^3T_2(F) + .06 ^3T_1(F)$$

A plot of energy vs Dq for values of B, C, and  $\lambda$  appropriate to ZnS:Ni is shown in Fig. 9. At the value Dq =  $475 \text{ cm}^{-1}$  the levels are appreciably mixed and  $T_2 - ^3A_2(F)$  has become highest. The same plot for Dq = 400, the value for CdS:Ni,

shows there is slightly less mixing and  $T_2 - {}^3A_2(F)$  is lowest. However, the ratio C/B is larger for the latter case and the effect is to push up the  ${}^1D$  levels by about  $1000 \text{ cm}^{-1}$ . The larger energy separation between the singlet and triplet states is evident in Fig. 1c. The singlet levels are still relatively intense, broad absorptions. In spite of the fact that there is a greater energy separation between the  ${}^1D$  and  ${}^3F$  levels in CdS:Ni, there is about the same amount of triplet character to the  ${}^1D$  states as there is for ZnS:Ni. The coefficients of the  ${}^3F$  functions decrease, but those of  ${}^3T_1(P)$  increase to 0.41 for E and 0.32 for  $T_2$ .

Attempts to observe the  $A_1 - {}^3T_1(F) \rightarrow T_2 - {}^3T_1(F)$  transition were generally unsuccessful, although the transition is symmetry allowed and was expected to be reasonably intense, based on the p - d mixing model to be discussed later. No absorption bands having energies less than about  $4000 \text{ cm}^{-1}$  on down to energies comparable to the strong lattice vibrational absorption of the host lattice were observed, with the exception of one weak, narrow band centered around  $1060 \text{ cm}^{-1}$  in a 3 mm thick crystal of CdS: ( ~ 1 percent Ni). The energy of the transition is approximately  $(9/2)\lambda$  in fields of  $T_d$  symmetry, and a measurement of the transition energy could provide a good means to determine  $\lambda$ . This would be true only if the energy difference between the levels were unaffected by low symmetry fields or if none were present. The calculations discussed above showed that the energy is drastically affected in some cases and the arguments given above to explain the breadth of certain bands, apply here as well. If the  $T_2 - {}^3T_1(F)$  level is split and broadened for small values of the distortion coordinates, as the calculations indicate, this would help to explain the failure to observe the transition except for the one uncertain case noted.

The local anisotropy about the metal atom position in the wurtzite structure has been discussed and it was pointed out that the anisotropy, measured by  $\delta/d$ , is largest for ZnO and is nearly zero for ZnS. The spectra for the two polarizations  $E \perp c$  and  $E \parallel c$  are found to be nearly identical for ZnS:Ni and CdS:Ni.

Nickel is expected to substitute for zinc without much distortion based on ionic size considerations only, and thus the spectra may be expected to partially reflect the trigonal ( $C_{3v}$ ) field component of the tetrahedra in the pure compounds. This would explain the observed isotropy of ZnS:Ni. In the case of CdS:Ni, the nickel ion substitutes for the larger cadmium ion and the lattice probably relaxes toward the smaller substituted ion. A totally symmetric shortening of the four distances is not unlikely since the forces in CdS tending to produce the  $C_{3v}$  symmetry are not large, based on the value  $\delta/d = -0.008$ . Of course, in both these cases there may be a local distortion, which if randomly oriented throughout the crystal, would lead to an apparent isotropy of the spectra. These distortions would be evident only by the observation of splitting of some of the levels degenerate in cubic symmetry.

ZnO provides an example where the polar nature of the pure host crystal is maintained upon the substitution of either cobalt, nickel, or copper for zinc. The pure crystal anisotropy of this compound is the largest of the three discussed and the similar ionic radii of these three transition ions and zinc apparently helps to preserve the anisotropy. Splitting of some of the spin-orbit components of  $^3T_1(P)$  for  $Ni^{++}$  in ZnO is clearly shown by the polarized spectrum presented in Fig. 4a. The  $T_1$  and  $T_2$  components are expected to split into  $A_2 + E$  and  $A_1 + E$ , respectively. From Table IV, we have the selection rules  $A_1 \rightarrow A_1$  only in the parallel spectrum and  $A_1 \rightarrow E$  allowed only in the perpendicular spectrum. Since the ground state is  $A_1$ , the band at  $15159\text{ cm}^{-1}$  for  $E \parallel c$  is  $A_1$  and the  $15200\text{ cm}^{-1}$  band for  $E \perp c$  is E and the observed splitting is  $41\text{ cm}^{-1}$ . The splitting energies of  $T_2-^3T_1(P)$  calculated by the use of Eq. (4) are

$$E(A_1) = \left( \frac{\delta}{d} \right) \frac{3e^2}{5d} \left\langle \frac{r^2}{d^2} \right\rangle$$

$$E(E) = - \left( \frac{\delta}{d} \right) \frac{3e^2}{10d} \left\langle \frac{r^2}{d^2} \right\rangle$$

and since  $\left(\frac{\delta}{d}\right)$  is negative for ZnO we see that  $A_1$  should be at a lower energy than  $E$ , which agrees with observation. There is no contribution from the fourth power term, since the states are derived from an orbital P state. Watson's H-F wave functions<sup>23</sup> for  $Ni^{++}$  were used to obtain  $\langle r^2 \rangle = 1.133$  and  $\langle r^4 \rangle = 3.021$ . Taking  $d = 3.7$  a.u. we find  $\left\langle \frac{r^2}{d^2} \right\rangle = 5.15 \left\langle \frac{r^4}{d^4} \right\rangle$ . If we use the observed value of  $Dq$  in order to obtain  $\left\langle \frac{r^4}{d^4} \right\rangle$  and the H-F ratio above, the trigonal field splitting is calculated to be  $350 \text{ cm}^{-1}$ . On the other hand, using the H-F value  $\left\langle \frac{r^2}{d^2} \right\rangle = 0.083$  directly, we calculate a splitting of  $66 \text{ cm}^{-1}$ . Analogous to the case of ZnO:Cu previously discussed, we find the H-F value of  $\langle r^2 \rangle$  gives good agreement with the observed splitting, whereas the H-F ratio  $\left\langle \frac{r^2}{d^2} \right\rangle / \left\langle \frac{r^4}{d^4} \right\rangle$  together with the observed value of  $Dq$  gives too large a splitting. The observed splitting was used to calculate  $\left\langle \frac{r^2}{d^2} \right\rangle = 0.053$  and therefore  $\langle r^2 \rangle = 0.725$ . The splitting of  $41 \text{ cm}^{-1}$  observed for ZnO:Ni, which is comparable to that observed for ZnO:Cu, seems to be a reasonable value for the trigonal distortion characteristic of the host lattice.

The  $T_1 - {}^3T_1(P)$  level has a calculated splitting of the same magnitude as  $T_2 - {}^3T_1(P)$ , however the pattern is inverted. The identification of the levels given in Table V together with the polarized spectra shown in Fig. 4a leads to the assignment that the  $15488 \text{ cm}^{-1} \begin{smallmatrix} E \\ \text{MM} \end{smallmatrix} \perp \begin{smallmatrix} c \\ \text{MM} \end{smallmatrix}$  band is the E component and the  $15500 \text{ cm}^{-1} \begin{smallmatrix} E \\ \text{MM} \end{smallmatrix} \parallel \begin{smallmatrix} c \\ \text{MM} \end{smallmatrix}$  band is the  $A_2$  component of  $T_1 - {}^3T_1(P)$ . The observed splitting is less than that for the  $T_2$  level but the order of the levels is in agreement with prediction. The selection rule  $A_1 \rightarrow A_1$  only for  $\begin{smallmatrix} E \\ \text{MM} \end{smallmatrix} \parallel \begin{smallmatrix} c \\ \text{MM} \end{smallmatrix}$  is not obeyed. The intensity of  $A_1 \rightarrow A_2$  is less than that for  $A_1 \rightarrow E$  however, and the selection rules seem to be obeyed for all observed transitions only in the sense that the "forbidden" transitions are usually weaker and broader than the "allowed" ones.

The large values for the  $f$  numbers and the quite good agreement between the observed and calculated spectra based on  $T_d$  symmetry for reasonable values of the crystal field parameters is good evidence that  $Ni^{++}$  occupies a regular metal atom lattice site in the three wurtzite-type compounds. Although the octahedral holes are large enough to accomodate a foreign ion, we have no evidence from the spectra that the sites are occupied by  $Ni^{++}$ . The nearby octahedron of metal atoms gives a positive energy contribution which is greater than the negative energy contribution of the anion near neighbors. If some of the neighboring cation sites were unoccupied, the octahedral crystal field stabilization energy of  $Ni^{++}$  could help to make the occupancy of these sites by  $Ni^{++}$  energetically favorable. A small fraction of the  $Ni^{++}$  ions may occupy the octahedral sites, but in concentrations too small to be detected in the spectra.

The spectra of  $Ni^{++}$  in  $Cs_2ZnCl_4$  and  $Cs_2ZnBr_4$  shown in Fig. 3 provide two further examples of  $Ni^{++}$  in fields of  $T_d$  symmetry. The  $Cs_2ZnX_4$  structure has no octahedral sites and a substituting foreign atom would have to replace a zinc atom in one of the discrete  $ZnX_4^{=}$  anions. In these structures it is expected that the resulting  $NiX_4^{=}$  tetrahedra could distort more readily than the tetrahedra in the wurtzite lattice since the ligand bonding to the rest of the lattice is weaker in the former case. Therefore, any tendency of a tetrahedral complex containing  $Ni^{++}$  to undergo a distortion to a lower symmetry because of the Jahn-Teller effect<sup>4,5</sup> is expected to be more readily observable in the  $Cs_2ZnX_4$  crystals than in the wurtzite-type crystals. The observed spectra are very similar to that of  $Ni^{++}$  in crystals having the wurtzite structure. The energy levels predicted based on  $T_d$  symmetry appear to fit the observed spectra equally as well as the cases formerly discussed. The splitting of the visible  ${}^3T_1(P)$  band is again not entirely accounted for by reasonable values of the spin-orbit parameters. The predicted levels shown in Fig. 3 were calculated for



$\lambda = -250 \text{ cm}^{-1}$  in both cases. Low temperature spectra of the visible band reveals that the lower energy component of the band is further split whereas the higher energy component remains broad, in analogy with the former spectra discussed. The values of  $Dq$  obtained are smaller for the halide ligands than for the oxides and sulfides. The  $Dq$  values given in Table II are in the order

$\text{Br}^- < \text{Cl}^- < \text{S}^{2-} \approx \text{O}^{2-}$  which is in agreement with the spectrochemical series based largely on results for ions in octahedral coordination.

The good agreement between the observed spectra and that calculated for a  $(3d)^8$  configuration in  $T_d$  symmetry indicates that perturbations of the energy levels by states of the odd parity  $(3d)^7(4p)$  configuration are negligible. The experimental evidence is thus in accord with the calculated estimates of  $p$ - $d$  mixing previously discussed. Even though the mixing coefficients are small, they still may account for the major part of the observed intensities of the transitions. This point is discussed under Intensities.

The calculated energies depend on four parameters  $B$ ,  $C$ ,  $\lambda$ , and  $Dq$ . The effect of  $\lambda$  and  $Dq$  on the energy levels has been discussed. The parameters  $B$  and  $C$  primarily affect the energies of the  $^3P$ ,  $^1D$ ,  $^1G$ , and  $^1S$  levels. In the free-ion the energy difference between  $^3F$  and  $^3P$  is given by  $15B$ , and  $B$  is found to be  $1020 \text{ cm}^{-1}$  for  $\text{Ni}^{++}$ . To a first approximation, the energy of the  $^3P$  level is  $15B + 6Dq \approx 17,500 \text{ cm}^{-1}$ . Examination of the spectra of  $\text{Ni}^{++}$  in the crystals discussed shows that the energy corresponding to the ground state to  $^3P$  transition is a function of the type of ligand and is in the order  $\text{S}^{2-} < \text{Br}^- < \text{Cl}^- < \text{O}^{2-}$ . This means that the value of  $B$  in the crystal is reduced from the free-ion value and the amount of reduction is dependent on the ligand type. Defining the ratio  $B(\text{crystal})/B(\text{free-ion})$  as  $\beta$ , we empirically find a linear relationship between  $\beta$  and the ligand polarizability which is shown in Fig. 10. The values of  $\alpha$  for the ligands<sup>27</sup> studied are indicated at the top of the figure and the

experimentally determined values of  $\beta$  for  $\text{Ni}^{++}$  are shown as crosses. The straight line fitted to the experimental data extrapolated to  $\alpha = 0$  gives  $\beta = 0.93$ , not the free ion value  $\beta = 1$ . Nevertheless, the empirical relationship is useful to give the approximate value of  $\beta$  to be expected in a crystal.

Jorgensen<sup>28</sup> has recently discussed the factors which influence the value of the  $F^k$  integrals in crystals. He has referred to the tendency to depress  $\beta$  below one as a function of the central ion and ligand type as the nephelauxetic (= cloud-expanding) series. The reduction of  $\beta$  below one can be qualitatively described as a decrease of the interelectronic repulsion energy because the charge clouds of the ligands penetrate in toward the ligand and screen the electronic charges of the inner metal ion from one another. The greater the ligand polarizability, the greater the penetration and hence a larger reduction in  $\beta$ . The nephelauxetic effect can also be described as an expansion of the charge cloud of the central atom which means that the average interelectronic separation is greater. Jorgensen considers that the reduction in  $\beta$  is direct evidence of covalent bonding and he discusses the effect for a number of  $\text{Mn}^{++}$  salts.

An attempt has been made to express the observed values of  $\beta$  in terms of the "covalency" parameter  $\epsilon$  introduced by Koide and Pryce<sup>29</sup> and used by Stout<sup>30</sup> to account for the relative depression of the free-ion levels in  $\text{MnF}_2$ . For an ion in tetrahedral coordination, the amplitude of the  $t_2$  radial functions is reduced by the factor  $\sqrt{1-\epsilon}$ . Calculation of the coefficients of the direct and exchange integrals yields the following electrostatic energies:

$${}^3T_1 (P) = (1 - 4.8\epsilon) (28A_0 - 35B_0 - 21C_0)$$

$${}^3A_2 (F) = (1 - 6\epsilon) (28A_0 - 50B_0 - 21C_0)$$

$${}^3T_2 (F) = (1 - 5\epsilon) (28A_0 - 50B_0 - 21C_0)$$

$${}^3T_1 (F) = (1 - 4.2\epsilon) (28A_0 - 50B_0 - 21C_0)$$

The energy difference between  $^3P$  and the weighted mean of the  $^3F$  levels is  $(1 - 4.8\epsilon) (15B_0)$ . Equating this to  $15B$ , one finds  $\beta = (1 - 4.8\epsilon)$ .

Using the observed values of  $\beta$ , one obtains values of  $\epsilon$  for the oxide, chloride, and sulfide of 0.051, 0.062, and 0.094 respectively. According to the idea of Koide and Pryce<sup>29</sup>, this means coefficients of the ligand  $\sigma$ -combinations of 0.23, 0.25, and 0.31 for these three cases.

#### Spectra of $Co^{++}$

The spectra of  $Co^{++}$  in ZnO, ZnS, and CdS have been interpreted on the basis of tetrahedral coordination about the cobalt ions. The energy level diagram for the  $d^7$  configuration given in Fig. 8 shows the effect of successive perturbations on the free ion levels. The crystal field splitting of the F state is inverted from that of  $Ni^{++}$ , which makes the orbital singlet  $A_2$  lowest. The orbital selection rules are  $A_2 \rightarrow T_1$  for electric dipole transitions. The lowest energy transition  $^4A_2 (F) \rightarrow ^4T_2 (F)$  should be weak, which has been found to be the case. The energy of this transition is about  $3500 \text{ cm}^{-1}$  and is shown to be a weak broad band in Fig. 2. The two principal bands seen in the spectra are the transitions  $^4A_2 (F) \rightarrow ^4T_1 (F)$  and  $^4A_2 (F) \rightarrow ^4T_1 (P)$ . The spin-orbit splitting of  $^4T_1 (F)$  is readily apparent in the  $77^\circ K$  spectra shown. The first order value for the splitting is given by  $6\lambda$ , where  $\lambda = -178 \text{ cm}^{-1}$  for the free-ion.

In spin-orbit coupling, the ground state is four-fold degenerate and transforms according to the double group representation G. The degeneracy is lifted in fields of lower symmetry. The effect of fields of less than cubic symmetry is, in general, to split the four-fold G levels into two doubly degenerate levels. In the low symmetry fields, all the states have two-fold degeneracy and are called Kramers doublets. This degeneracy is only removed by interaction with magnetic fields. The zero-field splitting of the ground state has been found to be about  $1 \text{ cm}^{-1}$  for both ZnS:Co and CdS:Co. The field acting on the

ground state appears to have axial symmetry but  $g_{\perp}$  and  $g_{\parallel}$  are nearly equal. The average values  $g = 2.35$  and  $g = 2.05$  have been measured for ZnS:Co and CdS:Co respectively\*. The selection rules given in Table IV are that transitions from G are allowed to all three of the double group representations;  $E_{1/2}$ ,  $E_{5/2}$ , and G. The small zero-field splitting of the ground state implies that the two Kramers doublets are equally populated at all temperatures used and the ground state is accurately represented as having four-fold degeneracy. The selection rules thus indicate allowed transitions to all the spin-orbit components of the upper state of an orbitally allowed transition, unlike the case of  $Ni^{++}$  where transitions from the ground state are allowed to only one spin-orbit component of the upper state.

The parameters were obtained by fitting the observed spectra to the calculated energy levels obtained by diagonalizing the matrix of  $J^+$ . A set of solutions for a range of parameters  $C/B$ ,  $Dq/B$ , and  $\lambda/B$  were used to construct plots of  $E/B$  vs. the parameters. The plots were used to obtain good graphical estimates of the parameters which best fit the spectra. The final set of parameters obtained are given in Table II and the calculated energies of the excited levels relative to the ground state set equal to zero are shown in Fig. 2. The data for  $Co^{++}$  in spinel shown in Table II was obtained by D. S. McClure and is included for comparison with ZnO:Co. The former spectrum is not shown, but is quite similar to the latter. The good agreement between the predicted and observed spectra indicates that the configuration is predominately  $(3d)^7$  (negligible  $3d - 4p$  mixing), and that cobalt is in a nearly regular tetrahedral environment of ligands.

---

\* The zero-field splitting and the  $g$  values were obtained from paramagnetic resonance spectra measured by R. E. Michel, RCA Princeton.

The polarized  $4^{\circ}\text{K}$  spectra of the visible bands are shown in Fig. 5. In complete analogy with the corresponding spectra of  $\text{Ni}^{++}$ , the spectra of  $\text{Co}^{++}$  in ZnS and CdS are isotropic whereas that of ZnO:Co is quite anisotropic. The anisotropy of the latter case can be explained by a  $C_{3v}$  component of the crystal field potential. The precise form of the splitting, its magnitude, and the identification of the components has not been worked out because of the complexity of the spectra. The discussion which follows is facilitated with the aid of Fig. 11 which is a plot of  $E/B$  vs.  $Dq/B$  for a value of  $\lambda/B = -0.30$  which is approximately correct for all three host crystals.  $Dq/B \approx 0.54$  for both ZnO:Co and CdS:Co and  $Dq/B = 0.50$  for ZnO:Co.

In the free-ion, all the doublet states lie at energies higher than  $^4P$ , however for values of  $Dq/B$  greater than about 0.3, three doublet states lie at lower energies than  $^4P$ . The doublets are  $G - ^2E$ ,  $E_{1/2} - ^2T_1$ , and  $G - ^2T_1$  where we have omitted writing the parent free-ion states since the crystal field states are mixtures of  $^2G$ ,  $^2H$ ,  $^2D$  and  $^2P$ , primarily the former two. These three states have very nearly the same crystal field configuration as the ground state, which has almost a pure  $e^4 t_2^3$  configuration. The three doublets lie quite close to the components of  $^4P$  and are strongly mixed with the latter for ZnO:Co. As  $Dq/B$  is increased, the  $^4P$  components and the three doublets rapidly diverge and do not mix appreciably. For  $Dq/B = 0.54$  the doublets have very little quartet character and are observed as weak transitions in the region  $12,000 - 13,000 \text{ cm}^{-1}$ . The broken upper curve in Fig. 2b is the spectrum of a very concentrated sample of ZnS:Co which clearly shows some of the doublets on either side of the prominent  $^4P$  band. In the case of ZnO:Co, there is considerably more mixing between the quartets and doublets and the sharp intense lines on the low energy side of the visible band shown in Fig. 5a are taken to be the doublet states.

With this identification, all the spin-orbit components of  $^4P$  lie in the region of broad band absorption in the energy range  $16300 - 17900 \text{ cm}^{-1}$ . As a further check on this assignment, the spectrum was measured using a sample in which the concentration times the optical path length was about a factor of 10 higher than for the crystal used to measure the spectra shown in Fig. 5a. No absorption lines were observed in the region  $9000 - 15000 \text{ cm}^{-1}$ , however several additional weak absorptions due to the higher energy doublets were observed in the region  $18000 - 22000 \text{ cm}^{-1}$ . The assignment also gives values of the parameter  $\beta$  for the oxide and sulfides which are close to the values obtained for  $\text{Ni}^{++}$  in the same crystals. The values for  $\text{Co}^{++}$  are shown as circles on the graph in Fig. 10 and indicate nearly the same linear dependence of  $\beta$  on  $\alpha$  as that found for  $\text{Ni}^{++}$ . Since the relative energy,  $E/B$ , of the transition to the lowest three doublets does not markedly depend on  $Dq/B$ , the fact that they lie at about  $2000 \text{ cm}^{-1}$  higher energy in the oxide than in the sulfides reflects the larger value of the parameter  $B$  for the oxide compared with that for the sulfides.

The anisotropy in the spectra of  $\text{ZnO:Co}$ , which is more pronounced in the region of the sharp transitions on the low energy side of the visible band, can be qualitatively explained by consideration of the selection rules for the group  $C_{3v}$ . In  $C_{3v}$ , the ground state becomes  $E_{1/2} + E_{3/2}$  and, as explained earlier, these levels are equally populated for the temperatures used. We see therefore from Table IV that transitions from the ground state are formally allowed to both doublets  $E_{1/2}$  and  $E_{3/2}$ . The orbital selection rules are

$$\begin{aligned} (e^4 t_2^3; A_2) &\rightarrow (e^3 t_2^4; A_2) & \text{for } E \parallel c \\ (e^4 t_2^3; A_2) &\rightarrow (e^3 t_2^4; E) & \text{for } E \perp c \end{aligned}$$

where the parent cubic crystal field configuration has been given preceding the  $C_{3v}$  representation. Transitions from the quartet ground state to the

doublet excited states are made allowed by virtue of mixing via spin-orbit or other interactions between the doublets and other quartets. Since the allowed transitions are to states with the configuration  $e^3 t_2^4$ , we will consider only how quartet states of different symmetries, but with this configuration, are mixed with the doublets and the configuration label will be dropped. The states will be labeled by two symbols, the first giving the representation in  $C_{3v}$  followed parenthetically by the  $T_d$  representation, e.g.  ${}^2E({}^2T_1)$  stands for the spin-doublet whose orbital function transforms according to E in  $C_{3v}$  which comes from an orbital  $T_1$  state in  $T_d$  when the symmetry is reduced from  $T_d$  to  $C_{3v}$ . Second order  $L \cdot S$  interaction couples  ${}^2E({}^2E)$  with  ${}^4E({}^4T_2)$  and  ${}^4A_1({}^4T_2)$  whereas  ${}^2A_2({}^2T_1) + {}^2E({}^2T_1)$  is mixed with  ${}^4A_2({}^4T_1)$ ,  ${}^4E({}^4T_1)$ ,  ${}^4A_1({}^4T_2)$ , and  ${}^4E({}^4T_2)$ . The trigonal potential can cause further mixing of states of the same symmetry in  $C_{3v}$ . From this analysis, one thus expects transitions from the ground state  ${}^4A_2({}^4A_2)$  to the excited states  ${}^2E({}^2E)$  and  ${}^2E({}^2T_1)$  for  $E \perp c$  and to  ${}^2A_2({}^2T_1)$  for  $E \parallel c$ . This is qualitatively confirmed by examination of Fig. 5a which shows that in the energy region corresponding to the doublet transitions, the  $E \perp c$  spectrum is more intense and has more components than the  $E \parallel c$  spectrum. This does not explain the large number of components having small energy differences which are observed. We think the large number of closely spaced lines must be connected with the coupling of vibrational and electronic motions.

Within the framework of cubic  $T_d$  symmetry only, the digital computer calculations have shown that there is appreciable mixing between  ${}^4T_1(P)$  components and  ${}^2E$ , and  ${}^2T_1$ . These calculations also show that the  $E_{1/2} - {}^2A_1$  state in ZnO:Co whose calculated transition energy is  $17706 \text{ cm}^{-1}$  has about 0.2  ${}^4P$  character. The absorption band observed on the high energy side of the visible band having an energy of  $17679 \text{ cm}^{-1}$  in the  $E \perp c$  spectrum is identified as the transition

$G = {}^4A_2(F) - E_{1/2} - {}^2A_1$ . This transition is observed at about  $15000\text{ cm}^{-1}$  in the sulfides and calculations show that the upper level has about  $0.3 {}^4P$  character.

The four principal absorption bands observed at  $77^\circ\text{K}$  in the region corresponding to the  ${}^4A_2(F) - {}^4T_1(F)$  transition have been interpreted as the four spin-orbit components of the upper state. The value of  $\lambda$  needed to account for the total splitting is about  $-200\text{ cm}^{-1}$  in all three cases. This rather large value also gives reasonably good agreement between the observed and calculated  ${}^4P$  components. Comparison between the calculated and observed spectra is presented in Table VI for  $\text{Co}^{++}$  in  $\text{ZnO}$ ,  $\text{ZnS}$ , and  $\text{CdS}$ . The calculated transition energies, together with the designation of the upper level, are also shown on the spectra in Fig. 2. In general, the agreement is good; however there are some absorption bands which cannot be specifically identified. These are probably due to transitions to different vibrational states of the electronic levels. There are, however, only a few instances of what look like obvious vibrational frequency intervals following a 0-0 electronic transition.  $\text{ZnO:Co}$  at  $4^\circ\text{K}$  has a set of sharp absorption bands at 6003, 6129, 6177, and  $6277\text{ cm}^{-1}$ . The 6003 band has a half-width of  $10\text{ cm}^{-1}$ , and the next three are successively broader. There appears to be progressions corresponding to frequency intervals of  $89\text{ cm}^{-1}$  and  $115\text{ cm}^{-1}$  in the set of sharp absorption bands to the low energy side of the visible absorption in  $\text{ZnO:Co}$ . The lowest energy component of  ${}^4T_1(F)$  in  $\text{CdS:Co}$  is an intense sharp band at  $5230\text{ cm}^{-1}$  with a half-width of about  $7\text{ cm}^{-1}$  at  $4^\circ\text{K}$ . This band is followed by two weaker and broader absorptions centered about 5300 and  $5355\text{ cm}^{-1}$ . A set of three relatively narrow absorption bands is also observed at energies of 5470, 5520, and  $5530\text{ cm}^{-1}$ . In this crystal, certain patterns of sharp bands seem to be repeated at intervals of approximately  $290\text{ cm}^{-1}$  which is close to the reported value of the longitudinal optical mode frequency  $\nu_L = 300\text{ cm}^{-1}$  of pure  $\text{CdS}$ <sup>31</sup>. The  $4^\circ\text{K}$  spectrum of  $\text{ZnS:Co}$  also has a



set of sharp absorption bands at low frequency intervals in the infrared. The energies are 5760<sup>\*</sup>, 5889, 5917, 5940<sup>\*</sup>, 5986, 6020, 6053, 6070, 6135, 6161<sup>\*</sup>, 6218, 6240<sup>\*</sup>, and 6277, where the four sharpest and most intense bands are marked with an asterisk.

The low frequency intervals may be due to an internal vibrational mode of the complex. However, in crystals with the wurtzite structure, the complex is an artificial construction and is really strongly coupled to the rest of the lattice. One then must be concerned not only with the nuclear motion of the transition metal ion and its nearest neighbors, but may have to consider the coupling of impurity modified lattice modes with the electronic processes. While we have not considered this problem, we wish to point out that the low frequency intervals may be due to the excitation of acoustic mode vibrations of the lattice.

It has been shown that the values of  $B$  obtained for  $\text{Co}^{++}$  show a reduction from the free-ion value of the same magnitude as that observed for the  $B$  parameters of  $\text{Ni}^{++}$  in the same crystals. In the latter case, qualitative arguments were given in order to rationalize the observed reduction. The same reasoning leads to the expectation of a reduction of the spin-orbit parameter  $\lambda$  when the transition metal ion is put in a crystal. The  $g$  values obtained from paramagnetic resonance spectra and magnetic susceptibility measurements of crystals containing tetrahedrally coordinated  $\text{Co}^{++}$  can be explained on the basis of a reduced value of  $\lambda^{7-10}$ . Nevertheless, interpretation of the optical spectra of  $\text{Co}^{++}$  we have measured indicates that  $\lambda$  is even larger than the free-ion value. It may be that  $\lambda$  has been overestimated since it has been obtained primarily on the basis of taking the entire splitting of the  ${}^3T_1(F)$  band as being due to spin-orbit splitting. Although the value  $\lambda = -200 \text{ cm}^{-1}$  gives agreement with the total splitting, the calculated intervals do not agree with the observed intervals.

If we take the two lowest energy absorption bands observed in the 77°K spectrum to be the  $E_{1/2}$  and G components of  $^3T_1$  (F), the values  $\lambda = -135 \text{ cm}^{-1}$  and  $\lambda = -130 \text{ cm}^{-1}$  are obtained for ZnS and CdS respectively. The two higher energy components calculated from these values of  $\lambda$  are  $E_{5/2} = 6680 \text{ cm}^{-1}$ ,  $G = 6780 \text{ cm}^{-1}$  for ZnS and  $E_{5/2} = 5990 \text{ cm}^{-1}$ ,  $G = 6095 \text{ cm}^{-1}$  for CdS. Comparison with the observed spectra shows that the two upper components lie close to the third main absorption band, and this identification leaves unexplained the highest energy band of the set which lies some  $400 \text{ cm}^{-1}$  higher than the third band. This alternative explanation is not completely unreasonable, since we have not taken into account the effect of fields of lower symmetry on the cubic field levels. In addition to the expected splitting of the G levels, low symmetry fields may alter the energy separations between the components. Similar effects on the cubic levels of  $Ni^{++}$  have been previously discussed. Calculation of the effect of low symmetry fields are being planned and the results are expected to be valuable for determining a better value of  $\lambda$ . Although one may be able to account for the observed splitting of the  $^3T_1$  (F) band by a smaller value of  $\lambda$  plus an additional low symmetry field, it should be noted that the larger value of  $\lambda$  gives reasonably good agreement between calculated and observed transition energies. The observed energies of the individual bands at low temperatures in the visible region for the two sulfides agree well with the calculated energies and only a few extra absorption bands are observed.

Another direct determination of the spin-orbit parameter of  $Co^{++}$  in crystals has been obtained from the infrared spectra of  $CoO$ ,  $CoBr_2$ ,  $CoCl_2$ , and  $CoF_2$ <sup>32</sup>. In these crystals, cobalt is octahedrally coordinated and the  $^4T_1$  (F) level is lowest. The most intense infrared absorption band observed was identified as the  $E_{1/2} - ^4T_1$  (F)  $\rightarrow G - ^4T_1$  (F) transition whose energy is given in first order by  $6\lambda$ . Values of  $\lambda$  in the range  $-190 \text{ cm}^{-1}$  to  $-210 \text{ cm}^{-1}$  were obtained. These values are in agreement with those indicated by the total splitting of  $^3T_1$  (F) for cobalt in the wurtzite type crystals. However, the spectra of the octahedral cobalt salts are also

complicated by the effects of low symmetry fields. At the present stage of the interpretation of the spectra, one can only conclude that the effective spin-orbit parameter obtained for  $\text{Co}^{++}$  in crystals is anomalously high.

The relation between  $\beta$  and  $\epsilon$  can be obtained for  $\text{Co}^{++}$  in a similar manner to that discussed for  $\text{Ni}^{++}$  and the result is  $\beta = (1 - 4.2 \epsilon)$ . The values of  $\epsilon$  for the oxide and sulfide are 0.052 and 0.093 respectively. These agree quite well with the values obtained for  $\text{Ni}^{++}$  and indicate that the amount of ligand mixing with the central atom  $d$ -electron functions is approximately the same for these two transition metal ions.

#### INTENSITIES OF THE TRANSITIONS

Ballhausen and Liehr<sup>33</sup> have given an account of the intensities of crystal field absorption bands of tetrahedral complexes by considering the effect of central ion  $3d - 4p$  mixing and also by using the molecular orbital (MO) approach. Although they were not concerned with the intensity of transitions between individual spin-orbit components, their methods may easily be extended to this case. The basic idea of the method is that some odd parity functions are mixed in with the even parity  $d$ -functions so that the first order functions are

$$\psi_1 = \psi_1^0 + \sum_p c_{ip} \phi_p^0 \quad \text{where } \psi_1^0 \text{ is the unperturbed } d\text{-function}$$

and  $\phi_p^0$  stands for an odd parity function. The terms which contribute to the electric dipole moment of the transition  $\psi_1 \rightarrow \psi_j$  are of the form

$$\langle \psi_1 | P | \phi_q^0 \rangle c_{jq} + \langle \phi_p^0 | P | \psi_j^0 \rangle c_{ip} \quad \text{where}$$

$P$  is the dipole moment operator  $\sum_i e r_{i1}$ . Considering central atom  $d$ - $p$  mixing, one finds that only the  $t_2$  orbitals of the  $d$ -electron are mixed with  $p$  orbitals by the third power potential term of Eq. (2), which is proportional to  $x y z$ . The coefficient  $c_{ip}$  is equal to

$$\frac{\langle \phi_p^0 | V_3 | \psi_i^0 \rangle}{E_i^0 - E_p^0}$$

in this case. Dipole moment matrix elements for the transition  $e \rightarrow t_2$  and  $t_2 \rightarrow t_2$  can be expressed in terms of a common parameter  $\omega$ , if it is assumed that the radial parts of the  $e$  and  $t_2$  orbitals are the same and the energy denominators  $E_i^0 - E_p^0$  are the same for all  $i$  and  $p$ . The moments for the cubic field basis functions

$$e_z^2 = R(r) Y_2^0$$

$$e_{x^2 - y^2} = \frac{1}{\sqrt{2}} R(r) (Y_2^2 + Y_2^{-2})$$

$$t_{yz} = \frac{1}{\sqrt{2}} R(r) (Y_2^1 + Y_2^{-1})$$

$$t_{xz} = -\frac{1}{\sqrt{2}} R(r) (Y_2^1 - Y_2^{-1})$$

$$t_{xy} = -\frac{1}{\sqrt{2}} R(r) (Y_2^2 - Y_2^{-2})$$

are given in Table VII. For the  $n$  electron case, once the wave functions are obtained as linear combinations of the product cubic field functions, the calculation of the intensity reduces to a sum over the moments of Table VII. In order to treat transitions between spin-orbit components, the integration over the spin is performed first for the linear combination of product functions. Since the mixing parameter  $\omega$  is small because of the large energy denominator, contributions to the moments of second order in  $\omega$  are negligible, and the intensities are obtained as multiples of  $\omega^2$ . One therefore directly obtains relative values of the intensities which may be compared with the observed relative values.

The consideration of  $\sigma$ -bonding by the MO method gives only slightly different results for the relative intensities. The  $\phi_p$ 's are linear combinations of ligand  $p_\sigma$  functions and, just as before, only the  $t_2$  central atom orbitals are mixed.

The model leads to the same set of basic moments given in Table VII, except that the  $t_2 \rightarrow t_2$  moments are reduced by a factor  $\gamma = \left( \frac{1 - \epsilon}{1 - 2S\sqrt{\epsilon - \epsilon^2}} \right)^{1/2}$  compared with the  $e \rightarrow t_2$  moments and the parameter  $\gamma A$  appears instead of  $\omega$ . The factor  $(1 - \epsilon)^{1/2}$  is the coefficient of the  $t_2$  function,  $S$  is the overlap integral between the  $t_2$  function and the ligand  $p_\sigma$  combination, and  $A$  is the ligand coupling integral. The parameters have been introduced in this way, since we wish to estimate the effect of ligand mixing by the formalism of Koide and Pryce<sup>29</sup>, and will take  $S$  to be zero, thus making  $\gamma = (1 - \epsilon)^{1/2}$ .

When one includes the effect of  $\pi$ -bonding, further corrections to the intensities are obtained. In this case the  $e$  orbitals combine with ligand  $p_\pi$  combinations and the  $t_2$  orbitals are coupled with both  $p_\sigma$  and  $p_\pi$  ligand combinations. The moments for  $\pi$ -bonding only are again the same as above, however multiplied by a third parameter  $B$ . Using the full MO scheme, the calculated intensity contains four parameters, three of which are the coefficients  $c_{ip}$  of  $\sigma$ - and  $\pi$ -combinations which are added to the  $e$  and  $t_2$  orbital functions, and one which gives the ratio of  $B$  to  $\gamma A$ . With such a large number of parameters, the model is not quantitatively useful unless some independent means is available to obtain some of the parameters. This was not the case and estimates of the correction to be expected because of  $\pi$ -bonding on the basis of physically reasonable parameters were found to be small. This aspect will therefore not be discussed and we shall only discuss the  $d - p$  mixing and  $\sigma$ -bonding models.

The actual intensity calculations were performed in a slightly different manner from that indicated above. It was more convenient to use the spherical harmonic representation for the  $d$ -functions, since all the symmetry functions employed were those which transform under the operations of the group  $T_d$  like the spherical harmonic basis functions<sup>34</sup>. The perturbed  $d$ -orbital functions for  $d-p$  mixing are

$$\delta_2 = d_2 + \frac{1}{2} \omega p_0$$

$$\delta_1 = d_1 - i \omega p_1$$

$$\delta_0 = d_0$$

$$\delta_1^- = d_1^- + i \omega p_1$$

$$\delta_2^- = d_2^- - \frac{1}{2} \omega p_0$$

where  $\omega$  is the same parameter referred to above. The dipole moments in this basis to first order in  $\omega$  are given in Table VIII. After expressing the basis functions for  $\mathcal{H}$ ,  $|d^n SLJ; \Gamma \gamma \rangle$ , in terms of the linear combination of Slater determinant  $n$ -electron product functions, they were corrected to first order by determining the linear combination of product  $d^{n-1} p$  functions to be added. The moments in the  $k$  direction for this basis denoted by  $P$  ( $LJT$ ,  $L' J'T'$ ) are given in Appendix II for the  $d^8$  and  $d^7$  configurations. The factors  $(1 + \text{Re})$  which appear arise from the diminishing of the  $t_2 \rightarrow t_2$  moments compared with the  $e \rightarrow t_2$  moments. In the first approximation, the mixing of central ion  $d$  and  $p$  functions is considered and  $\epsilon$  is set equal to zero.

The eigenfunctions obtained from the computer solutions of the matrix of  $\mathcal{H}$  are of the form

$\psi(E_1, \Gamma) = \sum c_{SLJ} |d^n SLJ; \Gamma \gamma \rangle$ . The intensity of the transition  $\psi(E_0, \Gamma) \rightarrow \psi(E_1, \Gamma')$  is given by

$$I = K(E_1 - E_0) \sum_{\gamma, \gamma'} \left\{ \sum \sum c_{SLJ} c'_{S'L'J'} \langle d^n SLJ; \Gamma \gamma | P | d^n SL'J'; \Gamma' \gamma' \rangle \right\}^2$$

where we have assumed that the degeneracy, including Kramers degeneracy, is effectively removed for the wave functions, and we sum over the squares of the moments. The moments in the expression are given in Appendix II. The calculated results for CdS:Ni and ZnS:Ni are given in Table IX, where the intensities are

all relative to the intensity of the transition  $A_1 - {}^3T_1(F) \rightarrow T_2 - {}^3T_1(P)$ , and the observed values were obtained from the area under the absorption peaks observed at 77°K. The calculated intensities of the two lowest energy transitions is much higher than observed and the comparison between calculated and observed intensities is only slightly improved by considering the effect of covalency through the use of the values of  $\epsilon$  previously obtained. The calculated value for the transition to  $T_2 - {}^1T_2(D)$  is comparable to that for the transition to  $T_2 - {}^3A_2(F)$  in both cases, which shows that the singlet state is appreciably mixed with triplet states. It is interesting to note that the triplet character is mostly  ${}^3A_2(F)$  for ZnS:Ni and the intensity is about one third of that for  ${}^3A_2(F)$ ; whereas the triplet character is  $0.31 {}^3T_1(P) + 0.25 {}^3A_2(F) + 0.10 {}^3T_2(F)$  for CdS:Ni and the intensity of the transition to  ${}^1D$  has a calculated value which is even larger than that for the transition to  ${}^3A_2(F)$ . It can be seen in Fig. 1 that  ${}^1D$  lies much closer to  ${}^3P$  for CdS:Ni than for ZnS:Ni. It has already been pointed out that in the latter case both  $E$  and  $T_2$  of  ${}^1D$  lie at lower energies than  $T_2 - {}^3A_2(F)$ .

The calculated intensity pattern for ZnS:Co is shown in Fig. 12. Comparison of this pattern with the observed spectra shows that whereas the total calculated intensity of the multiplets is in reasonable agreement with that observed, the observed relative strengths of the individual components within a multiplet do not agree well with the calculated values. The intensity ratio

$$\frac{I\{ {}^4A_2(F) - {}^4T_1(P) \}}{I\{ {}^4A_2(F) - {}^4T_1(F) \}}$$

obtained by taking the sum of the calculated components is 4.2 compared to the observed ratio of 4.6. The calculated ratio is more simply obtained by use of the cubic field configurations appropriate to the weak crystal field for the three levels involved<sup>33</sup>. The calculated results are only slightly altered by

taking  $\epsilon \neq 0$  and we have only indicated whether the intensity of the transition is increased or decreased by the sense of the arrow on each line in Fig. 12. The correction is almost always in the direction which gives better agreement with observed spectrum, however for  $\epsilon < 0.1$ , the correction never exceeds 5 percent of the intensity calculated for  $\epsilon = 0$ .

The calculated intensity pattern for ZnO:Co is quite close to that shown in Fig. 12, except that the values for the transitions to  $G - {}^2E$ ,  $E_{1/2} - {}^2T_1$ , and  $G - {}^2T_1$  are about twice as large as those shown. The observed relative intensities of the sharp bands in the spectrum which have been interpreted as being due to these transitions is much greater than the calculated values. Even though the model used seems to be only qualitatively correct, this is good indication that the doublet states are even more strongly mixed with quartet states than has been found by the diagonalization procedure for the parameters given in Table II. A serious limitation on the assessment of the validity of the intensity mechanism is that we have not tried to take into account the effect of fields of lower symmetry and the calculations are all based on strictly  $T_d$  symmetry. The calculations should be a good first approximation however, since the cubic field predominates. Since the total relative intensities of the multiplets is correctly given by the model, at least for the  $Co^{++}$  spectra, it is possible that lower symmetry fields may cause sufficient mixing of the spin-orbit components within a multiplet to account for the differences between calculated and observed intensities.

The discrepancies between the calculated and observed intensities for the case of  $Ni^{++}$  cannot be easily explained. The most serious disagreement is that the intensities of the transitions  $A_1 - {}^3T_1 (F) \rightarrow T_2 - {}^3T_1 (F)$  and  $A_1 - {}^3T_1 (F) \rightarrow T_2 - {}^3T_2 (F)$  are calculated to be much too large. Characteristically, the observed absorption bands are more intense, the higher the energy of the transition.



Qualitatively, one might expect that the relatively low energy charge transfer transition, which has a high oscillator strength, could give the most important contribution to the intensities of the lower energy, predominately  $d-d$  transitions. The terms which would contribute to the intensity are in this case

$$\frac{\langle \phi_c | V | \psi_1^0 \rangle}{E_1^0 - E_c} \langle \phi_c | \frac{P}{\omega} | \psi_f^0 \rangle + \frac{\langle \phi_c | V | \psi_f^0 \rangle}{E_f^0 - E_c} \langle \psi_1^0 | \frac{P}{\omega} | \phi_c \rangle$$

where  $\psi_1^0$  and  $\psi_f^0$  are the zero order approximation to the initial and final states with energies  $E_1^0$  and  $E_f^0$  respectively, and  $\phi_c$  is the charge transfer state with energy  $E_c$ . Therefore, the contribution from the second term is greater the higher the energy of the transition (the smaller the value of  $E_f^0 - E_c$ ). It is not clear just how important the first term would be, but since it only differs for different transitions by the factor  $\langle \phi_c | \frac{P}{\omega} | \psi_f^0 \rangle$  and since the energy denominator is larger than that for the second term, we expect its contribution to be less than that of the second term.

In a paper concerned with the intensities of octahedral complexes, Engman<sup>35</sup> recently presented a model in which the odd vibrations of the complex serve as the perturbing potential, and he discussed the relative contributions of the two terms above for those complexes. If we assume that the  $V_3$  potential of a tetrahedral complex causes the charge transfer state to mix with the  $d$ -electron states, and if the first term above is neglected, Engman's results may be used to calculate the ratio of the intensities of the transitions. The results for ZnS:Ni are, denoting the intensity of the transition by the upper level symbol,  ${}^3T_1(P) : {}^3A_2(F) : {}^3T_2(F) = 1 : 0.31 : 0.16$ . This model gives better agreement between calculated and observed intensities for the low energy transitions, however the model is not precisely defined as we have used it for the tetrahedral complexes, and is dependent almost entirely on the energy denominators  $E_f^0 - E_c$ , which of course leads to lower calculated values for the lower energy transitions.

The results merely serve to indicate how the charge transfer mixing can affect the relative intensities.

We shall probably have to take into account the actual form of the orbital angular momentum for the charge transfer states, together with ligand  $\sigma$ - and  $\pi$ -bonding in order to obtain a quantitative model which is capable of predicting the correct relative intensities. An important requirement for the model will be to obtain the potential function which acts on the electrons anywhere within the whole complex, e.g. central ion plus the ligand environment, since the odd power potential terms are the ones which cause mixing between states of opposite parity.

#### ACKNOWLEDGEMENTS

I am deeply grateful to Dr. D. S. McClure for his guidance and encouragement during the course of this work. I wish to thank Dr. S. R. Polo, whose work on the formal aspects of the theory was extremely valuable to me, and who helped with many of the computer calculations. I would also like to thank Mr. P. K. Baltzer who kindly provided some programs for large-scale matrix diagonalization and other help in crystal field calculations. Finally, I thank Mr. C. Neil who assisted me in performing the experimental work.

## References

1. D. S. McClure, J. Phys. Chem. Solids 3, 311 (1957).
2. D. M. Gruen and R. L. McBeth, J. Phys. Chem. 63, 393 (1959).
3. R. Pappalardo, J. Mol. Spectroscopy 6, 554 (1961).
4. W. Moffitt and C. J. Ballhausen, Ann. Rev. Phys. Chem. 7, 107 (1956).
5. D. S. McClure, Solid State Physics 9, 399 (1959).
6. W. Low and M. Weger, Phys. Rev. 118, 1119 (1960); 120, 2277 (1960).
7. W. Low, Paramagnetic Resonance in Solids (Academic Press, New York, 1960).
8. F. S. Ham, G. W. Ludwig, G. D. Watkins, and H. H. Woodbury, Phys. Rev. Letters 5, 468 (1960).
9. P. Cossee and A. E. vanArkel, J. Phys. Chem. Solids 15, 1 (1960).
10. R. H. Holm and F. A. Cotton, J. Chem. Phys. 31, 788 (1959).
11. J. W. Nielson and E. F. Dearborn, J. Phys. Chem. 64, 1762 (1960).
12. R. W. G. Wyckoff, Crystal Structures (Interscience, New York, 1948), Vol. 1.
13. B. Brehler, Z. Krist. 109, 68 (1957).
14. B. Morosin and E. C. Lingafelter, Acta Cryst. 12, 744 (1959).
15. O. G. Holmes and D. S. McClure, J. Chem. Phys. 26, 1686 (1957).
16. H. Kayser, Tabelle der Schwingungszahlen (Sittirzel, Leipzig, 1925).
17. H. A. Klasens, J. Electrochem. Soc. 100, 72 (1953).
18. R. J. Collins and D. A. Kleinman, J. Phys. Chem. Solids 11, 190 (1959).
19. A. D. Liehr and C. J. Ballhausen, Ann. Phys. 6, 134 (1959).
20. E. U. Condon and G. H. Shortley, The Theory of Atomic Spectra (Cambridge University Press, New York, 1953).
21. G. Racah, Phys. Rev. 62, 438 (1942); 63, 367 (1943).
22. A. D. Liehr, J. Phys. Chem. 64, 43 (1960).
23. R. E. Watson, Technical Report (Solid-State and Molecular Theory Group, M.I.T., Cambridge, Mass.) No. 12, June 15 (1959).

## References (cont.)

24. A. L. Schawlow, A. H. Piksis, and S. Sugano, Phys. Rev. 122, 1469 (1961).
25. a A. J. Freeman and R. E. Watson, Phys. Rev. 120, 1254 (1960).  
b Y. Tanabe and S. Sugano, J. Phys. Soc. (Japan) 11, 864 (1956).  
c W. H. Kleiner, J. Chem. Phys. 20, 1784 (1952).
26. L. E. Orgel, J. Chem. Phys. 23, 1824 (1955).
27. J. R. Tassman, A. H. Kahn, and W. Shockley, Phys. Rev. 92, 890 (1953).
28. C. K. Jorgensen, Acta Chem. Scand. (a) 11, 53 (1957); (b) 12, 903 (1958).
29. S. Koide and M. H. L. Pryce, Phil. Mag. 3, 607 (1958).
30. J. W. Stout, J. Chem. Phys. 31, 709 (1959).
31. F. A. Kroger, and H. J. G. Meyer, Physica 20, 1149 (1954).
32. R. Newman and R. M. Chrenko, Phys. Rev. 115, 1147 (1959).
33. C. J. Ballhausen and A. D. Liehr, J. Mol. Spectroscopy 2, 342 (1958).
34. S. R. Polo, (to be published).
35. R. Englman, Mol. Phys. 3, 48 (1960).

## Figure Captions

- Figure 1 Absorption spectra of  $\text{Ni}^{++}$  in crystals having the wurtzite type structure. Spectra measured at  $77^\circ\text{K}$  and  $298^\circ\text{K}$ ; (a)  $\text{ZnO:Ni}$ , axial spectrum; (b)  $\text{ZnS:Ni}$ ; (c)  $\text{CdS:Ni}$ , (d)  $\text{ZnO:Ni}$ , polarized with  $\vec{E} \perp c$  and  $\vec{E} \parallel c$ . The origin of the optical density scale is arbitrary and the curves have been shifted relative to one another in order to minimize overlap. The same crystal was used for the two different temperatures.
- Figure 2 Absorption spectra of  $\text{Co}^{++}$  in crystals having the wurtzite type structure. Spectra measured at  $77^\circ\text{K}$  and  $298^\circ\text{K}$ ; (a)  $\text{ZnO:Co}$ ; (b)  $\text{ZnS:Co}$ ; (c)  $\text{CdS:Co}$ . The origin of the optical density scale is arbitrary and the curves have been shifted relative to one another in order to minimize overlap. The same crystal was used for the two different temperatures.
- Figure 3 Room temperature absorption spectra of  $\text{Ca}_2(\text{Zn}_{1-y}\text{Ni}_y)\text{X}_4$  where  $y \approx 0.1$ . The curve labeled A is for  $\text{X}^- = \text{Cl}^-$  and B is for  $\text{X}^- = \text{Br}^-$ .
- Figure 4 Polarized absorption measured at  $4^\circ\text{K}$  in the region of the visible band of  $\text{Ni}^{++}$  in crystals having the wurtzite type structure; (a)  $\text{ZnO:Ni}$ ; (b)  $\text{ZnS:Ni}$ ; (c)  $\text{CdS:Ni}$ . The origin of the optical density scale is arbitrary and the absorption curves for the two polarizations have been shifted relative to each other in order to minimize overlap.
- Figure 5 Polarized absorption measured at  $4^\circ\text{K}$  in the region of the visible band of  $\text{Co}^{++}$  in crystals having the wurtzite type structure; (a)  $\text{ZnO:Co}$ ; (b)  $\text{ZnS:Co}$ ; (c)  $\text{CdS:Co}$ . The origin of the optical density scale is arbitrary and the curves for the two polarizations have been shifted relative to each other in order to minimize overlap.

- Figure 6 Absorption spectrum of ZnO:Cu; (a) axial spectrum measured at 298°K and 4°K; (b) polarized spectrum measured at 4°K.
- Figure 7 Energy level diagram for states of the  $d^8$  configuration in a crystal field of  $T_d$  symmetry.
- Figure 8 Energy level diagram for states of the  $d^7$  configuration in a crystal field of  $T_d$  symmetry.
- Figure 9 Energy level diagram for the states of the  $d^8$  configuration in a crystal field of  $T_d$  symmetry obtained by diagonalizing the matrix of  $\mathcal{H}$  for the parameters  $C/B = 4.5$ ,  $B = 560 \text{ cm}^{-1}$  and  $\lambda = -250 \text{ cm}^{-1}$ .
- Figure 10 Plot showing the variation of the normalized electrostatic repulsion parameter  $\beta = B/B_0$  with ligand polarizability,  $\alpha$ .
- Figure 11 Energy level diagram for the states of the  $d^7$  configuration in a crystal field of  $T_d$  symmetry obtained by diagonalizing the matrix of  $\mathcal{H}$  for the parameters  $C/B = 4.5$ , and  $\lambda/B = -0.30$ .
- Figure 12 Calculated intensity pattern showing the relative intensities of the spin-orbit components of ZnS:Co.

Table I. Oscillator strengths of the prominent room temperature bands for  $\text{Ni}^{++}$  and  $\text{Co}^{++}$  in  $\text{ZnO}$  and  $\text{ZnS}$ . The weight percent of impurity is given parenthetically after the host crystal and  $d$  is the sample thickness in microns.

Wavenumber of band maxima, $\text{cm}^{-1}$	$f$	Upper level designation
<b><math>\text{ZnO}</math> (0.072 <math>\text{Ni}</math>) , <math>d = 560</math></b>		
15260, 16180	$1.6 \times 10^{-3}$	$^3T_1(\text{P})$
8340	$8.6 \times 10^{-5}$	$^3T_1(\text{F})$
4600	$3.9 \times 10^{-5}$	$^3T_2(\text{F})$
<b><math>\text{ZnS}</math> (0.070 <math>\text{Ni}</math>) , <math>d = 90</math></b>		
12500, 13080	$1.9 \times 10^{-2}$	$^3T_1(\text{P})$
9350, 9390	$2.1 \times 10^{-3}$	$^3T_1(\text{F}), ^1T_2(\text{D})$
4940	$1.6 \times 10^{-3}$	$^3T_2(\text{F})$
<b><math>\text{ZnO}</math> (0.048 <math>\text{Co}</math>) , <math>d = 460</math></b>		
15310, 16360	$5.2 \times 10^{-3}$	$^4T_1(\text{P})$
6170, 7150, 7690	$7.8 \times 10^{-4}$	$^4T_1(\text{F})$
<b><math>\text{ZnS}</math> (0.19 <math>\text{Co}</math>) , <math>d = 32</math></b>		
13732, 14930	$1.3 \times 10^{-2}$	$^4T_1(\text{P})$
6640	$2.9 \times 10^{-3}$	$^4T_1(\text{F})$

Table II. Parameters obtained from the spectra measured at 77°K.

Ni <sup>+2</sup>						
	d(Å)	Dq(cm <sup>-1</sup> )	B(cm <sup>-1</sup> )	C/B	λ(cm <sup>-1</sup> )	E <sub>g</sub> (cm <sup>-1</sup> )
ZnO	1.95	420	770	4.6	(-250)	25 800
ZnS	2.34	475	560	4.5	(-250)	29 900
CdS	2.52	400	570	4.7	(-250)	19 400
Cs <sub>2</sub> ZnBr <sub>4</sub>	2.40	330	695	4.5		44 000
Cs <sub>2</sub> ZnCl <sub>4</sub>	2.24	385	725	4.5		50 000
Free Ion			1020	4.1	-340	
Co <sup>+2</sup>						
	d(Å)	Dq(cm <sup>-1</sup> )	B(cm <sup>-1</sup> )	C/B	λ(cm <sup>-1</sup> )	
MgAl <sub>2</sub> O <sub>4</sub> <sup>(a)</sup>	1.92	400	735	4.4	-210	
ZnO	1.95	390	775	4.5	-210	
ZnS	2.34	375	610	4.4	-195	
CdS	2.52	330	610	4.4	-195	
Free Ion			997	4.2	-178	
Cu <sup>+2</sup>						
ZnO		500				

(a) The data was obtained from an unpublished spectrum measured by D. S. McClure and is included for purposes of comparison with ZnO:Co.



Table III. Character table for the group  $T_d$  showing how some basis functions transform and also showing the correlation between the representations in  $T_d$  and  $C_{3v}$ .

$T_d$		E	$8C_3$	$3C_2$	$6S_4$	$6C_2$	Representations of some basis functions	Correlated representation in $C_{3v}$
Single	$A_1$	1	1	1	1	1		$A_1$
	$A_2$	1	1	1	-1	-1	xyz	$A_2$
	E	2	-1	2	0	0	$(3z^2-1), \sqrt{3}(x^2-y^2)$	E
	$T_1$	3	0	-1	1	-1	$R_x, R_y, R_z$	$A_2 + E$
	$T_2$	3	0	-1	-1	1	x, y, z	$A_1 + E$
Double	$E_{1/2}$	2	1	0	$\sqrt{2}$	0	$(\frac{1}{2} \frac{1}{2}), (\frac{1}{2} \frac{1}{2})$	$E_{1/2}$
	$E_{5/2}$	2	1	0	$-\sqrt{2}$	0		$E_{1/2}$
	G	4	-1	0	0	0	$(\frac{3}{2} \frac{3}{2}), (\frac{3}{2} \frac{1}{2}), (\frac{3}{2} \frac{1}{2}), (\frac{3}{2} \frac{3}{2})$	$E_{1/2} + E_{3/2}$

Table IV. Selection and polarization rules for electric dipole transitions. There are no polarization rules in  $T_d$  and a cross means allowed. The  $C_3$  axis of the group  $C_{3v}$  coincides with the hexagonal  $c$  axis of the wurtzite unit cell and  $||$  means allowed for  $E || c$  and  $\perp$  means allowed for  $E \perp c$ .

$T_d$	$A_1$	$A_2$	$E$	$T_1$	$T_2$	$E_{1/2}$	$E_{3/2}$	$G$
$A_1$					x			
$A_2$				x				
$E$				x	x			
$T_1$		x	x	x	x			
$T_2$	x		x	x	x			
$E_{1/2}$							x	x
$E_{3/2}$						x		x
$G$						x	x	x

$C_{3v}$	$A_1$	$A_2$	$E$	$E_{1/2}$	$E_{3/2}$
$A_1$	$  $	0	$\perp$		
$A_2$	0	$  $	$\perp$		
$E$	$\perp$	$\perp$	$\perp +   $		
$E_{1/2}$				$\perp +   $	$\perp$
$E_{3/2}$				$\perp$	$  $

Table V. Comparison of calculated and observed spectra of  $\text{Ni}^{++}$ . The parameters given in Table II, with the exceptions that  $Dq = 460 \text{ cm}^{-1}$  for  $\text{ZnS:Ni}$  and  $Dq = 385 \text{ cm}^{-1}$  for  $\text{CdS:Ni}$ , were used for the calculation. The slightly smaller values were used in order to obtain better agreement with the sharp lines at the origin of the bands. The observed spectra were measured at  $4^\circ\text{K}$ .

Energy in $\text{cm}^{-1}$		Energy in $\text{cm}^{-1}$		Energy in $\text{cm}^{-1}$		Designation of upper level
ZnO:Ni		ZnS:Ni		CdS:Ni		
Calc.	Obs. ( $E_{\perp G}$ )	Calc.	Obs.	Calc.	Obs.	
4226	4215	4390	4215 <sup>a</sup>	4001	3902 <sup>b</sup>	$T_1 - {}^3T_2$ (F)
4359	4248	4450	-	4070	-	$E - {}^3T_2$ (F)
4330	4312	4500	-	4161	-	$T_2 - {}^3T_2$ (F)
4552	4400	4650	4500	4332	4413	$A_2 - {}^3T_2$ (F)
8580	8340	9810	9750	7991	7840	$T_2 - {}^3A_2$ (F)
13091	12404	9180	8760	9736	9710	$T_2 - {}^1T_2$ (D)
13564	13365	9705	9180	9975	10254	$E - {}^1E$ (D)
15192	15200	12448	12436	12198	12199	$T_2 - {}^3T_1$ (P)
15262	15300	12495	12484	12284	12294	$E - {}^3T_1$ (P)
15543	15486	12785	12779	12500	12509	$T_1 - {}^3T_1$ (P)
15729	15635	12950	12933	12712	12623	$A_1 - {}^3T_1$ (P)
19655		15230	15320	14995	15100	$T_2 - {}^1T_2$ (G)

- a) A series of about eight sharp absorptions are observed in the energy range  $4215 - 4500 \text{ cm}^{-1}$
- b) A series of about fifteen individual sharp absorption lines are observed in the energy range  $3902 - 4413 \text{ cm}^{-1}$

Table VI. Comparison of calculated and observed spectra of  $\text{Co}^{++}$ . The calculated values are based on the parameters given in Table II and the observed spectra were measured at 4°K. The energies are all in  $\text{cm}^{-1}$ .

ZnO:Co ( $E \perp c$ )		ZnS:Co		CdS:Co		Designation of upper level
Calc.	Obs.	Calc.	Obs.	Calc.	Obs.	
6140	6001	5922	5920	5245	5220	$E_{1/2}$ } ${}^4T_1(P)$
6687	6643	6431	6221	5775	5604	G } ${}^4T_1(P)$
7327	7156	7016	6829	6366	6135	$E_{5/2}$ } ${}^4T_1(P)$
7474	7691	7158	7208	6519	6496	G } ${}^4T_1(P)$
15155	15145 <sup>a</sup>	12296	12377	11974	-	G - ${}^2E$
15425	-	12530	12437	12185	-	$E_{1/2} - {}^2T_1$
			12488			
15844	-	13052	13188	12742	13045	G - ${}^2T_1$
			13761			
16236	16262 <sup>b</sup>	13860	13881	13524	13541	G } ${}^4T_1(P)$
16292	-	13910	13974	13550	13618	$E_{5/2}$ } ${}^4T_1(P)$
16689	-	14057	14118	13829	13847	G } ${}^4T_1(P)$
16930	-	14455	14485	14126	14142	$E_{1/2}$ } ${}^4T_1(P)$
17906	17679	15056	15006	14574	14485	$E_{1/2} - {}^2A_1(G)^c$
18187	18094	15197	15345	14664	14760	G - ${}^2T_2(G)$

a) A series of sharp absorption bands are observed to higher energies. See Fig. 5a.

b) The four spin-orbit components lie in the broad band absorption region. See Fig. 5a.

c) The  $E_{1/2} - {}^2A_1(G)$  level has about 25 percent G -  ${}^4T_1(P)$  character.

Table VII. Dipole moment matrix elements for the cubic field basis functions

$$\begin{aligned}
 \langle e_z^2 \mid \underline{P} \mid t_{yz} \rangle &= -\sqrt{\frac{1}{15}} \omega \underline{i} \\
 \langle e_{x^2-y^2} \mid \underline{P} \mid t_{yz} \rangle &= \sqrt{\frac{1}{5}} \omega \underline{i} \\
 \langle e_z^2 \mid \underline{P} \mid t_{xz} \rangle &= -\sqrt{\frac{1}{15}} \omega \underline{j} \\
 \langle e_{x^2-y^2} \mid \underline{P} \mid t_{xz} \rangle &= \sqrt{\frac{1}{5}} \omega \underline{j} \\
 \langle e_z^2 \mid \underline{P} \mid t_{xy} \rangle &= \sqrt{\frac{4}{15}} \omega \underline{k} \\
 \langle t_{xz} \mid \underline{P} \mid t_{xy} \rangle &= \sqrt{\frac{4}{5}} \omega \sqrt{1-\omega^2} \underline{i} \\
 \langle t_{yz} \mid \underline{P} \mid t_{xy} \rangle &= \sqrt{\frac{4}{5}} \omega \sqrt{1-\omega^2} \underline{j} \\
 \langle t_{yz} \mid \underline{P} \mid t_{xz} \rangle &= \sqrt{\frac{4}{5}} \omega \sqrt{1-\omega^2} \underline{k}
 \end{aligned}$$

and

$$\langle \psi_i \mid \underline{P} \mid \psi_j \rangle = \langle \psi_j \mid \underline{P} \mid \psi_i \rangle$$

Table VIII. Dipole moment matrix elements for the spherical harmonic basis functions. The moments are given for circular polarization, where  $L = \frac{1}{\sqrt{2}} (i-j)$  and  $R = \frac{1}{\sqrt{2}} (i+j)$ . The entries in the table are multiplied by  $i\omega$ .

$$\langle \delta_{m_l} | P | \delta_{m_{l'}} \rangle$$

$\delta_{m_l} \backslash \delta_{m_{l'}}$	$\delta_2$	$\delta_1$	$\delta_0$	$\delta_{-1}$	$\delta_{-2}$
$\delta_2$		$\frac{1}{\sqrt{10}} R$	$-\sqrt{\frac{2}{15}} k$	$-\frac{3}{\sqrt{10}} L$	
$\delta_1$	$-\frac{1}{\sqrt{10}} L$		$-\sqrt{\frac{1}{15}} R$	$\frac{2}{\sqrt{5}} k$	$\frac{3}{\sqrt{10}} L$
$\delta_0$	$\sqrt{\frac{2}{15}} k$	$\sqrt{\frac{1}{15}} L$		$\sqrt{\frac{1}{15}} R$	$-\sqrt{\frac{2}{15}} k$
$\delta_{-1}$	$\frac{3}{\sqrt{10}} R$	$-\frac{2}{\sqrt{5}} k$	$-\frac{1}{15} L$		$-\sqrt{\frac{1}{10}} R$
$\delta_{-2}$		$-\frac{3}{\sqrt{10}} R$	$\sqrt{\frac{2}{15}} k$	$\sqrt{\frac{1}{10}} L$	

Table IX Comparison of calculated and observed intensities for ZnS:Ni and CdS:Ni. The observed intensities were obtained from the 77°K spectra. The moments, M, are in the  $k$  direction and are multiplied by  $100k$  for the p-d mixing model and by  $i\sqrt{A}k$  for the  $\sigma$ -bonding model, and the parameter  $\epsilon$  is explained in the text. The intensities are all relative to that of the transition  $A_1 - {}^3T_1 (F) \longrightarrow T_2 - {}^3T_1 (P)$  which has been set equal to one.

ZnS:Ni				
M	$I_{\text{calc. for } \epsilon = 0}$	$I_{\text{calc. for } \epsilon = 0.1}$	$I_{\text{obs.}}$	Designation of upper level
- 0.013 (1-0.77 $\epsilon$ )	0.004	0.003	0.007	$T_2 - {}^1T_2 (G)$
- 0.228 (1+0.1 $\epsilon$ )	1	1	1	$T_2 - {}^3T_1 (P)$
0.064 (1+0.47 $\epsilon$ )	0.062	0.067	0.079	$T_2 - {}^3A_2 (F)$
0.040 (1+0.5 $\epsilon$ )	0.023	0.025	0.040	$T_2 - {}^1T_2 (D)$
- 0.351 (1-0.28 $\epsilon$ )	0.83	0.77	0.052	$T_2 - {}^3T_2 (F)$
- 0.834 (1-0.36 $\epsilon$ )	1.18	1.08	-	$T_2 - {}^3T_1 (F)$
CdS:Ni				
M	$I_{\text{calc. for } \epsilon = 0}$	$I_{\text{calc. for } \epsilon = 0}$	$I_{\text{obs.}}$	Designation of upper level
- 0.019 (1-0.53 $\epsilon$ )	0.010	0.009	0.006	$T_2 - {}^1T_2 (G)$
- 0.206 (1+0.15 $\epsilon$ )	1	1	1	$T_2 - {}^3T_1 (P)$
- 0.076 (1+0.13 $\epsilon$ )	0.11	0.11	0.084	$T_2 - {}^1T_2 (D)$
0.046 (1+0.87 $\epsilon$ )	0.040	0.046	0.10	$T_2 - {}^3A_2 (F)$
- 0.319 (1-0.06 $\epsilon$ )	0.79	0.75	0.055	$T_2 - {}^3T_2 (F)$
- 0.829 (1-0.36 $\epsilon$ )	1.39	1.26	-	$T_2 - {}^3T_1 (F)$

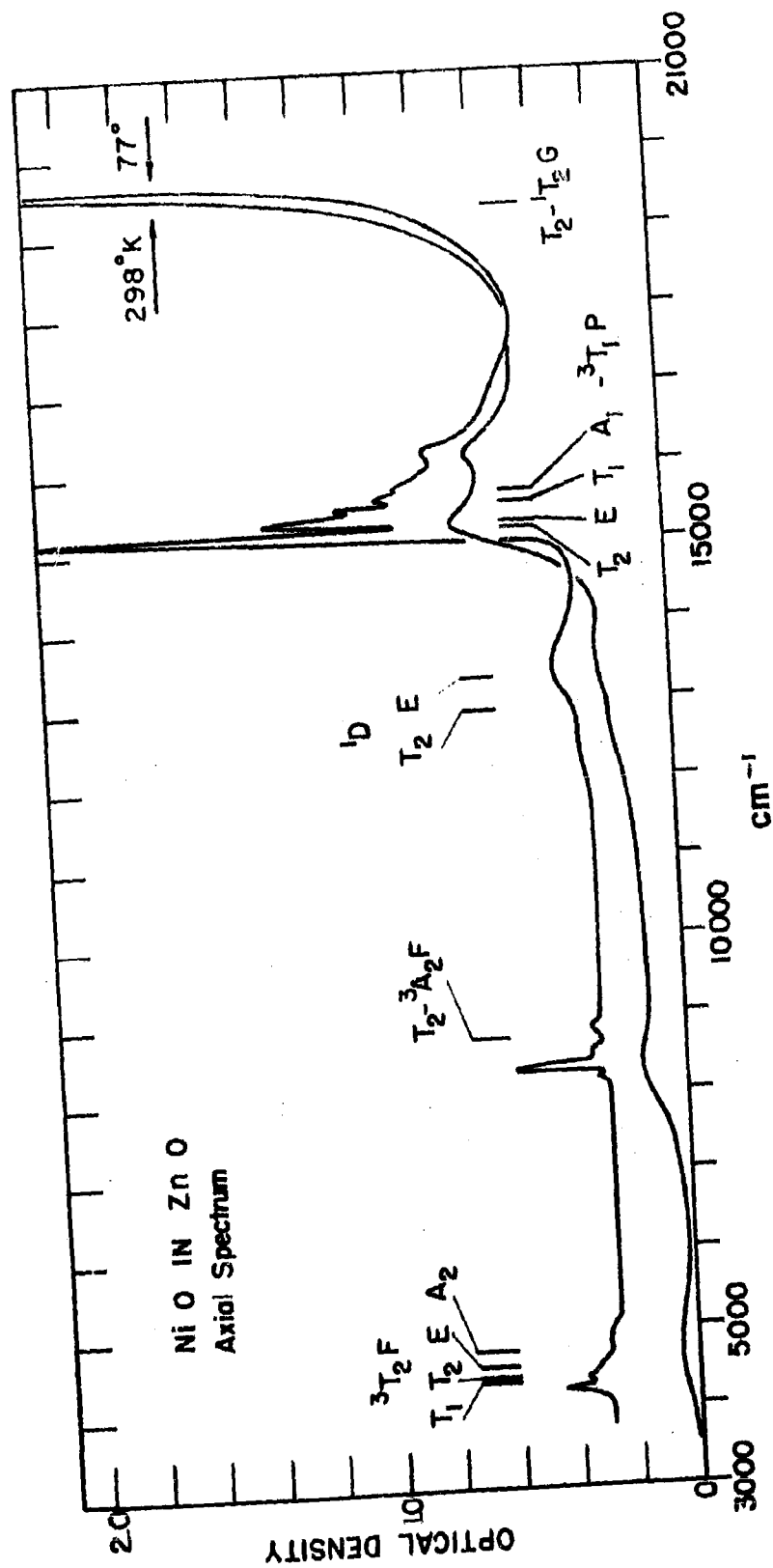


Fig. 1a



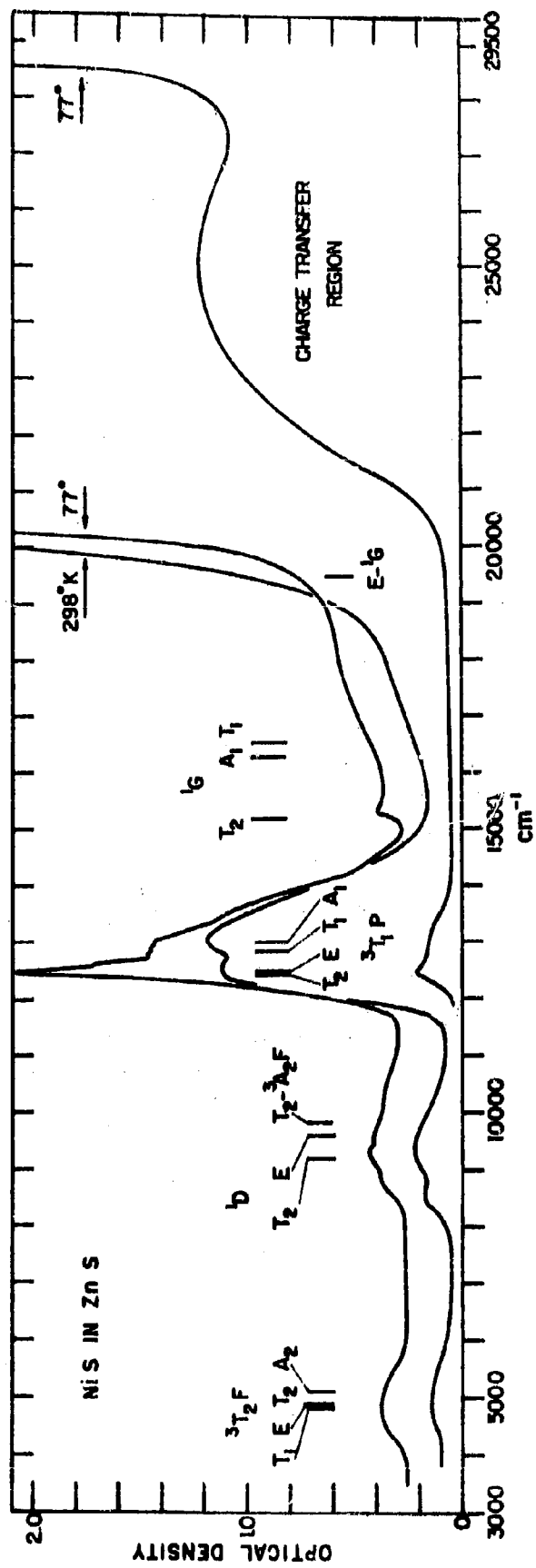


Figure 1b

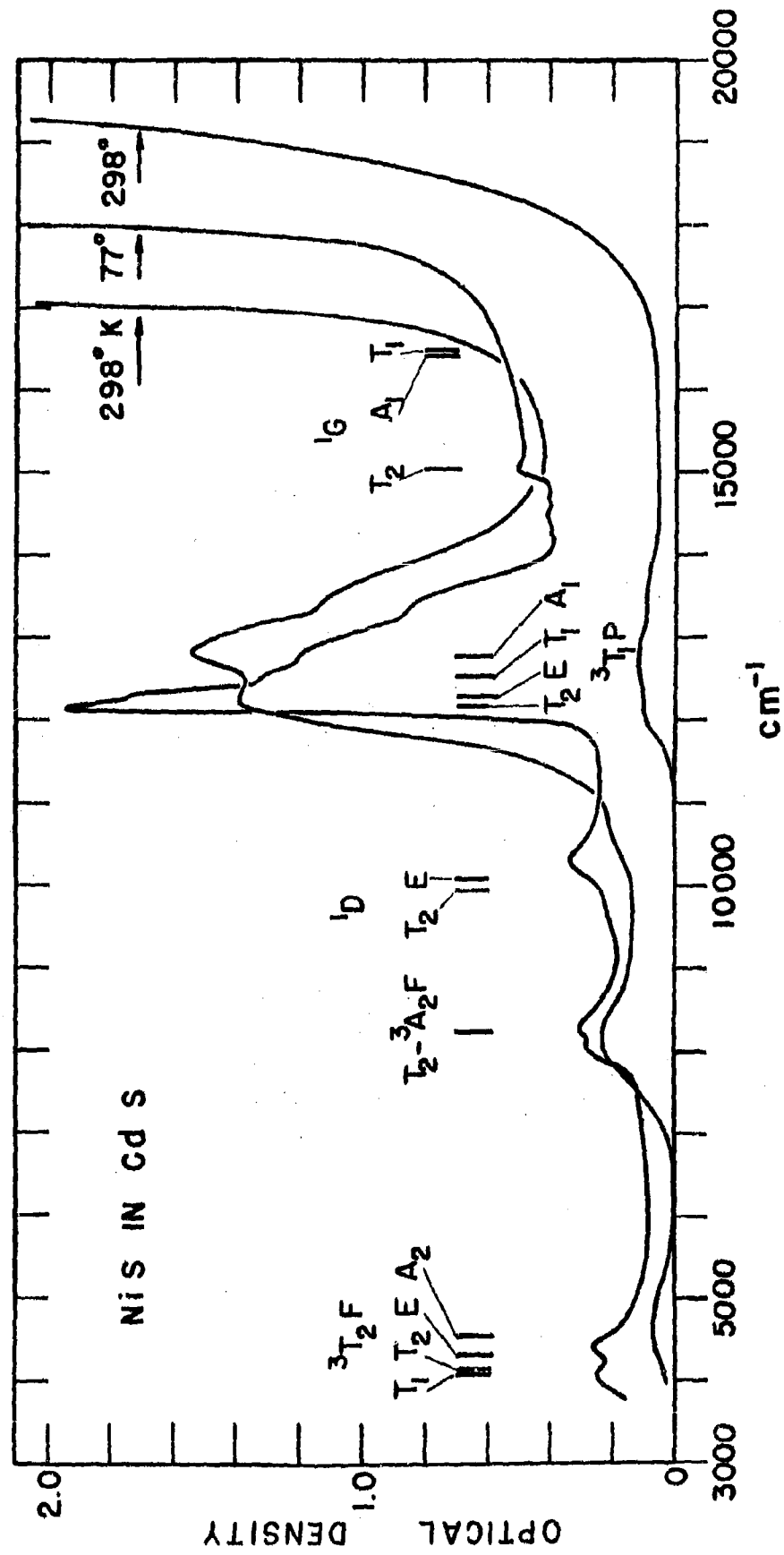


Figure 1c

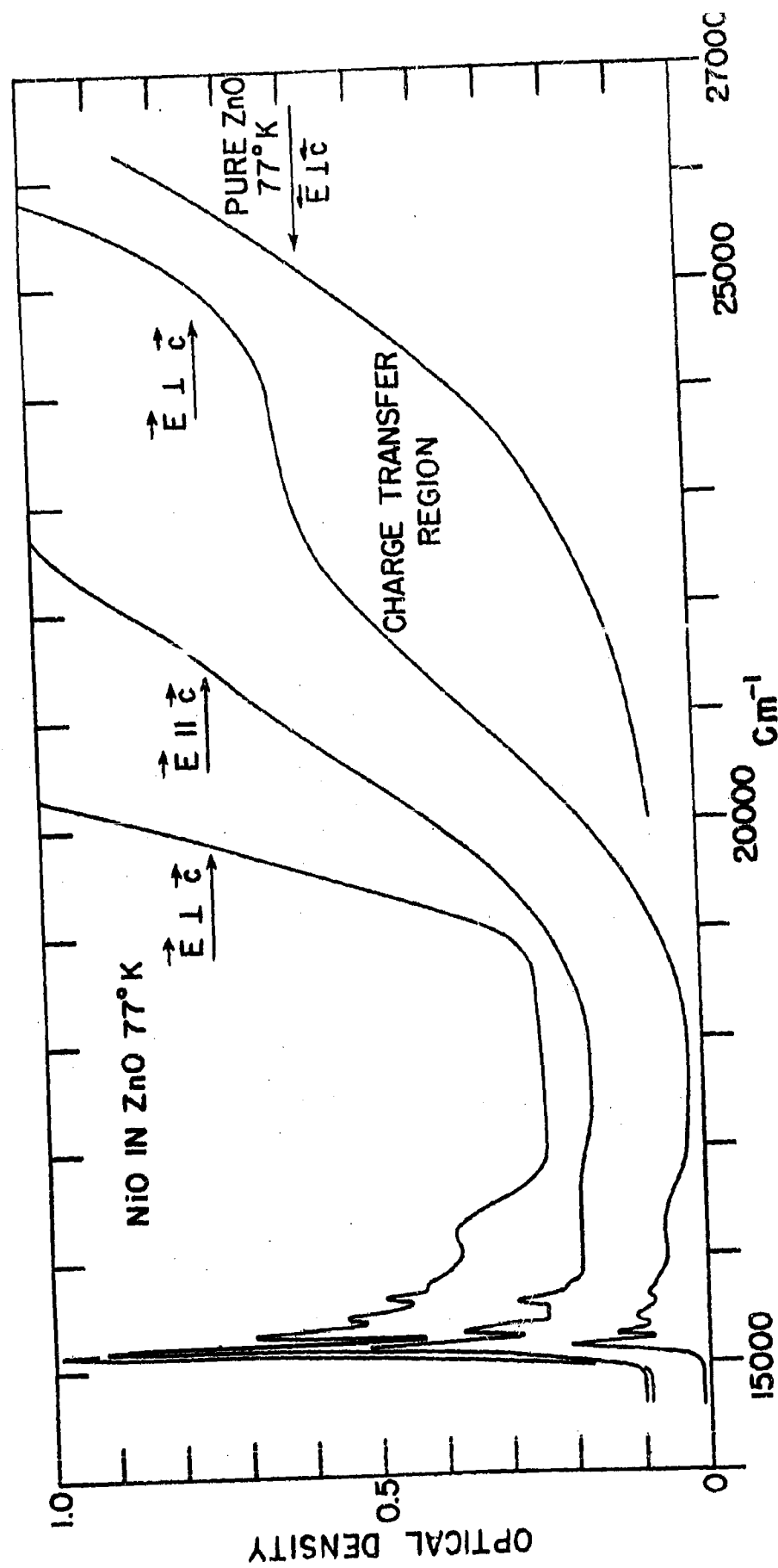


Figure 1d

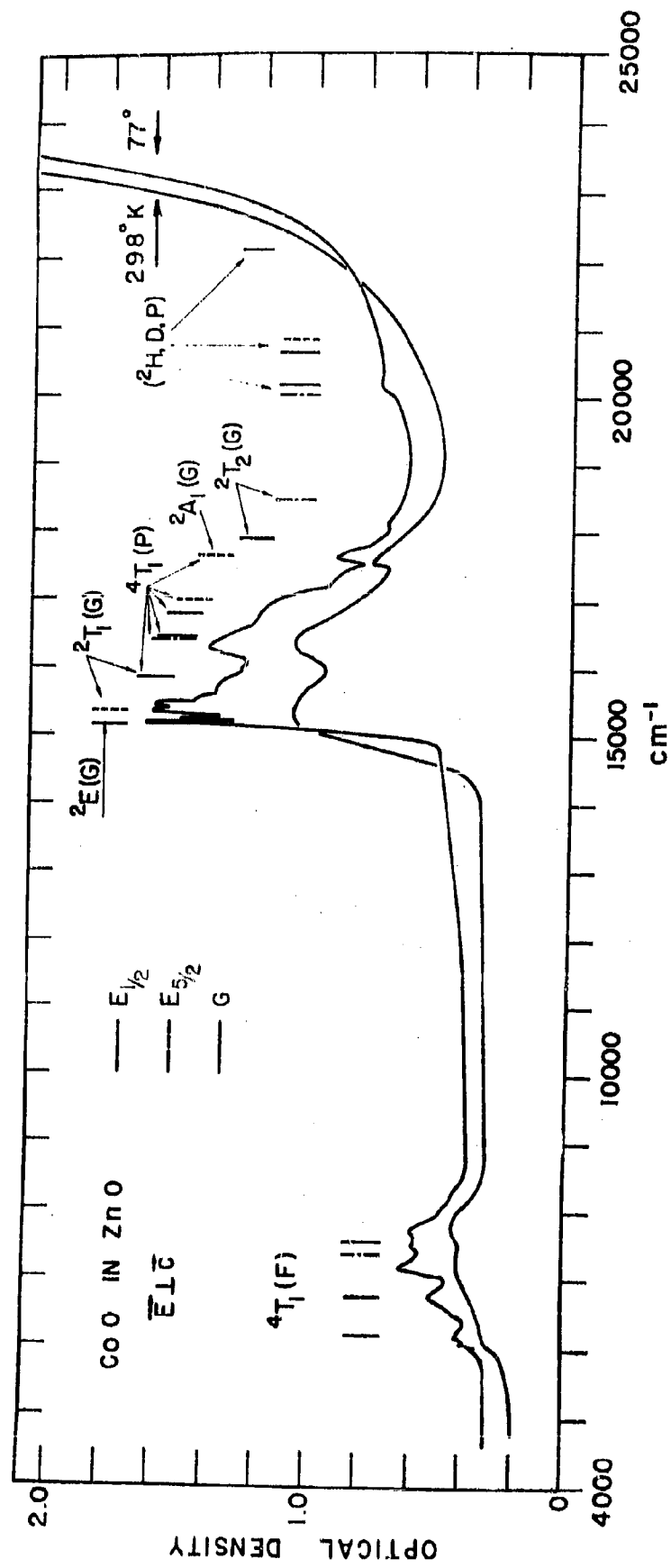


Figure 2a

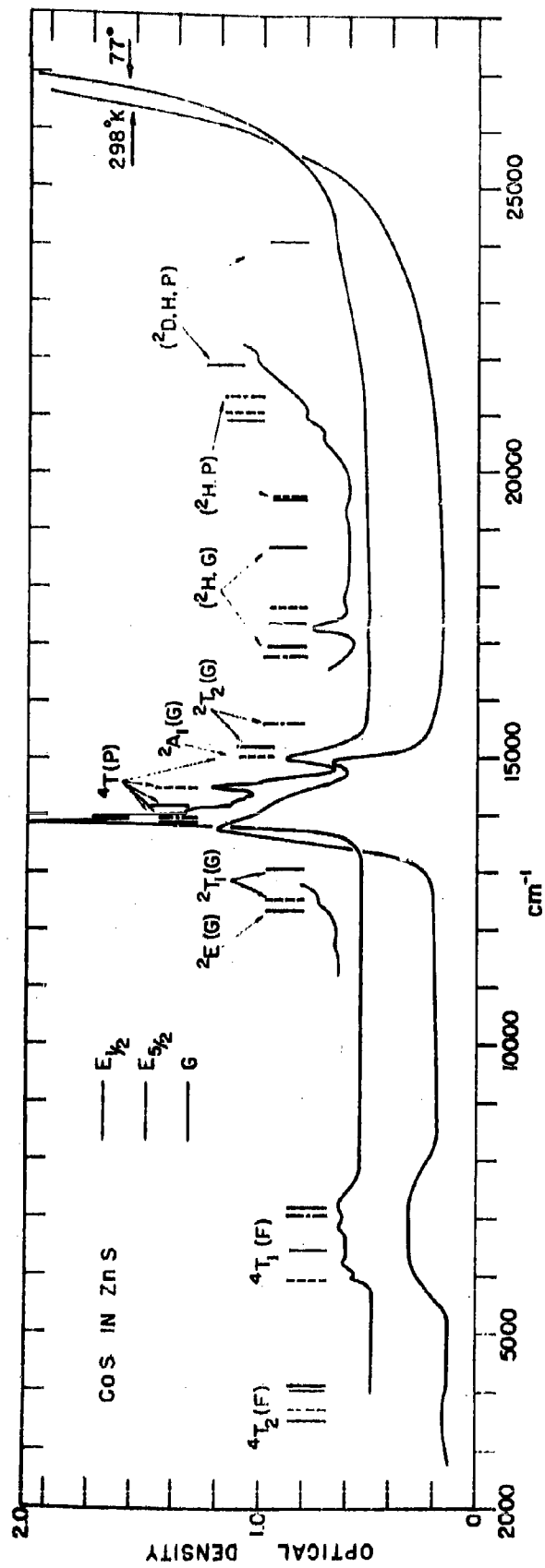


Figure 2b

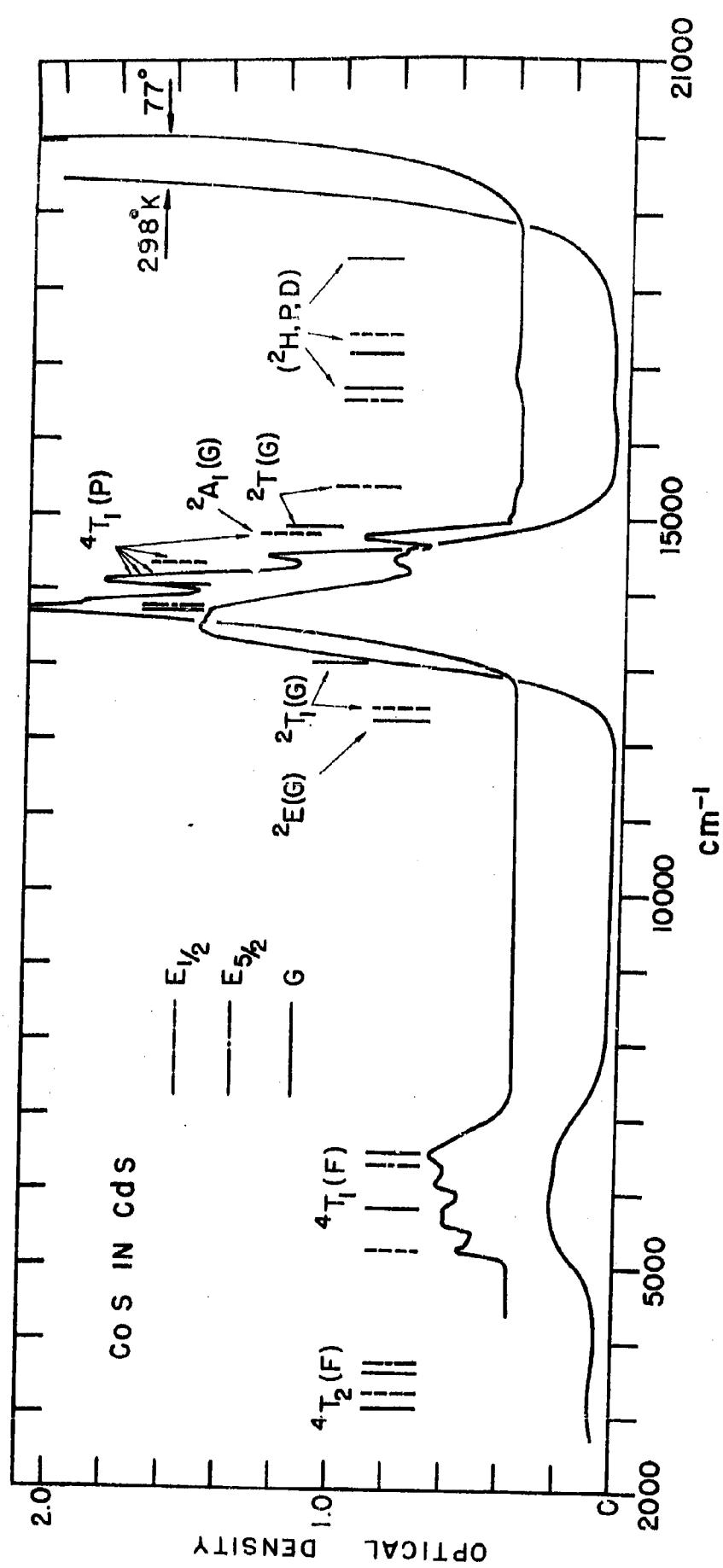


Figure 2c

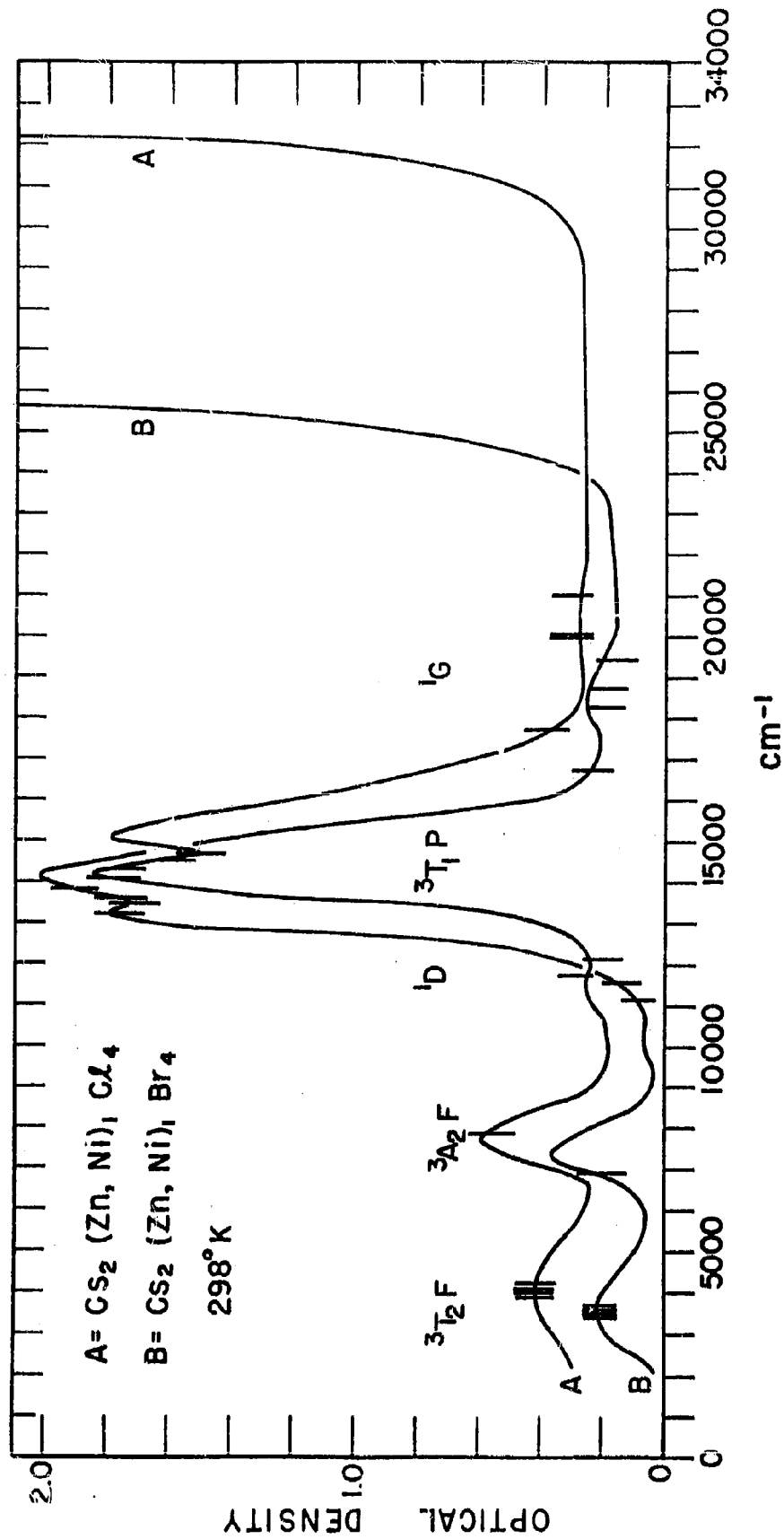
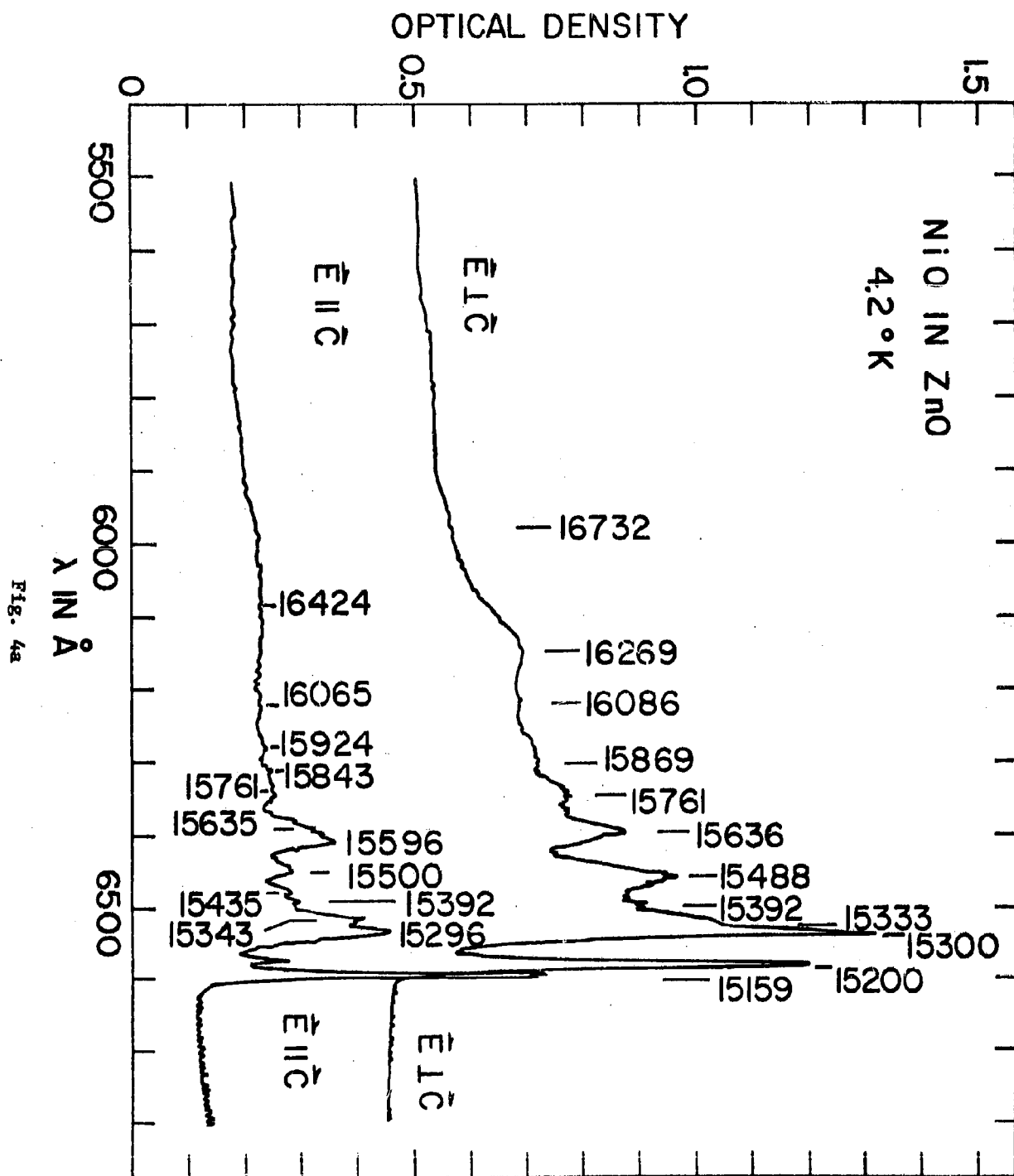


Figure 3





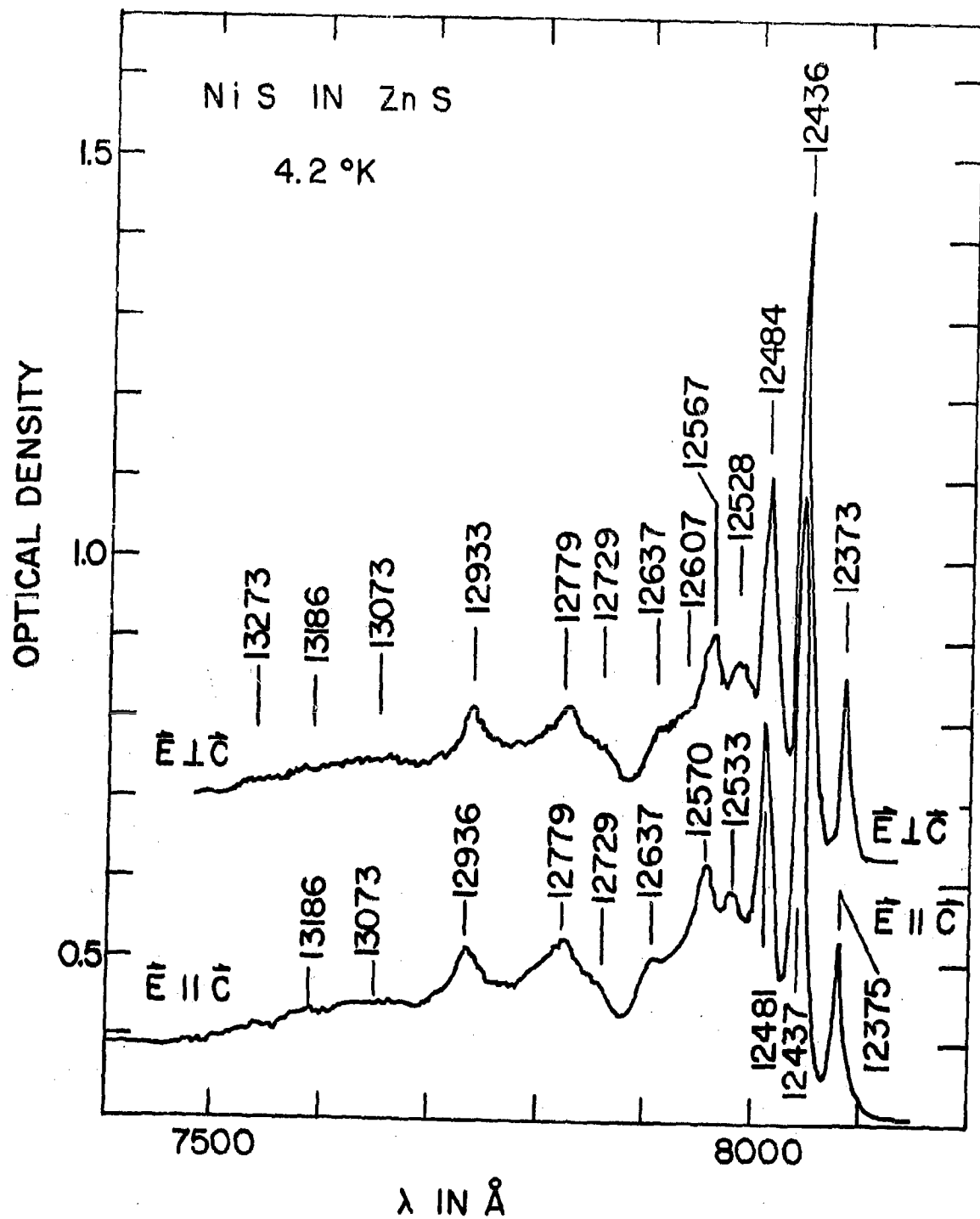


Fig. 4b

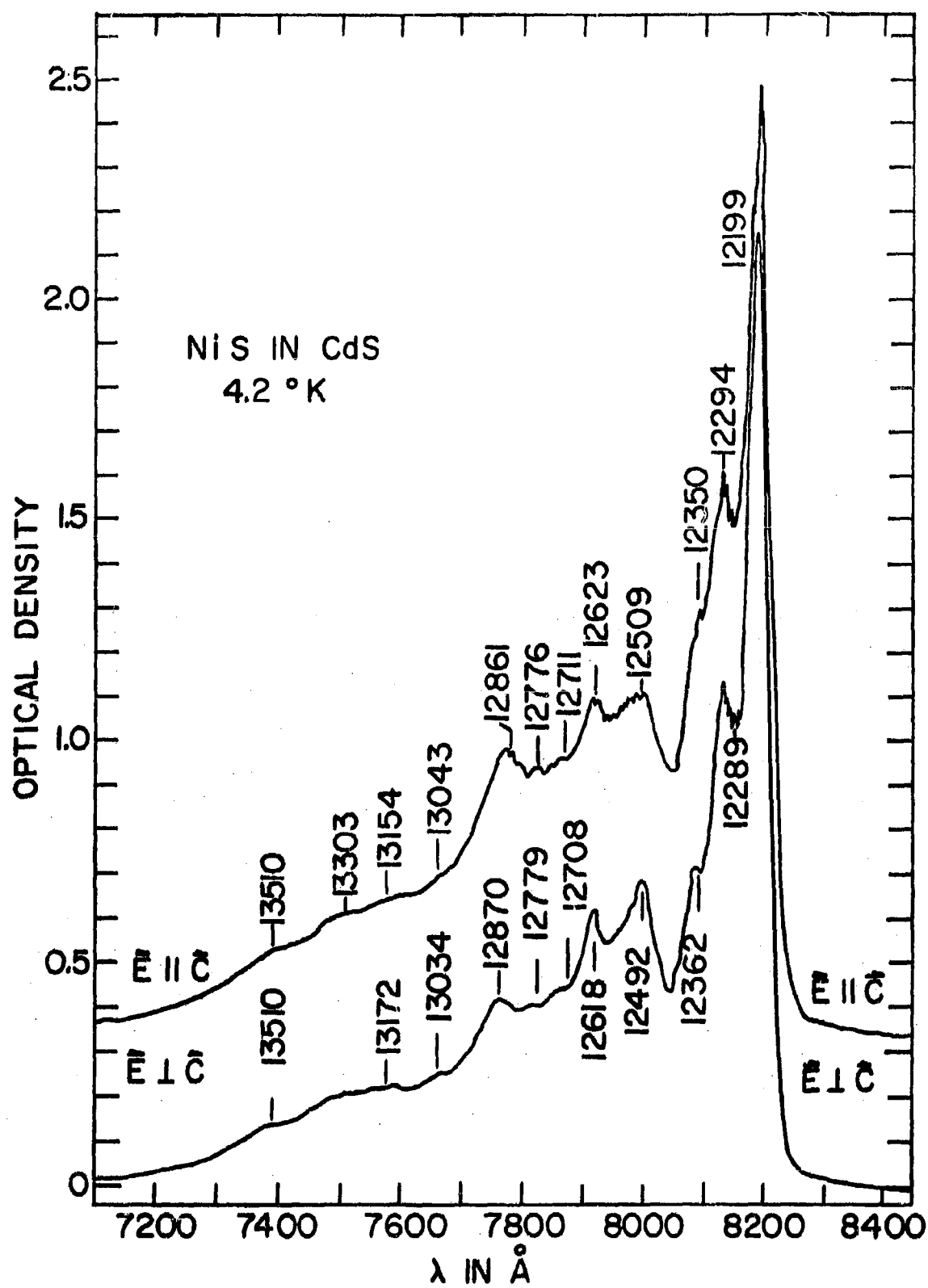


Fig. 4c

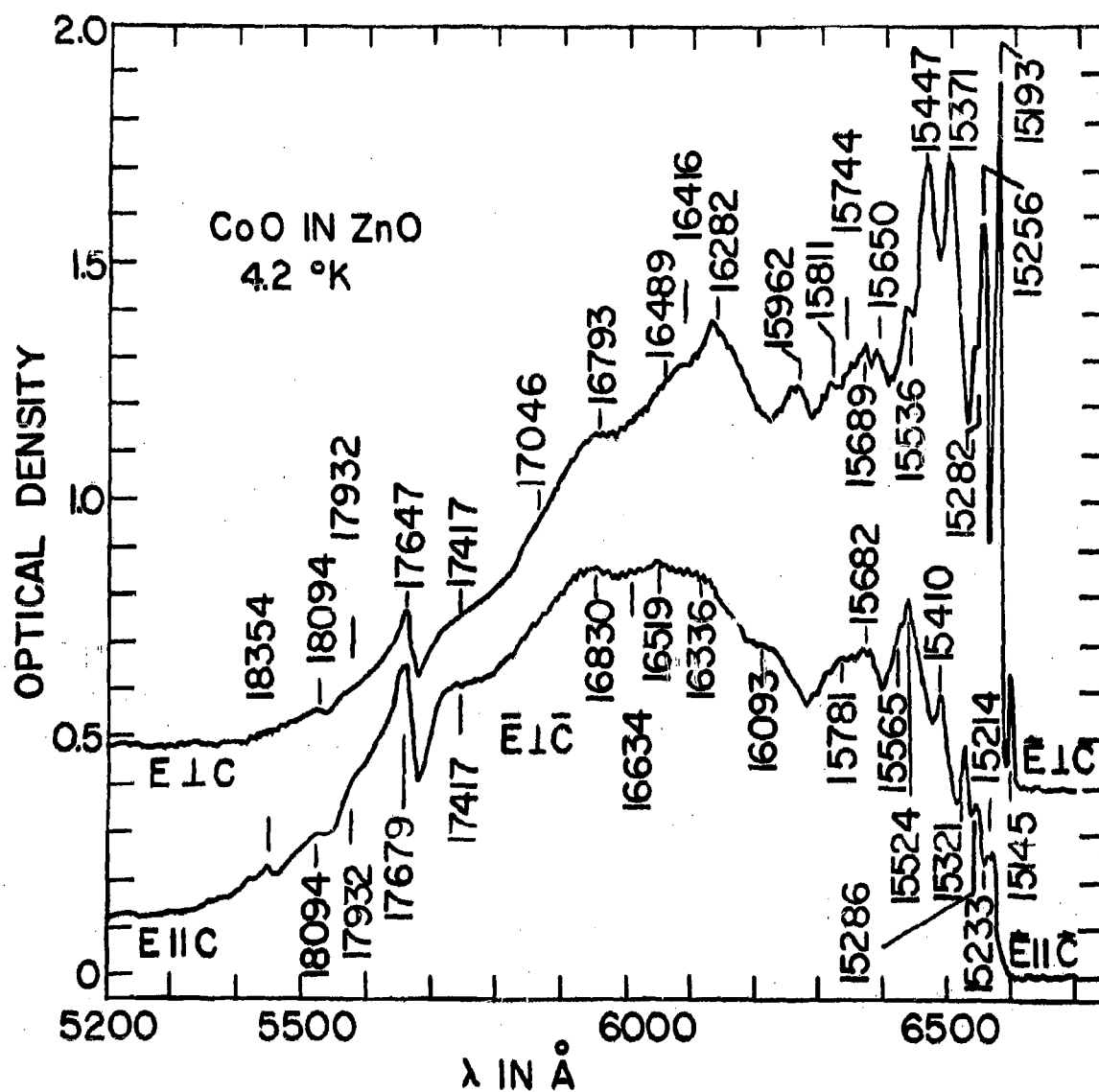


Fig 5a

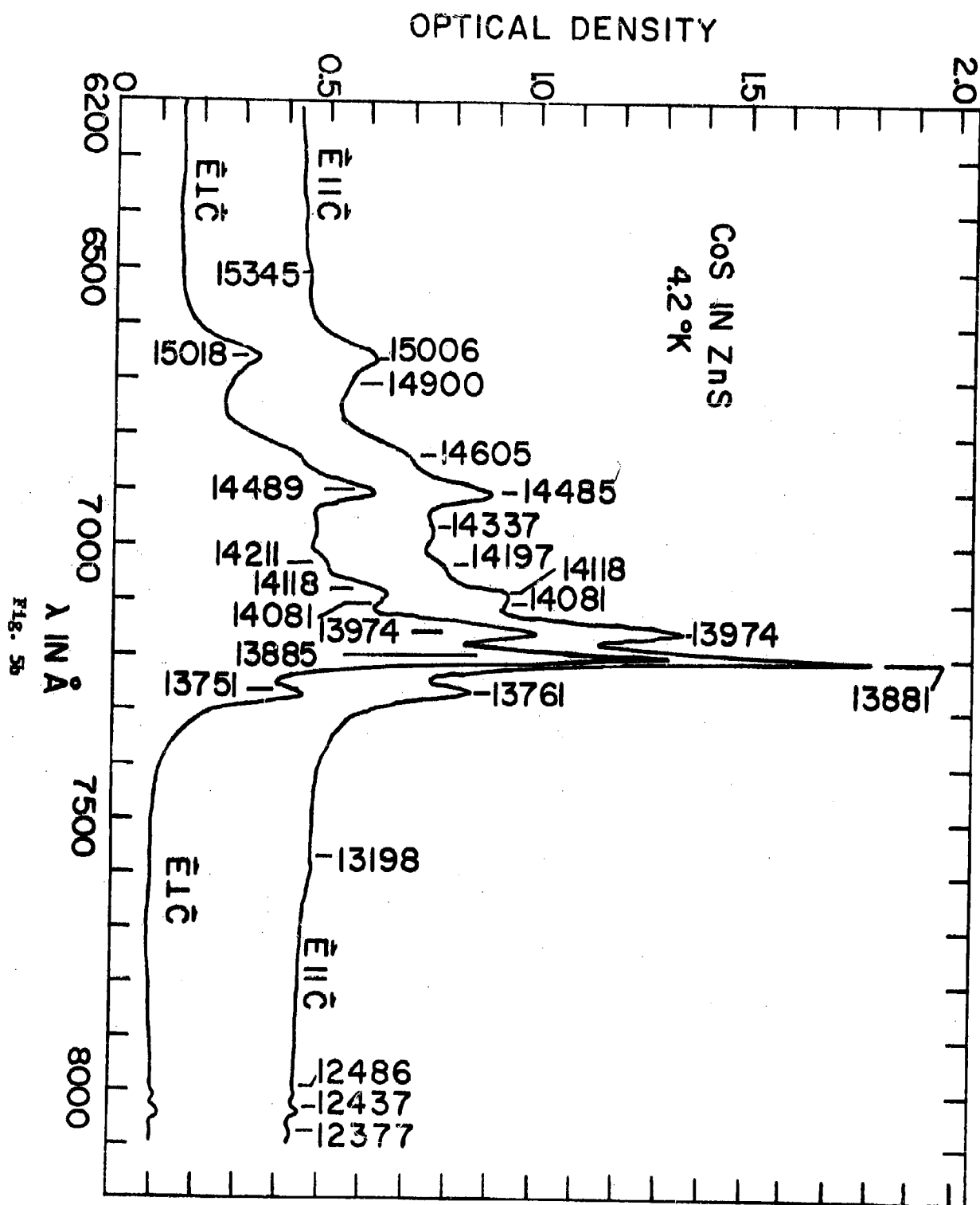
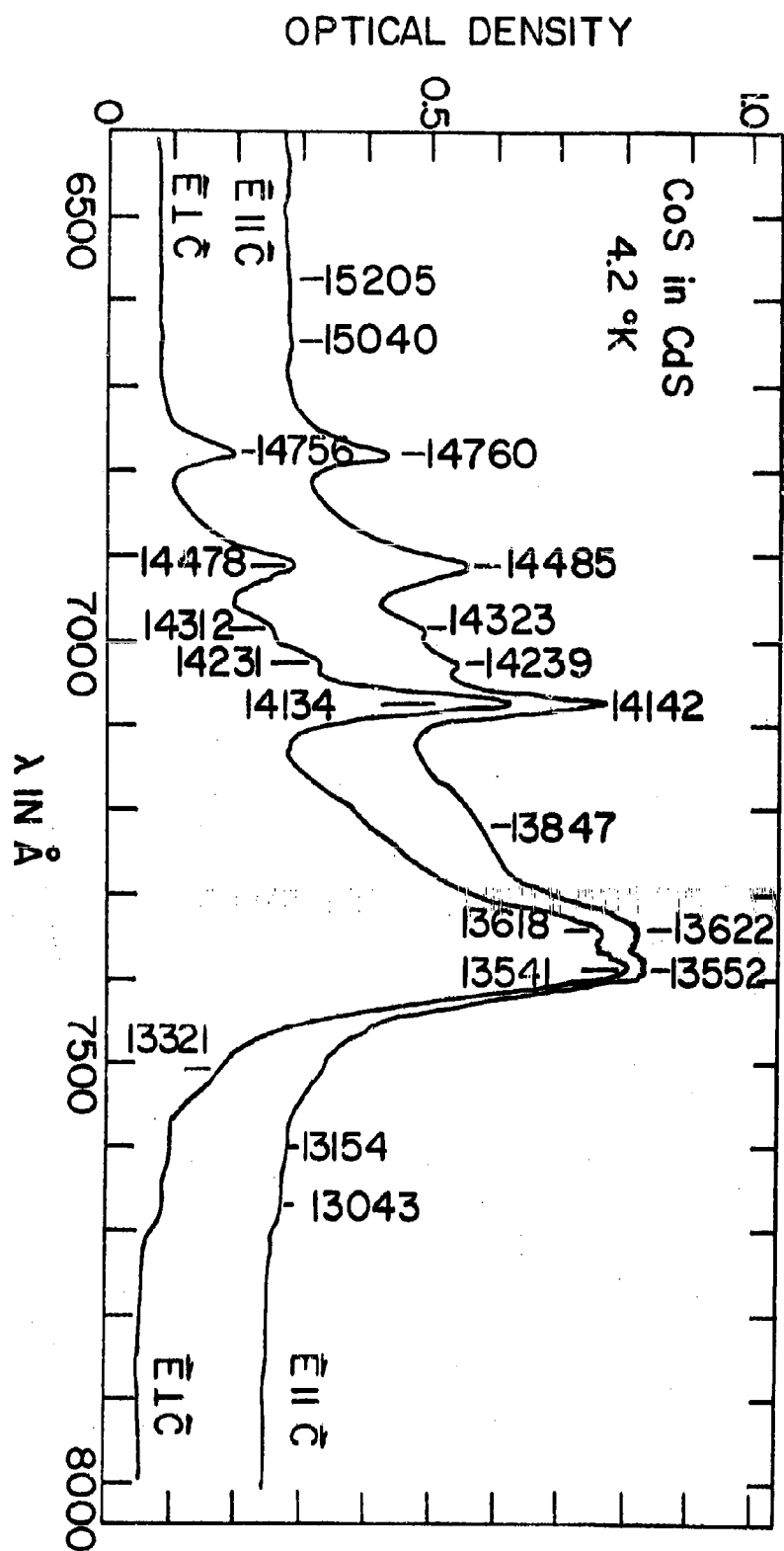


Fig. 5b



**Fig. 5c**

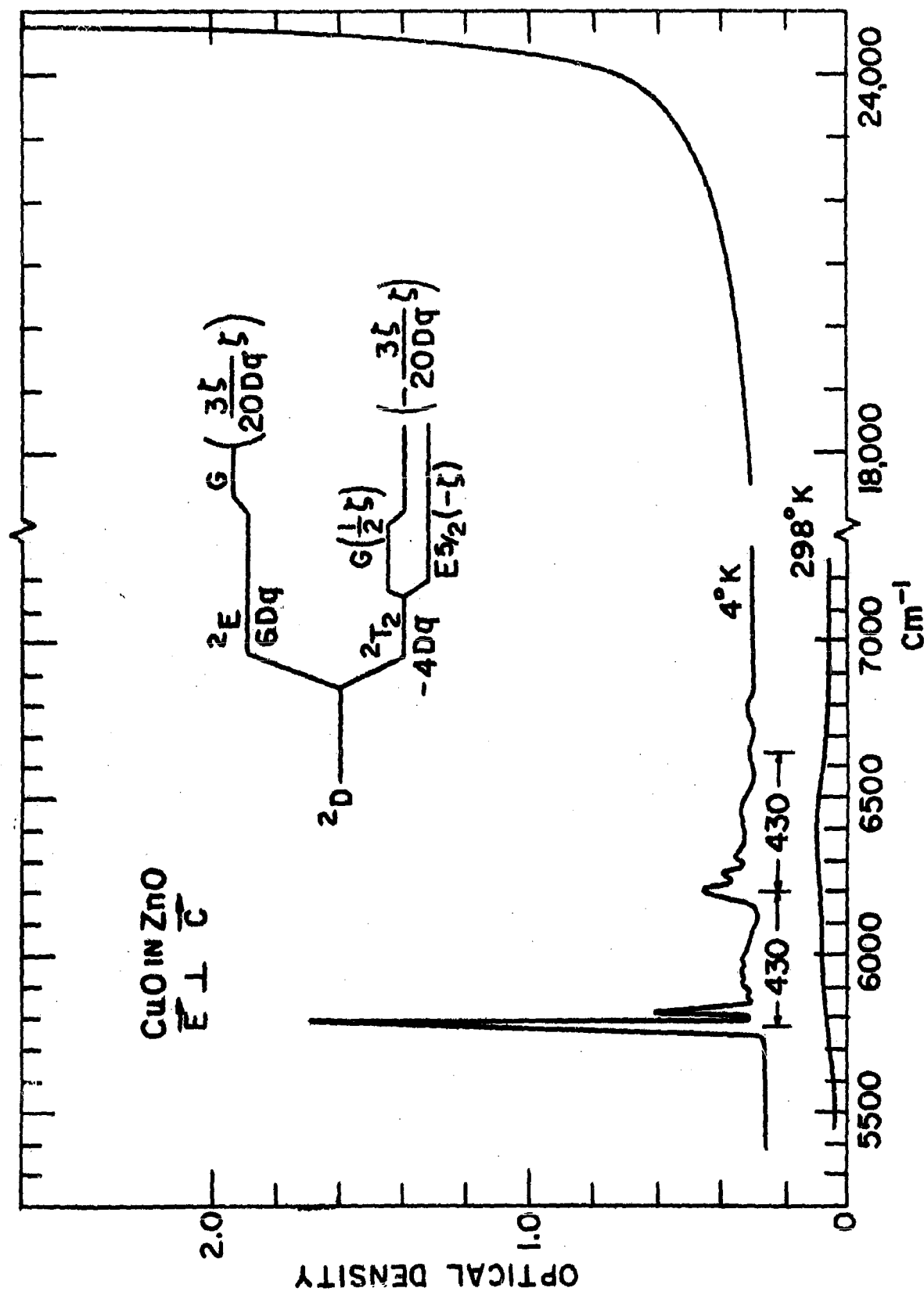


Figure 6a.

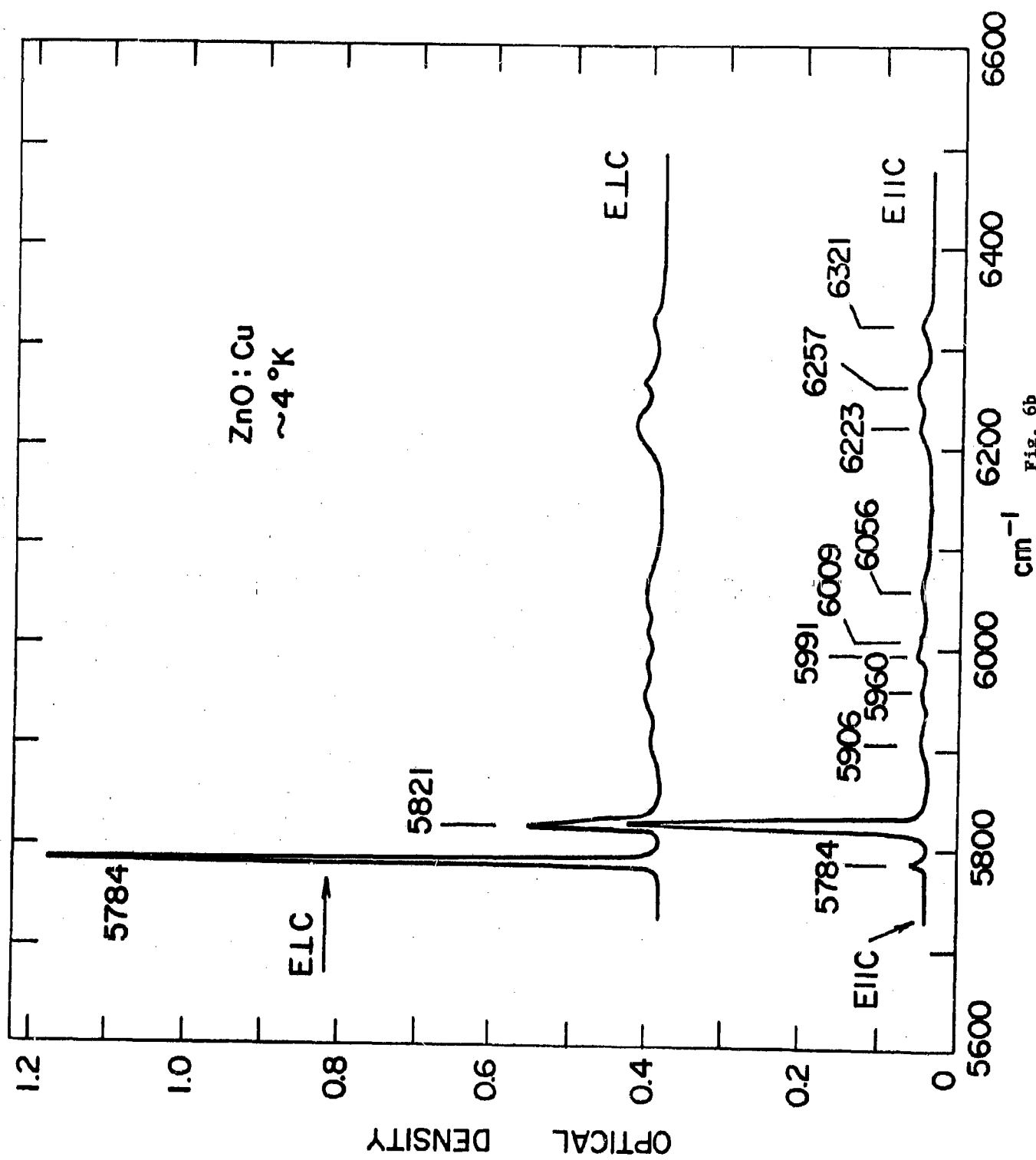


Fig. 6b

# ENERGY LEVEL DIAGRAM FOR $d^8$

$$\text{FREE ION} + (V_C)_{\text{TET.}} + \lambda \vec{L} \cdot \vec{S}$$

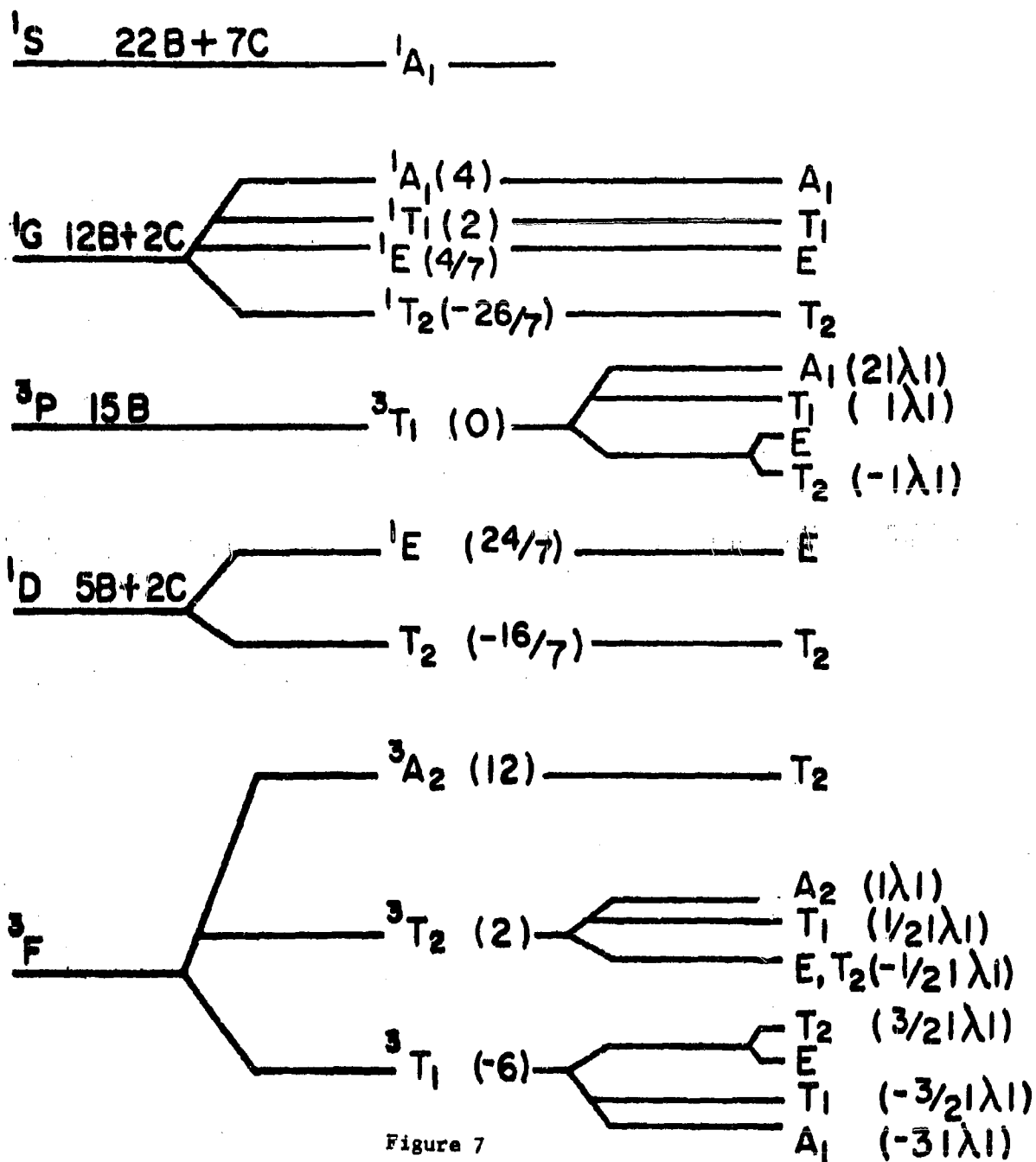


Figure 7



# ENERGY LEVEL DIAGRAM FOR $d^7$

FREE ION  $+(V_c)_{\text{TET.}}$   $+ \lambda \vec{L} \cdot \vec{S}$

${}^2F$   $24B+3C$

${}^2D_m$   $20B+5C$

${}^2H, {}^2P$   $9B+3C$

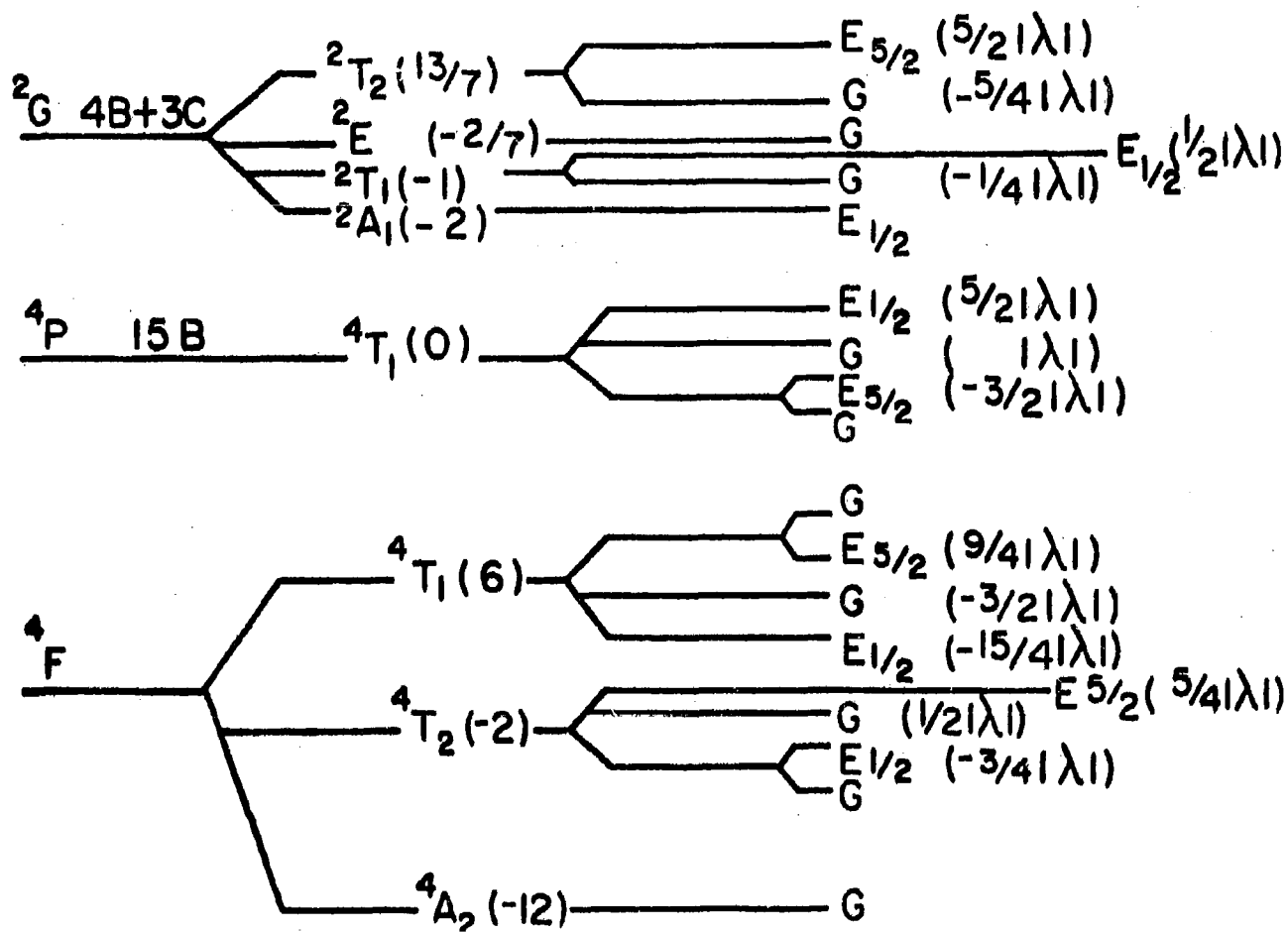


Figure 8

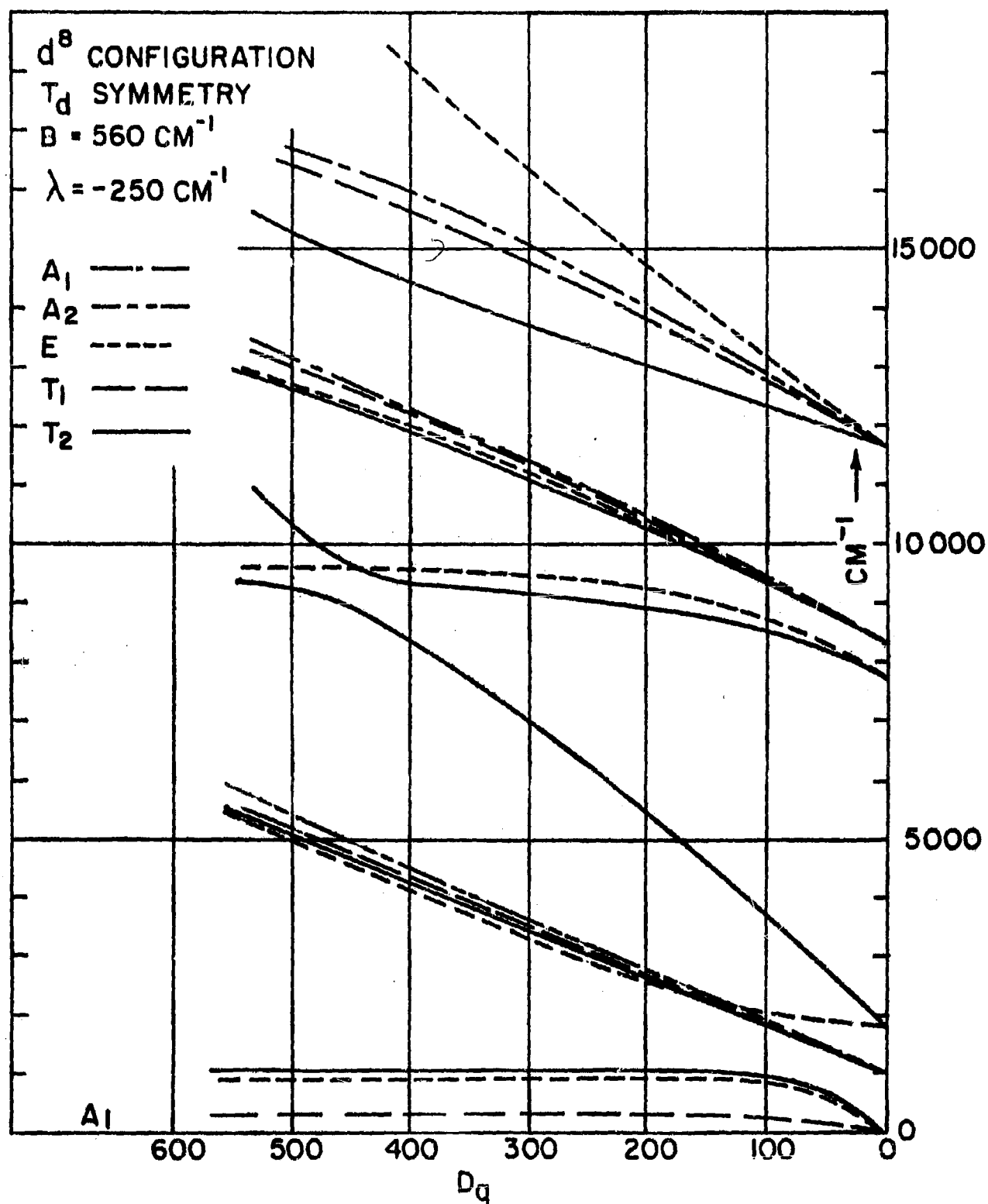


Figure 9

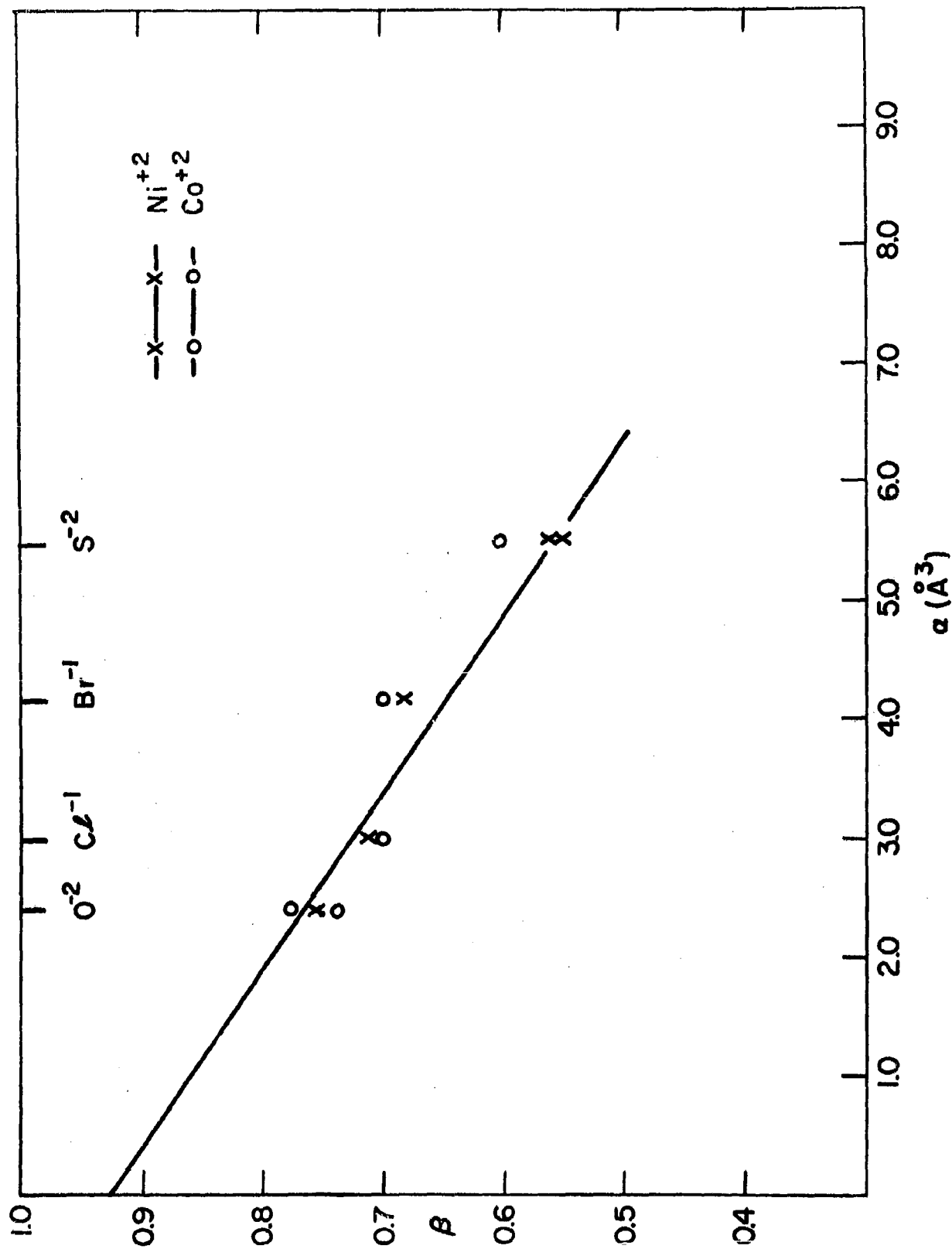


Figure 10

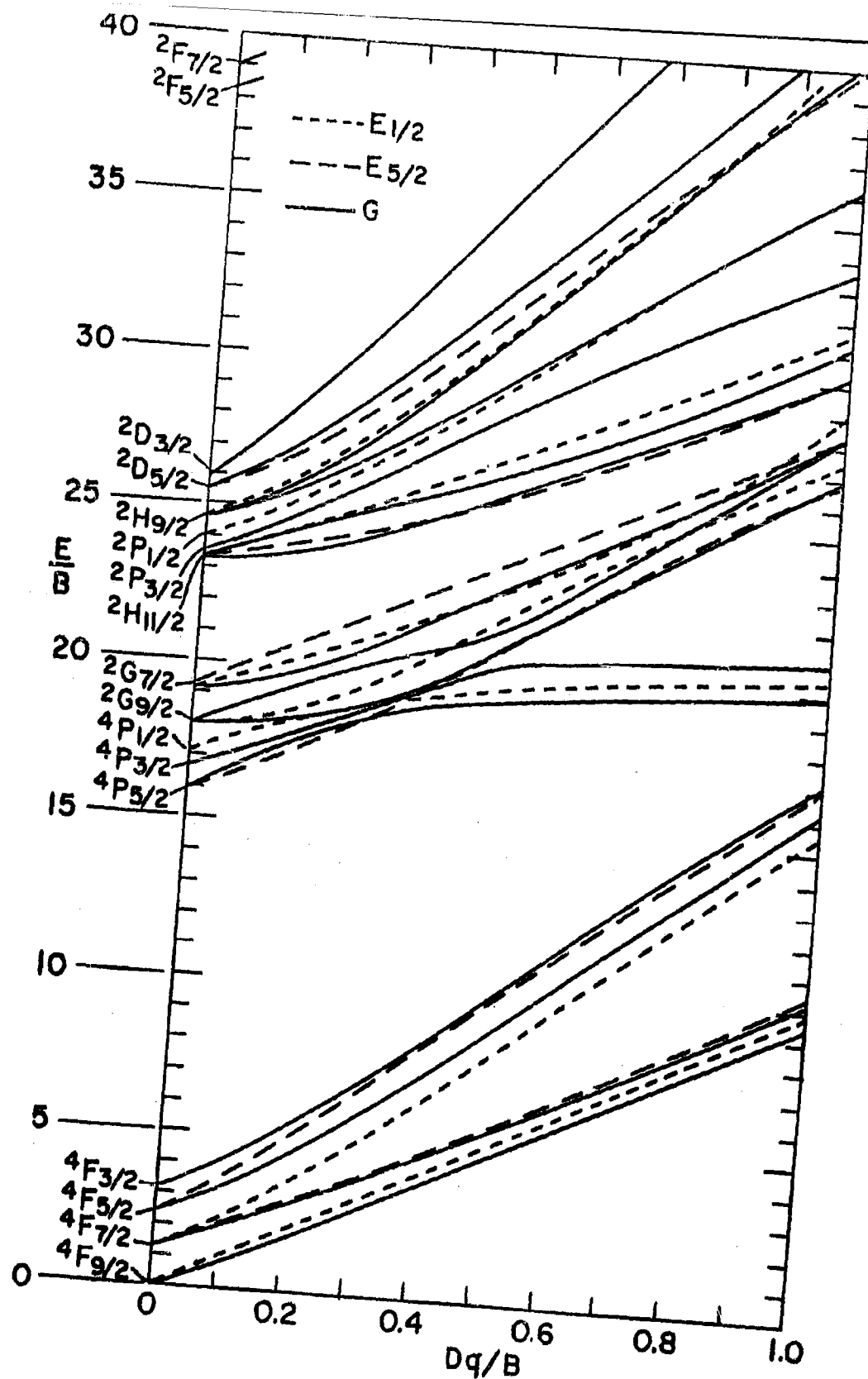


Figure 11

ENERGY LEVEL DIAGRAM FOR  $d^7$  IN A TETRAHEDRAL CRYSTAL FIELD WITH  $\frac{\lambda}{B} = -0.30$

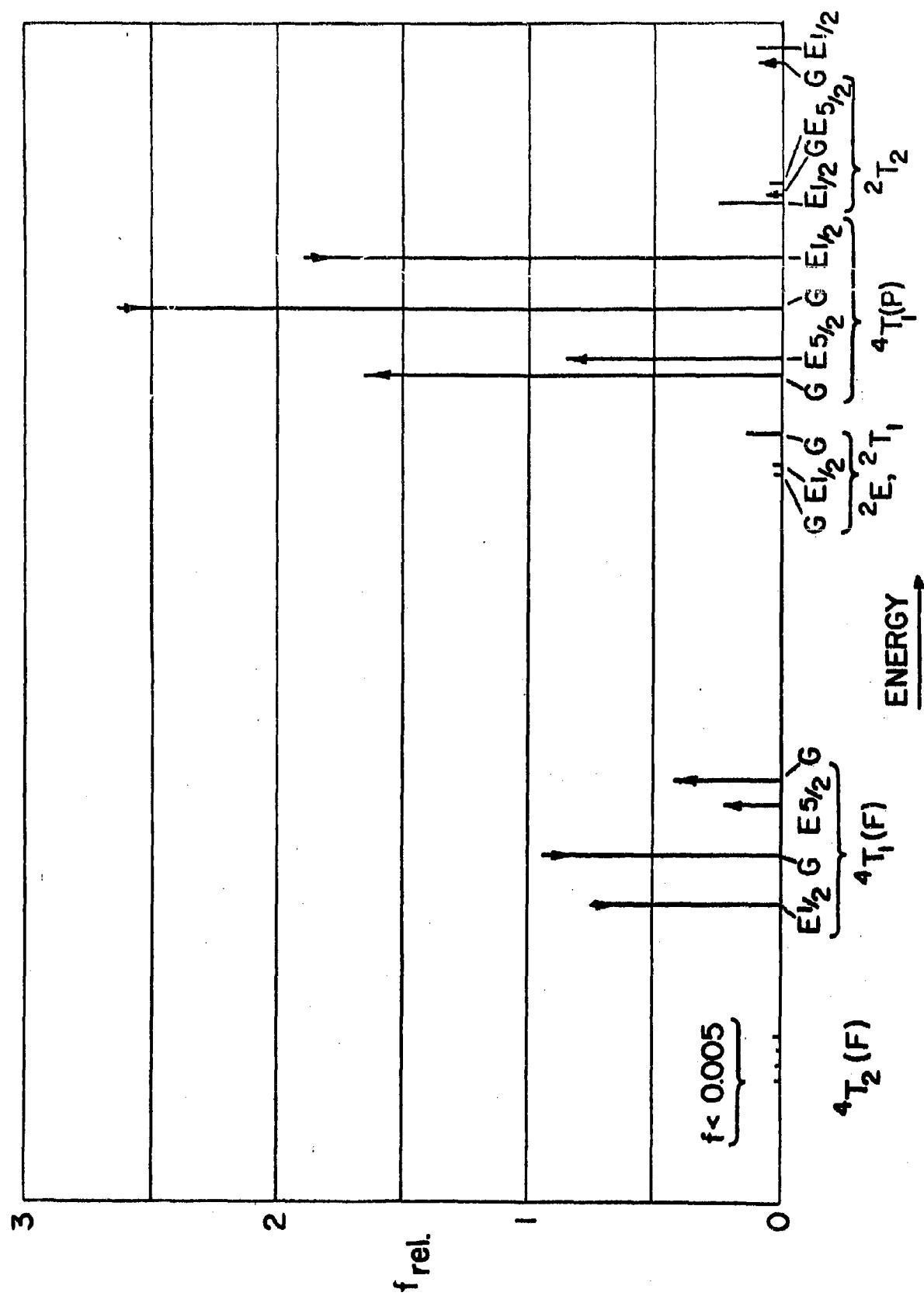


Figure 12

Appendix I. Evaluation of the matrix elements of electrostatic, spin-orbit, and cubic crystal field potentials for the configurations  $d^3$  and  $d^7$ .

The basis functions used for the calculations are those appropriate to the SLJM scheme. The relative phases are those specified by Condon and Shortley<sup>20</sup>, and are determined according to Eq. A1.

$$|SLJM\rangle = \sum_{M_S + M_L = M} \langle SLM_S M_L | JM \rangle |SLM_S M_L\rangle \quad (A1)$$

where  $\langle SLM_S M_L | JM \rangle$  is the Clebsch-Gordon coefficient. The phases of the  $|SLM_S M_L\rangle$  functions are fixed relative to the  $|SLSL\rangle$  function for each SL term according to the method of Gray and Wills by the use of the lowering operators  $L_x - iL_y$  and  $S_x - iS_y$ . The phase of each state with  $M_S = S$  and  $M_L = L$  is the same as that given by Condon and Shortley<sup>20</sup> who did not, however, specify the  $^2P$  state. This is specified by taking

$$|\frac{1}{2} \frac{1}{2} 1\rangle = \left(\frac{1}{890}\right)^{1/2} \left\{ 6(2^- 1^+ - 2^+) + 6(2^+ 1^- - 2^-) - 12(2^+ 1^+ - 1^-) - 5\sqrt{6}(2^- 0^+ - 1^+) \right. \\ \left. + \sqrt{6}(2^+ 0^- - 1^+) + 4\sqrt{6}(2^+ 0^+ - 1^-) - 9(1^+ 1^- - 1) - 9(1^+ 0^+ 0^-) \right\}$$

where the terms in parentheses stand for the Slater determinant product functions with quantum numbers  $m_L$  and  $m_S$ ;  $\prod_1^m m_L^S(1)$ . Since there are two D terms in the configuration, another classification is needed, which we will call R5. Both spin quartets have R5 = 11;  $^2H$ ,  $^2G$ ,  $^2F$ ,  $b^2D$ ,  $^2P$  have R5 = 21; and  $b^2D$  has R5 = 10, where the terms  $b^2D$  and  $a^2D$  are those given by Condon and Shortley.

The phases of the states of  $\underline{d}^7$  relative to those of  $\underline{d}^3$  are fixed by correlating the three electron function  $\pi_1(m_l^m)$  (i) with the seven electron product function whose three missing pairs of quantum numbers are the negatives of the three pairs in  $\underline{d}^3$ , where the standard order of listing according to Condon and Shortley is used, and the phase of the  $\underline{d}^7$   $LM_L$  state is  $(-1)^{M_L}$  times the phase of the correlated  $\underline{d}^3$   $LM_L$  state.

A. Matrix elements of electrostatic potential, Q.

The matrix elements for the states of the  $\underline{d}^3$  configuration are given below in terms of the Racah parameters.<sup>20</sup>

$$\langle {}^2H \mid Q \mid {}^2H \rangle = 3A - 6B + 3C$$

$$\langle {}^2G \mid Q \mid {}^2G \rangle = 3A - 11B + 3C$$

$$\langle {}^2F \mid Q \mid {}^2F \rangle = 3A + 9B + 3C$$

$$\langle {}^2D(10) \mid Q \mid {}^2D(10) \rangle = 3A + 7B + 7C$$

$$\langle {}^2D(21) \mid Q \mid {}^2D(21) \rangle = 3A + 3B + 3C$$

$$\langle {}^2D(10) \mid Q \mid {}^2D(21) \rangle = 3\sqrt{21} B$$

$$\langle {}^2P \mid Q \mid {}^2P \rangle = 3A - 6B + 3C$$

$$\langle {}^4P \mid Q \mid {}^4P \rangle = 3A$$

$$\langle {}^4F \mid Q \mid {}^4F \rangle = 3A - 15B$$

The matrix elements for the states of  $\underline{d}^7$  are obtained by adding  $18A - 28B + 14C$  to the diagonal matrix elements of the states of  $\underline{d}^3$  above. Since we are only interested in energy differences, it is unnecessary to use different values for the two configurations, and taking the  ${}^4F$  term to be zero, one obtains the electrostatic energy differences for the states of both  $\underline{d}^3$  and  $\underline{d}^7$  shown in Fig. 8.

### B. Matrix elements of $L \cdot S$

The matrix of  $L \cdot S = \sum_i \zeta(r_i) L_{i1} \cdot S_{i1}$  was obtained by direct diagonalization. The matrix of  $L \cdot S$  was calculated for the basis consisting of the nineteen Slater determinant one-electron product functions which have  $M = \sum_{i=1}^3 \{m_{s_i}(i) + m_{l_i}(i)\} = 1/2$ . There are also nineteen SLJ terms and each term has one and only one state with  $M = 1/2$ . The unitary transformation  $S$  which gives the  $|SLJ 1/2\rangle$  functions in terms of the Slater determinant functions was used to transform the matrix of  $L \cdot S$  in the  $m_s m_l$  scheme to the SLJM scheme.

The matrix elements  $\langle A | L \cdot S | B \rangle$  are given below for the states of the  $d^3$  configuration in units of  $\zeta_{3d}$ , the one-electron spin-orbit parameter. The matrix elements for states of the  $d^7$  configuration are the negatives of those for the same states of  $d^3$ . The table is arranged in five columns, each containing ten digits. Columns one and two give the symbols for A and B respectively in the form

$$2S + 1 \mid R \mid L \mid 2J \mid 00.$$

The third column gives the matrix element in decimal form with the sign following the number. This number is also given as the square of the ratio of the prime factors 2, 3, 5, 7, and 11. Column four is the numerator and column five is the denominator. The first two digits of each column give the exponent of the prime factor 2, the next two digits give the exponent of the prime factor 3, and so on. For example, the sixth entry



in the table

0221050900 0221040900 1.6248076~ 0101000001 0000020000

is the matrix element

$$\begin{aligned} \langle \underline{d}^3, {}^2H\ 9/2 \mid \underline{L} \cdot \underline{S} \mid \underline{d}^3, {}^2G\ 9/2 \rangle &= - \langle \underline{d}^7, {}^2H\ 9/2 \mid \underline{L} \cdot \underline{S} \mid \underline{d}^7, {}^2G\ 9/2 \rangle \\ &= - 1.6248076 \zeta = - \left( \frac{2 \cdot 3 \cdot 11}{5^2} \right)^{1/2} \zeta . \end{aligned}$$

C. Matrix elements of the cubic crystal field potential  $V_4$ .

The matrix of  $V_4$  is diagonal only with respect to S in the SLJM scheme, however it is diagonal with respect to  $\Gamma$ , the irreducible representations of the groups  $O_h$  or  $T_d$ , and is independent of  $\chi$ , the degeneracy label. The functions may be classified according to SLJ;  $\Gamma\chi$  and the correct linear combinations of  $\mid \text{SLJM} \rangle$  functions which form a basis transforming under the operations of the groups  $O_h$  or  $T_d$  like the spherical harmonics were obtained by the use of projection operators. The set of operators for each  $\Gamma$ , when applied to the individual  $\mid \text{JM} \rangle$  gives a set of functions which form a basis for the representation

$$P_{ij}^{\Gamma} \mid \text{JM} \rangle = \sum_R \Gamma_{ij}^{*(\Gamma)}(R) \cdot R \mid \text{JM} \rangle \quad (\text{A2})$$

where  $\Gamma_{ij}^{*(\Gamma)}(R)$  is the complex conjugate of the  $ij^{\text{th}}$  element of the transformation matrix of the irreducible representation  $\Gamma$  for the operation R. The expression for the operators applied to the spherical harmonics is given by<sup>31</sup>

$$P_{ij}^{\Gamma} \mid \text{JM} \rangle = \sum_{M'} \left( \sum_R \Gamma_{ij}^{*(\Gamma)}(R) e^{-i(M'\alpha + M\chi)} d_{M'M}^J(\beta) \right) \mid \text{JM}' \rangle \quad (\text{A3})$$

MATRIX ELEMENTS OF  $L \cdot S$  IN UNITS OF THE ONE ELECTRON PARAMETER ZETA FOR STATES OF THE OR  $4^7$  CONFIGURATION

	R5 L2J	R5 L2J		NUMERATOR 2 3 5 711	DENOMINATOR 2 3 5 711
J=11/2					
	221051100	221051100	.5000000		200000000
J=9/2					
	411030900	411030900	1.5000000	2000000	200000000
	411030900	221050900		10000	100000000
	411030900	221040900	1.5811383	2000000	20000
	221050900	221050900	.6000000-	101000001	20000
	221050900	221040900	1.6248076-	2000000	20000
	221040900	221040900	.6000000		
J=7/2					
	411030700	411030700		10000	300000000
	411030700	221040700	.7905692	1000000	300000000
	411030700	221030700	.6123725-	2000000	400000000
	221040700	221040700	.7500000-	1010000	400000000
	221040700	221030700	.9682458		400000000
	221030700	221030700	.2500000-		
J=5/2					
	411030500	411030500	1.1666666-	200	202000000
	411030500	411010500		10000	102000000
	411030500	221030500	.5270461-	100000100	1010000
	411030500	210020500	.9660918	100010000	2000000
	411030500	221020500	1.0540927-		200000000
	411010500	411010500	.5000000		
	411010500	221030500		201000000	10000
	411010500	210020500	1.5491934		
	411010500	221020500			2000000
	221030500	221030500	.3333333	100	1000000
	221030500	210020500	1.5275249-		2000000
	221030500	221020500	.3333333-		200000000
	210020500	210020500	.5000000		201000000
	210020500	221020500	.7637624-	100	202000000
	221020500	221020500	.1666666-		
J=3/2					
	411030300	411030300	2.0000000-	200000000	
	411030300	411010300		1000100	100010000
	411030300	210020300	1.4491376	10000	100000000
	411030300	221020300	1.5811383-		
	411030300	221010300			2000000
	411010300	411010300	.3333333-	100000000	10000
	411010300	210020300	.6324557		
	411010300	221020300		10100	2000000
	411010300	221010300	1.9720266-	2000000	400000000
	210020300	210020300	.7500000-	1000100	400000000
	210020300	221020300	1.1456440	100	300000000
	210020300	221010300	.9354143		400000000
	221020300	221020300	.2500000	3000000	300000000
	221020300	221010300	1.8371172-		2000000
	221010300	221010300	.3333333		
J=1/2					
	411010100	411010100	.8333333-	20000	202000000
	411010100	221010100	1.2472190-	100000100	202000000
	221010100	221010100	.6666666-	200000000	2000000

where  $\alpha\beta\gamma$  are the Eulerian angles for the rotation  $R(\alpha\beta\gamma)$ .

For the sake of completeness, we list the symmetry functions obtained in this way for the half-integral values of  $J$  up to  $11/2$ , the maximum needed for the configurations  $d^3$  or  $d^7$ . We only list the function for positive  $\gamma$ , where  $\gamma = \pm 1/2$  for  $E_{1/2}$ ,  $\gamma = \pm 1/2$  for  $E_{5/2}$ , and  $\gamma = \pm 1/2, \pm 3/2$  for  $G$ . The functions for negative  $\gamma$  are related to those for positive  $\gamma$  as follows: change the sign of the  $M$  values and multiply the function by  $(-1)^{(2J-1)/2}$  for  $\Gamma = E_{1/2}$  and  $E_{5/2}$ , change the sign of the  $M$  values and multiply the function by  $(-1)^{(2J+1)/2}$  for  $\Gamma = G$ . The axis system is oriented so that  $x$ ,  $y$ , and  $z$  are parallel to the two-fold axes of the groups.

J	Symmetry function $\sum C_M (J \Gamma_1 \gamma_j)  J, M\rangle$	$\gamma$	Representation in $O_h$ or $T_d$	
J = 1/2	$ 1/2, 1/2\rangle$	1/2	$E_{1/2}$	
J = 3/2	$ 3/2, 3/2\rangle$	3/2	}	G
	$ 3/2, 1/2\rangle$	1/2		
J = 5/2	$\frac{1}{\sqrt{6}} \{-\sqrt{5}  5/2, -3/2\rangle +  5/2, 5/2\rangle\}$	1/2	}	$E_{5/2}$
	$\frac{1}{\sqrt{6}} \{\sqrt{5}  5/2, -5/2\rangle +  5/2, 3/2\rangle\}$	3/2		G
	$-  5/2, 1/2\rangle$	1/2		
J = 7/2	$\frac{1}{\sqrt{12}} \{\sqrt{3}  7/2, -7/2\rangle + \sqrt{7}  7/2, 1/2\rangle\}$	1/2	}	$E_{1/2}$
	$\frac{1}{2} \{-  7/2, -3/2\rangle + \sqrt{3}  7/2, 5/2\rangle\}$	1/2		$E_{5/2}$
	$\frac{1}{2} \{  7/2, -5/2\rangle + \sqrt{3}  7/2, 3/2\rangle\}$	3/2		
	$\frac{1}{\sqrt{12}} \{\sqrt{7}  7/2, -7/2\rangle - \sqrt{5}  7/2, 1/2\rangle\}$	1/2		G

J	Symmetry function	A1-7
J = 9/2	$\frac{1}{\sqrt{24}} \left\{ \begin{aligned} & 9/2, -7/2\rangle + \sqrt{14}  9/2, 1/2\rangle + 3  9/2, 9/2\rangle \\ & 9/2, 3/2\rangle \end{aligned} \right\}$	$\begin{matrix} \delta & \Gamma_1 \\ 1/2 & E_{1/2} \\ 3/2 & \\ 1/2 & \end{matrix} \left. \vphantom{\begin{matrix} \delta \\ 1/2 \\ 3/2 \\ 1/2 \end{matrix}} \right\} G-1$
	$\frac{1}{4} \left\{ \begin{aligned} &\sqrt{7}  9/2, -7/2\rangle + \sqrt{2}  9/2, 1/2\rangle - \sqrt{7}  9/2, 9/2\rangle \\ & 9/2, -5/2\rangle \end{aligned} \right\}$	$\begin{matrix} 3/2 \\ 1/2 \end{matrix} \left. \vphantom{\begin{matrix} 3/2 \\ 1/2 \end{matrix}} \right\} G-2$
	$\frac{1}{\sqrt{48}} \left\{ \begin{aligned} &-5  9/2, -7/2\rangle + \sqrt{14}  9/2, 1/2\rangle - 3  9/2, 9/2\rangle \\ & 9/2, -5/2\rangle \end{aligned} \right\}$	$\begin{matrix} 3/2 \\ 1/2 \end{matrix} \left. \vphantom{\begin{matrix} 3/2 \\ 1/2 \end{matrix}} \right\} G-2$
J = 11/2	$\frac{1}{\sqrt{48}} \left\{ \begin{aligned} &-\sqrt{35}  11/2, -7/2\rangle + \sqrt{6}  11/2, 1/2\rangle - \sqrt{7}  11/2, 9/2\rangle \\ & 11/2, -5/2\rangle \end{aligned} \right\}$	$\begin{matrix} 1/2 & E_{1/2} \\ 3/2 & \\ 1/2 & \end{matrix} \left. \vphantom{\begin{matrix} 1/2 \\ 3/2 \\ 1/2 \end{matrix}} \right\} G-1$
	$\frac{1}{\sqrt{48}} \left\{ \begin{aligned} &-\sqrt{15}  11/2, -11/2\rangle + \sqrt{22}  11/2, -3/2\rangle + \sqrt{11}  11/2, 5/2\rangle \\ & 11/2, -5/2\rangle \end{aligned} \right\}$	$\begin{matrix} 1/2 & E_{3/2} \\ 3/2 & \\ 1/2 & \end{matrix} \left. \vphantom{\begin{matrix} 1/2 \\ 3/2 \\ 1/2 \end{matrix}} \right\} G-1$
	$\frac{1}{\sqrt{624}} \left\{ \begin{aligned} &-11  11/2, -5/2\rangle + 13\sqrt{2}  11/2, 3/2\rangle + \sqrt{165}  11/2, 11/2\rangle \\ & 11/2, -7/2\rangle \end{aligned} \right\}$	$\begin{matrix} 3/2 \\ 1/2 \end{matrix} \left. \vphantom{\begin{matrix} 3/2 \\ 1/2 \end{matrix}} \right\} G-1$
	$\frac{1}{\sqrt{208}} \left\{ \begin{aligned} &-\sqrt{3}  11/2, -7/2\rangle + \sqrt{70}  11/2, 1/2\rangle + 3\sqrt{15}  11/2, 9/2\rangle \\ & 11/2, -5/2\rangle \end{aligned} \right\}$	$\begin{matrix} 3/2 \\ 1/2 \end{matrix} \left. \vphantom{\begin{matrix} 3/2 \\ 1/2 \end{matrix}} \right\} G-2$
	$\frac{1}{\sqrt{78}} \left\{ \begin{aligned} &2\sqrt{5}  11/2, -7/2\rangle + \sqrt{42}  11/2, 1/2\rangle - 4  11/2, 9/2\rangle \\ & 11/2, -5/2\rangle \end{aligned} \right\}$	$\begin{matrix} 3/2 \\ 1/2 \end{matrix} \left. \vphantom{\begin{matrix} 3/2 \\ 1/2 \end{matrix}} \right\} G-2$

These symmetry functions were used to calculate the matrix elements  $\langle SLJ\alpha; \Gamma_i \gamma_j | V_4 | S'L'J'\alpha'; \Gamma'_i \gamma'_j \rangle$  where  $V_4$  given by Eq. (2) is equal to

$$D \left( \frac{21}{\sqrt{14}} \right) \sqrt{\frac{4\pi}{9}} \left\{ \sqrt{14} Y_4^0 + \sqrt{5} Y_4^4 + \sqrt{5} Y_4^{-4} \right\}$$

Since  $\langle SLJ\alpha; \Gamma_i \gamma_j | = \sum_M C_M (J\alpha \Gamma_i \gamma_j) \langle SLJM |$

(A4)

and using Eq. (A1), the matrix element may be expanded to give

$$\delta \Gamma_i \Gamma_i' \delta \gamma_j \gamma_j' \delta S S' \delta M_S M_S' \sum_{M M'} C_M(J \alpha \Gamma_i \gamma_j) C_{M'}(J' \alpha' \Gamma_i' \gamma_j') \langle SLM_S M_L | JM \rangle .$$

$$\langle S'L'M_S'M_L' | J'M' \rangle \langle SLM_L | V_4 | S'L'M_L' \rangle$$

where  $\alpha$  denotes the  $J\Gamma_i$  in case there is more than one combination for some  $J\Gamma_i$ . Using the Wigner-Eckart theorem<sup>31</sup>, we obtain

$$\langle SLM_L | V_4^\mu | S'L'M_L' \rangle = (-1)^{L-M_L} \begin{pmatrix} L & 4 & L' \\ -M_L & \mu & M_L' \end{pmatrix} (SL \parallel V_4 \parallel SL')$$

where  $\mu = 0$  or  $\pm 4$  and

$$\begin{pmatrix} L & 4 & L' \\ -M_L & \mu & M_L' \end{pmatrix} \text{ is Wigner's 3-J coefficient which is related to the}$$

Glebsch-Gordon coefficient and  $(SL \parallel V_4 \parallel SL')$  is the double bar matrix element, which is independent of the values of  $M_L$  and  $M_L'$ . The double bar matrix element was obtained by calculating the matrix element for one particular  $\langle SLM_L | V_4^\mu | S'L'M_L' \rangle$  for each SL term and applying the formula above. The matrix elements in the  $SLJ\alpha; \Gamma$  scheme were then calculated by the use of an IBM 650 program. The double bar matrix elements (twenty non-zero values) were stored in memory and the 3-J coefficients were calculated as needed by using a sub-routine written by S. R. Polo.<sup>31</sup> The coefficients  $C_M(J\alpha\Gamma_i\gamma_i)$  were fed in on punched cards for the values G, 3/2;  $E_{5/2}$ , 1/2, and  $E_{1/2}$ , 1/2.

The tables are presented in six groups, which separate the matrix elements for each of the three irreducible representations for the spin doublets and the spin quartets. There are five columns, each containing ten digits. The first column gives the symbols for  $\langle SLJ\alpha |$  as follows,  $2 \underline{S} + 1 | \underline{R} \underline{S} | \underline{L} | 2 \underline{J} | \underline{\alpha}$ . The second column denotes  $|SL'J'\alpha' \rangle$  in the same format. The third column gives the matrix elements in fixed decimal form in units of (positive)  $Dq$ , with the sign following the number. The next two columns give the matrix element as the square of the prime factors 2 to 47. The first two digits of column four are the exponent of 2, and so on up to 11. Each digit in column five is the exponent of the successive prime numbers 13, 17, 19, 23, 29, 31, 37, 41, 43, and 47. To these exponents must be added (algebraically) the number with modulus 55 given at the head of the group. For example, the first element under the heading spin doublets of G representation is

$$\begin{aligned} \langle {}^2H, J = 11/2, \alpha = 1 | V_4 | {}^2H, J = 11/2, \alpha = 1 \rangle &= -0.2144504 Dq \\ &= - \left( \frac{2^6 \cdot 3^2 \cdot 7^2 \cdot 23^2}{2^2 \cdot 3^4 \cdot 7^2 \cdot 11^2 \cdot 13^2} \right)^{1/2} = - \frac{4 \cdot 23}{3 \cdot 11 \cdot 13} Dq \end{aligned}$$

The matrix elements may be used for the states of  $\underline{d}^3$  and  $\underline{d}^7$  in  $O_h$  or  $T_d$  symmetry by taking  $Dq$  positive for  $\underline{d}^3$  in  $O_h$  and  $\underline{d}^7$  in  $T_d$  and by taking  $Dq$  negative for  $\underline{d}^3$  in  $T_d$  and  $\underline{d}^7$  in  $O_h$ .

MATRIX ELEMENTS OF CUBIC CRYSTAL FIELD POTENTIAL  
IN UNITS OF  $D_q$  FOR STATES OF THE  $d^3$  OR  $d^7$  CONFIGURATION

		$V_c$	PRIME	NUMBERS
			2 3 5 7 11	1112233444 3793917137
SPIN QUARTETS OF $E_{\frac{1}{2}}$ REPRESENTATION			5753555555	5555555555
30040060				
R5 L2J	R5 L2J		200	
411030901	411030901	4.6666665	200010000	
411030901	411030701	2.9814238	101010000	
411030901	411010101	3.6514835		
411030701	411030701	.6666663-	101000000	
411030701	411010101	1.6329923		
411010101	411010101			
SPIN QUARTETS OF $E_{\frac{3}{2}}$ REPRESENTATION			5755555355	5555555555
30040070				
R5 L2J	R5 L2J		2000000	
411030701	411030701	.8571417	202010000	
411030701	411030501	3.8332592-	100010100	
411030701	411010501	2.3904568	2	
411030501	411030501	3.1428566	102000100	
411030501	411010501	3.2071345-		
411010501	411010501			
SPIN QUARTETS OF G REPRESENTATION			5353555355	5555555555
30040080				
R5 L2J	R5 L2J		2000200	
411030901	411030901	.5000000	1040100	
411030901	411030902	2.7277236	901020000	
411030901	411030701	4.6656947	106000000	
411030901	411030501	.9091369	203000200	
411030901	411030301	1.7320508-	202000100	
411030901	411010501	.3779643	202000300	
411030901	411010301	2.6457513-	200	200000000
411030902	411030902	2.8333332-	700020100	
411030902	411030701	3.5634831-	107000100	
411030902	411030501	4.1661903	202000100	
411030902	411030301	.3779643-	203000200	
411030902	411010501	1.7320508	201000200	
411030902	411010301	.5779500-	400000000	
411030701	411030701	.0952365-	605000000	
411030701	411030501	2.9692298	502000002	
411030701	411030301	4.4446712	503000100	
411030701	411010501	1.8516401-	901000100	
411030701	411010301	2.4688536-	202000002	
411030501	411030501	1.5714283-	303000002	
411030501	411030301	3.8491981-	304000100	
411030501	411010501	1.6035672	304000100	
411030501	411010301	1.6035672-		
411030301	411030301		603000100	
411030301	411010501	2.6186145-		
411030301	411010301			
411010501	411010501			
411010501	411010301			
411010301	411010301			

## Crystal Field Matrix Elements (cont.)

SPIN DOUBLETS OF  $E_{\frac{1}{2}}$  REPRESENTATION  
30020060

5551555453

5555555555

R5 L2J	R5 L2J		
221051101	221051101	2.5454544	404000300
221051101	221050901	.6146576-	604010000
221051101	221040901	3.7451267-	307010001
221051101	221040701	4.1871789	107020001
221051101	221030701	1.8018748-	104030001
221051101	221010101		
221050901	221050901	2.5454544-	404000300
221050901	221040901	3.4465616	303000301
221050901	221040701	3.8533730-	103010301
221050901	221030701	.4264012-	104000101
221050901	221010101	5.0142653	404000003
221040901	221040901	1.5555555-	200000302
221040901	221040701	.4969034-	200010102
221040901	221030701	1.1547004-	203000102
221040901	221010101	1.8516401-	305000002
221040701	221040701	1.4444442-	102
221040701	221030701	1.2909942	3010102
221040701	221010101	2.0701966	105010002
221030701	221030701	1.0000000	4000102
221030701	221010101	5.8797472-	104000004
221010101	221010101		

2000000000

SPIN DOUBLETS OF  $E_{\frac{1}{2}}$  REPRESENTATION  
30020070

5553555355

5555555555

R5 L2J	R5 L2J		
221051101	221051101	1.3333330-	400000200
221051101	221040701	1.6035672-	104000100
221051101	221030701	.6900652	101010100
221051101	221030501	.7968186-	300010100
221051101	210020501	7.3029674-	501010200
221051101	221020501	1.5936380	500010100
221040701	221040701	1.8571427	2000000
221040701	221030701	1.6598500-	5010000
221040701	221030501	1.9166296	204010000
221040701	210020501	2.9277001	203010100
221040701	221020501	3.8332593-	404010000
221030701	221030701	1.2857142-	6000000
221030701	221030501	.8247860-	201020000
221030701	210020501	3.7796447	202020100
221030701	221020501	1.6495720	401020000
221030501	221030501	1.0476187-	200000002
221030501	210020501	4.3643578-	401020100
221030501	221020501	1.9047616-	600020000
210020501	210020501	2.0000000-	202000200
210020501	221020501	2.1821787	201020100
221020501	221020501	1.8095237	200000000

2000000000

20000000



SPIN DOUBLETS OF G REPRESENTATION  
30020080

5351555353

3555555555

R5 L2J	R5 L2J			
221051101	221051101	.2144504-	602000200	2000000
221051101	221051102	2.0344721-	704010200	2000000
221051101	221050901	1.0893539-	703020300	1000000000
221051101	221050902	.7131493-	704020200	1000000000
221051101	221040901	6.6374644-	406020301	1000000000
221051101	221040902	4.3452408-	407020201	1000000000
221051101	221040701	.2322628	307000101	1000000000
221051101	221030701	.0999500-	304010101	1000000000
221051101	221030501	.2383946-	1102000101	1000000000
221051101	210020501	2.1849238-	1303000201	1000000000
221051101	210020301	2.3414775	604000401	1000000000
221051101	221020501	.4767892	1302000101	1000000000
221051101	221020301	.5109520-	603000301	1000000000
221051101	221010301	3.7547173	706000301	1000000000
221051102	221051102	.3916082-	804000400	
221051102	221050901	.2214520	407010100	1000000000
221051102	221050902	.5637934	404030200	1000000000
221051102	221040901	1.3493254	110010101	1000000000
221051102	221040902	3.4352145	107030201	1000000000
221051102	221040701	2.5706791-	207010301	1000000000
221051102	221030701	1.1062441	204020301	1000000000
221051102	221030501	.4947272	204010301	1000000000
221051102	210020501	4.5342518	405010401	1000000000
221051102	210020301	1.5866575	506010201	1000000000
221051102	221020501	.9894544-	404010301	1000000000
221051102	221020301	.3462369-	505010101	1000000000
221051102	221010301	2.5443125	608010101	1000000000
221050901	221050901	.2727269-	206000200	2000000000
221050901	221050902	1.4878491-	205040100	2000000000
221050901	221040901	.3692736	105000201	2000000000
221050901	221040902	2.0145572	104040101	2000000000
221050901	221040701	6.0302260-	604020201	2000000000
221050901	221030701	.6672848-	605010001	2000000000
221050901	221030501	.3232862	203000001	4000000000
221050901	210020501	.7977236-	204000301	2000000000
221050901	210020301	5.8620498-	307000301	2000000000
221050901	221020501	.1740775	203000201	2000000000
221050901	221020301	1.2792040	306000201	2000000000
221050901	221010301	2.0889318	605000201	2000000000
221050902	221050902	1.5454543	204000200	2200000000
221050902	221040901	2.0145572	104040101	2000000000
221050902	221040902	2.0925551-	103000201	2200000000
221050902	221040701	4.6056618	403020301	2000000000
221050902	221030701	.5096469	404010101	2000000000
221050902	221030501	1.4814874	204000101	4000000000
221050902	210020501	3.6556307-	205000401	2000000000
221050902	210020301	1.2792040-	306000201	2000000000
221050902	221020501	.7977236	204000301	2000000000
221050902	221020301	.2791451	305000101	2000000000

## Crystal Field Matrix Elements (cont.)

## Spin doublets of G representation (cont.)

221050902	221010301	.4558421	604000101	2000000000
221040901	221040901	.1666643-	2000202	2000000000
221040901	221040902	.9092409-	1040102	2000000000
221040901	221040701	.7776156-	701020002	2000000000
221040901	221030701	1.8070157-	704010002	2000000000
221040901	221030501	.3030445-	106000002	2000000000
221040901	210020501	.9258196	305000102	2000000000
221040901	210020301	2.6457513-	204000302	2000000000
221040901	221020501	1.2121827-	506000002	2000000000
221040901	221020301	3.4641016	405000202	2000000000
221040901	221010301	2.1213203	106000202	2000000000
221040902	221040902	.9444443	202	2200000000
221040902	221040701	.5939133	500020102	2000000000
221040902	221030701	1.3801308	503010102	2000000000
221040902	221030501	1.3887300-	107000102	2000000000
221040902	210020501	4.2426407	306000202	2000000000
221040902	210020301	.5773500-	203000202	2000000000
221040902	221020501	5.5549201-	507000102	2000000000
221040902	221020301	.7559285	404000102	2000000000
221040902	221010301	.4629093	105000102	2000000000
221040701	221040701	.2063468-	200000002	4000000000
221040701	221030701	.1844261	203010002	2000000000
221040701	221030501	1.4846147-	407000002	2000000000
221040701	210020501	2.2677868-	406000102	2000000000
221040701	210020301	3.3946736	303000104	2000000000
221040701	221020501	2.9692298	607000002	2000000000
221040701	221020301	4.4446712-	504000004	2000000000
221040701	221010301	1.7320508	205000202	2000000000
221030701	221030701	.1428565	204000002	2000000000
221030701	221030501	.6388763	404010002	2000000000
221030701	210020501	2.9277001-	405010102	2000000000
221030701	210020301	3.5856857-	306010102	2000000000
221030701	221020501	1.2777531-	604010002	2000000000
221030701	221020301	1.5649214-	505010002	2000000000
221030701	221010301	3.5138210	204010004	2000000000
221030501	221030501	.5238091	202000004	2000000000
221030501	210020501	2.1821787	403020102	2000000000
221030501	210020301	2.6726124	304020102	2000000000
221030501	221020501	.9523807	602020002	2000000000
221030501	221020301	1.1664236	503020002	2000000000
221030501	221010301	4.7142856	206000004	2000000000
210020501	210020501	1.0000000	204000202	2000000000
210020501	210020301	2.4494897-	305000202	2000000000
210020501	221020501	1.0910893-	203020102	2000000000
210020501	221020301	2.6726124	304020102	2000000000
210020501	221010301			
210020301	210020301			
210020301	221020501	2.6726124	304020102	2000000000
210020301	221020301			
210020301	221010301			
221020501	221020501	.9047618-	202000002	2020000000
221020501	221020301	2.2162048	303000002	2020000000
221020501	221010301			
221020301	221020301			
221020301	221010301			
221010301	221010301			

Appendix II. Electric dipole moments for the cubic field basis functions of the configurations  $\underline{d}^8$  and  $\underline{d}^7$ .

A. The  $\underline{d}^8$  configuration

The ground state of  $\text{Ni}^{++}$  in  $T_d$  symmetry has the symmetry  $A_1$ , and is primarily  $|^3F_4; A_1\rangle$  with a small amount (0.1 - 0.15) of  $|^3P_0; A_1\rangle$ . The eight terms required to calculate the intensity of transitions are given below for the  $k$  direction. The common parameter  $Q$  equals  $\omega$  and  $\epsilon = 0$  for the  $p - d$  mixing model, and is equal to  $\gamma A$  with  $\epsilon \neq 0$  for the  $\sigma$ -bonding model.

$$\begin{aligned} \langle ^3F_4; A_1 | P | ^3P_2; T_2 Y_0 \rangle &= -i \frac{2}{5} \left(\frac{1}{30}\right)^{1/2} Q (1 + \epsilon) k \\ \langle ^3F_4; A_1 | P | ^3F_2; T_2 Y_0 \rangle &= -i \frac{38}{15} \left(\frac{1}{105}\right)^{1/2} Q \left(1 - \frac{6}{19}\epsilon\right) k \\ \langle ^3F_4; A_1 | P | ^3F_3; T_2 Y_0 \rangle &= i \frac{4}{3} \left(\frac{1}{3}\right)^{1/2} Q \left(1 - \frac{3}{8}\epsilon\right) k \\ \langle ^3F_4; A_1 | P | ^3F_4; T_2 Y_0 \rangle &= i \frac{16}{5} \left(\frac{1}{21}\right)^{1/2} Q \left(1 - \frac{9}{32}\epsilon\right) k \\ \langle ^3P_0; A_1 | P | ^3P_2; T_2 Y_0 \rangle &= i \frac{4}{5} \left(\frac{1}{30}\right)^{1/2} Q (1 - 3\epsilon) k \\ \langle ^3P_0; A_1 | P | ^3F_2; T_2 Y_0 \rangle &= -i \frac{8}{5} \left(\frac{1}{105}\right)^{1/2} Q (1 - 3\epsilon) k \\ \langle ^3P_0; A_1 | P | ^3F_3; T_2 Y_0 \rangle &= 0 \\ \langle ^3P_0; A_1 | P | ^3F_4; T_2 Y_0 \rangle &= -i \frac{12}{5} \left(\frac{1}{21}\right)^{1/2} Q \left(1 - \frac{2}{3}\epsilon\right) k \end{aligned}$$

In a weak crystal field of  $T_d$  symmetry, the four spin triplet levels have nearly the following configurations.

$${}^3T_1 (P) = \left(\frac{1}{5}\right)^{1/2} \{ t_2^6 e^4 - 2t_2^5 e^3 \}$$

$${}^3A_2 (F) = t_2^6 e^2$$

$${}^3T_2 (F) = t_2^5 e^3$$

$${}^3T_1 (F) = \left(\frac{1}{5}\right)^{1/2} \{ 2 t_2^6 e^4 + t_2^5 e^3 \}$$

The moments for the spin-orbit components in this basis are

$$\langle A_1 - {}^3T_1 (F) | P | T_2 - {}^3T_1 (P) \rangle = -i \frac{2}{5} \left(\frac{1}{30}\right)^{1/2} Q (1 + \epsilon) k_m$$

$$\langle A_1 - {}^3T_1 (F) | P | T_2 - {}^3A_2 (F) \rangle = -i \frac{2}{15} Q k_m$$

$$\langle A_1 - {}^3T_1 (F) | P | T_2 - {}^3T_2 (F) \rangle = i \frac{\sqrt{2}}{3} \left(1 - \frac{3}{10}\epsilon\right) Q k_m$$

$$\langle A_1 - {}^3T_1 (F) | P | T_2 - {}^3T_1 (F) \rangle = -i \frac{26}{5} \left(\frac{1}{30}\right)^{1/2} \left(1 - \frac{9}{26}\epsilon\right) Q k_m$$

$$\langle A_1 - {}^3T_1 (P) | P | T_2 - {}^3T_1 (P) \rangle = i \frac{4}{5} \left(\frac{1}{30}\right)^{1/2} Q \left(1 - \frac{3}{2}\epsilon\right) k_m$$

$$\langle A_1 - {}^3T_1 (P) | P | T_2 - {}^3A_2 (F) \rangle = -i \frac{4}{15} Q k_m$$

$$\langle A_1 - {}^3T_1 (P) | P | T_2 - {}^3T_2 (F) \rangle = -i \frac{7}{15} \sqrt{2} Q \left(1 - \frac{3}{7}\epsilon\right) k_m$$

$$\langle A_1 - {}^3T_1 (P) | P | T_2 - {}^3T_1 (F) \rangle = -i \frac{2}{5} \left(\frac{1}{30}\right)^{1/2} Q (1 + \epsilon) k_m$$

#### B. The $d^7$ configuration

The moments for the spin quartets are given both in the  $|SLJ \alpha, \Gamma \gamma\rangle$  and  $|t_2^m e^n ({}^4\Gamma') \gamma\rangle$  bases. The transformation matrices connecting these two bases are given below.

$E_{1/2}$	$t_2^2 e (^4T_2)$	$t_2^2 e (^4T_1)$	$t_2 e^2 (^4T_1)$
$^4F_{9/2}$	$\frac{1}{\sqrt{6}}$	$-\frac{1}{\sqrt{6}}$	$-\frac{2}{\sqrt{6}}$
$^4F_{7/2}$	$-\frac{5}{\sqrt{30}}$	$-\frac{1}{\sqrt{30}}$	$-\frac{2}{\sqrt{30}}$
$^4P_{1/2}$		$\frac{2}{\sqrt{5}}$	$-\frac{1}{\sqrt{5}}$

$E_{5/2}$	$t_2^2 e (^4T_2)$	$t_2^2 e (^4T_1)$	$t_2 e^2 (^4T_1)$
$^4F_{7/2}$	$-\frac{3}{\sqrt{14}}$	$-\frac{1}{\sqrt{14}}$	$-\frac{2}{\sqrt{14}}$
$^4F_{5/2}$	$-\frac{5}{\sqrt{70}}$	$\frac{3}{\sqrt{70}}$	$\frac{6}{\sqrt{70}}$
$^4P_{5/2}$		$\frac{2}{\sqrt{5}}$	$-\frac{1}{\sqrt{5}}$

G	$t_2^3(^4A_2)$	$t_2^2e(^4T_2)-1$	$t_2^2e(^4T_2)-2$	$t_2^2e(^4T_1)-1$	$t_2^2e(^4T_1)-2$	$t_2e^2(^4T_1)-1$	$t_2e^2(^4T_1)-2$
$^4F_{9/2}-1$	$\frac{3}{2\sqrt{21}}$	$-\frac{9}{4\sqrt{35}}$	$\frac{13}{4\sqrt{35}}$	$\frac{7}{4\sqrt{35}}$	$-\frac{1}{4\sqrt{35}}$	$\frac{7}{2\sqrt{35}}$	$-\frac{1}{2\sqrt{35}}$
$^4F_{9/2}-2$	$-\frac{1}{2}$	$\frac{9}{4\sqrt{15}}$	$\frac{7}{4\sqrt{15}}$	$\frac{1}{4\sqrt{15}}$	$-\frac{3}{4\sqrt{15}}$	$\frac{1}{2\sqrt{15}}$	$-\frac{3}{2\sqrt{15}}$
$^4F_{7/2}$	$-\frac{2}{\sqrt{14}}$	.....	$-\frac{5}{\sqrt{210}}$	$\frac{4}{\sqrt{210}}$	$\frac{3}{\sqrt{210}}$	$\frac{8}{\sqrt{210}}$	$\frac{6}{\sqrt{210}}$
$^4F_{5/2}$	$\sqrt{\frac{3}{14}}$	$\frac{7}{2\sqrt{70}}$	$-\frac{9}{2\sqrt{70}}$	$\frac{3}{2\sqrt{70}}$	$-\frac{3}{2\sqrt{70}}$	$\frac{3}{\sqrt{70}}$	$-\frac{3}{\sqrt{70}}$
$^4F_{3/2}$	$\frac{1}{\sqrt{7}}$	$\frac{6}{\sqrt{105}}$	$\frac{3}{\sqrt{105}}$		$\frac{3}{\sqrt{105}}$		$\frac{6}{\sqrt{105}}$
$^4P_{5/2}$					$\frac{2}{\sqrt{5}}$		$-\frac{1}{\sqrt{5}}$
$^4P_{3/2}$				$\frac{2}{\sqrt{5}}$		$-\frac{1}{\sqrt{5}}$	

Only the moments in the  $k$  direction are given and we have

$$I(G \rightarrow E_{1/2}) = [2M(G, 3/2 \rightarrow E_{1/2}, -1/2)]^2$$

$$I(G \rightarrow E_{5/2}) = [2M(G, -1/2 \rightarrow E_{5/2}, -1/2)]^2$$

$$I(G \rightarrow G) = [2M(G, -1/2 \rightarrow G, 3/2)]^2 + [2M(G, 3/2 \rightarrow G, -1/2)]^2$$

The moments in the  $|t_2^{m_n}(^4\Gamma'); \gamma\rangle$  basis are given below

$G, 3/2$	$E_{1/2}, -1/2$			$G, -1/2$	$E_{5/2}, -1/2$		
	$t_2^2 e(^4T_2)$	$t_2^2 e(^4T_1)$	$t_2^2 e(^4T_1)$		$t_2^2 e(^4T_2)$	$t_2^2 e(^4T_1)$	$t_2^2 e(^4T_1)$
$t_2^3(^4A_2)$		-0.2981		$t_2^3(^4A_2)$		0.2981	
$t_2^2(^4T_2)-1$	0.1155	0.5774	0.1925	$t_2^2 e(^4T_2)-1$	-0.1155	0.3464	0.1155
" -2	-0.2309			" -2	-0.2309	0.4619	0.1540
$t_2^2 e(^4T_1)-1$	0.3464	-0.1155	-0.1155	$t_2^2 e(^4T_1)-1$	-0.5773	0.1155	0.1155
" -2	-0.4619	-0.2309	-0.2309	" -2		0.2309	0.2309
$t_2 e^2(^4T_1)-1$	0.1155	-0.1155	-0.2309	$t_2 e^2(^4T_1)-1$	-0.1925	0.1155	0.2309
" -2	-0.1540	-0.2309	-0.4619	" -2		0.2309	0.4619

$G, -1/2$	$G, 3/2$						
	$t_2^3(^4A_2)$	$t_2^2 e(^4T_2)-1$	$t_2^2 e(^4T_2)-2$	$t_2^2 e(^4T_1)-1$	$t_2^2 e(^4T_1)-2$	$t_2 e^2(^4T_1)-2$	$t_2 e^2(^4T_1)-1$
$t_2^2(^4A_2)$				-0.4	-0.1333		
$t_2^2 e(^4T_2)-1$		0.2066	-0.1549	0.3098	-0.1549	0.1039	-0.0516
" -2		0.3615	0.0516	0.1549	0.5680	0.0516	0.1893
$t_2^2 e(^4T_1)-1$	0.1333	-0.1033	0.4648	0.2066	-0.3615	0.2066	-0.3615
" -2	-0.4	-0.4648	0.1549	0.1549	0.0516	0.1549	0.0516
$t_2^3(^4T_1)-1$		-0.0344	0.1549	0.2066	-0.3615	0.4131	-0.7230
" -2		-0.1549	0.0516	0.1549	0.0516	0.3098	0.1033

Finally, we list the moments in the  $|SLJ\alpha; \Gamma\gamma\rangle$  basis.

The same rules for calculation of the intensity apply. There are four columns of ten digits each. The first column gives  $\langle SLJ\alpha; \Gamma\gamma |$  in the format

$$- \underline{L} | \underline{2J} | - \underline{\alpha} | - \underline{\Gamma_1} | - \underline{\gamma_j}$$

where

$\Gamma_1 = 6$  stands for  $E_{1/2}$  and  $\gamma_j = 1, 2$  stands for  $1/2, -1/2$

$\Gamma_1 = 7$  stands for  $E_{5/2}$  and  $\gamma_j = 1, 2$  stands for  $1/2, -1/2$

$\Gamma_1 = 8$  stands for  $G$  and  $\gamma_1 = 1, 2, 3, 4$  stands for  $3/2, 1/2, -1/2, -3/2$

The second column gives  $|SL'J'\alpha'; \Gamma'\gamma'\rangle$  in the same format. The third and fourth columns give the moments  $M$  and  $M'$  respectively for the total moment expressed in the form

$$\langle 3/2 L J \alpha; \Gamma\gamma | P_m | 3/2 L' J' \alpha'; \Gamma' \gamma' \rangle = (M + \frac{6}{2} M') Q_m, \text{ where}$$

$Q$  has been defined previously.



$d^7$  CONFIGURATION DIPOLE MOMENTS

 $G \rightarrow E_{1/2}$ 

$L2J \alpha \Gamma \gamma$	$L2J \alpha \Gamma \gamma$	M	M'
309010801	309010602	.3320079	.1593638-
309010801	307010602	.1128436	.1247219-
309010801	101010602	.2618614-	.1745743
309020801	309010602	.4260064-	.2434322
309020801	307010602	.3538151-	.1905158
309020801	101010602	.4000000	.2666666-
307010801	309010602	.3903600	.3253000-
307010801	307010602	.0872871	.0581914-
307010801	101010602	.1069044	.0712696-
305010801	309010602	.0488311-	.0450748
305010801	307010602	.4753953-	.3678854
305010801	101010602	.0658360	.1975082-
303010801	309010602	.0828078	.0552052-
303010801	307010602	.2839181	.1728197-
303010801	101010602	.1209486	.3628458-
105010801	309010602	.0983819-	.2529822
105010801	307010602	.3331258	.3394112-
105010801	101010602	.0923760-	.2771281
103010801	309010602	.1264911	.0843274-
103010801	307010602	.2262741-	.3016988
103010801	101010602	.0461880-	.1385640

 $G \rightarrow E_{5/2}$ 

$L2J \alpha \Gamma \gamma$	$L2J \alpha \Gamma \gamma$	M	M'
309010803	307010702	.1999622	.1825741-
309010803	305010702	.4937860	.3265986-
309010803	105010702	.1891221	.0872871-
309020803	307010702	.0664015	.0398409-
309020803	305010702	.0772088	.0712696-
309020803	105010702	.1555555	.4000000-
307010803	307010702	.0141972-	.0851835
307010803	305010702	.3301587	.2476190-
307010803	105010702	.2256872-	.2138089
305010803	307010702	.0811482	.0221312-
305010803	305010702	.1088717-	.1451623
305010803	105010702	.0370327	.0740656
303010803	307010702	.4156136-	.2529822
303010803	305010702	.5576042	.3394112-
303010803	105010702	.3830039	.2418972-
105010803	307010702	.0276026-	.0552052-
105010803	305010702	.0370327	.0740656
105010803	105010702	.0923760	.2771281-
103010803	307010702	.3312314	.4416419-
103010803	305010702	.2756886	.2715738-
103010803	105010702	.0461880	.1385640-

$d^7$  CONFIGURATION DIPOLE MOMENTS

G → G

L2J $\alpha$ $\Gamma$ $\gamma$	L2J $\alpha$ $\Gamma$ $\gamma$	M	M'
309010803	309010801	.3381175	.2397561-
309010803	309020801	.3662335	.3098898-
309010803	307010801	.1656431-	.0752923
309010803	305010801	.1495369	.1199773-
309010803	303010801	.0766651-	.0511101
309010803	105010801	.1886740	.4293960-
309010803	103010801	.1171080-	.0780720
309020803	309010801	.0469530-	.1408590
309020803	309020801	.2151657	.2151657-
309020803	307010801	.0690065	.0230021-
309020803	305010801	.3399761	.2310775-
309020803	303010801	.2342160	.1561440-
309020803	105010801	.1689473	.1788854-
309020803	103010801	.3577708	.2385139-
307010803	309010801	.6876699	.4366954-
307010803	309020801	.2990284	.1610152-
307010803	307010801		.0491807
307010803	305010801	.1888235	.1320344-
307010803	303010801	.5529389-	.3964468
307010803	105010801	.1221789-	.0956182
307010803	103010801	.1912365	.1274910
305010803	309010801	.1043281	.0782460-
305010803	309020801	.2709184	.1673320-
305010803	307010801	.3875851-	.1661079
305010803	305010801	.3408225	.2109853-
305010803	303010801	.4445258-	.3397189
305010803	105010801	.3643546-	.2649851
305010803	103010801	.1269720-	.0331231-
303010803	309010801	.1916629	.1277753-
303010803	309020801	.0585540	.0390359-
303010803	307010801	.3442827	.2295218-
303010803	305010801	.0433683	.1301051-
303010803	303010801	.0354101	.1062303-
303010803	105010801	.0180299	.0540898-
303010803	103010801	.0540898	.1622696-
105010803	309010801	.0975900	.1951800-
105010803	309020801	.0298142	.1788854
105010803	307010801	.1753001	.0956182
105010803	305010801	.3643546-	.2649851
105010803	303010801	.2974942-	.2163594
105010803	105010801	.0206558	.0619677-
105010803	103010801	.0619677	.1859032-
103010803	309010801	.2927700	.1951800-
103010803	309020801	.0894427	.0596284-
103010803	307010801	.1912365-	.1274910
103010803	305010801	.1177711-	.3533135
103010803	303010801	.0540898	.1622696-
103010803	105010801	.1445913-	.4337741
103010803	103010801	.0826236	.2478709-

The Optical Absorption Spectrum of  $\text{NiSiF}_6 \cdot 6\text{H}_2\text{O}$ 

Donald S. McClure

R.C.A. Laboratories, Princeton, N. J.

## ABSTRACT

A detailed study of the visible and near infrared absorption bands of  $\text{NiSiF}_6 \cdot 6\text{H}_2\text{O}$  has revealed many features commonly found in polyatomic molecular spectra. The most important result is the discovery that the excited states are not usually stable in the nearly cubic symmetry characterizing the ground state. This leads to the breadth of the absorption bands. The true electronic origins of many of these bands have been located approximately. The multiplet splittings which appear too large for the known value of the spin-orbit coupling energy, are understood when it is realized that some multiplet components are stable in the cubic configuration and others are not.

## I. INTRODUCTION

The optical absorption of  $\text{NiSiF}_6 \cdot 6\text{H}_2\text{O}$  arises from the  $d^8$  shell of the  $\text{Ni}^{++}$  ion. There is one such ion per unit cell of the rhombohedral lattice. Each  $\text{Ni}^{++}$  is surrounded by six  $\text{H}_2\text{O}$  lying at the corners of an octahedron which is compressed slightly along a 111 cube axis. The  $\text{SiF}_6$  groups and the  $\text{Ni}(\text{H}_2\text{O})_6$  groups are packed as in the  $\text{CsCl}$  structure, but with a 111 trigonal distortion superimposed. The relevant structural data are shown in Table I.

Because of this simple structure the  $\text{NiSiF}_6 \cdot 6\text{H}_2\text{O}$  crystal is especially suitable for a spectral study of the absorption spectrum of  $\text{Ni}^{++}$ . The crystal field is almost cubic, but the small trigonal field provides a useful perturbation to help in identifying spectral features. The orientation of the trigonal axis at the  $\text{Ni}^{++}$  ions coincides with the trigonal axis of the crystal. The substitution of  $\text{D}_2\text{O}$  for  $\text{H}_2\text{O}$  provides another useful variable.

The principal absorption bands in the spectrum have already been identified. Only a few of the singlet levels have not been observed. The purpose of this paper is to report on the fine structure observed throughout the spectrum and to give an interpretation of the band shapes. This leads to a consideration of the effects of Jahn-Teller distortions and other instabilities in excited levels. It is shown in detail how the spectra are modified by the change in shape of the complex upon excitation.

## II. GENERAL DESCRIPTION OF SPECTRA

### a. Energy Levels in the Crystal Field

The energy levels of the  $d^8$  configuration in a cubic crystal field have been given in great detail by Liehr and Ballhausen<sup>(1)</sup>. The ground state in an octahedral field is  $^3A_2$ . The calculated positions of the other levels are shown in Fig. 1, using parameters which best fit the  $\text{NiSiF}_6 \cdot 6\text{H}_2\text{O}$  spectrum at low temperatures. The calculated and experimental level positions are in good agreement, as Fig. 1 shows. The parameters used are:  $Dq = 910 \text{ cm}^{-1}$ ,  $\lambda = 300$ ,  $B = 880$ ,  $C = 3960$  (or  $F_2 = 1446$ ,  $F_4 = 113.2$ ), using the standard notation<sup>(1)</sup>. The positions and identification of individual components of a multiplet are not obvious, but the calculated triplet widths are in approximate agreement with observed band widths. Only in the broad band at  $15,000 \text{ cm}^{-1}$ , the  $^3T_1$  (F) state is gross structure clearly discernable. The width of this structure is appreciably greater than the calculated width.

### b. Band Structure

Some of the most interesting features of the spectrum are the regions of fine structure near the origins of the stronger bands. This structure is observable at  $4.2^\circ\text{K}$  in crystals 2 - 4 mm thick. It has been observed at the origins of  $^3T_1$  (F),  $^1T_2$  (D) and  $^3T_1$  (P). Pappalardo<sup>(2)</sup> has already reported the latter. Figures 2, 3 and 4 show the fine structure of these three regions. The spectra were taken with a Cary 14 spectrophotometer and with a three-meter grating spectrograph. Tracings of the photographic plates showed no more structure than did the Cary records, but the resolution was somewhat better and the wavelength measurements were more accurate. These measurements are given on the figures.

Both normal and deuterated salts showed substantially the same fine structure. The widths of the narrowest lines measured from the plates were  $4\text{ cm}^{-1}$  for the  ${}^3T_1(P)$  and  ${}^3T_1(F)$  bands, and  $1 - 2\text{ cm}^{-1}$  for the  ${}^1T_2(D)$  band. The fine structure is partially polarized; in fact it is more strongly polarized than the main spectral bands. It is observed in all cases at least halfway up the side of the band after which it becomes less well resolved and merges with the coarser structure.

The  ${}^3T_2(F)$  band origin is overlaid with overtone absorption of the  $H_2O$  molecules; therefore  $D_2O$  was substituted. Some fine structure was observed, but it could all be attributed to  $H_2O$  impurity or  $D_2O$  overtones. However, the structure of the main band was brought out more clearly by deuteration. This structure is seen in Fig. 1.

The  ${}^3T_1(F)$  band has the complex and interesting structure at  $4.2^\circ K$  shown in Fig. 5. The two broad peaks on the long wavelength side are more intense in the polarization perpendicular to the c-axis. The short wavelength peak at  $15970\text{ cm}^{-1}$  is the sharpest of the strong features and appears to have the same frequency and intensity in both polarizations. The companion peak at  $15780\text{ cm}^{-1}$  on the other hand shows structure which is different in the two polarizations. This is the only intense feature in the entire spectrum to show such behavior. Associated with these two sharp peaks are progressions of what appears to be a totally symmetric Ni-O frequency. An O-H frequency is also distinguishable. Piper<sup>(3)</sup> established the identity of the O-H bands by noting their shift on deuteration. These vibration bands are reminiscent of those of molecular spectra. They appear only in this one spectral region.

The  $^1T_2(D)$  band is the strongest of the intercombination bands so it was possible to resolve the fine structure in a crystal 4 mm thick. In fact more lines were found here than in the other two bands.

The  $^3T_1(P)$  band shows no evidence of resolved multiplet components and is featureless except for the fine structure at the origin.

### III. INTERPRETATION OF BAND STRUCTURE

#### a. Sources of Spectral Structure

The structure of these absorption bands is expected to be complicated for three reasons. First is the fact that they are forbidden and may only appear by way of odd vibrational perturbations which destroy the center of symmetry. Second, almost all of the excited levels are degenerate and may suffer Jahn-Teller distortions. Even states which are not degenerate may become stabilized in unsymmetrical positions through the effects of coupling to nearby states. Third, the equilibrium configuration of the atoms in the excited state may differ by a totally symmetric displacement from that of the ground state.

Due to the action of the Franck-Condon Principle, progressions of symmetric vibrations would be excited. Their intensity maxima would occur at various distances from the origin depending on the amount of displacement. In the case of the unsymmetrical upper state, progressions of non-totally symmetric vibrations will appear. The Jahn-Teller effect is a special case of this in which certain intensity anomalies may occur.

For a given upper state one of these processes may be the principal factor determining the band shape; to determine it theoretically one would have to determine the stable geometric arrangement in the excited state and then apply the Franck-Condon Principle and vibrational electronic-coupling theory. We have carried out a much simpler and more

qualitative procedure. A crystal field perturbation of low symmetry is applied by using the point charge model and its effects on each of the various states are calculated. If a state is found to depend strongly on an unsymmetrical displacement, it ought to have a broad absorption band, and the normal vibrational modes which can produce the displacement should appear in the spectrum. The four components of the  ${}^3T_1(F)$  state should have approximately the same behavior toward the totally symmetric distortion but they may behave differently toward other symmetry types. The components of this state therefore provide a good example on which to test this procedure.

#### b. Origin of Structure of the ${}^3T_1(F)$ Multiplet

In Fig. 6 is shown the energy of the  ${}^3T_1(F)$  multiplet, and the nearby levels which interact strongly with it, as a function of  $Dq$ , the cubic crystalline field strength. If we set  $Dq = Dq_0 + bS(A_{1g})$  this diagram shows how the levels change with a totally symmetric displacement  $S(A_{1g})$ . The slopes of all the lines are nearly the same, indicating that all the multiplet components will suffer the same totally symmetric displacement in their excited states. According to the bandwidth criterion of Orgel (4) the components would then all have the same bandwidth (making the reasonable assumption that the force constants are the same in each state). If the identifications given in Fig. 5 are accepted, this is clearly incorrect. The conclusion must be that the displacements occur in some non-totally symmetric coordinate, and that it is by a different amount, or a different coordinate in each state.

Before going to this let us estimate the intensity distribution of the Franck-Condon series which would arise from a totally symmetric displacement. The magnitude of the displacement can be estimated as follows. The contraction



of the ion-ligand separation observed for NiO, compared to the hypothetical crystal not having a crystal field stabilization is  $0.07 \text{ \AA}^{(3)}$ . In the  $^3T_1(F)$  state the energy decreases as  $Dq$  decreases, hence there should be an increase of the ion ligand separation. Relative to the ground state this expansion will be  $\frac{18}{12} \times 0.07 \text{ \AA}$ , using the ratio of the dependences of the two effects on  $Dq$ . Taking  $0.1 \text{ \AA} = x$  as a reasonable estimate, the intensity ratio of the 0-0 and 0-1 bands according to the Franck-Condon Principle (for harmonic vibrations) is

$$\frac{I_{10}}{I_{00}} = \frac{\alpha x^2}{2} = 1$$

where  $\alpha = 4\pi^2 \text{ cym/h}$  and is taken to be  $2 \times 10^{18}$ , corresponding to  $\nu \approx 425$ . Thus we should expect progressions of totally symmetric vibrations which have their maxima near the origin. This is not what is observed, and it reinforces the conclusion already arrived at that the non-totally symmetric modes are important in determining the spectral structure.

The next possibility to be considered is the tetragonal distortion represented by a partner of the  $e_g$  normal mode of an octahedron. Figure 7 shows this and other normal displacements. In Figure 8, the energy is plotted as a function of  $S_{2a}$ . It is seen that each energy level behaves differently under this displacement. The calculation on which this figure is based is a complete diagonalization of the  $d^8$  energy matrix under a tetragonal perturbation\*. The latter is defined by a point charge model with the potential:

$$V_{\text{tetrag}} + V_{\text{cubic}} = Ar^2 Y_2^0 + Q r^4 Y_4^0 + \frac{D r^4}{5} \left[ Y_4^0 + \sqrt{\frac{5}{14}} (Y_4^4 + Y_4^{-4}) \right]$$

where  $A = \gamma \left( \frac{1}{c^3} - \frac{1}{a^3} \right)$ ;  $Q = \gamma \left( \frac{1}{c^5} - \frac{1}{a^5} \right)$ ;  $D = \frac{35}{4} \frac{\gamma}{a^5}$

and  $\gamma$  is the charge on the ions.

\* The calculation was performed by machine under the direction of P. K. Baltzer.

Here,  $c$  is the Ni-O distance in the direction of the tetragonal distortion ( $z$ ) and  $a$  is the distance in the perpendicular direction. The displacement coordinate  $S_{2a}$  is:

$$S_{2a} = 2(z_3 - z_6) - (x_1 - x_4) - (y_2 - y_5)$$

where the atoms are numbered as in Fig. 7. For infinitesimal displacements we have

$$A = -\frac{9r}{c^3} \frac{S_{2a}}{c}$$

$$Q = -\frac{75}{4} \frac{r}{c^5} \frac{S_{2a}}{c}$$

A positive value of  $S_{2a}$  means a lengthening of the  $c$ -axis. The calculations were carried out for the ratio  $\frac{A}{Q} \frac{p}{q} = 1.2$  where  $p = \frac{r^2}{105}$  and  $q = \frac{2}{105} r^4$ . This ratio is obtained when  $\frac{r^4}{2} = .25 R^2$ , where  $R$  is the bond length. This is close to the value given by SCF functions.

This mode of distortion,  $e_g$ , is the one commonly considered in calculations of the Jahn-Teller effect<sup>(5)</sup>. It has the correct symmetry to split the  $E_g$ ,  $T_{1g}$  and  $T_{2g}$  states of a cubic configuration. The partner  $S_{2a}$  is thought to lead to the lowest part of the resultant energy surface although a combination of  $S_{2a}$  and  $S_{2b}$  may be the lowest energy configuration under some conditions (5). In the present connection we assume that the upper states are all subjected to a tetragonal ( $S_{2a}$ ) potential which may or may not lead to appreciable distortions into a tetragonal shape. We will examine the band widths in the spectrum to see if they can be explained as vertical transitions to such distorted upper states.

Figure 5 shows the pattern of bands to be compared to Fig. 8. The two lowest components  $A_1$  and  $T_1$  are here identified with the two broad peaks at 14100 and 14400  $\text{cm}^{-1}$ . Fig. 8 shows that the  $T_1$  band is highly unstable under a tetragonal distortion. For a negative distortion

of one percent of the bond length (z-bond length increased two percent, x-bond length decreased by one percent) the energy of the E component decreases  $1000 \text{ cm}^{-1}$ . The zero point excursions are about two percent of the bond length and the zero point energy in the  $e_g$  coordinate is about  $150 \text{ cm}^{-1}$ . Therefore the destabilizing forces are considerably greater than the restoring forces, and a distorted equilibrium configuration is to be expected.

Both the  $T_2$  and E components show minor instabilities which are no more than the zero point energy in a displacement equal to the zero point displacement.

The  $A_1$  component can have no first order energy change since it is non-degenerate, but coupling to other  $A_1$  states leads to powerful second order effects of the distortion. Within half the zero point excursion, its energy is lowered by twice the zero point energy, and this state must become unstable in the cubic configuration.

The sharp peaks therefore correspond to levels which are not unstable under tetragonal distortions and the broad ones to levels which are unstable. The good correspondence between theory and experiment for the  ${}^3T_1(F)$  multiplet of  $\text{NiSiF}_6 \cdot 6\text{H}_2\text{O}$  is encouraging and suggests that such correlations will be found for other bands and for other substances.

#### c. Vibrational Structure of ${}^3T_1(F)$

In this section it will be shown that two true electronic origins in the  ${}^3T_1(F)$  multiplet may be identified. These give the multiplet width, and provide an independent path to the conclusion reached in the last section.

The sharp bands at  $15780$  and  $15970\text{ cm}^{-1}$  (called bands III and IV) are the origins of progressions of about  $500\text{ cm}^{-1}$  vibrations. Three members beyond the origin are discernable. The two peaks are barely distinguishable in the O-2 region. In order to explain the shapes of the blurred O-2 and O-3 features, we must say that the  $15970$  progression falls off more rapidly than the  $15780$  progression. There is no observable shift of the interval from  $15970$  upon deuteration; a minimum shift of  $40\text{ cm}^{-1}$  would have been detected. A  $40\text{ cm}^{-1}$  reduction on deuteration was observed for the interval measured from  $15780\text{ cm}^{-1}$ ; but since the  $15780$  peak is multiple, three parts being distinguishable, the shift may only represent differences in the relative intensities of the three O-1 members. It seems probable therefore that the  $500\text{ cm}^{-1}$  interval represents a vibration associated mainly with the Ni-O bonds. The fact that it appears in a regular progression shows that it is totally symmetric in the symmetry group common to upper and lower states. The previous arguments suggest that this group is the symmetry group of the ground state, and that the  $500\text{ cm}^{-1}$  interval is essentially  $\nu_1$  of an octahedral molecule.

One or two OH frequencies of the water molecules appear in the spectrum. Added to an OH interval is a series of  $500\text{ cm}^{-1}$  intervals. Our object here is to assign these bands and determine their origin.

There is a total of four normal modes of the  $\text{Ni}(\text{H}_2\text{O})_6$  complex for each normal mode of the water molecule in the group  $D_{3d}$  and they are  $A_u, E_u, A_g, E_g$ . Raman assignments have been reported for  $\text{ZnSiF}_6 \cdot 6\text{H}_2\text{O}$  (6) where the vibrations should be very similar to those of the  $\text{Ni}^{++}$  compound.

Although no deuterated material was studied, these vibrations in other hydrates are reduced by a factor of  $1.36 \pm .02$  (7). The frequencies of the vibrations given in Ref. 6, and the corresponding values for the deuterated molecule assuming this factor are:

3456	2450	Eg	} symmetric OH stretching
3492	2565	Ag	
3515	2582	Ag	} antisymmetric OH stretching
3519	2585	Eg	

Since we know the positions of the absorption bands we can subtract the OH or OD frequencies to find their origins:

$$\begin{array}{rcl}
 \text{H} & 19068 - \begin{Bmatrix} 3456 \\ 3515 \end{Bmatrix} & = \begin{Bmatrix} 15612 \\ 15553 \end{Bmatrix} \\
 \text{D} & 18176 - \begin{Bmatrix} 2540 \\ 2582 \end{Bmatrix} & = \begin{Bmatrix} 15636 \\ 15594 \end{Bmatrix}
 \end{array}$$

Since these do not coincide with observed bands, one of them must be a hidden electronic origin. The electronic origins of the normal and deuterated species should not coincide exactly because of the zero point energy shift.

Since we have been able to locate the origins of several electronic transitions of  $\text{NiSiF}_6 \cdot 6\text{H}_2\text{O}$  we have some idea of the magnitude of this shift. Going from H. to D there is a blue shift of  $73 \text{ cm}^{-1}$  for the  ${}^3\text{T}_1(\text{P})$  band,  $45 \text{ cm}^{-1}$  for the  ${}^3\text{T}_1(\text{F})$  band and  $110 \text{ cm}^{-1}$  for  ${}^1\text{T}_2(\text{D})$ .

These numbers were determined from the fine structure near the origins of the bands. Thus it is reasonable to expect anything from about 30 to  $150 \text{ cm}^{-1}$ . The possible origins above are therefore reasonable.

Whichever pair is chosen, it is necessary to assume that the O-H vibration observed does not add to either of the observed bands 15793 or 15957, but instead adds to some different origin. We suppose this to

be a true electronic origin. If so, the OH vibrations must be u, not g, since they have appeared in a single quantum in a  $g \longrightarrow g$  electronic transition. The Raman data do not give us the u modes, but from the energy difference between the Ag and Eg-modes we can see that the coupling of the OH vibrations of different water molecules is weak; therefore the u-modes will not differ much from the g. This leaves an uncertainty of perhaps  $40 \text{ cm}^{-1}$  in the calculated position of the electronic origin.

An additional uncertainty arises from not knowing whether the symmetric or antisymmetric stretching mode is the more active one. In the  $\text{D}_2\text{O}$  compound, the first O-D peak is double with a splitting of about  $80 \text{ cm}^{-1}$ . This may indicate that both modes appear, with the lower one, supposedly symmetric, the more intense. Although there may be other explanations of this doubling we take this as a reasonable possibility. Then the position of the origin, (averaging over both the A and E components, since both should appear in the spectrum), should be 15594 (H) or 15623(D). The deuteration shift is reasonable in magnitude and in the correct direction.

The electronic origin at 15594 could be associated with either of the sharp peaks 15793 or 15957. The respective intervals, which must be single quanta of a u-vibration, are 199 and  $363 \text{ cm}^{-1}$ . Because of the uncertainty in the location of the origin, and our lack of knowledge of the infrared frequencies, we cannot choose between these two possibilities, since each is a reasonable one. In fact it is now possible to ascribe both peaks to the same electronic transition.

In an attempt to distinguish these choices the temperature dependence of the intensity in this region has been measured. The intensity should increase with temperature according to the function  $f/f_0 = 1 + e^{-\theta/T}$  where  $\theta = 1.44 \omega$ , with  $\omega$  the vibration frequency in  $\text{cm}^{-1}$ . The other parts of the  ${}^3T_1(F)$  band should increase more rapidly since many lower frequency vibrations are effective. Bands III and IV actually increase much less rapidly with temperature than the bands I and II at the low energy end of the  ${}^3T_1(F)$  absorption region. Figure 9 shows the  ${}^3T_1(F)$  band at a series of temperatures. The extinction coefficient at the 6280 Å peak increases by 27 percent from 4.2°K to 300°K while in the 6900 Å region it increases by 100 percent in the same temperature range. The formula given above actually predicts an increase of 17 percent in the total absorption for the 363  $\text{cm}^{-1}$  choice and 38 percent for the 199  $\text{cm}^{-1}$  choice. Since we do not know the true area attributable to the bands of interest we again cannot distinguish between the two possible u-vibration frequencies. However, the temperature dependence experiments do tell us that the interpretation of the sharp peaks of the  ${}^3T_1(F)$  band as O-1 bands is essentially correct.

The vibrational structure at the red end of the  ${}^3T_1(F)$  band is probably associated with the lowest of the predicted multiplet components,  $A_1$ . This structure appears to begin at 12690  $\text{cm}^{-1}$  (12735 in the  $D_2O$  compound). There is some evidence for a progression of 380  $\text{cm}^{-1}$  vibrational modes. As Fig. 5 shows, there is a series of sharp bands having the same intensity spaced 50 ~ 100  $\text{cm}^{-1}$  apart, then, at 380  $\text{cm}^{-1}$  a rise of intensity followed by a similar series of small intervals. After four of these 380  $\text{cm}^{-1}$  intervals the first peak at 14150  $\text{cm}^{-1}$  is

reached. This idealization of the band structure is illustrated in Fig. 10.

The approximately  $380\text{ cm}^{-1}$  interval must be a non-totally symmetric g-vibrational mode because of its uniformly increasing intensity in the progression. Since the lower two levels of the  ${}^3T_1(F)$  multiplet were shown to be highly unstable with respect to  $E_g$  displacements, the 380 mode is probably an  $E_g$  mode. Now, since the upper state cannot be reached except via u-vibrational modes, where are these modes in the spectrum? They must surely be the series of low frequency modes observed at the beginning of the spectrum and, apparently, superposed on each 380 quantum as suggested by Fig. 10. There is no a priori reason why the approximately  $363\text{ cm}^{-1}$   $\tau_{1u}$  mode postulated for the 15594 band should not also appear, and perhaps it is present but not resolved.

The new and interesting feature of this band, according to the foregoing interpretation, is that the odd modes do not induce a large transition moment by themselves, but do so only when accompanied by several quanta of the even  $E_g$  mode. This is not surprising, however. The simultaneous excitation of the two kinds of vibrations is necessary in order both to destroy the center of symmetry and to provide a large vibrational overlap integral.

It is not known what the low frequency modes are. The 230 could be one of the  $\tau_{1u}$  modes of the  $\text{Ni}(\text{H}_2\text{O})_6^{++}$  octahedron, but 35 and 88 are too small for internal modes. They may correspond to motions mainly of the entire complex having some contributions from internal motions.



It has become obvious that a complete study of the infrared spectrum of the crystal is needed in order to analyze the optical spectrum. But for the main purpose of this paper, it is enough to have established that there is an electronic origin of some multiplet component at 15594, or possibly about  $50\text{ cm}^{-1}$  lower; and another origin at about  $12690\text{ cm}^{-1}$ .

The difference between the two established electronic origins of the  ${}^3T_1(F)$  band is now known to be about  $2850 - 2900\text{ cm}^{-1}$ . This is probably the entire electronic width of the multiplet. It is more than twice as wide as one calculates from the "complete" theory of  $\text{Ni}^{++}$  in a cubic field using  $\lambda = -275\text{ cm}^{-1}$ . This value of  $\lambda$  is consistent with measured g-factors and it ought to be about the same for excited states as for the ground state. The discrepancy therefore cannot be blamed on the value of  $\lambda$ . The extra multiplet width is undoubtedly a result of the instability of the lower multiplet component which causes its electronic origin to be red-shifted by the mechanism discussed in Sec. II, and illustrated by Fig. 8. The additional multiplet width therefore represents the stabilizing energy gained by the lowest multiplet component by the tetragonal distortion.

#### IV. CONCLUSIONS

We have now shown by two experimental criteria, measurement of band widths, and measurement of electronic energy differences in a multiplet, that components of the  ${}^3T_1(F)$  multiplet have different equilibrium shapes. The other bands of  $\text{Ni}^{++}$  have smaller spin-orbit coupling, so that the individual components are not resolved. But as far as can be learned, these bands also contain upper states which are unstable in the cubic configuration.

Table I

Structural Data for  $\text{NiSiF}_6 \cdot 6\text{H}_2\text{O}$

- a) one formula unit per unit rhombohedral cell.  $a = 6.21$   $\alpha = 96^\circ 53'$
- b) approximate atomic positions in rhombohedral coordinates

Si    0       0       0

Ni     $\frac{1}{2}$        $\frac{1}{2}$        $\frac{1}{2}$

F     $\pm$  (xyz, zxy, yzx);  $x = 0.14$      $y = 0.31$      $z = 0.94$

O     $\pm$  ( "    "    " )  $x = 0.64$      $y = 0.81$      $z = 0.44$

- c) nearest Ni-O distance:  $2.07 \text{ \AA}$

- d) angle between C-axis and Ni-O direction:  $55.8^\circ$

(for regular octahedron,  $54.8^\circ$ )

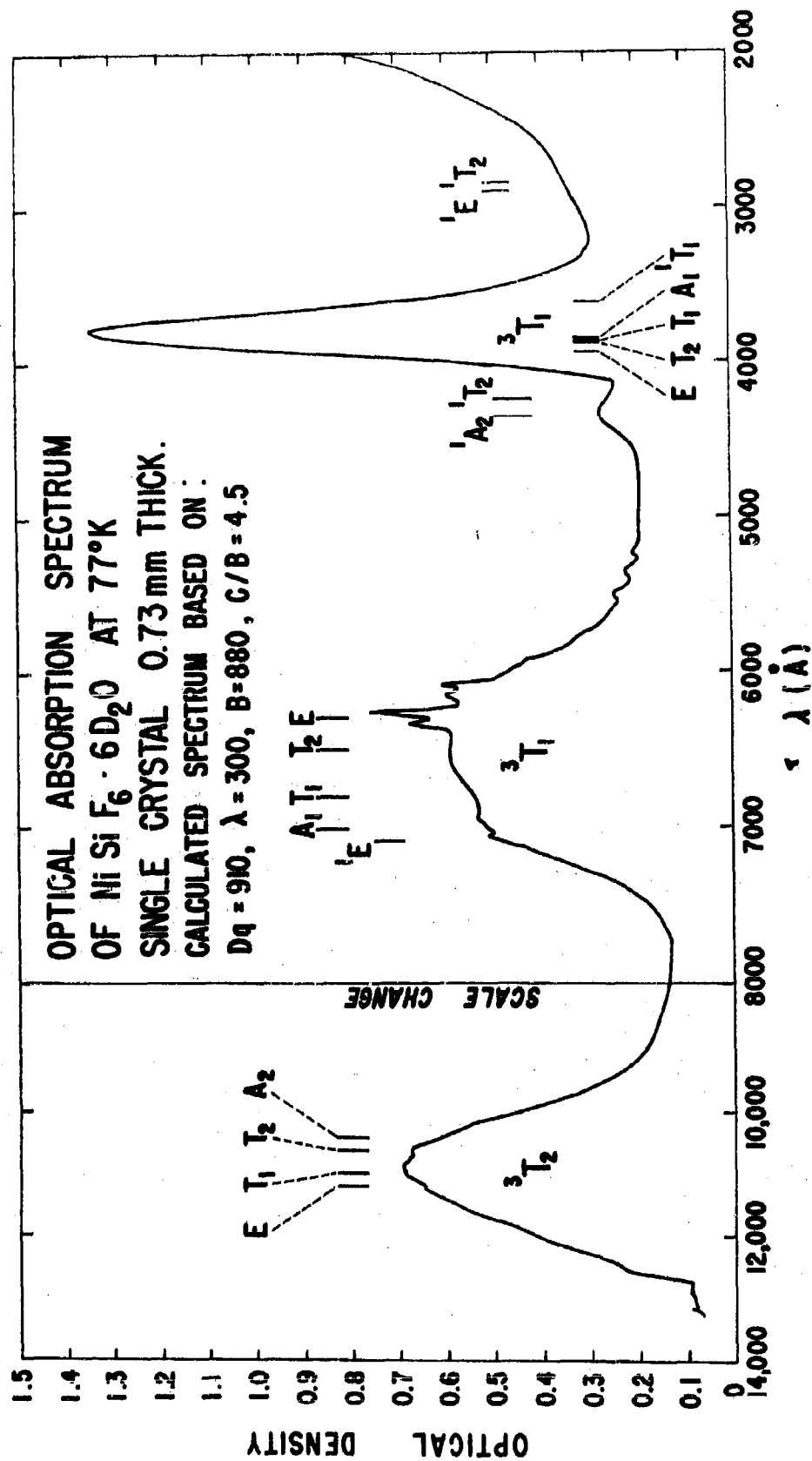
# FIGURE CAPTIONS

1. Absorption spectrum of nickel fluosilicate. The portion from  $8000 \text{ \AA}$  to shorter wavelengths is taken from a crystal of  $\text{NiSiF}_6 \cdot 6\text{H}_2\text{O}$  at  $77^\circ\text{K}$ .

The portion from  $8000 \text{ \AA}$  to longer wavelengths is taken from a crystal of  $\text{NiSiF}_6 \cdot 6\text{D}_2\text{O}$  at about  $10^\circ\text{K}$ .

The theoretical positions of the absorption bands calculated using the following parameters are also shown:  $Dq = 910$ ,  $B = 880$ ,  $\lambda = 300$   $C/B = 4.5$ .

2. Fine structure near origin of  ${}^3T_1$  (F) band.
3. Fine structure near origin of  ${}^1T_2$  (D) band.
4. Fine structure near origin of  ${}^3T_1$  (P) band.
5. The  ${}^3T_1$  (F) band of  $\text{NiSiF}_6 \cdot 6\text{D}_2\text{O}$  for two thicknesses of crystal at  $4.2^\circ\text{K}$ . The apparent origins III and IV are marked as well as the progressions following them.
6. Energy of multiplet components of  ${}^3T_1$  (F) as a function of a totally symmetric distortion ( $Dq$ ).
7. Normal displacements (or vibrations) of an octahedron showing standard notation for frequencies.
8. Energy of multiplet components of  ${}^3T_1$  (F) as a function of tetragonal distortion,  $e_g$  (the partner shown in Fig. 7). The diagram has been calculated for the parameter values  $Dq = 900$ ,  $B = 800$ ,  $C/B = 4.5$ ,  $\lambda = 320$ . The tetragonal distortion potential is based on a point charge model (see text). The horizontal scale width is about equal to the zero point displacement in the  $e_g$  vibration. The negative sign corresponds to an elongation of the octahedron.
9. The absorption in the  ${}^3T_1$  (F) region at various temperatures ( $^\circ\text{K}$ ). Successive tracings are separated in the vertical scale.
10. An idealization of the structure near the origin of the  ${}^3T_1$  (F) band showing the progression of  $380 \text{ cm}^{-1}$  which appears to be present. This figure is to be compared to the original record shown in Fig. 2.



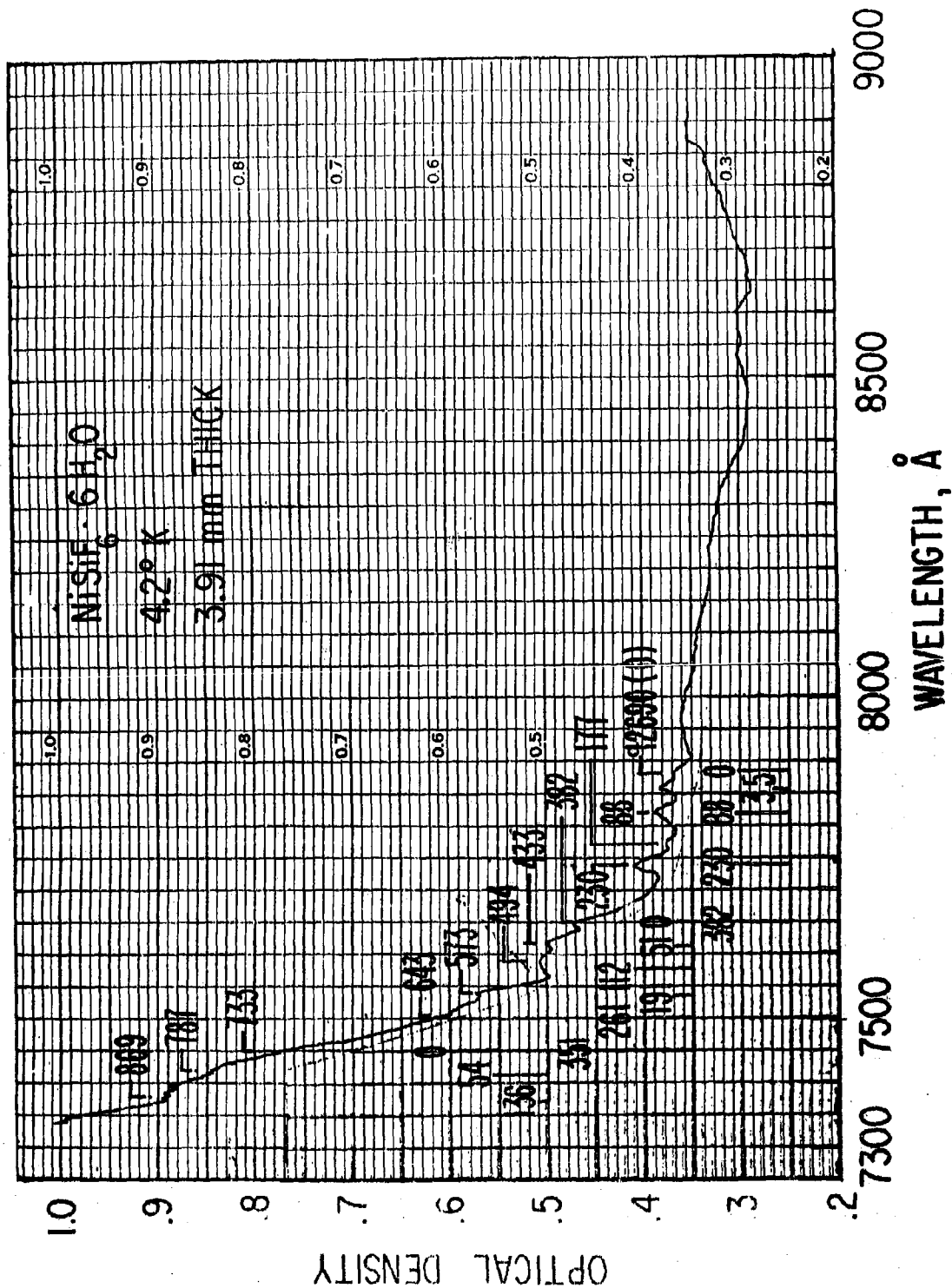


Figure 2 - III

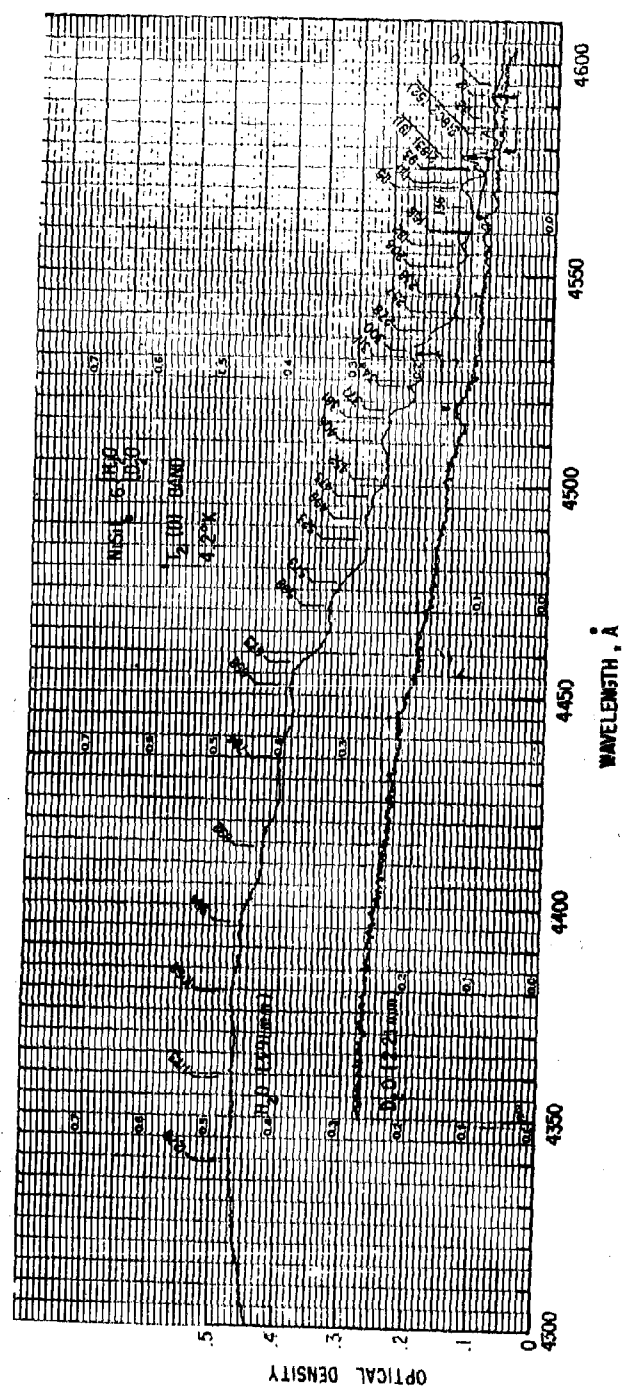
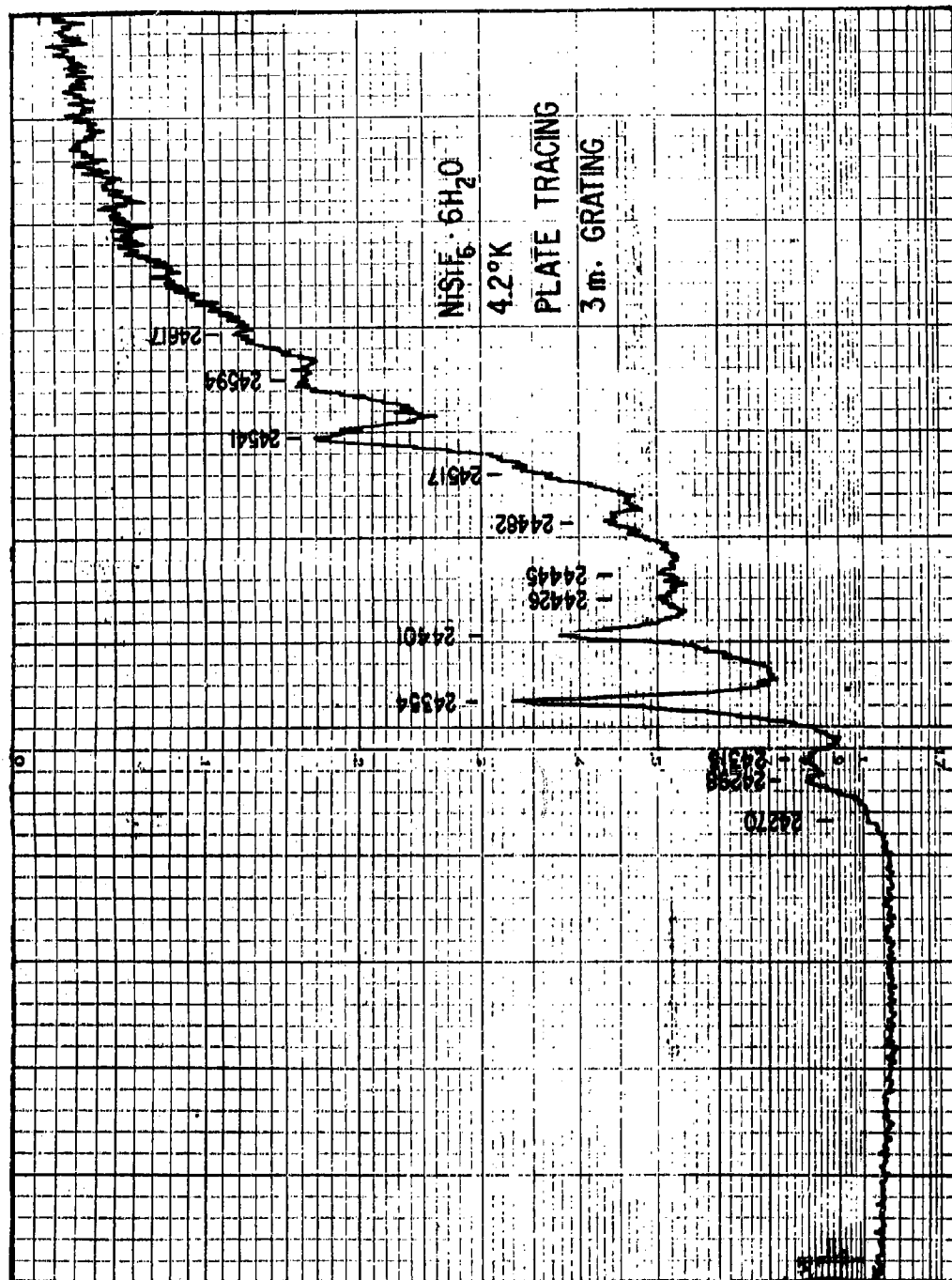


Figure 3 - III



**Figure 4 - III**

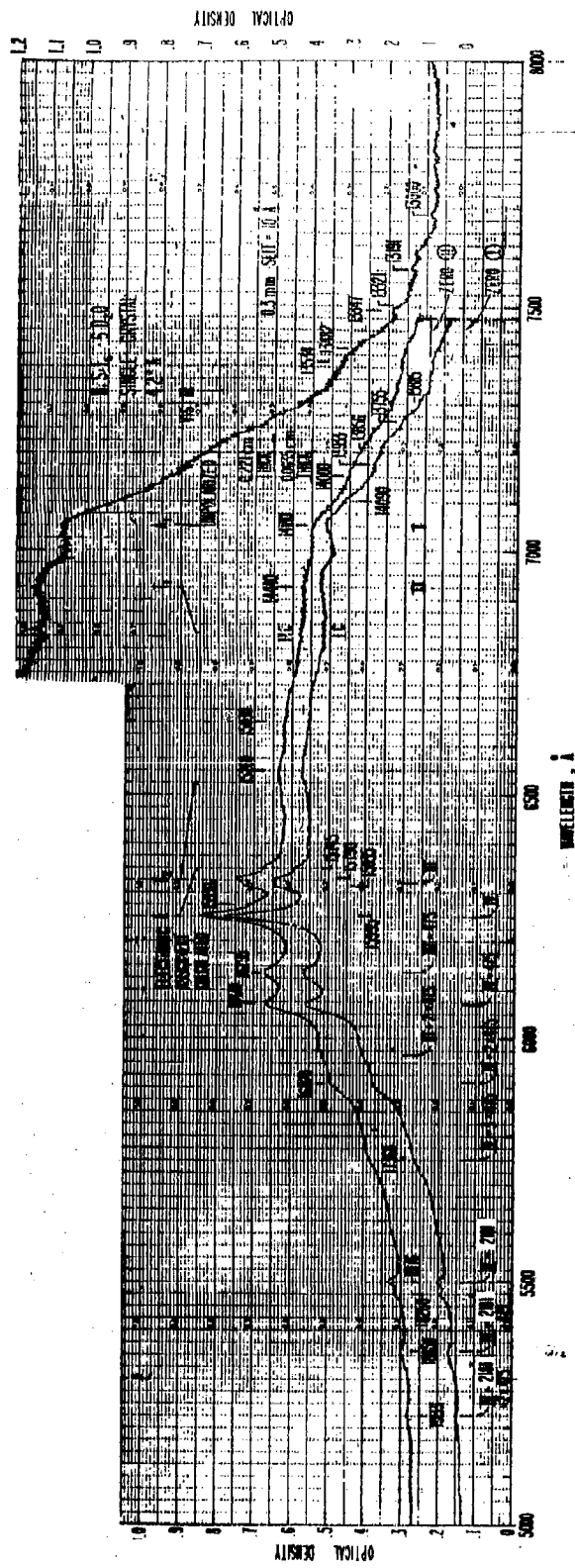


Figure 5 - III



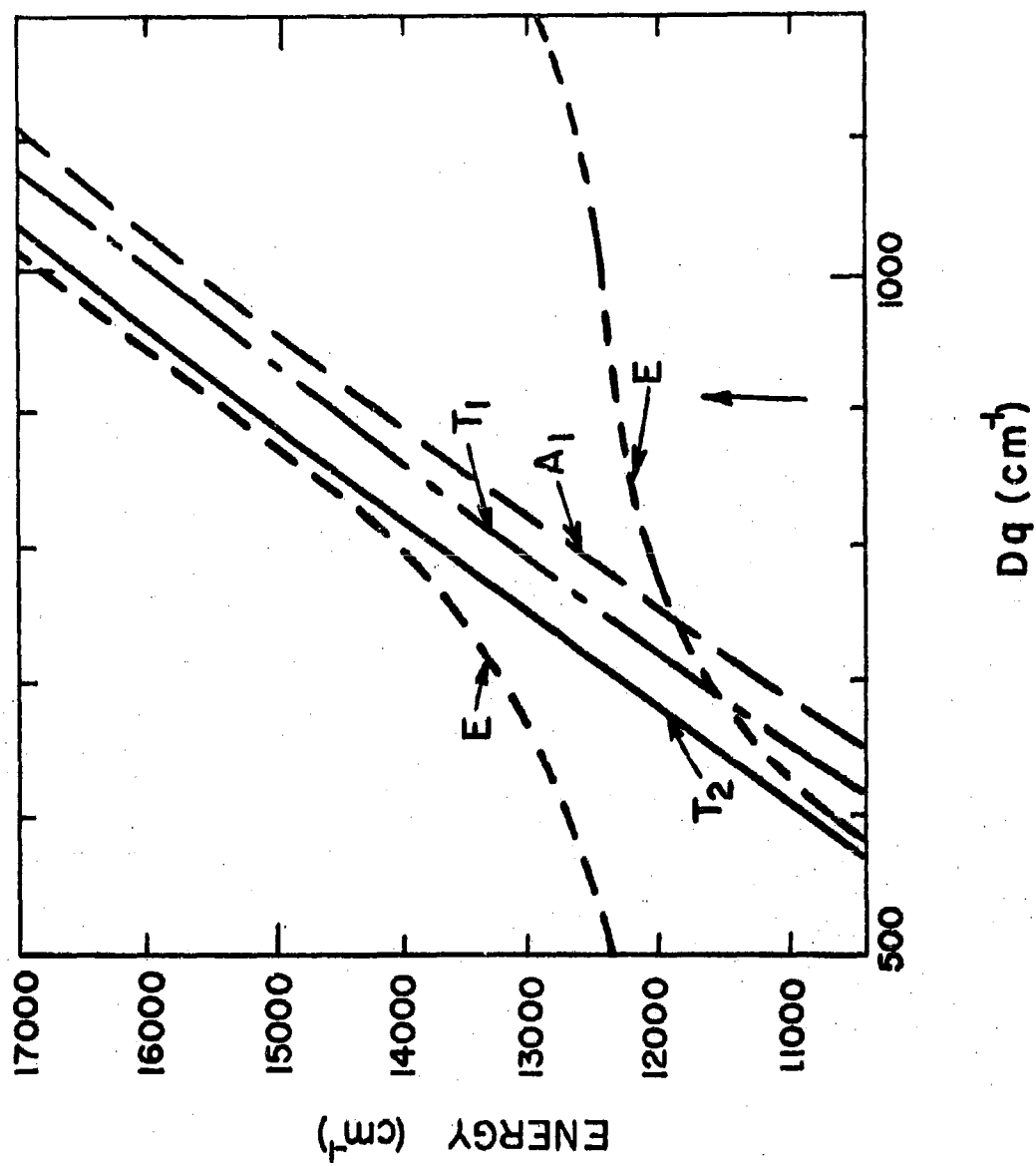
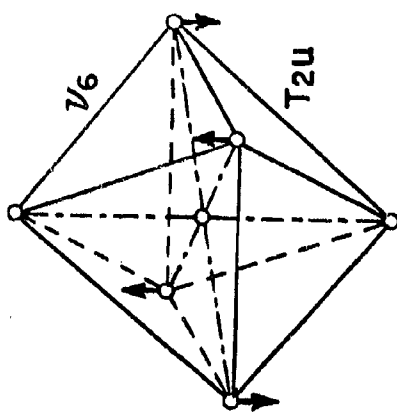
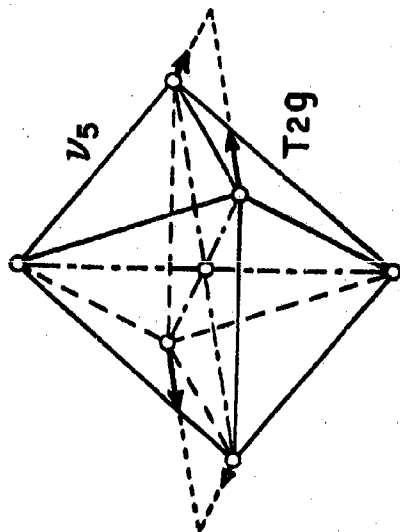
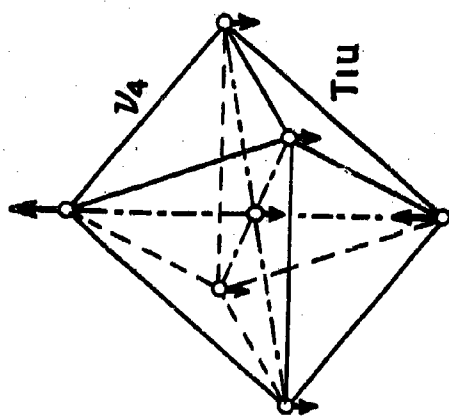
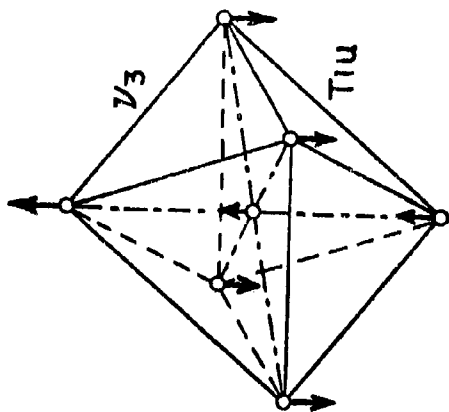
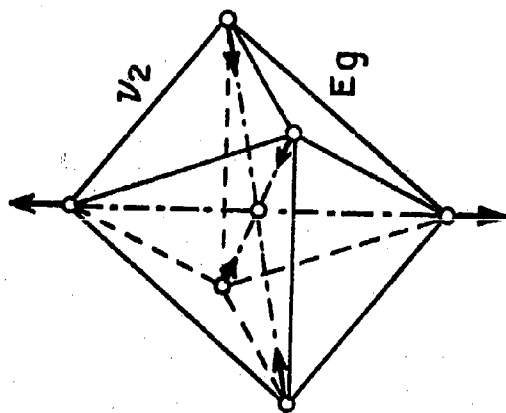
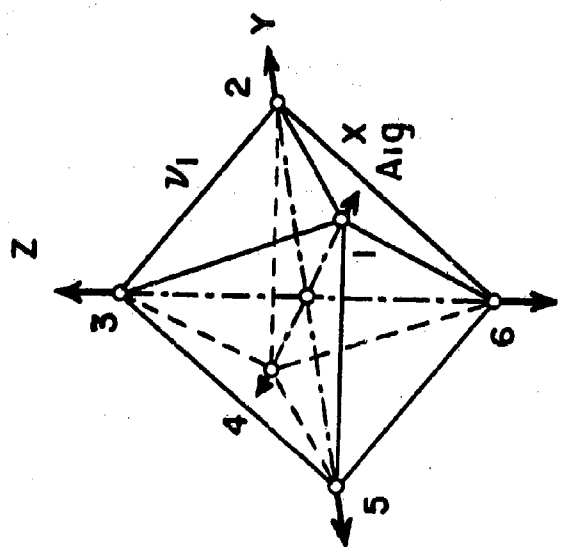


Figure 6 - III



NORMAL VIBRATIONS OF AN OCTAHEDRAL  $XY_6$  MOLECULE  
(POINT GROUP  $O_h$ )-ONLY ONE COMPONENT OF EACH DE-  
GENERATE VIBRATION IS SHOWN.

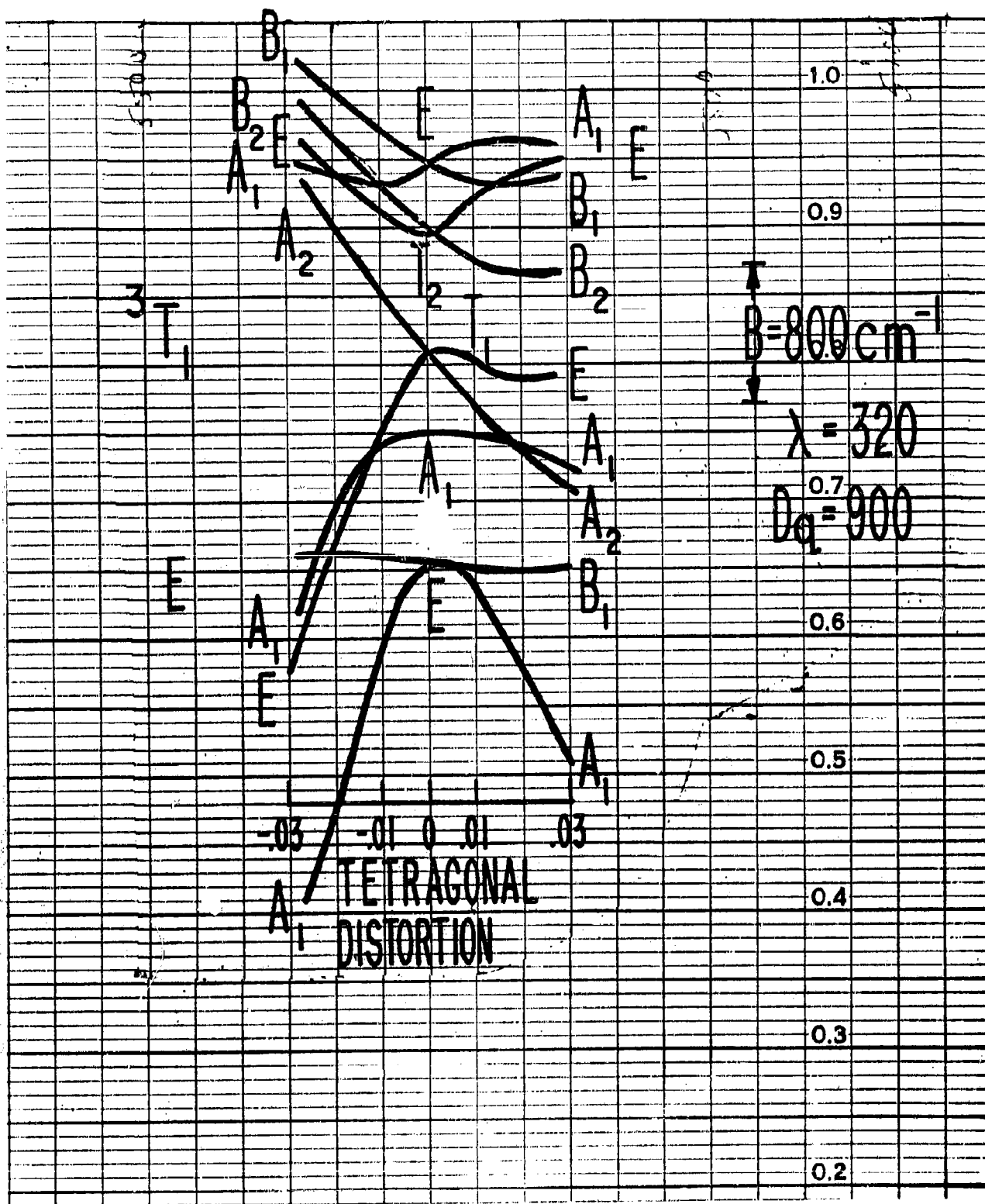


Figure 8 - III

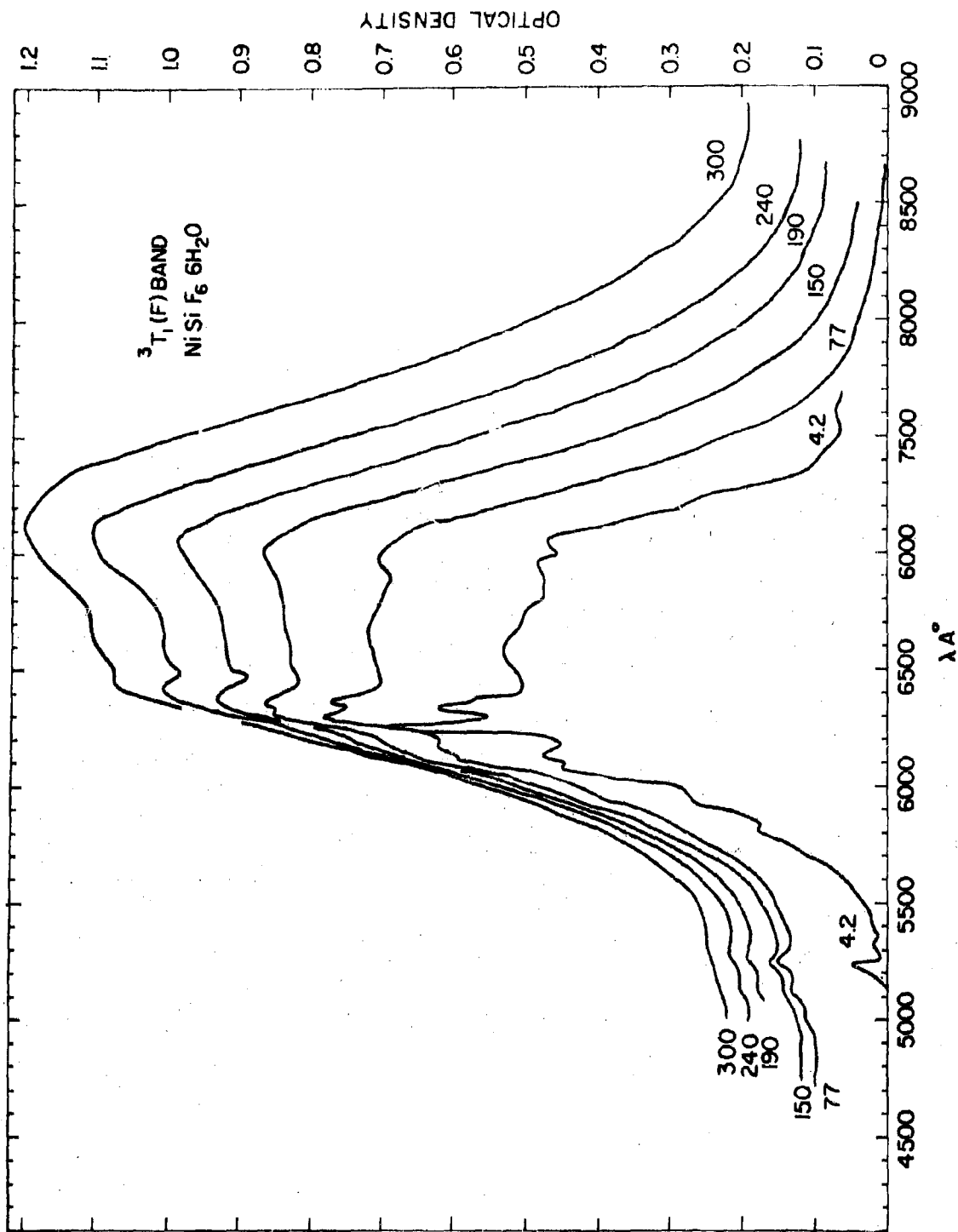


Figure 9 - III

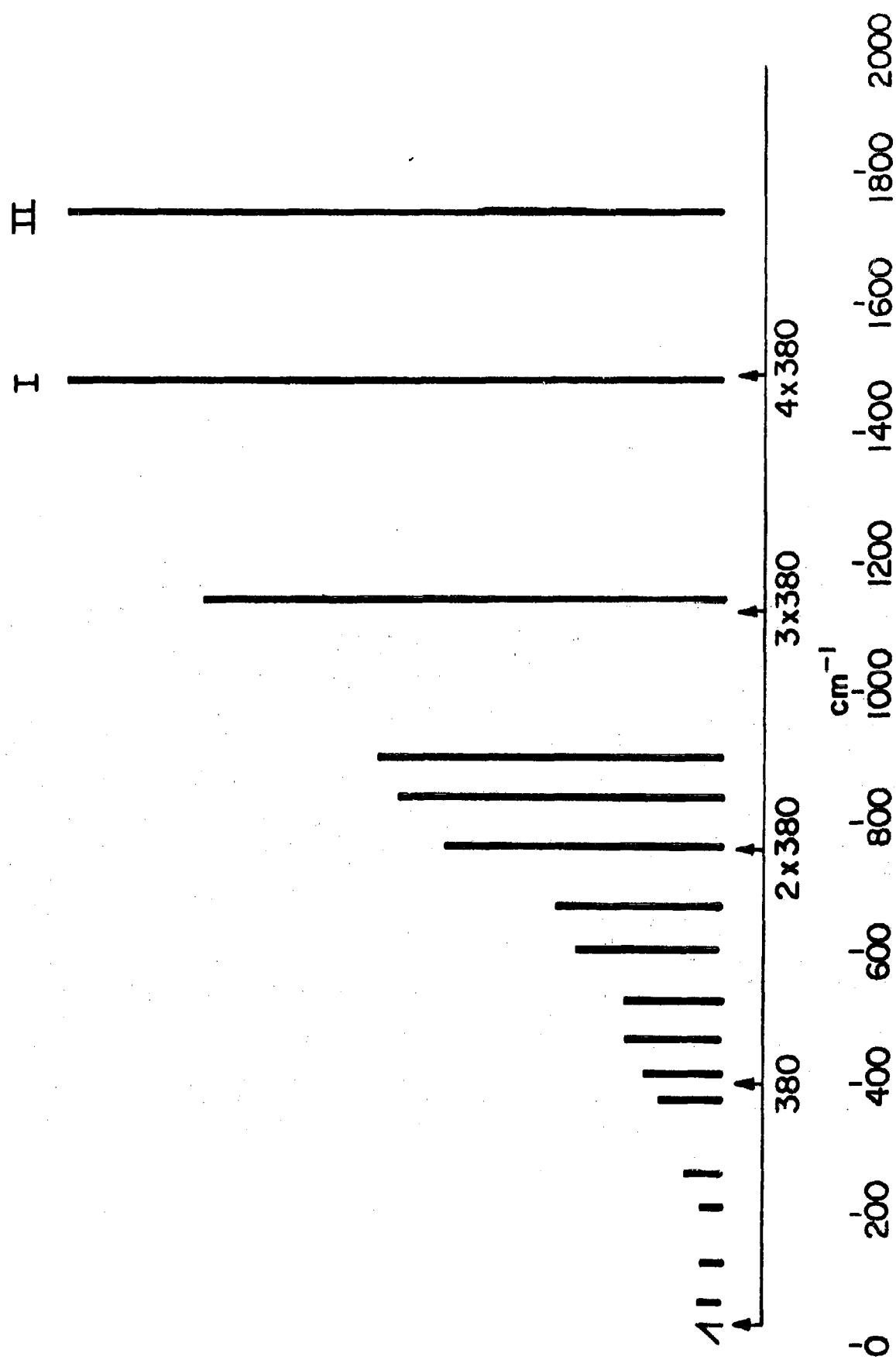


Figure 10 -III

Exchange Coupled  $Mn^{++}$  Ions in ZnS Single Crystals

Donald S. McClure

RCA Laboratories, Princeton, N.J.

## ABSTRACT

Evidence for exchange coupling between  $Mn^{++}$  ions in ZnS:MnS mixed crystals is manifested in the optical spectrum in two ways; the intensity of absorption is not proportional to concentration of  $Mn^{++}$  and temperature dependent absorption lines appear. The latter give a measure of the exchange integral in the ground state of  $25^{\circ}K$ , which is larger than the exchange integral of  $12^{\circ}K$  derived for pure MnS from its high temperature susceptibility curve. There is also spectral evidence for triples of  $Mn^{++}$ . These appear at concentrations above 8 percent and appear to be responsible for luminescence quenching.

# Exchange Coupled $Mn^{++}$ Ions in ZnS Single Crystals

Donald S. McClure

RCA Laboratories, Princeton, N. J.

There is now both optical and microwave evidence for the existence of exchange-coupled ion pairs in crystal lattices. Owen (1) has studied the  $Mn^{++}$  pairs in MgO by spin-resonance, finding a value of the exchange integral  $J$ , of  $30\text{ cm}^{-1}$  for the 110 pairs. This is about twice the value expected by comparison with the  $J$  value in MnO where the lattice constant is only slightly smaller than in MgO. Statz and Koster (2) and Schawlow (3) have observed  $Cr^{+3}$  pairs in  $Al_2O_3$ . The present note concerns optical evidence for  $Mn^{++}$  pairs in ZnS. The initial indication of interaction between  $Mn^{++}$  ions came from a study of the  $5300\text{ Å}$  broad band absorption of the  $Mn^{++}$  ion at various concentrations in ZnS single crystals. The intensity of absorption increased faster than the concentration. Later, experiments at  $4.2^\circ K$  and above on the absorption spectrum in the sharp line region at  $4600\text{ Å}$ , revealed temperature dependent lines which were absent in dilute samples. These extra lines arise from the thermally excited pair states.

**Experimental:** The specimens of ZnS:MnS were prepared by the vapor transport method using iodine as the carrier\*. The deposition temperature varied from  $750$  to  $900^\circ C$ , and the  $Mn^{++}$  content varied from 1 to 11 percent. Most of the samples were the cubic form of ZnS. They were from 1 to 5 mm in largest dimension. Pieces of crystal were polished with parallel faces and mounted in our optical dewar in the vacuum space. Thermal contact was provided by silver paste. A copper-constantan thermocouple was silver pasted to the sample.

\*Prepared by R. Nietsche and M. Lichtensteiger, RCA Zurich.

Spectra were obtained with a Cary 14 spectrophotometer. Temperatures between 4.2 and 77°K were obtained by letting the liquid helium evaporate and making the spectral runs during warm-up. The temperature change during such a run was never more than 5°.

Results: Figure 1 shows spectra of crystals of several concentrations, including some pure MnS. The latter has the NaCl structure rather than the ZnS structure, so is not strictly comparable with the mixed crystals. The crystal thickness and approximate percentage of Mn are given in the figure and are also shown in Table I. The percentage Mn was determined by chemical analysis of crystals which deposited during preparation near the one chosen for study. There was a nearly uniform decrease of Mn concentration from the hottest region of the deposition zone to the coldest. Analysis of the actual samples must await completion of spin-resonance studies. The product of concentration and thickness is proportional to the number of Mn atoms in the light path, and in the absence of interaction between  $Mn^{++}$  ions this product would be proportional to the optical density. Consequently we give in Table I the molar extinction coefficient,  $\epsilon$ , at the peaks of the main absorption bands, where

$$\epsilon = p/cl$$

$p$  = optical density,  $\log I_0/I$ ,  $C$  = concentration in moles/liter

$l$  = path length in crystal in cm. For a given band, this quantity should be a constant independent of concentration, but as Table I shows, it increases with concentration. In view of the uncertainty of the chemical analysis, and the obvious exception to the general trend of results in the case of sample 263B, the conclusions to be drawn from Table I are somewhat weakened. It is safe to say that the absorption coefficient increases with concentration, but we cannot say by exactly how much.



Figure 2 shows the results of an experiment in which the spectrum of a 5 percent crystal was obtained at various temperatures. Only the 4600 Å region showing sharp line structure was covered by these experiments as the other regions did not show any dramatic temperature effects. The arrows in Fig. 2 point out the positions of absorption lines which are absent at 4.2°K but which grow with rising temperature. These evidently must arise from a level (or levels) near the ground state and within  $kT$  of it.

The optical density of a temperature dependent line was corrected by subtracting the optical density of the background at the same wavelength. The background was taken to be the optical density at 4.2°K where there was no trace of the temperature dependent absorption line. This procedure would give the line strength if the width of all absorption lines in this region were to remain constant with rising temperature. Some broadening does occur but it is very slight. The rate of change with temperature is probably underestimated slightly. Table II gives the optical density as a function of temperature and the corrected optical density for a sample containing 5 percent Mn. If the logarithm of corrected optical density is plotted against  $1/T$ , a straight line is obtained whose slope is given by a Boltzmann factor. The 4653.4 Å peak gave 29.6°K and the 4590 Å peak gave 35.8°K. Considering the errors involved in the corrections, especially for the weaker 4590 Å peak, these two results are probably within experimental error. It will be seen that the two lines almost certainly arise from the same thermally excited level near the ground state.

A second sample of the 5 percent crystal gave  $\Theta = 28.5^\circ\text{K}$  for the 4653.4 Å peak.

A sample of 2 percent Mn in ZnS (1.27 mm thick)\* gave a value  $\Theta = 37.8^\circ\text{K}$  for the  $4653.4 \text{ \AA}$  peak (see fig. 3). Although this is again somewhat high it is felt that the same type of thermally excited level as is present in the 5 percent sample is involved.

Figure 4 shows the temperature dependence of the  $4600 \text{ \AA}$  region in an 8 percent sample. The structure is not as clearly marked, but the intensity increases strongly with temperature.

The correct analysis of the data is actually somewhat more involved than the use of a simple Boltzmann factor. This will be discussed in the next section.

Discussion: The absorption spectrum of  $\text{Mn}^{++}$  arises from transitions between a  $^6\text{S}$  ground state and various quartet excited states. For purposes of orientation, the spectrum of the trans-  $\text{Mn}(\text{H}_2\text{O})_4\text{Cl}_2$  molecule is shown in Fig. 5. All of the spectral assignments are shown in this figure, using the approximation that the crystal field is cubic. The resemblance of this spectrum to that of  $\text{Mn}^{++}$  in ZnS is obvious.

Assignment of transitions in the spectrum is based on the similarity of all  $\text{Mn}^{++}$  spectra and on the theoretical term splitting diagram shown in Fig. 6. The parameter  $Dq$  measures the strength of the cubic field, and in order to fit the spectrum of Mn in ZnS, we must take  $Dq = 260 \text{ cm}^{-1}$ . The parameter,  $B$ , which measures the atomic term separations does not give all the level positions very well, but is about the same as for the  $\text{Mn}^{++}$  halides,  $615 \text{ cm}^{-1}$ . A better analysis of the term positions of the ion is provided by the covalency parameter of Stout (4). The value of this parameter must be quite large for MnS in ZnS, and larger still for

---

\* The "2 percent" sample, # 263B, is probably closer to 4 percent, according to Table I.

MnSe in ZnSe. Fig. 7 shows the covalency parameter for a number of  $Mn^{++}$  compounds. The single parameter does not give a perfect fit by any means, but it does arrange the ligands in an order which makes sense chemically.

The transition in the region of  $4600 \text{ \AA}$  in  $MnS:ZnS$  has two electronic levels for its upper states, the  ${}^4A_1$  and  ${}^4E$  levels, which are degenerate in a purely ionic model of the crystal field. The effect of covalency on the two is somewhat different, however, and the  ${}^4E$  level is expected to lie somewhat below  ${}^4A_1$ . This is indicated in Fig. 7. It is difficult to separate these two levels in the spectrum, as their absorption regions overlap. In the  $MnS:ZnS$  spectrum it appears that the origins of these transitions are:  ${}^4E$   $4700 \text{ \AA}$  ( $21270 \text{ cm}^{-1}$ );  ${}^4A_1$   $4637 \text{ \AA}$  ( $21560 \text{ cm}^{-1}$ ), a separation of  $290 \text{ cm}^{-1}$ . The additional lines of about  $100 \text{ cm}^{-1}$  separation from the origin are probably vibrational intervals.

When the  $MnS$  concentration is above one percent, there is an appreciable statistical probability that for a given  $Mn^{++}$  there will be a like ion in the neighboring cation lattice site. These coincidences will be referred to as pairs. There is only one geometrically distinct type of pair in the cubic  $ZnS$  lattice. At concentrations above 5 percent the number of triples becomes appreciable. There are many ways to place three foreign cations in the  $ZnS$  crystal such that only a single anion separates two of them. Fig. 8 shows the totals in these categories. The sum in all categories should be unity; at a composition of 10 percent only 89 percent of the atoms are accounted for by singles, pairs and triples, so that quadruples and higher clusters are beginning to become important.

The exchange coupling in antiferromagnetic materials is usually found to be given to a good approximation by the isotropic spin-spin coupling hamiltonian:

$$H = - 2J S_1 \cdot S_2 \quad (1)$$

where  $J$  is the exchange integral, and  $S_1, S_2$  are the total spins of the two ions. This same approximation should be equally valid for the ground state of ion pairs in ZnS. The resultant energy level system is given by:

$$E = J (-\lambda (\lambda + 1) + 2S(S + 1)) \quad (2)$$

where  $\lambda = S_1 + S_2$ ,  $S_1 + S_2 - 1 \dots 0$ ; and  $S = |S_1| = |S_2|$ .

For  $J < 0$ ,  $\lambda = 0$  is the lowest level, a non-degenerate level.

The next higher level is  $\lambda = 1$  at  $2J$ , a triply degenerate level. The partition function for the system is:

$$Q = \sum_{\lambda=0}^5 (2\lambda + 1) e^{-\lambda(\lambda + 1)\Theta/T} \quad (3)$$

where  $\Theta = -J/k$ . We need to know the population of the level  $\lambda = 1$  as a function of temperature. This is:

$$\frac{N_1(T)}{N_0(0)} = \frac{3e^{-2\Theta/T}}{Q} \quad (4)$$

The intensity of the temperature dependent lines should be proportional to  $N_1(T)$ . This must replace the Boltzmann factor used earlier.  $Q$  may be obtained from tables of the partition function of a rotator.

For the 2 percent sample, the value of  $J/k$  obtained from this analysis is  $-25 \pm 2^\circ\text{K}$ . Extremely accurate analyses of the high temperature susceptibility curve of  $\beta$ -cubic MnS (ZnS structure) by Doneban and Stevens (5) give  $J/k = -12.45^\circ\text{K}$ . One would not expect such a large difference between these two values because the metal-sulfur distance for  $\beta$ -MnS is  $2.425 \text{ \AA}$ , and that for ZnS is  $2.35 \text{ \AA}$ . However, Owens' results on Mn in MgO (1) were

similar to these.

The failure of Beer's law cannot be explained by the use of the hamiltonian (1). Physically, the phenomenon can be understood in the following way. The transition in single ions is forbidden by the selection rule  $\Delta S = 0$ , since the ground state is a sextet,  $S = 5/2$ , and the excited states are quartets,  $S = 3/2$ . The transitions in single ions are observed only because spin-orbit coupling partially destroys the spin as a good quantum number. In the pairs, there are many values of the total spin, as we have seen in dealing with the ground state. The total spin in the ground state ranges from 0 to 5 while in the excited state, assuming only one excitation per pair we have  $S = 5/2 + 3/2, 5/2 + 3/2 - 1, \dots, 5/2 - 3/2$ , or 4, 3, 2, 1. As we have just seen, the ground state having  $S = 1$  is populated appreciably at  $20^\circ\text{K}$  and above, and it may make transitions to an upper pair state having  $S = 1$  without violating the spin selection rule. Even so, the transitions would not be any more intense than single ion transitions if the operator (1) were the only effect as an analysis of the eigenfunctions of the operator (1) will show. However, the same spin states are generated by any other interaction operator, since they arise because of symmetry properties, and it is only a matter of finding the operator which has the effect of increasing the intensity of the  $S = 1 \longrightarrow S = 1$  transitions above that due to the single ion transitions.

One form of such an operator is (6)

$$H' = \sum_{i,k} s_i^{(1)} \cdot s_k^{(2)} j_{ik} \quad (5)$$

where  $i,k$  sum over all spins of the two ions and 1,2 refer to the two ions.

This operator is also isotropic and provides for the possibility of uncoupling

the spins  $s_i$  from the total spin  $S$  within single ions. The total spin of a single ion is therefore not preserved as it was by operator (1), and this provides the possibility of intensity increments in the transition. We do not expect that (5) will have much effect on the energy so that (1) is still valid in connection with the discussion of the ground state splitting.

A theory of the intensity has not been worked out quantitatively, nor has the theory of the splitting of the excited states. The two lines at 4590 and 4653 are probably the  $S = 1$  lines of excited states derived from a  ${}^4A_1 + {}^6S$  and a  ${}^4E + {}^6S$  pair respectively.

According to the spin selection rules, we should not see absorption from the ground state of a pair to its excited states, since there are no excited pair states having  $S = 0$ . However, the absorption spectrum should actually be observable through the same mechanism which permits transitions in isolated ions. In this case then should we not see these transitions appearing like single ion transitions but blue shifted by  $35/2 J$  or about  $440 \text{ cm}^{-1}$ ? They do not obviously appear in the spectrum. They would be weak because there is no mechanism to intensify them, but no weaker than absorption due to isolated ions. On a statistical basis in a 5 percent sample there are 54 percent of  $\text{Mn}^{++}$  ions having no near neighbor  $\text{Mn}^{++}$ , and 34 percent having one n.n.  $\text{Mn}^{++}$ . Thus the spectra due to unexcited pairs ought to be nearly as strong as the spectra of individuals.

It would be desirable to unravel the spectra due to the two thermally accessible pair states (at low temperatures) from the spectra of individuals, but so far this has not been possible. There are definite differences,

however, between the spectra of 2 percent and 5 percent samples in the temperature independent regions as Figures 2 and 3 show. The spectrum of the one percent sample is so weak that only the two prominent lines at 4653 and 4590 Å are observable.

The spectrum of the 8 percent sample has temperature dependent regions, (Fig. 4) but individual lines are not well resolved. It appears that at the lowest temperatures the absorption is stronger than in the 5 percent sample. There are twice as many triples in the 8 percent sample, and they may make an important contribution. When three  $Mn^{++}$  ions couple in three equivalent pairs, a  $\lambda = 3/2$  state is lowest ( $J < 0$ ) and since  $\lambda = 3/2$  is possible in the excited states, thermal excitation is not required to match the multiplicities of the combining levels. This is probably why the extinction coefficient becomes rapidly larger at 8 - 11 percent where the number of triples is comparable to the number of pairs and singles. There are several different kinds of triples, whereas in this lattice there is only one kind of pair; therefore the spectra of the more concentrated crystals become very complicated. In the 11 percent samples, no detailed structure may be observed for this reason.

There is an interesting connection between this work and luminescence efficiency. It is known that Mn phosphors begin to lose their efficiency when the Mn concentration is higher than one or two percent. Leverenz and North(7) showed that above one percent, the number of isolated  $Mn^{++}$  ions in  $Zn_2SiO_4$  (rbhd1) begins to decrease rapidly, following the curve of efficiency rather closely. Qualitative observations of the  $ZnS:MnS$  crystals showed that the 1 and 2 percent samples fluoresced brightly under 3660 Å illumination, the 8 percent sample was appreciably dimmer and the 11 percent sample had no observable fluorescence. These results are

similar to those reported for  $\text{Zn}_2\text{SiO}_4\text{:Mn}$ . The quenching of fluorescence in the case of  $\text{ZnS:Mn}$  appears, however, to be more closely correlated to the increasing number of triples rather than pairs, as can be seen by referring to Fig. 8.

Acknowledgement: The writer wishes to thank Mr. Manfred Lichtensteiger and Dr. Rudolf Nietsche of RCA, Zurich, for the preparation and analysis of the  $\text{ZnS:MnS}$  samples used in this work.



Exchange Coupled  $Mn^{++}$  Ions in ZnS Single Crystals

## References

1. B. A. Goles, J. W. Orton and J. Owen, Phys. Rev. Letters 4 116 (1960)
2. Rimai, Statz, Weber, deMars and Koster, Phys. Rev. Letters 4, 125 (1960).
3. A. L. Schawlow, D. L. Wood and A. M. Clogston, Phys. Rev. Letters 3, 271 (1959).
4. J. W. Stout, J. Chem. Phys. 31, 709 (1959).
5. Doneban and Stevens, Letter to P. J. Wojtowicz.
6. L. E. Orgel, private communication.
7. H. W. Leverenz and D. O. North, Phys. Rev. 85, 930 (1952).

Table I

Molar extinction coefficient,  $\epsilon$ , at 4.2°K for principal peaks in ZnS:MnS absorption spectrum as a function of concentration. C, in mole percent, is the analysis of a batch of crystals rather than the one for which the spectrum was measured, and is therefore only approximate. The so-called 2 percent sample must be closer to 4 percent. For the 100 percent sample, pure MnS, the  $\epsilon$  values are given for the bands which correspond to those of ZnS:MnS mixtures. Peak  $\epsilon$  values for a band are given in all cases.

Sample	C, %	l, mm	5300 Å		5100 Å		4600 Å		4200 Å	
			$\rho$	$\epsilon$	$\rho$	$\epsilon$	$\rho$	$\epsilon$	$\rho$	$\epsilon$
262A	1	1.05	0.02	0.41	0.085	1.80	0.115	2.40		
263B	4	1.27	0.13	1.30	0.43	3.65	0.60	5.10	0.52	4.40
263C-2	5	1.18	0.18	0.66	0.55	2.04	0.79	2.89	0.65	2.38
262D	8	0.55	0.16	0.78	0.55	2.72	0.70	3.40	0.54	2.63
224	11	0.48	0.67	2.72	2.03	8.20	2.52	10.40	1.46	5.95
246	100	0.05	0.66	2.80	0.61	2.55	1.62	6.80	-	-

Table II

Strength of temperature dependent line at 4654 Å as a function of temperature in two samples.  $p$  = optical density. The corrected optical density, e.g.,  $p - .35$  is divided by the maximum optical density in the last column for each sample.

5°/o Sample, # 263C-1 4654 Å			"2°/o" sample # 263B 4655 Å	
T°K	$p$	$\left(\frac{p-.35}{.91-.35}\right)$	T	$p' = \left(\frac{p-.23}{.45}\right)$
4.2	0.35	.0	4.2	.0
18	.52	.295	12.5	.01
28.5	.65	.536	17.5	.211
33.8	.71	.643	22.5	.373
43.6	.78	.778	26.0	.477
52.2	.84	.886	29.0	.544
64.5	.86	.912	34.0	.677
77.5	.91	1.	39.0	.755
88.5	.91	1.	46.0	.867
			58.0	1.01
			68.0	1.00

# FIGURE CAPTIONS

1. a. Absorption spectra of mixed crystals of ZnS:MnS at 4.2°K for various concentrations. All are cubic zinc blende structures except for the pure MnS which has the NaCl structure. The concentrations, thicknesses and sample numbers are given in the figure.  
  
b. Spectrum of ZnS:MnS (approx 5 percent MnS) at 4.2 and 77°K, showing spectral details. Note that 21481 and 21780 appear only in the 77°K spectrum. The line 21262 at 4.2° and 21280 at 77° are probably the same transition.
2. The 4650 Å band of ZnS: 5 percent MnS at a series of temperatures showing the two temperature sensitive bands (marked by arrows).
3. The 4650 Å band of ZnS: 2 percent MnS at a series of temperatures.
4. The 4650 Å band of ZnS: 8 percent MnS at a series of temperatures. The one distinct temperature sensitive band is marked by an arrow.
5. The absorption spectrum of Mn (H<sub>2</sub>O)<sub>4</sub>Cl<sub>2</sub> single crystal at room temperature showing the spectral assignments.
6. The energy of the Mn<sup>++</sup> states in a cubic field as a function of Dq.
7. The covalency parameter E for various compounds of Mn<sup>++</sup>.
8. Statistical probability of various species of agglomerates in ZnS:MnS mixed crystals.

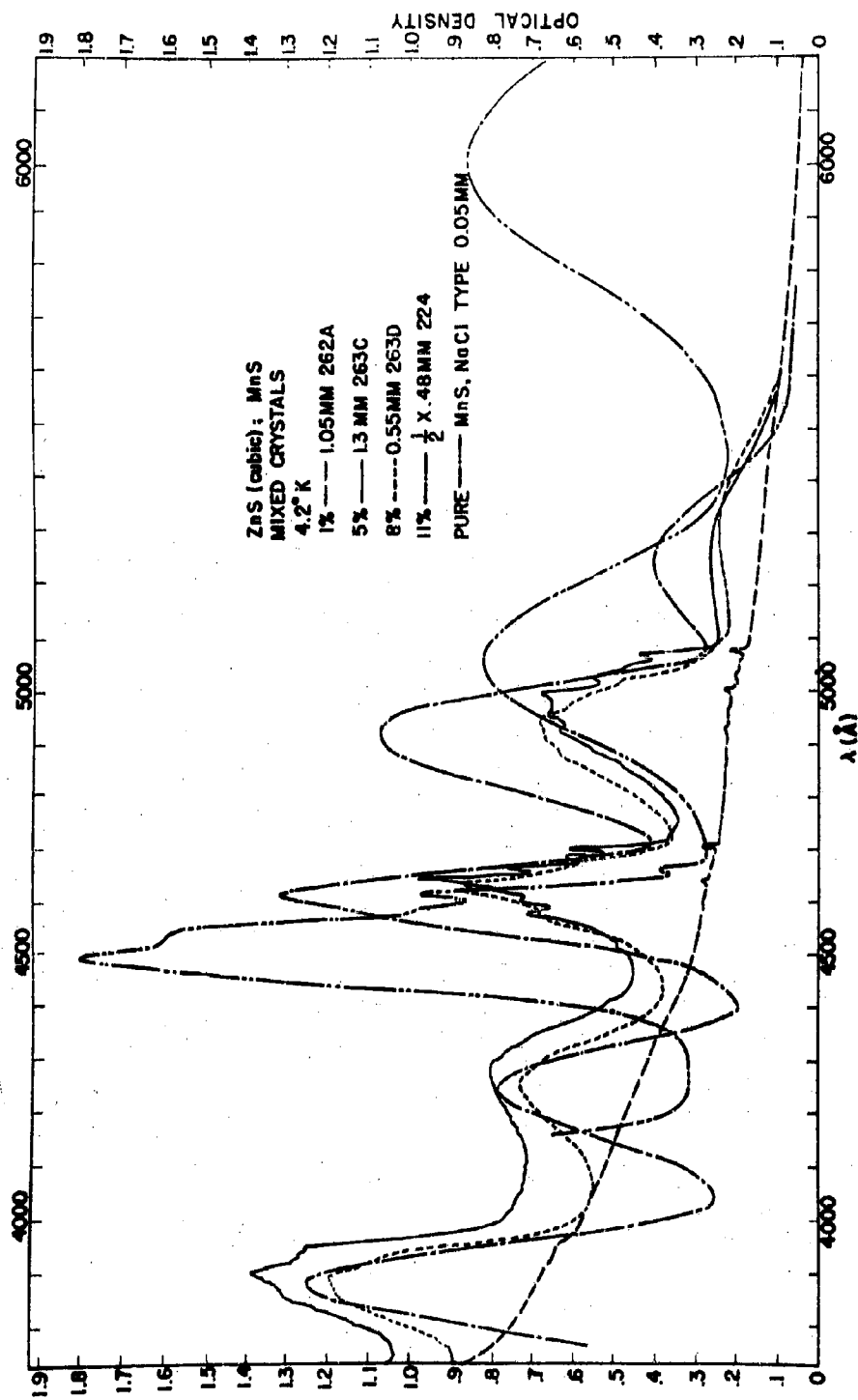


Figure 1a - IV

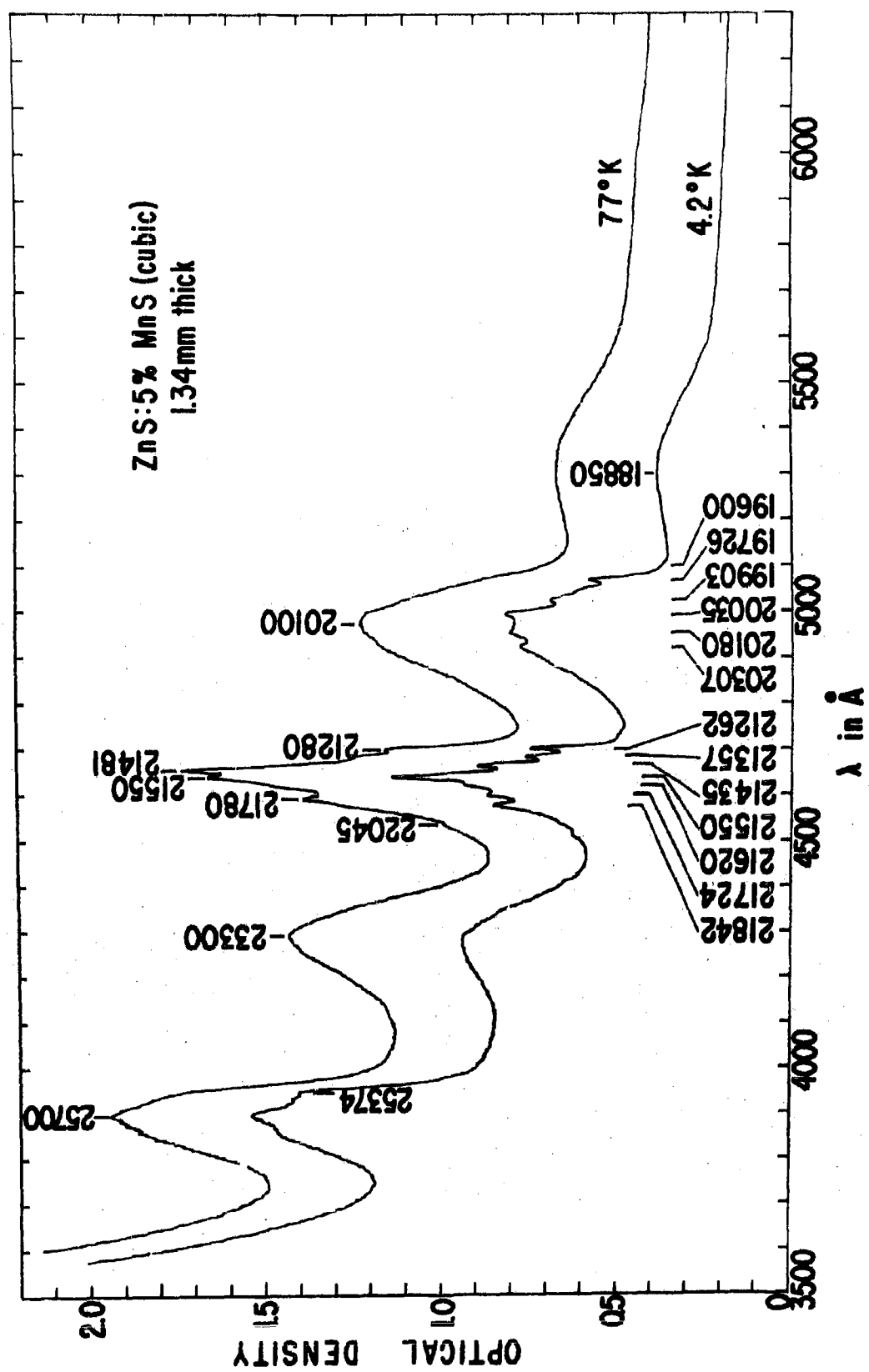


Figure 1b - IV

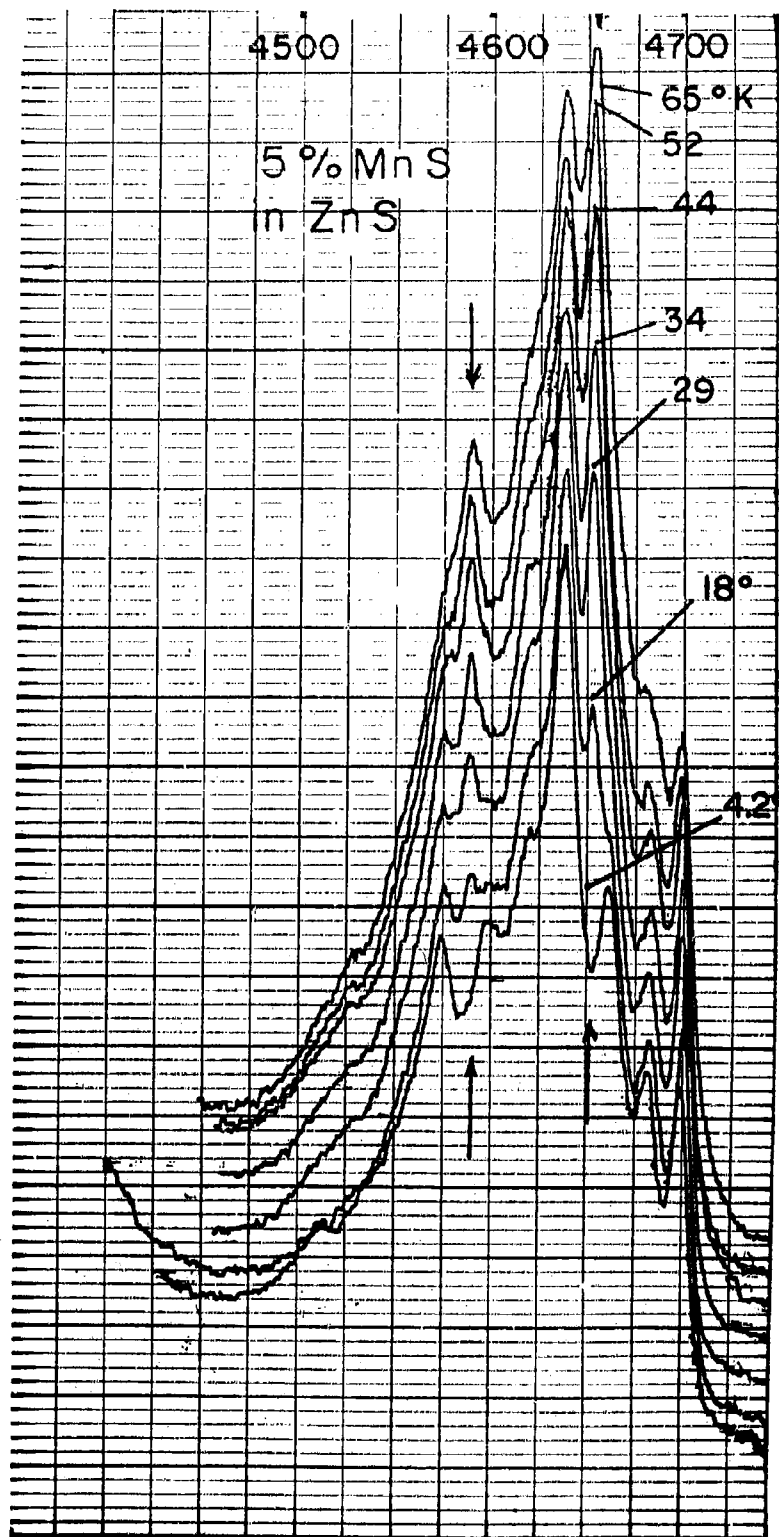


Figure 2 - IV

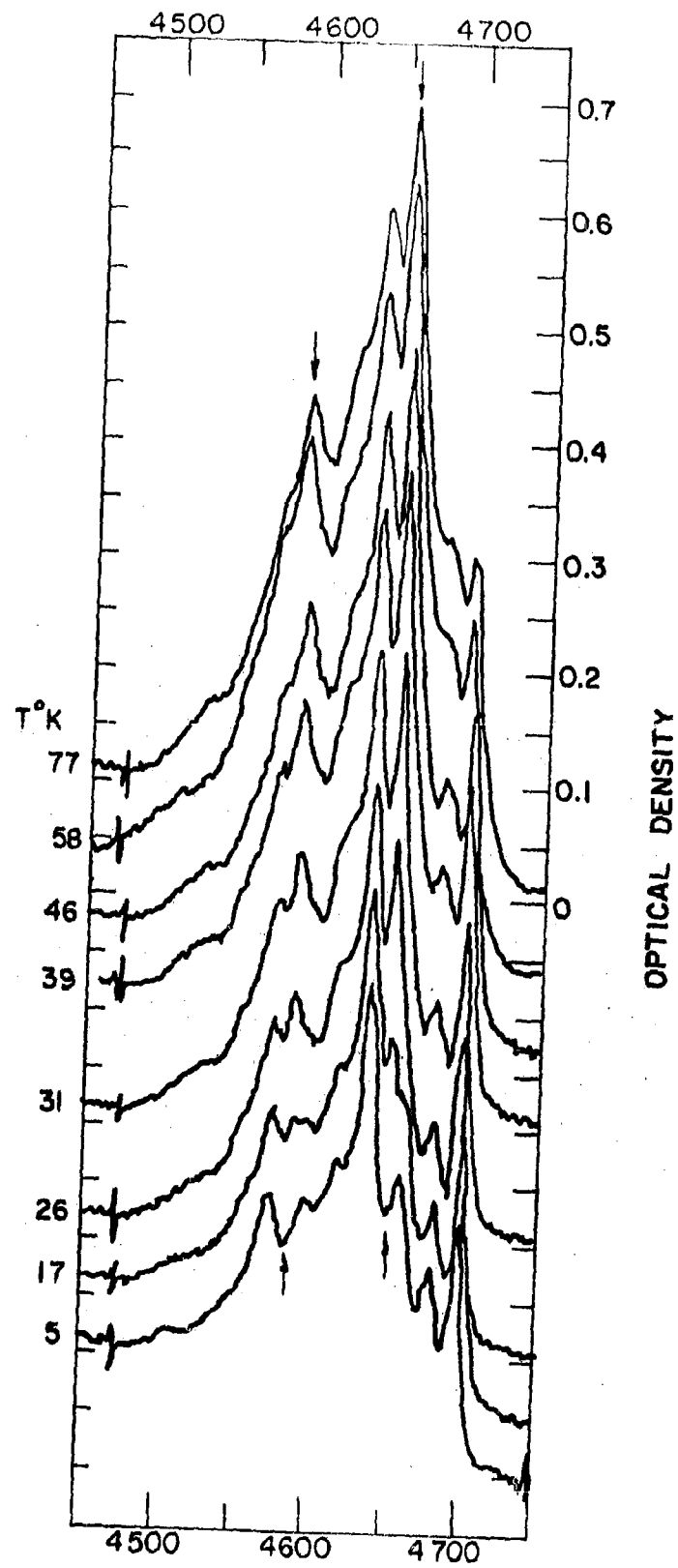


Figure 3 - IV



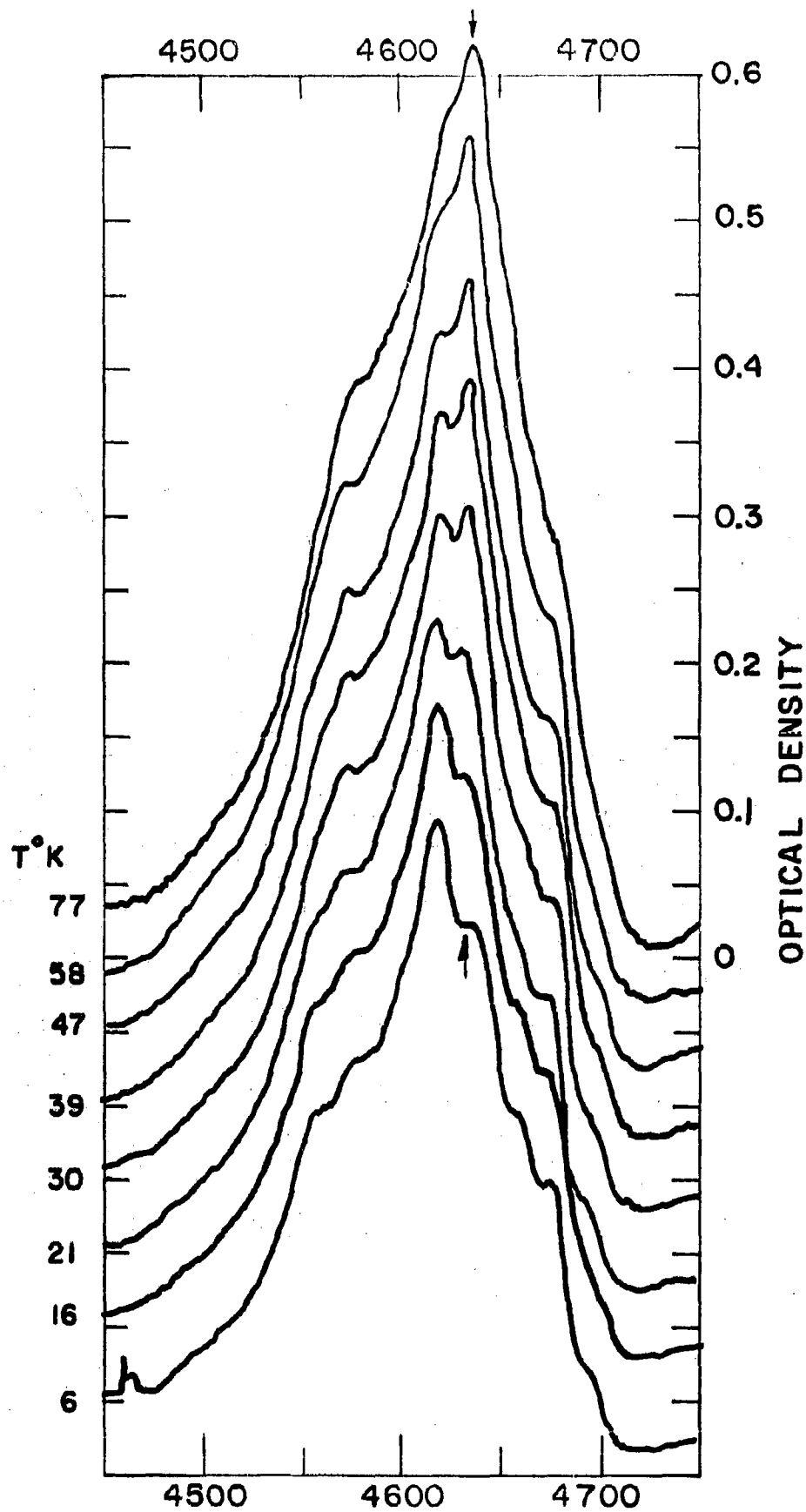


Figure 4 - 70

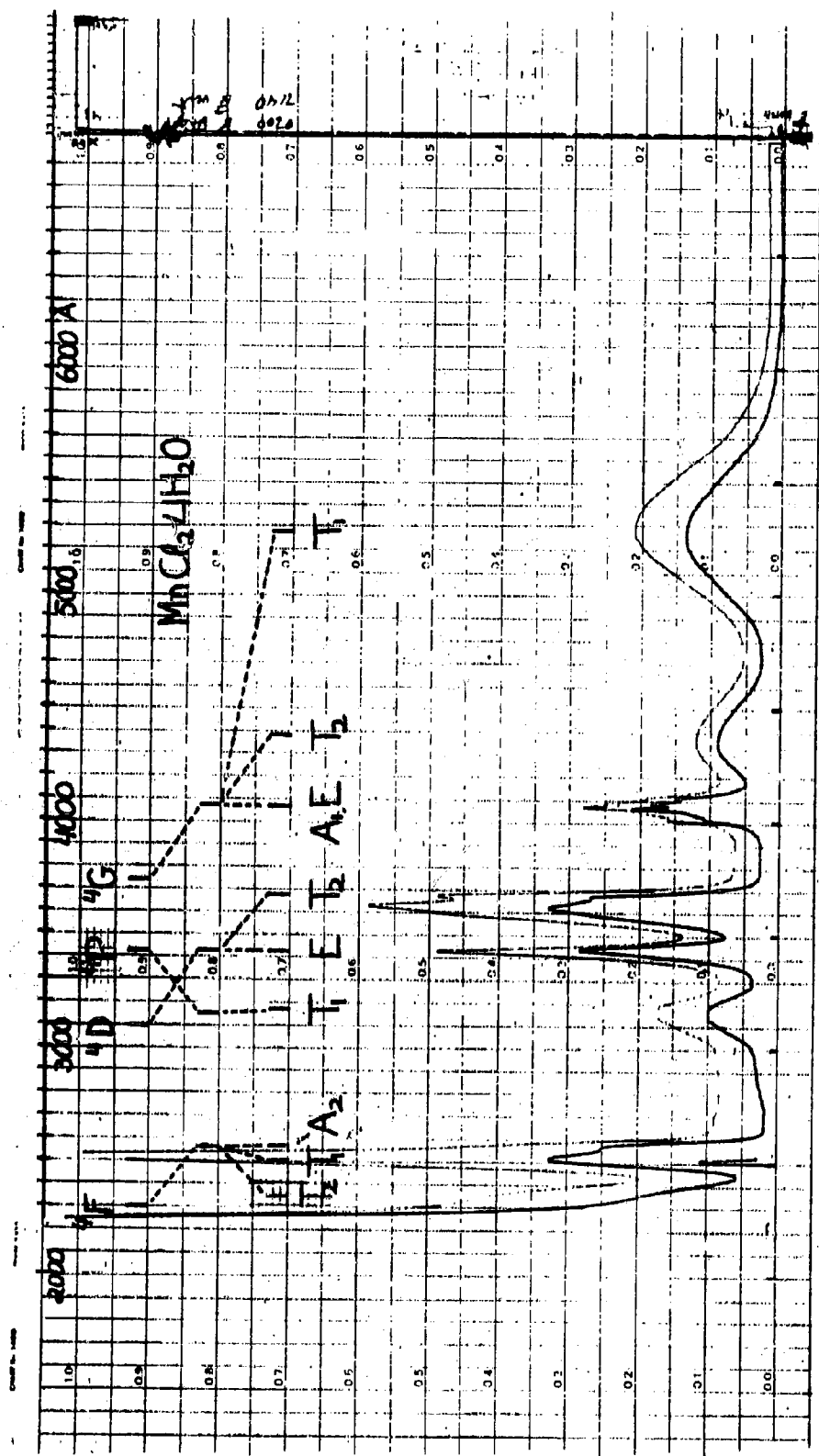


Figure 5 - IV

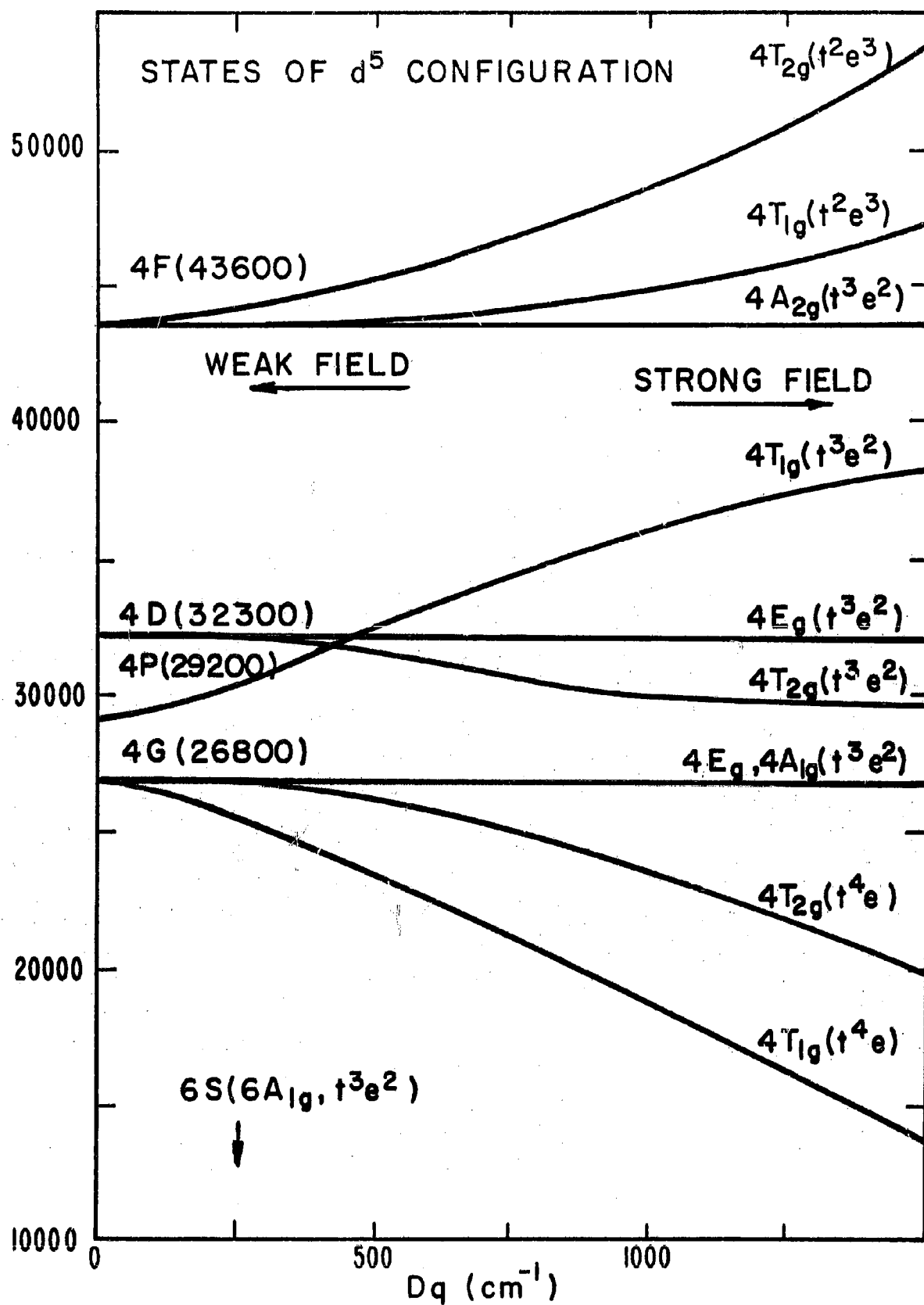


Figure 6 - IV

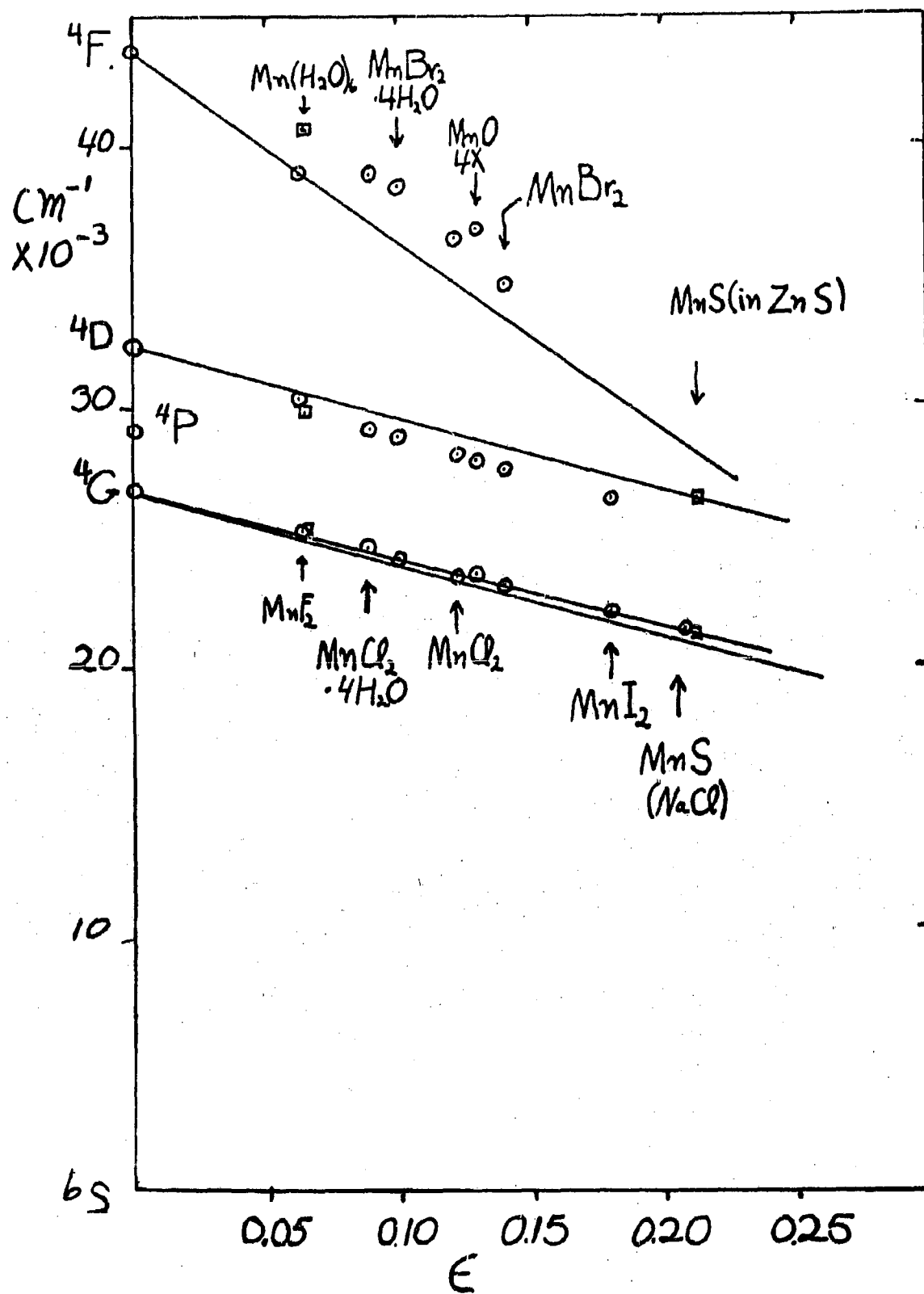
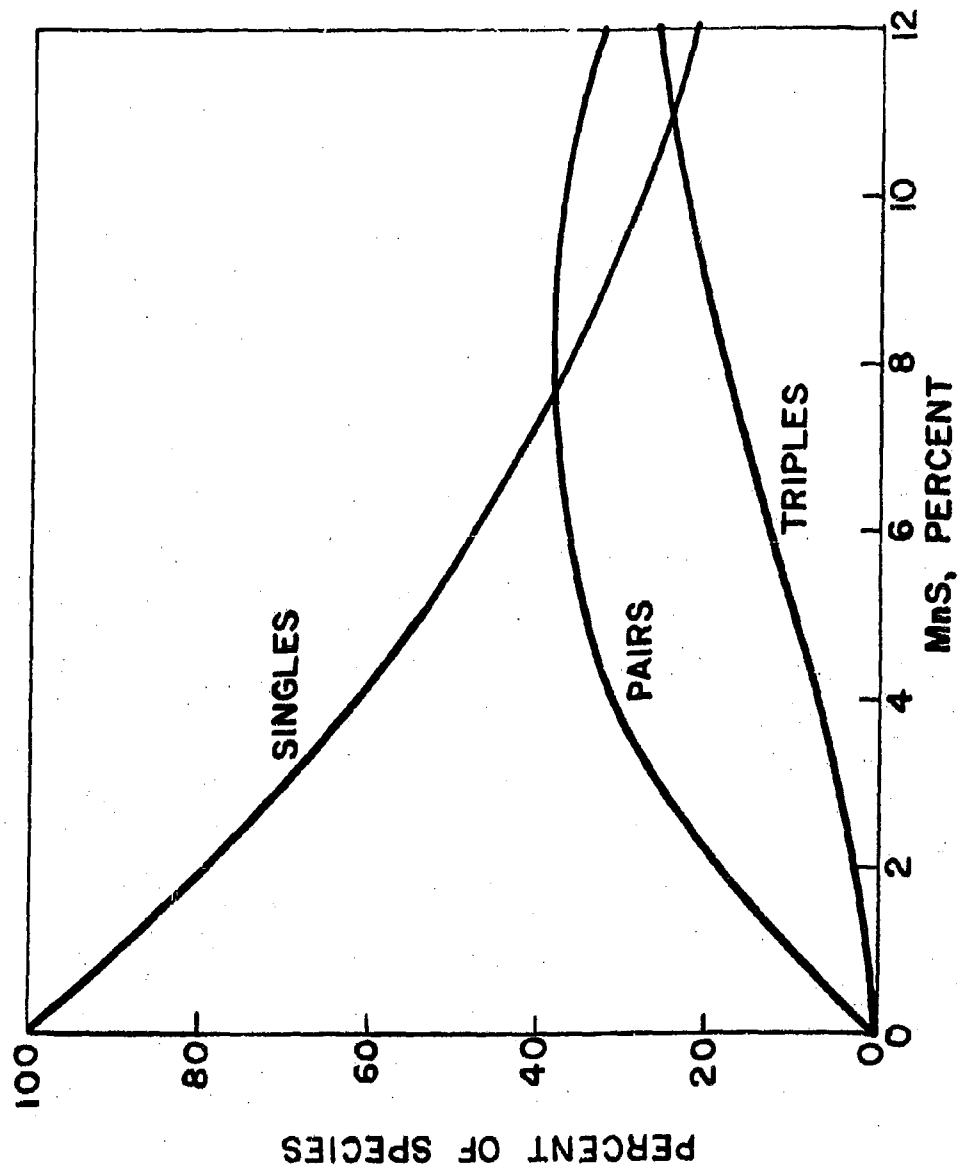


Figure 7 - IV



STATISTICAL PROBABILITY OF VARIOUS SPECIES  
IN ZnS (CUBIC): MnS